ON THE REPRESENTATION OF AEROSOL-CLOUD INTERACTIONS IN
ATMOSPHERIC MODELS

A Thesis
Presented to
The Academic Faculty

By

Donifan Barahona

In Partial Fulfillment
of the Requirements for the Degree
Doctor of Philosophy in the
School of Chemical and Biomolecular Engineering

Georgia Institute of Technology
August 2010

ON THE REPRESENTATION OF AEROSOL-CLOUD INTERACTIONS IN ATMOSPHERIC MODELS

Approved by:

Dr. Athanasios Nenes, Advisor
School of Chemical and Biomolecular
Engineering
Georgia Institute of Technology

Dr. Martha Grover
School of Chemical and Biomolecular
Engineering
Georgia Institute of Technology

Dr. Amyn Teja
School of Chemical and Biomolecular
Engineering
Georgia Institute of Technology

Dr. Judy Curry
School of Earth and Atmospheric Sciences
Georgia Institute of Technology

Dr. Irina Sokolik
School of Earth and Atmospheric Sciences
Georgia Institute of Technology

Date Approved: June 10, 2010

To Maricela,

there is nothing like finding the path together

ACKNOWLEDGEMENTS

TABLE OF CONTENTS

LIST OF TABLES

LIST OF FIGURES

LIST OF SYMBOLS AND ABBREVIATIONS

A	$\dfrac{g\Delta H M_w}{c_p R T^2} - \dfrac{g M_a}{RT}$
α_d	Water vapor to ice deposition coefficient
α_c	Water vapor to liquid uptake coefficient
B	$\dfrac{M_a p}{M_w p_i^o} - \dfrac{\Delta H^2 M_w}{c_p R T^2}$
γ	$\dfrac{\Gamma_2}{\Gamma_1};$
CCN	Cloud condensation nuclei
CDNC	Clod droplet number concentration
c_p	Specific heat capacity of air
D_c	Volume sphere-equivalent diameter of an ice particle
ΔH_s	Enthalpy of sublimation of water
ΔH_v	Enthalpy of vaporization of water
D_{IN}	Volume sphere-equivalent diameter of an IN
Δs	$s_{max} - s_o'$
Δs_{char}	$s_{max} - s_{char}$
Δs_{char}^*	Growth integral
D_v	Water vapor mass transfer coefficient
E	Entrainment rate
e_c	Critical entrainment rate
$e_{f,j}$	Maximum freezing efficiency of the jth IN species

$f_{c,hom},\ f_c$	Fraction of frozen particles at s_{hom} with and without IN present, respectively.
$f_{h,j}$	Shape factor of the jth IN species
G	Acceleration of gravity
G	$\left[\dfrac{\rho_i RT}{4 p_i^o D_v' M_w} + \dfrac{\Delta H_s \rho_i}{4 k_a T}\left(\dfrac{\Delta H_s M_w}{RT}-1\right)\right]^{-1}$
Γ_1	$\dfrac{\rho_i RT}{4 p_i^o D_v M_w} + \dfrac{\Delta H_s \rho_i}{4 k_a T}\left(\dfrac{\Delta H_s M_w}{RT}-1\right)$
Γ_2	$\dfrac{\rho_i RT}{2 p_i^o M_w}\sqrt{\dfrac{2\pi M_w}{RT}}\dfrac{1}{\alpha_d}$
H, H_v	Heaviside's function
I_e	Condensation integral
IF	Indirect forcing
IN	Ice Nuclei
$J(s_i),\ J$	Nucleation rate coefficient at s_i
$J_{hom}(s_{hom})$	Homogenous nucleation rate coefficient at s_{hom}
$J_{h,j}(s_{h,j})$	Heterogeneous nucleation rate coefficient at the freezing threshold of the jth IN population
$k(T)$	Freezing parameter defined
k_a	Thermal conductivity of air
k_{hom}	Homogeneous freezing parameter, $\ln\dfrac{J_{hom}(s_{hom})}{J_{hom}(s_i)}(s_{hom}-s_i)^{-1}$
λ	$\sqrt{\dfrac{1}{\alpha V \Gamma_1 \gamma^2}}$
$m_{1...nx}$	Multidimensional variable that symbolizes the mass fraction of the nx chemical species present in an aerosol population
m_j	Wettability parameter of the jth IN species, $\cos(\theta_j)$

$M_w,\ M_a$	Molar masses of water and air, respectively
N^*	$\sqrt{2}\left(\alpha V\,\Gamma_1\right)^{3/2}\left(\beta\dfrac{\pi}{2}\dfrac{\rho_i}{\rho_a}\right)^{-1}$
$N_{a,j}$	Number concentration of the jth insoluble aerosol species
N_c	Total ice crystal number concentration
$n_c(D_c,D_{IN},\widehat{m},t)$	Number distribution of the ice crystals
N_d	Droplet number concentration
N_{dust}	Dust number concentration
N_{soot}	Soot number concentration
N_{het}	Ice crystals number concentration from heterogeneous freezing
$N_{het}(s_i)$	Cumulative heterogeneous nucleation spectrum
$N_{hom}(s_i)$	Cumulative homogeneous nucleation spectrum
N_{IN}	IN number concentration
N_{lim}	Limiting N_{IN} that would prevent homogeneous nucleation
N_o	Number concentration of the supercooled liquid droplet population
$n_s(s_i)$	Heterogeneous nucleation spectrum
Nsp	Number of externally mixed IN populations
Nx	Number of chemical species present in the aerosol population
P	Ambient pressure
P_f	Freezing probability
p_i^o	Ice saturation vapor pressure
P_s	Saturation probability
Q_{aut}	Autoconversion rate
q_i	Ice water content
q_{tot}	Total water content

R	Universal gas constant
R_{eff}	Effective radius
RH	Relative humidity
ρ_i, ρ_a	Ice and air densities, respectively
$s_{h,j}$	Freezing threshold of the *jth* IN species
S	Supersaturation
s_c	Critical supersaturation
s_{char}	Characteristic freezing threshold of the heterogeneous IN population
s_{hom}	Homogeneous freezing threshold
s_i	Water vapor supersaturation ratio with respect to ice
S_i	Water vapor saturation ratio with respect to ice
S_{max}, s_{max}	Maximum saturation and supersaturation ratio
S_o	Mean saturation ration of a cloudy layer
s_o'	Freezing threshold of an IN
T	Temperature
T'	Ambient temperature
T_o	Initial temperature of the cloudy parcel
T	Time
T	Timescale
θ_j	Contact angle between the jth IN species surface and water
V, u	Vertical velocity
$\bar{v}_o$	Mean volume of the droplet population
w_i	Ice mass mixing ratio
W	Liquid water mass mixing ratio
X, U	Domain of integration
x, y	Dimensionless variable

$\bar{\Omega}_j$ Mean surface area of the jth insoluble aerosol population

SUMMARY

Anthropogenic atmospheric aerosols (suspended particulate matter) can modify the radiative balance (and climate) of the Earth by altering the properties and global distribution of clouds. Current climate models however cannot adequately account for many important aspects of these aerosol-cloud interactions, ultimately leading to a large uncertainty in the estimation of the magnitude of the effect of aerosols on climate. This thesis focuses on the development of physically-based descriptions of aerosol-cloud processes in climate models that help to address some of such predictive uncertainty. It includes the formulation of a new analytical parameterization for the formation of ice clouds, and the inclusion of the effects of mixing and kinetic limitations in existing liquid cloud parameterizations. The parameterizations are analytical solutions to the cloud ice and water particle nucleation problem, developed within a framework that considers the mass and energy balances associated with the freezing and droplet activation of aerosol particles. The new frameworks explicitly account for the impact of cloud formation dynamics, the aerosol size and composition, and the dominant freezing mechanism (homogeneous vs. heterogeneous) on the ice crystal and droplet concentration and size distribution. Application of the new parameterizations is demonstrated in the NASA Global Modeling Initiative atmospheric and chemical and transport model to study the effect of aerosol emissions on the global distribution of ice crystal concentration, and, the effect of entrainment during cloud droplet activation on the global cloud radiative properties. The ice cloud formation framework is also used within a parcel ensemble

model to understand the microphysical structure of cirrus clouds at very low temperature. The frameworks developed in this work provide an efficient, yet rigorous, representation of cloud formation processes from precursor aerosol. They are suitable for the study of the effect of anthropogenic aerosol emissions on cloud formation, and can contribute to the improvement of the predictive ability of atmospheric models and to the understanding of the impact of human activities on climate.

CHAPTER 1

INTRODUCTION

Widespread manufacturing, transportation, food production, and urbanization led to a much improved way of life, compared to the so-called preindustrial times, for a large fraction of the human population [6]. However, the constant exploitation of Earth's resources, as well as the production of solid waste and gas emissions associated with human activities, has been a significant factor driving climate change over the last two centuries [91]. There is overwhelming evidence that the anthropogenic influence on climate caused, among others, an increase in the Earth's mean temperature by at least 0.5 °C [91]. The warming of the climate system has brought about changes in sea level, ocean circulation, ice-covered surface, planetary reflectivity, and atmospheric dynamics [91], and has deeply affected many vulnerable animal species increasing their extinction risk [244]. Mitigation of these effects requires the understanding of the role that different anthropogenic and natural factors play on climate. This is however very challenging due to the multiple, highly non-linear, interactions between the many different climate elements [217]. It is further complicated by poor understanding of many climate processes, their wide range of scales (from micrometers to hundreds of kilometers), the difficulty of their quantification and observation, and the limitations in computational power available for climate studies [91]. Within this context, cloud processes have proven to be highly influential on climate, prone to anthropogenic influence, and very difficult to represent in climate models [91]. This study focuses on the study of the

formation of clouds, their modification by anthropogenic particle emissions, and their representation in climate and atmospheric models.

1.1. Clouds and Climate

The formation and evolution of clouds is one of the most important, yet least understood, components of the climate system [151, 126, 10]. Clouds modify the energy balance of the earth by scattering and absorbing solar and thermal radiation [245]; they can act either as warming or cooling agents [214, 33]. Low level, warm, clouds (e.g., stratocumulus and cumulus) tend to have a net cooling effect as they are efficient at reflecting shortwave without significantly modifying outgoing longwave radiation [146] (with the exception of polar regions, where they enhance warming and promote sea ice melting [39]). High level, cold, clouds, i.e. cirrus, anvils, and contrails, tend to warm climate as they interact more strongly with thermal than with solar radiation [145, 61]. Colds clouds also play a role in regulating the ocean temperature [213], maintaining the water vapor budget of the upper troposphere [78], and in the heterogeneous chemical reactions taking place at very low temperature [196, 161]. Warm clouds control the transport of water vapor in the lower troposphere and the availability of fresh water at the surface [208]. Due to the interplay of clouds with many different climatic processes, climate change assessments are very sensitive to assumptions regarding cloud properties [126].

Warm and cold clouds differ in their particle type, which is primarily a function of the temperature of cloud formation [208]. Warm clouds are made of liquid droplets and typically form between 260 and 280 K [41, 230]; cold clouds are made of ice crystals and form below 235 K [208, 253]. Mixed-phase clouds exist between these limits where liquid droplets and ice crystals are both formed together. Despite being mostly composed

2

of water, ice crystals and cloud droplets greatly differ in their shape, radiative properties [146], size, growth and evaporation rates, falling velocity, and collision rates [208]. They also come about by different formation processes, that is, cloud droplets form by "activation" of aerosol particles (defined as the onset of unstable growth), whereas ice crystals form by aerosol freezing (i.e., ice nucleation within, or mediated by, an aerosol particle). For this reason, cold and warm clouds are thought to exhibit a diverse range of susceptibility to pollution [151] and climate impacts [230, 146].
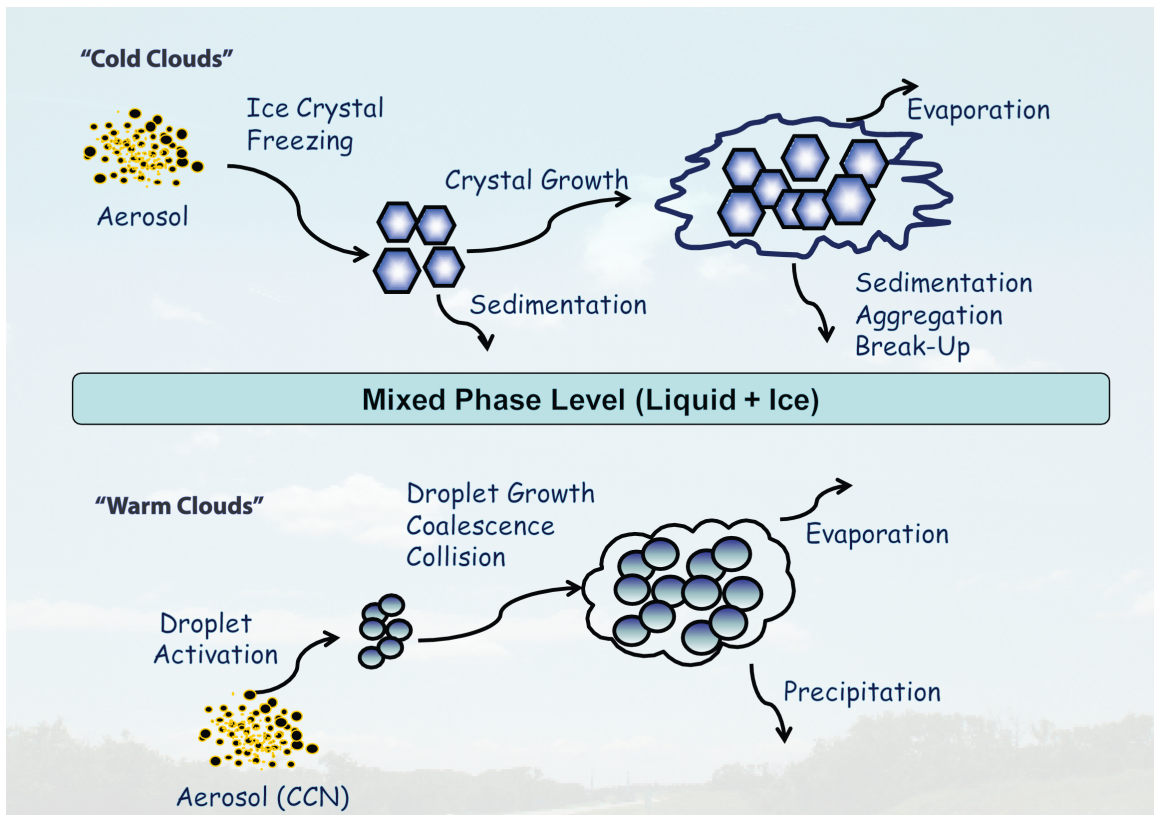
Figure 1.1. Scheme of microphysical processes occurring during the formation and evolution of clouds.

Large-scale (from tens to hundreds of kilometers) and microphysical (from micrometers to meters) processes play a role in the formation and evolution of clouds, as well as in defining their properties [230]. For example, cloud reflectivity is a function of the size, shape, and number of droplets/ice crystals, as well as, on the vertical extension of the cloud [146]. Similarly, the precipitation rate in warm clouds is to a large extent controlled by droplet size which is influenced by the number concentration of droplets and the cloud liquid water content [208]. Large scale dynamics set the conditions of relative humidity and temperature that allow cloud particles to be formed; it also controls the vertical and horizontal extension of the cloud. Microphysical processes like activation/freezing, evaporation, collision, coalescence, and sedimentation interact and control the number concentration of droplets and ice crystals present in a cloud (Figure 1.1). In this work special attention is given to the formation of cloud particles (i.e., droplet activation and ice crystal freezing) as this is one of the microphysical processes that can be most influenced by anthropogenic emissions.

1.2. The Formation of Cloud Particles

Atmospheric dynamics is not capable of producing the very high supersaturation (~ 200%) required to nucleate a new liquid or ice phase directly from the vapor phase [113]. All cloud formation processes thus involve nucleation of hydrometeors upon preexisting aerosol particles dispersed in the atmosphere. These aerosol particles lower the supersaturation needed for the formation of a new phase allowing cloud formation at atmospheric conditions [208]. In warm clouds the aerosol particles precursor to cloud droplets are termed Cloud Condensation Nuclei (CCN). The ability of an aerosol to act as a CCN, is controlled by its physicochemical properties; thus, the aerosol size distribution

4

and mixing state [163], the solubility and hygroscopicity of the aerosol components [136, 163, 8], the presence of soluble gases, the formation of surfactant layers that can change surface tension and water vapor uptake rate [162], and the rate at which solutes dissolve in water [7] play an important role in the formation of new droplets. Besides these factors, the dynamical (e.g., updraft velocity [193], mixing and entrainment [11]) and thermodynamical state (temperature, pressure, relative humidity) of the cloudy air mass profoundly impact the droplet formation process. The measurement and characterization of CCN in the atmosphere have been under development for more than fifty years and very efficient techniques are currently available [187, 176]. They have shown that sea salt, sulfates, nitrates, ammonium, organics, and carbonaceous material are the main components of CCN [230].

In a large number of cases CCN activation can be adequately modeled using simple thermodynamic arguments (i.e., Köhler theory [128]), describing the equilibrium of a liquid droplet with its environment. Within this picture, activation occurs after CCN are exposed to some "critical supersaturation" which depends on their size and composition, and marks the onset of unstable growth [208, 230]. Difficulties in applying Köhler theory may arise in describing the activation of partially soluble or insoluble substances [163], determining the activities of individual components in solution [160], or when the aerosol particles are far from their thermodynamic equilibrium at the point of activation [32, 200, 18], for which corrections to Köhler theory are needed [160]. CCN activation is a heterogeneous process in the sense that the new phase (liquid water) is formed after wetting of a solid surface (and often subsequent deliquescence) rather than directly from the vapor phase [208].

The formation of ice crystals from precursor aerosol particles, i.e., the mechanism of formation cold clouds, is less understood than the activation of CCN into cloud droplets [208]. Ice nucleation is an stochastic process where spontaneous density fluctuations trigger the formation of the ice phase [208]. Thermodynamic variables like relative humidity, temperature, composition, and size, define the probability of occurrence of these fluctuations [113], however the mechanism by which they result in the nucleation of ice is still not completely elucidated. This is further complicated by the interaction of the solid, liquid and vapor phases during freezing. Whereas CCN activation depends almost exclusively on the interaction between the liquid (i.e., the deliquesced aerosol) and the vapor phase (with the exception of dust activation [135]), during freezing, the solid phase plays an active role providing active sites where nucleation of the new ice phase can readily occur [56-57, 251]. Thus, freezing mechanisms are classified as "homogeneous" when only liquid and vapor interact during freezing, and "heterogeneous" when freezing is mediated by a surface [208]. Aerosol particles that freeze homogeneously are usually termed "supercooled droplets", whereas those that freeze heterogeneously are termed Ice Nuclei (IN).

Homogeneous freezing occurs mainly in $(NH_4)_2SO_4$ and H_2SO_4 solution droplets [225, 27, 143], although the presence of partially soluble organic material may also be significant [107]. Extensive experimental studies [e.g., 129] as well as modeling efforts now allow the calculation of homogeneous freezing rates [117] with some degree of accuracy. For some time, homogenous freezing was considered to be the dominant mechanism of cold cloud formation [85]. Notable advances in describing the freezing of supercooled droplets made during the last decade revise somewhat this picture [129, 43,

76, 117]. Recent studies however suggest that freezing of IN likely plays a significant role on the formation of cold clouds [28, 263, 43, 47] and the interplay of homogenous and heterogeneous freezing is still matter of debate. Some studies have shown that by enhancing ice formation at low relative humidity, heterogeneous effects may suppress homogeneous freezing [44, 108, 69, 76, 13-14]. Others have reported heterogeneous freezing is only significant over continents, whereas over oceans, homogeneous freezing prevails [27, 76, 1]. Recently it has been proposed that at very low temperatures heterogeneous freezing is the main path of cloud formation [1, 94, 183] (although this is cast under question in Chapter 6).

The heterogeneous nucleation of ice is a very complex process and its current understanding is very limited. Heterogeneous freezing rates depend on the specific interaction between solid, liquid, and vapor phases at the moment of freezing, which are usually referred to as freezing modes. Typical examples are deposition, where water vapor is directly adsorbed onto the solid surface and then transformed into ice, contact, where freezing is initiated at the moment of contact between the IN and a supercooled droplet, condensation, where the IN acts as a CCN forming a drop which freezes during the condensation stage, and immersion, where freezing is started by the action of an insoluble IN immersed into a liquid droplet [208]. New modes have been discovered very recently including those mediated by glasses [183] and evaporation [49]. Atmospheric sources of IN are associated with the long range transport of dust [47, 224] and pollution [61], and the aerosol emissions from aircrafts [229, 169]. It has been shown that IN can be composed of mineral dust [47, 224], sulfates [1], crustal material [263, 90], carbonaceous material (soot and non-soot carbon rich) [19, 38, 261], and metallic

particles (Al, Fe, Ti, Cr, Zn, and Ca) [28, 43], however the reasons underlying their freezing activity are still not known.

1.3. The Anthropogenic Aerosol Indirect Effect on Climate

Human activities emit large amounts of aerosol particles (mainly composed of sulfates, black carbon, organics, and dust [214]), which significantly alter the natural background aerosol concentration. These aerosol emissions can modify the scattering and absorption of thermal and solar radiation in the atmosphere ("aerosol direct effect") [24, 170, 214, 91]. They can also alter concentration of CCN and IN in the atmosphere and therefore perturb cloud formation processes. The climatic response to the modification of cloud properties from aerosol emissions is known as the aerosol indirect effect on climate [248, 170, 151, 91].

The aerosol indirect effect is currently the second largest anthropogenic forcing on climate, thought to offset about half of the warming caused by greenhouse gas emissions [170, 91, 180]. It is also the single largest source of uncertainty in the assessment of human- induced climate change [91]. This uncertainty originates from the limited understanding of the formation of cloud droplets and ice crystals [186, 151], the large sensitivity of climate model results to the representation of cloud properties [164, 126], and the limited representation of cloud formation processes in climate models [41, 29, 151]. The latter arises because the formation of droplets and ice crystals occurs at a much smaller scale than large-scale climate models can resolve (which is typically hundreds of kilometers [151]). Detailed description of cloud formation from aerosols is also complex and computationally expensive. Furthermore, aerosol composition and sizes vary widely

around the planet [91], posing a difficulty to the prediction of aerosol properties in climate models.

The study of the aerosol indirect effect on climate requires a computationally efficient, analytical, link between the large-scale properties of the cloud and the microscopic properties of the precursor aerosol, usually referred to as a cloud formation parameterization. Initial attempts to parameterize cloud formation used empirical formulations based on cloud measurements [21, 151]. It is now recognized that a physically-based approach is required to account for all the spatial and temporal variability in cloud formation conditions and aerosol characteristics occurring in the Earth's atmosphere [151].

1.4. Thesis Outline

This thesis is based in deriving simple but comprehensive relationships describing the main processes of cloud formation in the atmosphere, explicitly revealing the role of aerosol properties and cloud formation conditions on the ice crystal and droplet size distribution. These relationships can be found by solving the particle population, mass and energy balances associated with cloud formation. They are intended for use as parameterizations in atmospheric models for studying the aerosol indirect effect on climate. Chapters 2 to 4 are dedicated to developing such relationships for cold cloud formation driven by homogeneous and heterogeneous freezing. Chapter 5 presents the application of these relations within a global climate model to study the global effect of aerosol emissions on the global concentration of ice crystals. Chapter 6 extents these formulations using a stochastic approach to demonstrate the existence of pseudo-equilibrium states in cold clouds at very low temperatures.

The parameterizations of warm cloud formation developed in Chapters 7 and 8 build upon the works of Nenes and Seinfeld [189] and Fountoukis and Nenes [58], who formulated analytical solutions to the mass and energy balances associated with cloud droplet activation. In Chapter 7, a parameterization accounting for the effect of mixing and entrainment of dry air during cloud formation is developed. Chapter 8 considers the effect of very large, kinetically limited particles during droplet activation. Chapter 9 applies these formulations to the study of the effect of mixing and entrainment on global cloud droplet number and size, precipitation rate, and aerosol indirect forcing associated with warm, liquid clouds. Chapter 10 discusses future directions in the parameterization of cloud formation for large scale models.

CHAPTER 2

CIRRUS FORMATION BY HOMOGENEOUS FREEZING[1]

This study presents a new physically-based parameterization of cirrus cloud formation for use in large scale models which is robust, computationally efficient, and links chemical effects (e.g., water activity and water vapor deposition effects) with ice formation via homogenous freezing. The parameterization formulation is based on ascending parcel theory, and provides expressions for the ice crystal size distribution and the crystal number concentration, explicitly considering the effects of aerosol size and number, updraft velocity, and deposition coefficient. The parameterization is evaluated against a detailed numerical cirrus cloud parcel model (also developed during this study) where the solution of equations is obtained using a novel Lagrangian particle tracking scheme. Over a broad range of cirrus forming conditions, the parameterization reproduces the results of the parcel model within a factor of two and with an average relative error of -15%. If numerical model simulations are used to constraint the parameterization, error further decreases to $1 \pm 28\%$.

---

[1] This chapter appears as reference [12]: BARAHONA, D. and NENES, A. (2008). Parameterization of Cirrus Formation in Large Scale Models: Homogeneous Nucleation. Journal of Geophysical Research, 113, D11211, doi:10.1029/2007JD009355.

2.1. Motivation

The effect of aerosols on clouds and climate is one of the major uncertainties in anthropogenic climate change assessment and prediction [91]. Cirrus is one of the most poorly understood cloud systems, yet they can strongly impact climate. Cirrus are thought to have a net warming effect because of their low emission temperatures and small thickness [145]. They also play a role in regulating the ocean temperature [213] and maintaining the water vapor budget of the upper troposphere and lower stratosphere [78]. Concerns have been raised on the effect of aircraft emissions [195, 169, 237, 91] and long-range transport of pollution [61] changing the properties of upper tropospheric clouds, i.e., cirrus and anvils, placing this type of clouds in the potentially warming components of the climate system.

Cirrus clouds form by the homogenous freezing of liquid droplets, by heterogeneous nucleation of ice on ice nuclei, and the subsequent grow of ice crystals [208]. This process is influenced by the physicochemical properties of the aerosol particles (i.e., size distribution, composition, water solubility, surface tension, shape), as well as by the thermodynamical state (i.e., relative humidity, pressure, temperature) of their surroundings. Dynamic variability (i.e., fluctuations in updraft velocity) also impact the formation of cirrus clouds potentially enhancing the concentration of small crystals [142, 112, 86].

The potential competition between homogeneous and heterogeneous mechanisms has an important impact on cirrus properties. For instance, by enhancing ice formation at low relative humidity, heterogeneous effects may suppress homogeneous freezing and decrease the ice crystal concentration of the newly formed cloud [44, 108, 69, 76]. It has

been suggested that heterogeneous freezing is the dominant path of cirrus formation over polluted areas [27, 76, 1], at low updraft velocities (less than 10 cm s^{-1}) [45-46, 110], and at temperatures higher than -38 °C where homogenous nucleation is not probable [208, 43]. Conversely, homogenous freezing is thought to be the prime mechanism of cirrus formation in unpolluted areas, high altitudes, and low temperatures [85, 98, 143, 76, 23, 121].

A major challenge in the description of cirrus formation is the calculation of the nucleation rate coefficient, J_{hom}, i.e., the rate of generation of ice germs per unit of volume for homogeneous freezing. Historically this has been addressed with application of classical nucleation theory [45, 208, 243], or using empirical correlations [i.e., 129]. The former requires the accurate knowledge of thermodynamic properties, such as surface and interfacial tensions, densities, and activation energies [23]. With appropriate extensions [i.e., 44-45, 122, 27, 143], theory included in cirrus formation simulations shows agreement with experimental measurements and field campaigns [i.e., 27, 5, 121]. Still, the physical properties of aqueous solutions and ice at low temperatures are subject to large uncertainty. Until now, the most reliable methods to calculate J_{hom} are based on laboratory measurements [143]. *Koop et al.* [129] used experimental data to develop a parameterization showing J_{hom} as a function of water activity and temperature (rather than on the nature of the solute), which has been supported by independent measurements of composition and nucleation rate during field campaigns and cloud chamber experiments [i.e., 75, 174].

The formation of cirrus clouds is modeled by solving the mass and energy balances in an ascending (cooling) cloud parcel [e.g., 208]. Although models solve the same equations (described in section 2.1), assumptions about aerosol size and composition, J_{hom} calculation, deposition coefficient, and numerical integration procedure strongly impact simulations. This was illustrated during the phase I of the Cirrus Parcel Model Comparison Project [143]; for identical initial conditions, seven state-of-the-art models showed variations in the calculation of ice crystal concentration, N_c, (for pure homogeneous freezing cases) up to a factor of 25, which translates to a factor of two difference in the infrared absorption coefficient. *Monier, et al.* [175] showed that three orders of magnitude difference in the value of J_{hom}, which is typical among models at temperatures above -45 °C, will account only for about a factor of two variation in N_c calculation. The remaining variability in N_c results from the numerical scheme used in the integration, the calculation of the water activity inside the liquid droplets at the moment of freezing, and the value of the water vapor deposition coefficient.

Introducing ice formation microphysics in large scale simulations requires a physically-based link between the ice crystal size distribution, the precursor aerosol, and the parcel thermodynamic state. Empirical correlations derived from observations are available [i.e., 127]; their applicability however for the broad range of cirrus formation presented in a GCM simulation is questionable. Numerical simulations have been used to produce prognostic parameterizations for cirrus formation [223, 147], which relate N_c to updraft velocity and temperature (the *Liu and Penner* parameterization also takes into account the dependency of N_c on the precursor aerosol concentration, and was incorporated into the NCAR Community Atmospheric Model (CAM3) [149]). Although

14

based on theory, these parameterizations are constrained to the values of parameters (i.e., deposition coefficient, aerosol composition and characteristics) used during the parcel model simulations (the uncertainty of which is quite large). *Kärcher and Lohmann* [109, 108] introduced a physically-based parameterization solving analytically the parcel model equations. In their approach, a "freezing time scale" is used (related to the cooling rate of the parcel) to approximate the crystal size distribution at the peak saturation ratio through a function describing the temporal shape of the freezing pulse. This function, along with the freezing time scale, should be prescribed (the freezing pulse shape and freezing time scale may also change with the composition and size of the aerosol particles). An analytical fit of the freezing time scale based on *Koop et al.* [129] data was provided by *Ren and Mackenzie* [216]. The parameterization of *Kärcher and Lohmann* has been applied in GCM simulations [152, 154] and extended to include heterogeneous nucleation and multiple particle types [106]. All parameterizations developed to date provide limited information on the ice crystal size distribution, which is required for computing the radiative properties of cirrus clouds [145].

This study presents a new physically-based parameterization for ice formation from homogeneous freezing. The parameterization unravels much of the stochastic nature of the cirrus formation process by linking crystal size with the freezing probability, and explicitly considers the effects the deposition coefficient and aerosol size and number, on N_c. With this approach, the requirement of prescribed parameters is relaxed and the size distribution, peak saturation ratio, and ice crystal concentration can be computed. The parameterization is then evaluated against a detailed numerical parcel model (also

presented here), which solves the model equations using a novel Lagrangian particle tracking scheme.

2.2. Numerical Cirrus Parcel Model

Homogenous freezing of liquid aerosol droplets is a stochastic process resulting from spontaneous fluctuations of temperature and density within the supercooled liquid phase [208]. Therefore, only the fraction of frozen particles at some time can be computed (rather than the exact moment of freezing). At anytime during the freezing process, particles of all sizes have a finite probability of freezing; this implies that droplets of the same size and composition will freeze at different times, so even freezing of a perfectly monodisperse droplet population will result in a polydisperse crystal population. This conceptual model can be extended to a polydisperse droplet population; each aerosol precursor "class" will form an ice crystal distribution with its own composition and characteristics, which if superimposed, will represent the overall ice distribution. In this section, the formulation of a detailed numerical model, taking into account these considerations, is presented. The equations of the model share similar characteristics with those proposed by many authors [208, 143, and references therein] as the ascending parcel framework is used for their development.

2.2.1. Formulation of the Parcel Equations

The equations that describe the evolution of ice supersaturation, s_i (defined as the ratio of water vapor pressure to equilibrium vapor pressure over ice minus one), and temperature, T, in an adiabatic parcel, with no initial liquid water present, are [208].

$$\frac{ds_i}{dt} = -\frac{M_a p}{M_w p_i^o}\frac{dw_i}{dt} - (1+s_i)\left[\frac{\Delta H_s M_w}{RT^2}\frac{dT}{dt} - \frac{gM_a}{RT}V\right] \qquad (2.1)$$

$$\frac{dT}{dt} = -\frac{gV}{c_p} - \frac{\Delta H_s}{c_p}\frac{dw_i}{dt} \qquad (2.2)$$

where ΔH_s is the latent heat of sublimation of water, g is the acceleration of gravity, c_p is the heat capacity of air, p_i^o is the ice saturation vapor pressure at T [179], p is the ambient pressure, V is the vertical velocity, M_w and M_a are the molar masses of water and air, respectively, and R is the universal gas constant. For simplicity, radiative cooling effects have been neglected in equation, (2.2) although in principle they can be readily included. By definition, the ice mixing ratio in the parcel, w_i, is given by [12]

$$w_i = \frac{\rho_i}{\rho_a}\frac{\pi}{6}\int_{D_{o,min}}^{D_{o,max}}\int_{D_{c,min}}^{D_{c,max}} D_c^3 n_c(D_c, D_o)dD_c dD_o \qquad (2.3)$$

where ρ_i and ρ_a are the ice and air densities, respectively. D_c is the volume-equivalent diameter of an ice particle (assuming spherical shape), D_o is the wet diameter of the freezing liquid aerosol, $n_c(D_c, D_o) = \dfrac{dN_c(D_o)}{dD_c}$ is the ice crystal number distribution function, $N_c(D_o)$ is the number density of ice crystals in the parcel formed at D_o; $D_{o,min}$, and $D_{o,max}$ limit the liquid aerosol size distribution, and $D_{c,min}$ and $D_{c,max}$ the ice crystal size distribution. Taking the time derivative of (2.3) we obtain

$$\frac{dw_i}{dt} = \frac{\rho_i}{\rho_a}\frac{\pi}{2}\int_{D_{o,min}}^{D_{o,max}}\int_{D_{c,min}}^{D_{c,max}} D_c^2 \frac{dD_c}{dt} n_c(D_c, D_o)dD_c dD_o \qquad (2.4)$$

where the term $D_c^3 \dfrac{\partial n_c(D_c, D_o)}{\partial t}$ was neglected as instantaneous nucleation does not contribute substantially to the depletion of water vapor in the cloudy parcel. The growth term in Eq. (2.4) is given by [208, 230, 12]

17

$$\frac{dD_c}{dt} = \frac{(s_i - s_{i,eq})}{\Gamma_1 D_c + \Gamma_2} \tag{2.5}$$

with

$$\Gamma_1 = \frac{\rho_i RT}{4 p_i^o D_v M_w} + \frac{\Delta H_s \rho_i}{4 k_a T}\left(\frac{\Delta H_s M_w}{RT} - 1\right) \qquad \Gamma_2 = \frac{\rho_i RT}{2 p_i^o M_w}\sqrt{\frac{2\pi M_w}{RT}}\frac{1}{\alpha_d} \tag{2.6}$$

where k_a is the thermal conductivity of air, D_v is the water vapor diffusion coefficient from the gas to ice phase, $s_{i,eq}$ is the equilibrium supersaturation with respect to ice, and α_d is the water vapor deposition coefficient.

The crystal size distribution, $n_c(D_c, D_o)$ is calculated by solving the condensation equation [65, 230]

$$\frac{\partial n_c(D_c, D_o)}{\partial t} = -\frac{\partial}{\partial D_c}\left(n_c(D_c, D_o)\frac{dD_c}{dt}\right) \tag{2.7}$$

subject to the boundary and initial conditions (neglecting any change of volume upon freezing),

$$\left.\frac{\partial n_c(D_c, t)}{\partial t}\right|_{D_c = D_o} = n_o(D_o, t)\frac{\partial P_f(D_o, t)}{\partial t} \equiv \psi(D_o, t) \quad ; \quad n_c(D_c, D_o, 0) = 0 \tag{2.8}$$

where $n_o(D_o, t)$ is the liquid aerosol size distribution function, $\psi(D_o, t)$ is the nucleation function which describes the number concentration of droplets frozen per unit of time, and $P_f(D_o, t)$ is the cumulative probability of freezing, given by [208, 12]

$$P_f(D_o, t) = 1 - \exp\left(-\frac{\pi}{6}\int_0^t D_o^3 J_{\text{hom}} dt\right) \tag{2.9}$$

and

$$\frac{\partial P_f(D_o,t)}{\partial t} = \frac{\pi}{6} D_o^3 J(t) \exp\left(-\frac{\pi}{6} \int_0^t D_o^3 J_{\text{hom}} dt\right) \tag{2.10}$$

J_{hom} is the homogeneous nucleation rate coefficient, and describes the number of ice germs formed per unit of volume of liquid droplets per unit of time [208]. Equation (2.7) is a simplified version of the continuous general dynamic equation for the ice crystal population [66], where the nucleation term has been set as a boundary condition to facilitate its solution [65, 157, 210]. This can be done since the size of the ice particles equals the size of the precursor aerosol only at the moment of freezing.

The evolution of the liquid droplets size distribution, $n_o(D_o,t)$, is calculated using an equation similar to (2.7),

$$\frac{\partial n_o(D_o,t)}{\partial t} = -\frac{\partial}{\partial D_o}\left(n_o(D_o)\frac{dD_o}{dt}\right) - \psi(D_o,t) \tag{2.11}$$

The first term of the right hand side of Eq. (2.11) represents the growth of aerosol liquid particles by condensation of water vapor, and the second term the removal of liquid particles by freezing. Boundary and initial conditions for (2.11) are simply the initial aerosol size distribution and the condition of no particles at zero diameter.

2.2.2. Numerical Solution of Parcel Model Equations

Several methods have been proposed to solve condensation-type equations like (2.7) and (2.11) [65, 157, 210 and references therein]. They are mostly based on the numerical method of lines (although methods of moments, weighted residuals and Montecarlo simulations are also employed [210]). Typically, Eq. (2.7) is split into a system of time-dependent ordinary differential equations discretized along in size using a fixed grid. This however introduces numerical diffusion along the size axis, particularly for stiff

nucleation and size dependent growth rate [see for example Figure 7 in 210]. Thus for ice nucleation using a fixed grid may lead to overestimation of the surface area of ice crystals, and therefore introduce biases in the calculation of N_c. This is avoided by using a particle tracking grid for the ice crystal population (the growth of groups of ice crystals is followed after freezing) coupled to a moving grid scheme (the liquid aerosol population is divided into bins the size of which is changing with time), for the liquid aerosol population. Within this scheme, a new "line" of integration is defined at each time step and droplet size. This is referred to as the "Lagrangian particle tracking scheme" and is illustrated in Figure 2.1.
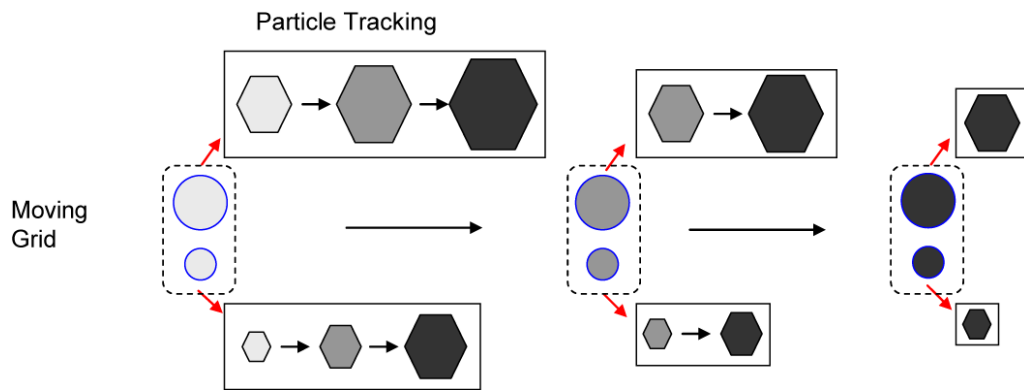
Figure 2.1. Lagrangian particle-tracking scheme for a hypothetical population of two liquid droplets during three successive time steps. Circles represent supercooled liquid droplets, and hexagons ice crystals. Black arrows indicate growth and aging whereas red arrows onset of freezing. Transition of light to darker shady indicates temporal evolution [12].

At any $t = t'$, the number of frozen aerosol particles is calculated using Eq. (2.9) and placed in a node of the particle tracking grid, in which their growth is followed. This group of ice crystals represents a particular solution of Eq. (2.7) for the case in which all particles freeze at the same time and have the same size and composition. Since a

particular solution of Eq. (2.7) can be obtained for each time step and droplet size, the general solution of Eq. (2.7) is obtained from the superposition of all generated ice crystal populations during the freezing process; w_i can then be calculated and Eqs. (2.1) to (2.4) readily solved. To describe the evolution of $n_o(D_o, t)$, a moving grid is employed, where frozen particles are removed from each size bin (which is in turn updated to its equilibrium size [208, 188, 12]) after each time step.

Since all ice particles are allowed to grow to their exact sizes, the effect of numerical diffusion on the simulation is minimized. The discretization of Eq. (2.7) transforms the partial differential equation into a system of ordinary differential equations, each of which represents the growth of a monodisperse ice crystal population. Thus, simple integration schemes can be used without compromising solution accuracy, although a large grid size may be required: the total number of nodes in the particle tracking grid is the product of the number of time steps by the number of nodes of the liquid aerosol moving grid. However, the particle tracking grid size can be substantially reduced by grouping the newly frozen particles in a fewer number of sizes [i.e., 118, 12],

$$\frac{\partial n_c(D_c, \bar{D}_o', t)}{\partial t}\bigg|_{D_c = D_o'} = \frac{1}{D_{upper} - D_{lower}} \int_{D_{lower}}^{D_{upper}} n_o(D_o, t) \frac{\partial P_f(D_o, t)}{\partial t} \, dD_o \qquad (2.12)$$

where $\bar{D}_o'$ is the assumed size of the frozen particles. If all aerosol particles freeze at the same size, the integral in Eq. (2.12) is evaluated over the entire size spectrum of the liquid aerosol population. A further reduction in the size of the particle tracking grid is achieved by recognizing that the freezing process occurs after some threshold s_i is reached [129, 223, 109]. The initial time step size is set to $2V^{-1}$ s, and reduced to $0.05V^{-1}$ s

(with V in m s^{-1}) when the nucleation event starts ($J > 10^4$ m^{-3}s^{-1}) and growth of ice particles needs to be accounted for.

2.2.3. Baseline Simulations

The formulation of the parcel model was tested using the baseline protocols of *Lin et al.* [143]. Pure ice bulk properties were used to calculate the growth terms (Eqs. (2.5) and (2.6)). D_o was assumed to be the equilibrium size at s_i, given by Köhler theory [208], and solved iteratively using reported solution bulk density and surface tension data [240, 184]. This assumption may bias the results of the parcel model simulations at low T and high V [143]. Alternatively, the aerosol size can be calculated using explicit growth kinetics, although the water vapor uptake coefficient from the vapor to the liquid phase is uncertain [143] (experimental measurements indicate a value between 0.4 and 0.7 [68]). J_{hom} was calculated using the *Koop et al.* [129] parameterization due to its simplicity and its widely accepted accuracy for a broad range of atmospheric conditions [i.e., 1] (in principle any model for J_{hom} can be used). The dry aerosol population was assumed to be pure H$_2$SO$_4$, lognormally distributed with geometric mean diameter, $D_{g,\ dry}$ = 40 nm, geometric dispersion, $\sigma_{g,\ dry}$ = 2.3, and total number concentration, N_o = 200 cm^{-3}. The runs were performed using 20 size-bins for the liquid aerosol; the newly frozen particles were grouped into 4 size classes, producing a grid between 1500 and 2000 nodes; numerical results showed that little accuracy was gained by using a finer grid (not shown). Runs of the parcel model using a regular PC (2.2 GHz processor speed and 1 GB of RAM), usually took between 5 and 12 min.
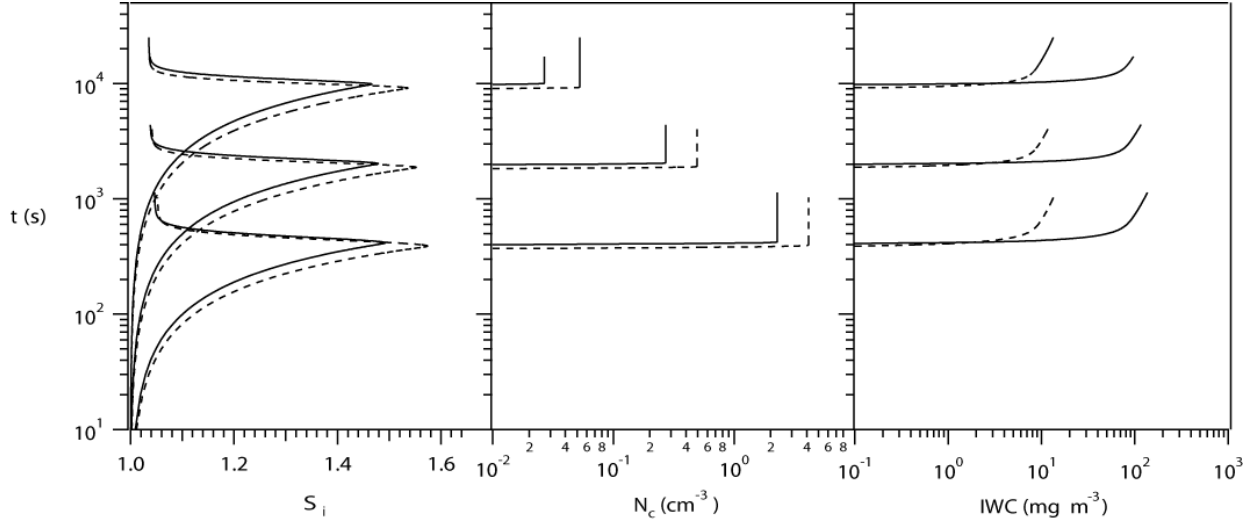
Figure 2.2. Ice saturation ratio, $S_i = s_i + 1$, N_c, and ice water content (IWC) profiles obtained from the numerical solution of the parcel model. Cases considered are those of *Lin et al.* [143]. Solid lines indicates $T_o = 233$ K and dashed lines $T_o = 213$ K. $V=0.04$ m s^{-1} (upper), 0.2 m s^{-1} (middle), and 1 m s^{-1} (lower).

Figure 2.2 shows results of the performed simulations for the protocols of *Lin, et al.* [143] and $\alpha_d = 1$, these simulations are intended to provide a common basis for comparison with other models.. The value of α_d is still uncertain and may impact N_c [143]. Simulations using $\alpha_d = 0.1$ (not shown) produced N_c (cm^{-3}) of 0.20, 2.87, 24.06, for the cases Ch004, Ch020 and Ch100, respectively, and 0.043, 0.535, and 5.98 for the cases Wh004, Wh020 and Wh100, respectively. Similarly to Figure 2.2, "Ch" corresponds to $T = 213$ K and "Wh" to $T = 233$ K, whereas the numbers correspond to the value of V used in cm s^{-1}.

Results from the INCA campaign summarized by *Gayet, et al.* [64] indicate $N_c \sim$ 1.71 cm^{-3} for T between -43 and -53 °C, and $N_c \sim 0.78$ cm^{-3} for T between -53 and -63

23

°C (V was mainly below 1 m s^{-1}, at conditions favorable for homogeneous freezing) [76].

These values are consistent with a low value for α_d (around 0.1) which is supported by

independent studies [70, 86, 121, 175]. However, direct comparison of the results of a

single parcel model with experimental results may presuppose a rather simplistic view of

the cirrus formation process, and overlook other effects (i.e., variation in aerosol

characteristics, V and T fluctuations [112, 107], see also Chapter 6). Theoretical

calculations and direct experimental observations have reported α_d values from 0.03 to 1

at temperatures within the range 20 to 263 K [i.e., 79, 258]. Due to these considerations,

α_d is still an uncertain parameter for which more study is required. Therefore sensitivity

of the results of this study to α_d is included.

2.3. Parameterization of Ice Nucleation and Growth

2.3.1. Parameterization of $n_c(D_c, D_o)$

As mentioned in Section 2.1, the study of the impact of anthropogenic aerosol emissions

on cirrus requires the development of an approximate analytical solution of Eqs. (2.4) to

(2.12). This is accomplished as follows: First, a link is established between ice particle

size and their probability of freezing at the time of nucleation, so that $n_c(D_c, D_o)$ can be

defined at each instant during the freezing pulse. $n_c(D_c, D_o)$ is then determined for a

given s_i profile by tracing back the growth of a group of ice crystals particles of size D_c

down to D_o (Figure 2.3).
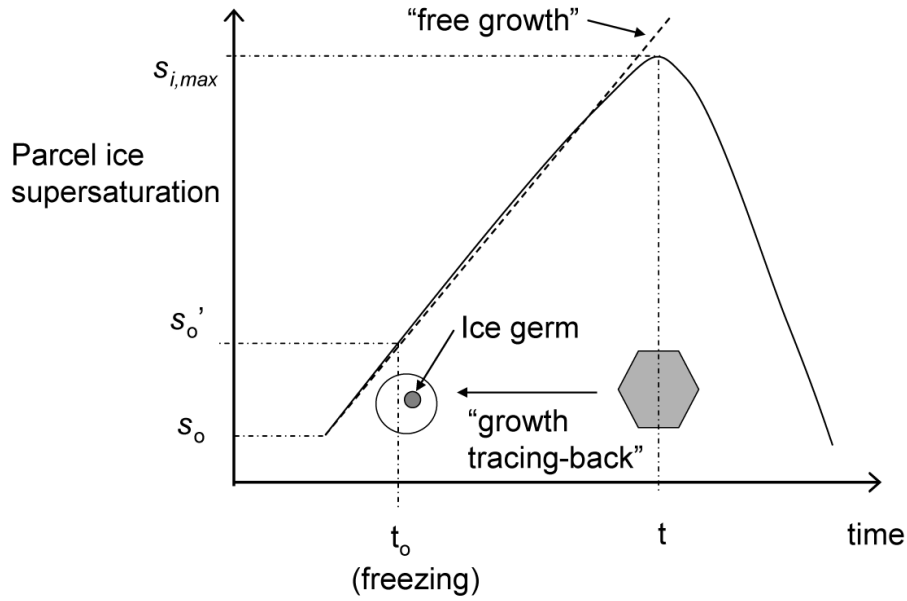
Figure 2.3. Sketch of the parameterization concept. Circles represent supercooled liquid droplets, and hexagons ice crystals [12].

In the following derivation we assume that most of the crystals are nucleated before maximum supesaturation ratio, $s_{i,\max}$, is reached (the implications of this assumption are discussed in section 2.4). We start by writing a solution of Eq.(2.7) in the form

$$n_c(D_c, D_o) = -\bar{n}_o(D_o)\frac{\partial P_f(s_o')}{\partial D_c} \tag{2.13}$$

where s_o' is a value of $s_i < s_{i,\max}$ at which the ice crystals were formed and $P_f(s_o')$ represents the current fraction of crystals of size D_c, that come from liquid aerosol particles of size D_o. $\bar{n}_o(D_o)$ is the average $n_o(D_o)$ during the freezing interval, and is taken to be constant since N_c is usually much less than N_o [i.e., 143] and freezing occurs over a very narrow range [109]. Since in a monotonically increasing s_i, field $P_f(s_o')$

25

decreases with increasing D_c (as explained below), a negative sign is introduced in Eq.(2.13).

Calculation of s_o' is key for solving Eq.(2.13); this is done by combining Eqs. (2.1) and (2.2),

$$\frac{ds_i}{dt} = \alpha V(s_i + 1) - \beta \frac{dw_i}{dt} \tag{2.14}$$

where $\alpha = \frac{g \Delta H_s M_w}{c_p R T^2} - \frac{g M_a}{RT}$, $\beta \approx \frac{M_a p}{M_w p_i^o} - \frac{\Delta H_s^2 M_w}{c_p R T^2}$. Before the nucleated ice crystals substantially impact saturation ("free growth", Figure 2.3), $\frac{dw_i}{dt} \approx 0$, and the integration of Eq. (2.14) from s_o' to $s_{i,max}$ gives

$$t - t_o \approx \frac{1}{\alpha V} \left(1 - \frac{s_o' + 1}{s_{i,max} + 1} \right) \tag{2.15}$$

where the approximation $\ln(x) \approx x - 1$ has been used. Equation (2.15) is similar to the "upper bound" expression derived by *Twomey* [246] for liquid water clouds. Numerical simulations (section 2.4) support that "free growth" holds up to s_i values very close $s_{i,max}$; for $s_i \rightarrow s_{i,max}$ however, Eq.(2.15) may underestimate t-t_o and its effect is discussed in section 2.4.

By definition, t-t_o should equal the time for growth of the ice particles from D_o to D_c (Figure 2.3), which is found by integration of Eq. (2.15),

$$t - t_o = \frac{1}{s_i} \left[\frac{\Gamma_1}{2} (D_c^2 - D_o^2) + \Gamma_2 (D_c - D_o) \right] \tag{2.16}$$

where s_i has been assumed constant as parcel model simulations suggest that nucleation occurs in a very narrow s_i range (i.e., Figure 2.5). The calculation of $P_f(s_o')$ using Eq.(2.9) requires the knowledge of J_{hom} as an explicit function of s_i; this can be further simplified using the approximation [i.e., 117, 12],

$$\ln \frac{J_{\text{hom}}(s_{i,\max})}{J_{\text{hom}}(s_i)} (s_{i,\max} - s_i)^{-1} \approx k_{\text{hom}}(T) \tag{2.17}$$

$k_{\text{hom}}(T)$ is obtained by fitting the *Koop et al.* [129] data for J between 10^8 and 10^{22} $\text{m}^{-3}\text{s}^{-1}$,

$$k_{\text{hom}}(T) = 0.0240 T^2 - 8.035 T + 934.0 \tag{2.18}$$

with T in K. $k_{\text{hom}}(T)$ can also be derived for any aerosol type and composition using classical nucleation theory [122, 117, 13]. Using (2.14) and (2.17), (2.9) is solved under the assumption of free growth (i.e., $\frac{dw_i}{dt} \approx 0$) to give

$$P_f(D_o, s_o') \approx \frac{1}{\alpha V s_{i,\max}} \int_{s_o}^{s_o'} v_o J_{\text{hom}} ds_i = \frac{J_{\text{hom}}(s_{i,\max}) v_o}{\alpha_i V k_{\text{hom}}(T) s_{i,\max}} \exp\left[-k(T)(s_{i,\max} - s_o')\right] \tag{2.19}$$

where $v_o = \frac{\pi D_o^3}{6}$, and the approximations $1 - \exp\left(-\int_0^t v_o J_{\text{hom}} dt\right) \approx \int_0^t v_o J_{\text{hom}} dt$ and

$\int_0^t v_o J(t) dt \approx v_o \int_{s_o}^{s_o'} J_{\text{hom}} \left(\frac{ds_i}{dt}\right)^{-1} ds_i$ have been used.

The lower integration limit, s_o, in Eq. (2.19) represents the beginning of the freezing pulse, where supersaturation is assumed to be low enough so that $\exp\left[-k(T)(s_{i,\max} - s_o')\right] \gg \exp\left[-k(T)(s_{i,\max} - s_o)\right]$. The integration is not very sensitive

to this assumption, as most of the ice crystals form for s_i close to $s_{i,max}$ [i.e., 108, 12]. Combining (2.15) and (2.16) to find $s_{i,max} - s_o'$, and replacing into (2.19) gives

$$P_f(D_o, D_c) = \frac{J_{hom}(s_{i,max})v_o}{\alpha_i V k_{hom}(T)(s_{i,max}+1)} \exp\left[-\mu \Gamma(D_c, D_o)\right] \tag{2.20}$$

where $\mu = \dfrac{\alpha_i V k_{hom}(T)(s_{i,max}+1)}{s_{i,max}}$, and $\Gamma(D_c, D_o) = \dfrac{\Gamma_1}{2}(D_c^2 - D_o^2) + \Gamma_2(D_c - D_o)$. The ice

number distribution function at $s_{i,max}$ is obtained after computing $\dfrac{\partial P_f(D_o, D_c)}{\partial D_c}$ from Eq.

(2.20) and substituting into Eq. (2.13)

$$n_c(D_c, D_o)\big|_{s_{i,max}} = \bar{n}_o(D_o)\frac{J_{hom}(s_{i,max})v_o}{s_{i,max}}\left(\Gamma_1 D_c + \Gamma_2\right)\exp\left[-\mu\Gamma(D_c, D_o)\right] \tag{2.21}$$

Since ice particles attain large sizes after freezing, the spectrum of D_c values spans over several orders of magnitude [i.e., 44, 175, 12]. Typically variation in D_o is much smaller and is further reduced because P_f is significant only for a fraction of the liquid droplets (generally those with larger sizes and low solute concentrations [208, 129]). With this, the value of $\exp\left[-\mu\Gamma(D_c, D_o)\right]$ will be dominated by variation in D_c, so that $\exp\left[-\mu\Gamma(D_c, D_o)\right]$ can be approximated with $\exp\left[-\mu\Gamma(D_c, \bar{D}_o)\right]$. Obtaining the crystal size distribution then is done by integration of Eq. (2.21) over the contribution from each droplet size class,

$$n_c(D_c)\big|_{s_{i,max}} = \frac{J_{hom}(s_{i,max})}{s_{i,max}}\left(\Gamma_1 D_c + \Gamma_2\right)\exp\left[-\mu\Gamma(D_c, \bar{D}_o)\right]\int \bar{n}_o(D_o)v_o dD_o \tag{2.22}$$

which for a lognormal distribution of $\bar{n}_o(D_o)$ gives

$$n_c(D_c)\big|_{s_{i,\max}} = \frac{N_o \bar{v}_o e^{9/2\ln^2 \sigma_g} J_{\text{hom}}(s_{i,\max})}{s_{i,\max}}\left(\Gamma_1 D_c + \Gamma_2\right)\exp\left[-\mu\Gamma(D_c,\bar{D}_o)\right] \quad (2.23)$$

or

$$n_c(\ln D_c)\big|_{s_{i,\max}} = \frac{N_o \bar{v}_o e^{9/2\ln^2 \sigma_g} D_c J(s_{i,\max})}{(s_{i,\max}-1)}\left(\Gamma_1 D_c + \Gamma_2\right)\exp\left[-\mu\Gamma(D_c,\bar{D}_o)\right] \quad (2.24)$$

where $\bar{v}_o = \dfrac{\pi}{6}\bar{D}_o^3$ and σ_g is the geometric dispersion of the droplet size distribution.

Equation (2.23) is the final expression used for the size distribution of the ice crystals at $s_{i,\max}$. Equations (2.21) to (2.23) demonstrate the probabilistic character of ice nucleation: at any time particles of all sizes have finite freezing probabilities; i.e., the population of ice crystals of a given size D_c results from the freezing of droplets with different sizes. From this, the freezing of a monodisperse aerosol size population produces a polydisperse ice crystal population. Since for values below $s_{i,\max}$, s_i increases monotonically with time, the number of crystals generally increases as D_c decreases. For a given droplet size, $P_f(D_o, s_i)$ will increase with time so that the number of newly formed crystals will increase. These crystals in turn will have less time to grow before s_i reaches $s_{i,\max}$; in other words, the most recently formed crystals will have the largest probability of freezing, i.e., $P_f(D_c = \bar{D}_o, s_{i,\max})$. The maximum in the distribution may be shifted to $D_c > \bar{D}_o$ if the time scale for the growth of the newly formed particles is smaller than the timescale of change of probability (section 2.4).

2.3.2. Calculation of N_c at $s_{i,max}$

The deposition rate of water vapor upon ice crystals can be approximated by substituting Eq.(2.23) into (2.4),

$$\frac{dw_i}{dt} = \frac{\rho_i}{\rho_a} \frac{\pi}{2} N_o \bar{v}_o e^{9/2\ln^2 \sigma_g} J_{hom}(s_{i,max}) \int_{D_o}^{D_{c,s_{max}}} D_c^2 \exp\left[-\frac{\mu}{2\bar{\Gamma}}(D_c^2 - \bar{D}_o^2)\right] dD_c \quad (2.25)$$

where $D_{c,s_{max}}$ is the equivalent diameter of the largest ice crystal at $s_{i,max}$ (calculated in section 2.2.3) and $\bar{\Gamma}$ is given by [i.e., 58]

$$\bar{\Gamma} = \frac{\int_{\bar{D}_o}^{D_{c,s_{max}}} \frac{D_c}{\Gamma_1 D_c + \Gamma_2} dD_c}{D_{c,s_{max}} - \bar{D}_o} = \frac{1}{\Gamma_1}\left[1 + \frac{\Gamma_2}{\Gamma_1} \frac{\ln\left(\frac{\Gamma_2 + \Gamma_1 D_{c,s_{max}}}{\Gamma_2 + \Gamma_1 \bar{D}_o}\right)}{D_{c,s_{max}} - \bar{D}_o}\right] \quad (2.26)$$

Integration of Eq.(2.25) gives

$$\frac{dw_i}{dt} = \frac{\rho_i}{\rho_a} \frac{\pi}{2} N_o \bar{v}_o e^{9/2\ln^2 \sigma_g} J_{hom}(s_{i,max}) \frac{e^{\frac{\mu}{2\bar{\Gamma}}\bar{D}_o^2}}{4\left(\frac{\mu}{2\bar{\Gamma}}\right)^{3/2}}\left[\sqrt{\pi} erf(\sqrt{\frac{\mu}{2\bar{\Gamma}}}D_c) - 2\sqrt{\frac{\mu}{2\bar{\Gamma}}}D_c e^{-\frac{\mu}{2\bar{\Gamma}}D_c^2}\right]_{\bar{D}_o}^{D_{c,s_{max}}}$$

$$(2.27)$$

An order of magnitude estimation of parameters based on parcel simulations (not shown) suggest that $\bar{D}_o \sim 10^{-7}$ m, $D_{c,s_{max}} \sim 10^{-5}$ m and $\frac{\mu}{2\bar{\Gamma}} \sim 10^{10}$ m^{-2}. Therefore, the term in brackets in Eq.(2.27) tends to approach $\sqrt{\pi}$ in most conditions, that is,

$$\frac{dw_i}{dt} = \frac{\rho_i}{\rho_a} N_o \bar{v}_o e^{9/2\ln^2 \sigma_g} J_{hom}(s_{i,max}) \frac{e^{\frac{\mu}{2\bar{\Gamma}}\bar{D}_o^2}}{\left(\frac{2\mu}{\pi\bar{\Gamma}}\right)^{3/2}} \quad (2.28)$$

after substitution of Eq. (2.28) into Eq.(2.14), at $\dfrac{ds_i}{dt} = 0$,

$$\alpha V(s_{i,\max} + 1) = \beta \frac{\rho_i}{\rho_a} N_o \bar{v}_o e^{9/2\ln^2 \sigma_g} J_{\hom}(s_{i,\max}) \frac{e^{\frac{\mu}{2\bar{\Gamma}}\bar{D}_o^2}}{\left(\dfrac{2\mu}{\pi\bar{\Gamma}}\right)^{3/2}} \tag{2.29}$$

the fraction of frozen particles, f_c, at $s_{i,\ max}$ is found at the maximum P_f, given by Eq. (2.20)

$$f_c = \frac{1}{N_o} \int \bar{n}_o(D_o) P_f(D_c = \bar{D}_o, \bar{D}_o) dD_o = \frac{\bar{v}_o e^{9/2\ln^2 \sigma_g} J_{\hom}(s_{i,\max})}{\alpha V k_{\hom}(T)(s_{i,\max} + 1)} \tag{2.30}$$

combining Eqs. (2.29) and (2.30) we obtain,

$$f_c = \frac{\rho_a}{\rho_i} \frac{\left[k_{\hom}(T)\right]^{1/2}}{\beta N_o} \left[\frac{2\alpha V(s_{i,\max} + 1)}{\pi \bar{\Gamma} s_{i,\max}}\right]^{3/2} \exp\left[-\frac{\mu}{2\bar{\Gamma}} \bar{D}_o^2\right] \tag{2.31}$$

The exponential term in (2.31) approaches unity, which is a result of the assumption made in (2.13) that freezing depletes a negligible amount of aerosol (i.e., $\bar{n}_o(D_o)$ is constant during the nucleation process). Since the term $J_{\hom}(s_{i,\max})$ has been eliminated from (2.31), f_c is not strongly influenced by small variations in $s_{i,\max}$. Thus, $s_{i,\max}$ can be taken as the saturation freezing threshold obtained solving the *Koop et. al.* [129] parameterization for $J_{\hom}(s_{i,\max}) = 10^{16}$ s^{-1} m^{-3}, which is close to the nucleation rate of pure water at -38 °C [208, 223], and represents an average of $J_{\hom}(s_{i,\max})$ over a wide set of simulations (section 2.4). The total number of crystals would be given by, $N_c = N_o f_c$, however such result will not be constrained by N_o as upper limit. Instead, lifting the

assumption made in Eq. (2.19), f_c can be associated with the solution of the integral in

Eq. (2.9), i.e., $f_c \approx \int_0^t v_o J(t)dt$ so that

$$N_c = N_o e^{-f_c}(1 - e^{-f_c}) \qquad (2.32)$$

where $N_o e^{-f_c}$ represents the number of remaining unfrozen droplets. Eq. (2.32) is valid

for f_c below 0.6 which covers the vast majority of atmospheric relevant cases [143].

2.3.3. Calculation of $D_{c,s_{max}}$

$D_{c,s_{max}}$ is required for calculating the ice growth rate (Equation (2.26)). Two methods are

used to calculate it. The first one is based on theoretical arguments, and assumes $D_{c,s_{max}}$

as the diameter of the ice crystal at which $\dfrac{P_f(D_c = D_o, D_o)}{P_f(D_c, D_o)} = 10^{-6}$ (i.e., the size above

which the number of crystals is below $10^{-6} N_c$). With this, Eq.(2.20) can be solved

for $D_{c,s_{max}}$,

$$D_{c,s_{max}}^2 + \frac{2\Gamma_2}{\Gamma_1} D_{c,s_{max}} - \frac{2\ln(10^{-6})s_{i,max}}{\alpha V k(T)(s_{i,max}+1)\Gamma_1} = 0 \qquad (2.33)$$

where we have assumed $D_{c,s_{max}} \gg D_o$ (supported by numerical simulations).

Since $\Gamma_2 \propto \dfrac{1}{\alpha_d}$ (Eq. (2.6)), the value of $D_{c,s_{max}}$ would increase as α_d decreases. For low

values of α_d ice crystals grow slowly, and non-continuum effects limit the condensation

rate; when ice become large enough, gas-to-particle mass transfer is in the continuum

regime and the crystals grow quickly [208]. When growth of the newly frozen ice crystals

is delayed, water vapor water tends to preferentially condense on preexisting ice crystals.

Slow uptake effects became important for α_d lower than 0.1, i.e., when Γ_2 becomes comparable to Γ_1 [143, 70]. Alternatively, $D_{c,s_{max}}$ can be computed using an empirical fit to numerical simulations obtained with the parcel model (for $T > 190$ K),

$$D_{c,s_{max}} = \min\left\{(1.6397\times10^{-14}T - 3.1769\times10^{-12})V^{-0.05}(N_o D_{g,dry}^3)^{-0.373};\ 10^{-4}\right\} \quad (2.34)$$

where V is in m s^{-1}, T is in K, N_o in cm^{-3} and $D_{g,\ dry}$ in m. Equation (2.34) was generated over a broad set of T, p, V, N_o, $D_{g,\ dry}$, and α_d (Table 2.1, section 2.4). The T and V dependencies in Eq. (2.34) are introduced to adjust the effective growth of the particles correcting for the "free growth" assumption (section 2.3.1). Variability in the formulation of Eq. (2.34) from aerosol property changes is not accounted for. Since $n_o(D_o)$ is in equilibrium with the dry aerosol size distribution, a larger $D_{g,\ dry}$ will enhance P_f, as the total volume of the liquid aerosol particles is increased. This would produce a longer freezing pulse and increase N_c. The same effect can be achieved by reducing the effective growth of the particles, and explains why $D_{c,Smax}$ scales with the average volume of the dry aerosol population, i.e., $\sim \left(N_o D_{g,dry}^3\right)^{1/3}$ (Eq. (2.34)).

2.3.4. Implementation of the Parameterization

The application of the parameterization is presented in Figure 2.4. As input, one requires the conditions of cloud formation T, P, V, α_d and the aerosol size distribution (i.e., N_o and $D_{g,dry}$); the outputs are N_c and ice crystal size distribution. To apply the parameterization, first $\overline{\Gamma}$ is calculated (Equation (2.26)), using $D_{c,s_{max}}$ computed from either Eq. (2.33) or Eq. (2.34), the latter being preferred for $T > 190$K. $s_{i,max}$ is obtained by solving $J_{hom}(s_{i,max}) = 10^{16}$ s^{-1} m^{-3} [129], for which reported fits relating can be

employed [i.e., 216]. N_c is calculated from Eq. (2.32) using f_c calculated from (2.31).

After f_c is calculated, $J_{\text{hom}}(s_{i,\text{max}})$ can be corrected using

$$J_{\text{hom}}(s_{i,\text{max}}) = 10^{16} = \frac{f_c \alpha V k(T)(s_{i,\text{max}}+1)}{\overline{v}_o e^{9/2\ln^2 \sigma_g}}$$ (Eq. (2.30)); $n_c(D_c, D_o)$ is then obtained from

Eqs. (2.23) and (2.24).

Input: p, T, V, α_d and aerosol characteristics.

Calculate $D_{c,S_{\text{max}}}$, $\overline{\Gamma}$

Estimate $S_{i,\text{max}}$ at $J(S_{i,\text{max}}) = 10^{16}$ m^{-3} s^{-1}

$$f_c = \frac{\rho_a}{\rho_i} \frac{[k(T)]^{1/2}}{\beta N_o} \left[\frac{2\alpha V S_{i,\text{max}}}{\pi \overline{\Gamma}(S_{i,\text{max}}-1)} \right]^{3/2} \exp\left[-\frac{\alpha V k(T) S_{i,\text{max}}}{2\overline{\Gamma}(S_{i,\text{max}}-1)} \overline{D}_o^2 \right]$$

Re-calculate $J(S_{i,\text{max}}) = \frac{f_c \alpha V k(T) S_{i,\text{max}}}{\overline{v}_o e^{9/2\ln^2 \sigma_g}}$

Output: $n_c(D_c)\big|_{S_{i,\text{max}}}$, equation(2.23)

Output: $N_c = N_o e^{-f_c}(1-e^{-f_c})$
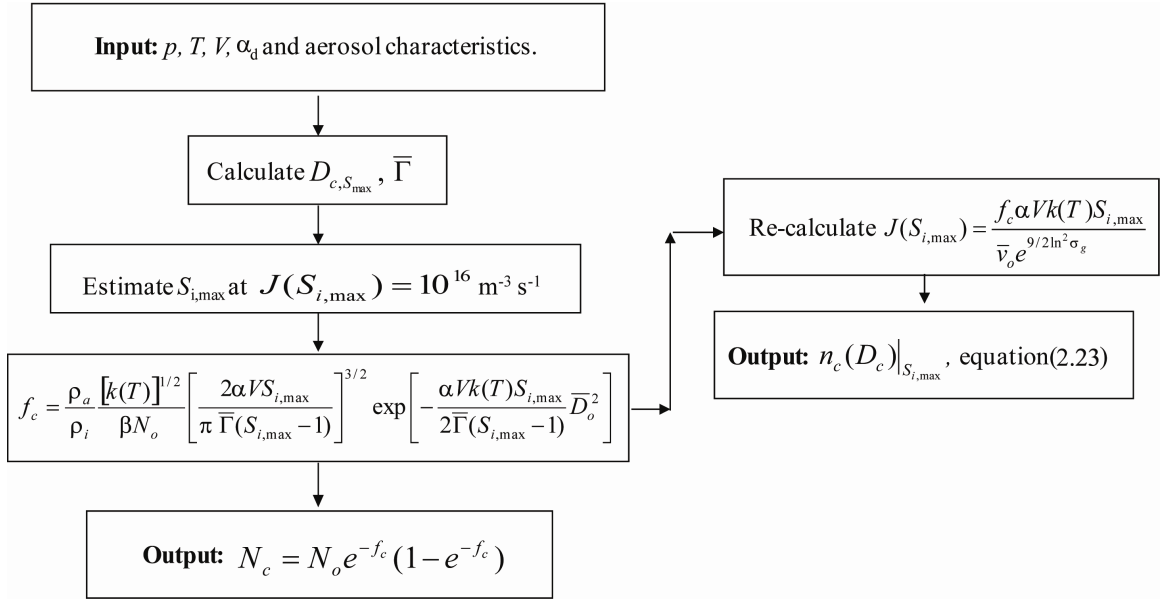
Figure 2.4. Parameterization algorithm.

2.4. Evaluation of the Parameterization

The parameterization was evaluated against the detailed numerical solution of the parcel model over a wide range of T, V, $D_{g,\,dry}$, N_o, and α_d (Table 2.1), for a total of 1200 runs that that reflect the uncertainty in α_d [143] and the range of cirrus cloud formation conditions expected in a GCM simulation. The parcel model was run using initial $S_i = 1.0$; initial p was estimated as in hydrostatic equilibrium at T using a dry adiabatic lapse

rate. The dry aerosol was assumed to follow a lognormal size distribution and be composed of pure H_2SO_4. "Aged", "unperturbed", and "perturbed" aerosol is represented by setting the geometric dispersion of the dry aerosol distribution, $\sigma_{g,\,dry}$ to 1.7, 2.3 and 2.9, respectively [230]. The aerosol was assumed to be deliquesced and in equilibrium with S_i in all simulations. Calculated N_c ranged from 0.001 to 100 cm^{-3} and $S_{i,max}$ varied between 1.4 and 1.6, which agrees with the reported values for cirrus formation by homogeneous freezing [i.e., 85, 143].

Table 2.1. Cloud formation conditions used in evaluation.

Property	Values
T (K)	200-235
V (m s^{-1})	0.02-5
α_d	0.05-1.0
$\sigma_{g,\,dry}$	1.7, 2.3, 2.9
N_o (cm^{-3})	10-5000
$D_{g,\,dry}$ (nm)	20-160

Two main assumptions were introduced in the development of the parameterization, *i)* N_c is calculated at $s_{i,max}$ rather than at the end of the freezing pulse, i.e., $N_c \approx N_c|_{S_{max}}$, and, *ii)* the newly formed crystals have a negligible impact of on s_i before $s_{i,max}$ is reached ("free growth"). Figure 2.5 shows how these assumptions may impact the results of the parameterization for high and low V and T (1-0.04 m s^{-1}, 233-203 K). By using free growth regime to estimate the evolution of s_i (dotted black line), $s_{i,max}$ is overestimated by ~ 0.5 % at low V (bottom left) and ~ 2% at high V (top right). At high T (right panels) this overestimation does not impact parameterization performance, as $s_{i,max}$ is low and small overestimations thereof do not significantly influence $J_{hom}(s_{i,max})$. However, as T decreases and V increases, $s_{i,max}$ reaches higher values during the parcel ascent; J (which

is a very nonlinear function of $s_{i,max}$), and P_f become very sensitive to small changes in $s_{i,max}$. As a result, an overestimation in N_c may be expected.
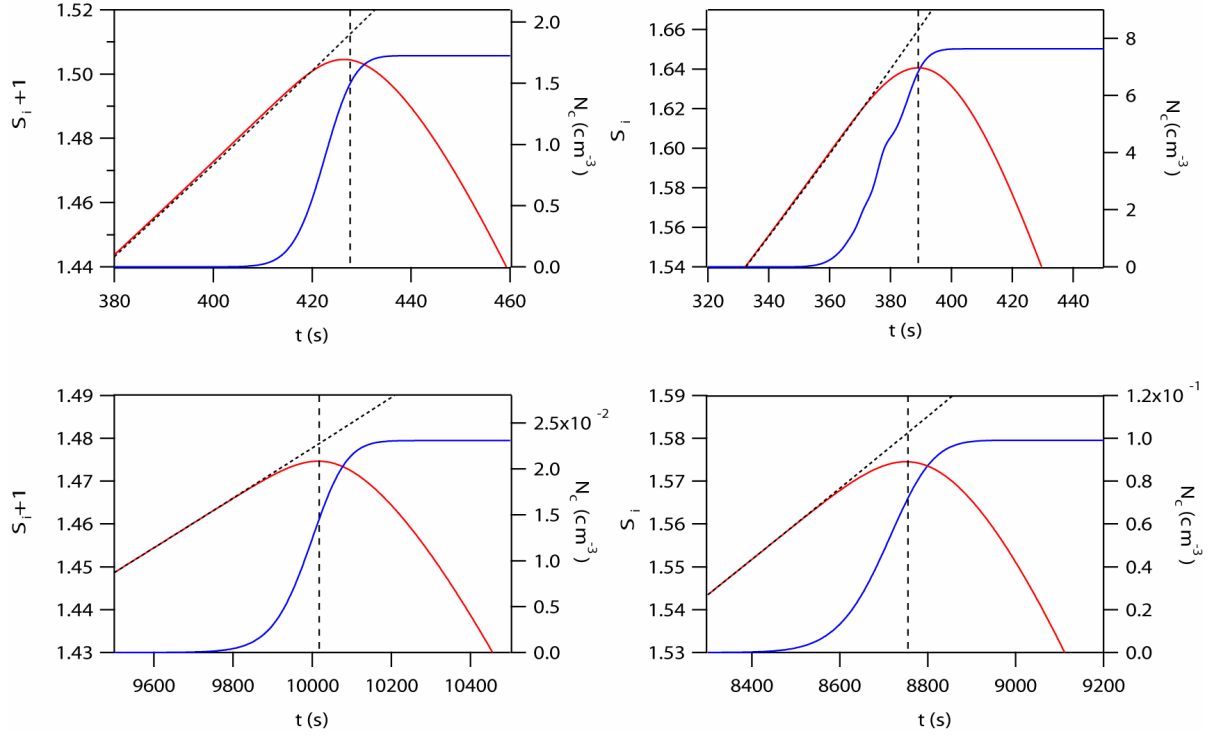
Figure 2.5. S_i (red, left axes) and N_c (blue, right axes) evolution calculated by the parcel model. T and V conditions shown are 233 K and 1 m s^{-1} (top left), 203 K and 1 m s^{-1} (top right), 233 K and 0.04 m s^{-1} (bottom left), and 203 K and 0.04 m s^{-1} (bottom right). Dashed lines represent the time at which $S_{i,max}$ is reached and dotted lines S_i evolution under "free growth". N_o=200 cm^{-3}, and $D_{g,dry}$ = 20 nm.

Conversely, Figure 2.5 shows that at low V (bottom panels), $N_c|_{S_{max}}$ underestimates the actual N_c by nearly a factor of 2; since few ice crystals (low $s_{i,max}$) are formed, it takes a longer time to deplete the available water vapor, resulting in longer freezing pulses. At high V (top panels), $N_c|_{S_{max}}$ is close to N_c, since $s_{i,max}$ is reached rapidly and a larger

number of crystals is formed; this effect will be more important at low T as higher $s_{i,max}$ values are reached .

2.4.1. Calculation of $n_c(D_c)$

Figure 2.6 presents the parameterized $n_c(D_c)$ (Eq. (2.24)) for two representative cirrus cases, along with $n_c(D_c)\big|_{S_{i\max}}$ obtained from parcel model simulations. Although the effect of the droplet size distribution parameters is explicitly considered in Eq. (2.24), it cancels out with its effect on f_c (which is a result of assuming constant $\overline{n}_o(D_o)$), and a single crystal size distribution is obtained for the three values of $\sigma_{g,\,dry}$ tested (although small variations in $n_c(D_c)\big|_{S_{i\max}}$ may occur due to differences in T at $s_{i,max}$). The latter is not a critical issue, as N_c variations with respect to $\sigma_{g,\,dry}$ are generally small (i.e., Figure 2.6). $\overline{D}_o$ was approximated with the equilibrium size of $D_{g,\,dry}$ at $S_{i,\,max}$. $n_c(D_c)$ was calculated using the outline in section 2.3.4 (Figure 2.4), from which $J_{\text{hom}}(s_{i,max})$ is corrected using equations (2.30) and (2.32) (therefore enforcing $N_c \approx \int\limits_{D_c=\overline{D}_o}^{D_{c,\max}} n_c(D_c)\,dD_c$). Generally, the parameterized $n_c(D_c)$ reproduces well the numerical results at $s_{i,max}$; however, it predicts a continuous size distribution down to $\overline{D}_o$, which differs from the numerical simulations. This can be attributed to the discrete nature of the size distribution in the numerical integration. After freezing, the newly formed ice crystals "jump" to larger sizes leaving "gaps" in the distribution, and eliminating part of the left tail of the size distribution. Due to the continuous nature of the parameterized $n_c(D_c)$, it would tend to overpredict $N_c\big|_{S_{\max}}$. The adjusted $J_{\text{hom}}(s_{i,max})$ will then be slightly below the obtained in numerical

simulations to satisfy $N_c = N_c|_{S_{max}}$. This works well in the cold case ($T=213$, $V=1$ m s^{-1}, Figure 2.6, left) as more crystals are to be produced after $s_{i,\,max}$ is reached. In the warm case ($T=233$, $V=0.2$ m s^{-1}, Figure 2.6, right), the freezing pulse is shorter and the correction in $J_{hom}(s_{i,max})$ produces a reduction in the peak of the distribution. The influence of these factors on the resulting effective radius of the cirrus cloud, and its radiative properties, will require the time integration of $n_c(D_c)$, and the comparison with numerical simulations at different stages after cloud formation. Although such a task may be readily achieved, it is out of the focus of this manuscript and will be undertaken in a future study.
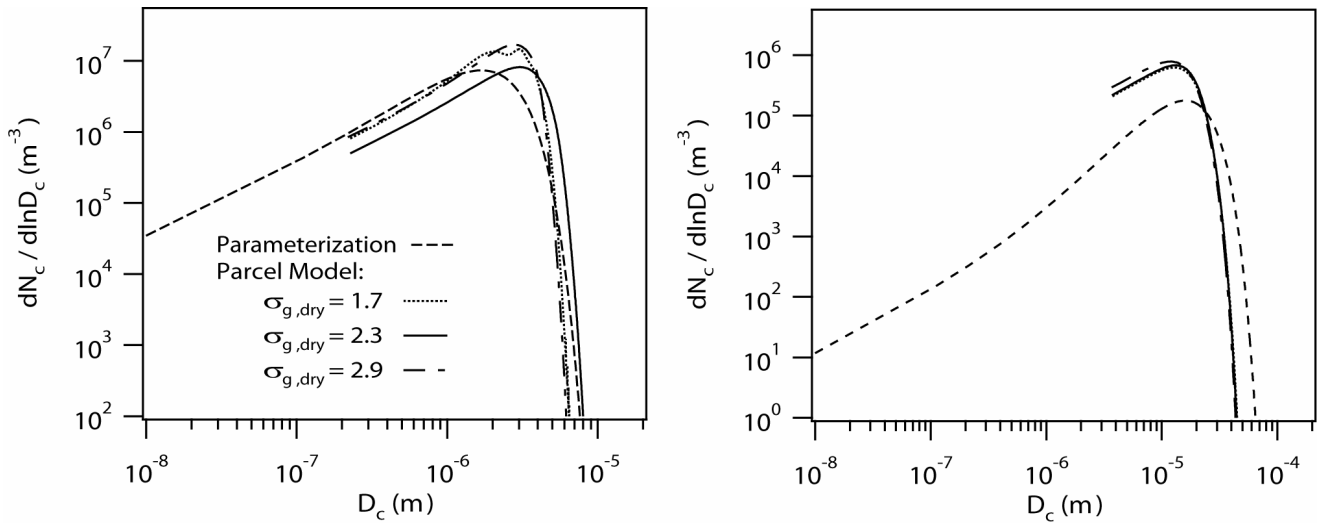
Figure 2.6. Crystal size distribution calculated by the parcel model and the parameterization at $S_{i,max}$. Left, $T=213$ K $V= 1.0$ m s^{-1}. Right, $T=233$ K $V= 0.2$ m s^{-1}. $\sigma_{g,\,dry}$ is the geometric dispersion of the aerosol size distribution.

2.4.2. Calculation of N_c

Figure 2.7 shows the comparison of N_c predicted by the parcel model and the parameterization (Eq. (2.32)) using the theoretical calculation of $D_{c,s_{max}}$ (right, Eq. (2.33)) and using the empirical correlation for $D_{c,s_{max}}$ (left, Eq. (2.34)). The effects of assuming "free growth" and the approximation of N_c as $N_c|_{S_{max}}$ are expected to cancel out at moderate T and V. However at low V and high T (hence low N_c), the parameterization tends to underestimate N_c with respect to the parcel model results; the opposite tendency occurs at very high V (>2 m s^{-1}) and low T (hence, high N_c). The behavior at these T,V extremes is not typical of cirrus formation [i.e., 85, 64], hence not expected to be a source of significant bias in GCM simulations. Overall, using the theoretically calculated $D_{c,s_{max}}$ gives a parameterized N_c that agrees within a factor of 2 of the parcel model simulations, with a mean relative error about -15% (for all runs in Table 1). When using the empirically calculated $D_{c,s_{max}}$ (Eq. (2.34)), the parameterized N_c is much closer to the numerical parcel model (average relative error 1% ± 28%), as Eq. (2.34) allows more flexibility in reproducing the parcel model results, and accounts for the additional variability due to effect of aerosol size and number.

2.4.3. Comparison Against Other Parameterizations

The new parameterization is evaluated against several published schemes for different combinations of V, N_o, $D_{g, dry}$, T, and α_d. The parameterizations used in this section are those of *Liu and Penner* [147 , hereafter LP2005], *Sassen and Benson* [223, hereafter SB2000], and *Kärcher and Lohmann*, [108, hereafter, KL2002, 58]. SB2000 is based on an empirical fit to numerical simulations relating N_c to T and V. A similar approach is

used in LP2005 where an additional dependency on N_o is included. In both cases, J_{hom} is calculated through classical nucleation theory (the latter using the effective temperature method [i.e., 44]). KL2002 is physically based and employs the freezing timescale and the threshold supersaturation as input parameters. It resolves explicitly the dependency of N_c on T, V, α_d, and D_o, and uses N_o as upper limit for N_c. Although the freezing of polydisperse aerosol is discussed in KL2002, not explicit solution is presented; their monodisperse solution is therefore used for comparison.
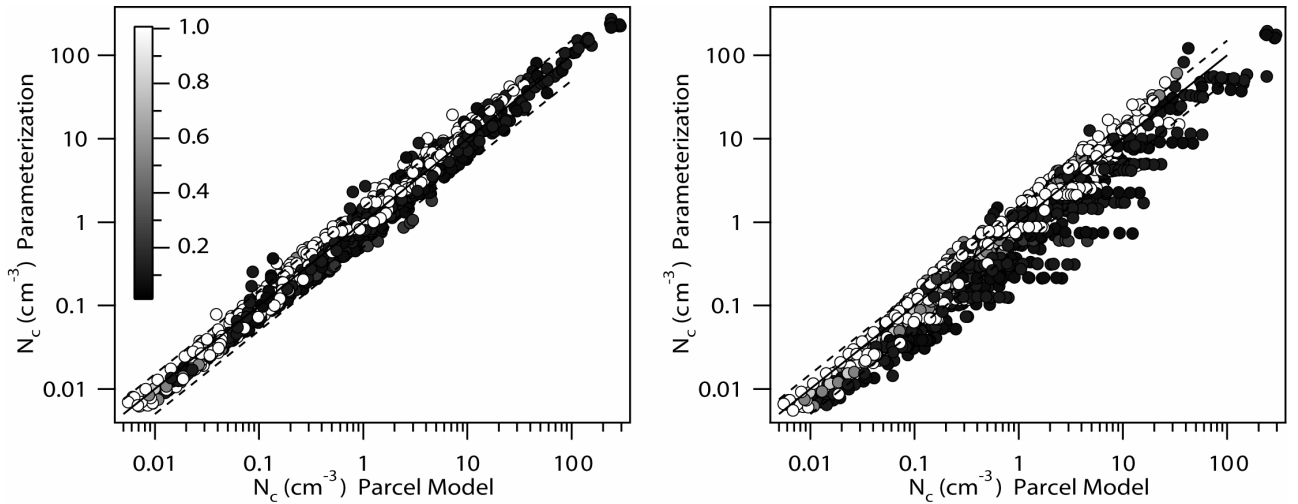
Figure 2.7. Ice crystal number concentration calculated by the parcel model and the parameterization. $D_{c,s_{max}}$ was calculated using either equation (2.33) (right) or (2.34) (left). Gray scale represents the value of α_d used in the calculations; dashed lines represent the $\pm$ 50 % difference.

The freezing timescale and supersaturation threshold are calculated using the analytical fits to *Koop et al.* [129] data provided by *Ren and Mackenzie* [216]. $\overline{D}_o$ in this case was taken as in equilibrium with the volume-weighted geometric mean diameter of the dry

size distribution. By using this definition of $\overline{D}_o$, the best agreement between the parcel

model simulations and the results of the KL2002 parameterization was obtained. The

three parameterizations were compared to the solution of Eq. (2.32) using theoretically

calculated $D_{c,max}$, Eq. (2.33) (although termed "theoretical", $k_{hom}(T)$ was derived from an

empirical fit to J_{hom}), and using the empirically adjusted $D_{c,max}$ Eq. (2.34) , (termed

"adjusted"). $\overline{D}_o$ was calculated as the equilibrium size of $D_{g,dry}$ at $s_{i,max}$. All

parameterizations are evaluated using T obtained at $s_{i,max}$ from the parcel model

simulations. α_d was set to 0.1 and 1.0 to test both diffusionally and non-difusionally

limited cases (see section 2.3.3).

2.4.3.1 Dependency on V

Figure 2.8 presents N_c predicted from all parameterizations at T_o= 213 (left panel, T

between 208.6 and 209.4 K) and 233 K (right panel, T between 228.8 and 229.2 K), and

α_d = 0.1 (black) and 1.0 (blue). At T_o=233 K, all parameterizations agree fairly well when

α_d = 0.1 and $V <$ 1 m s^{-1}. At higher V, KL2002 and LP2005 predict a larger N_c, whereas

SB2000 predicts a lower N_c with respect to the parcel model results and becomes

significant when $V >$ 3 m s^{-1}. At these conditions the adjusted parameterization follows

well the parcel model results, whereas the theoretical parameterization slightly

underpredicts N_c at low V. Runs made using α_d =1 (blue) showed a good agreement

between the parcel model and KL2002, the adjusted and theoretical parameterizations.

This is not surprising, as Eq. (2.31) bears the same dependency on V and p_i^o, reported by

KL2002 in their "fast growth" solution (i.e., $N_c \propto V^{3/2}$), and further emphasized by more

recent work [69, 216]. At high f_c (i.e., low T, low α_d, and high V) the exponential term in

Eq. (2.32) dampens the effect of V (also because $D_{c,s_{max}}$ scales with V) and N_c scales almost linearly with V. Results for $\alpha_d = 1$ lie below those of LP2005 and SB2000, who used lower α_d values for their numerical simulations (LP2005 used $\alpha_d = 0.1$ and SB2000 used $\alpha_d = 0.36$ [143]). At $T_o=213$ K and $\alpha_d = 0.1$ (left, black), the parameterizations agree only for V below 0.3 m s^1 whereas for large V they diverge, being N_c calculated using KL2002, the largest over the whole V interval. At very high V (>3 m s^{-1}) the adjusted parameterization underpredicts N_c with respect to the parcel model results which is a result of the exponential term introduced in (2.34). As with $T_o = 233$ K, KL2002, the adjusted and theoretical parameterizations agree well with the numerical results when $\alpha_d = 1$, and $T_o=213$ K (left, blue).
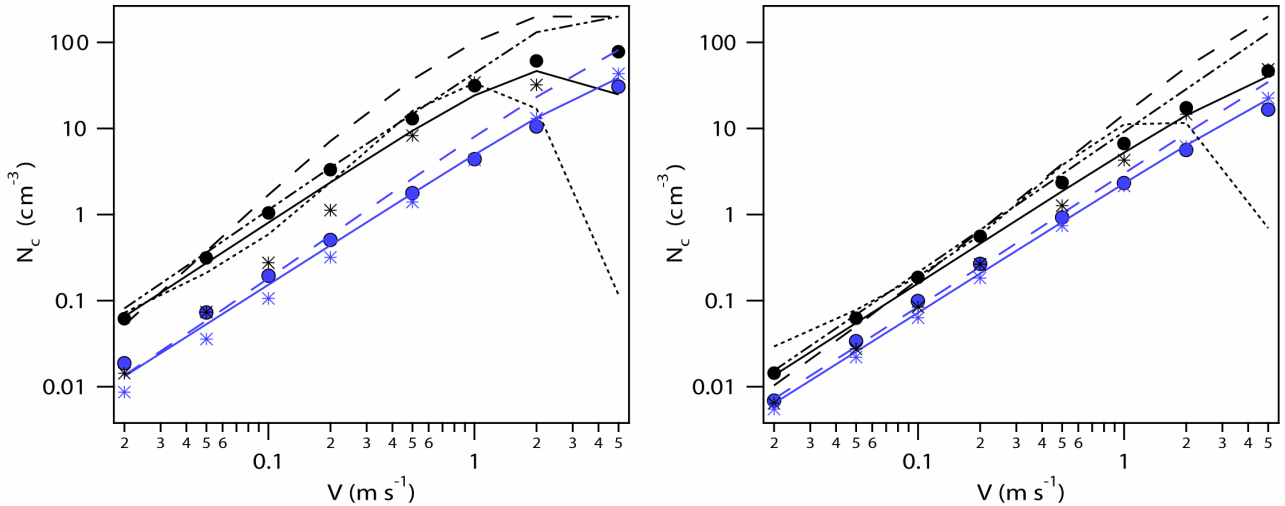
Figure 2.8. Ice crystal number concentration as a function of the updraft velocity, calculated using the parcel model (circles), KL2002 (dashed line), LP2005 (dashed-dotted line), SB2000 (dotted line), and the theoretical (stars), and adjusted (solid line) parameterizations. Results are shown for $T=233$ K, $p=34000$ Pa (right) and $T = 213$ K, $p=17000$ Pa (left), and $\alpha_d = 0.1$ (black) and $\alpha_d = 1.0$ (blue). $N_o=200$ cm^{-3}, and $D_{g,dry} = 40$ nm.

2.4.3.2 Dependency on N_o

Figure 2.9 presents N_c as a function of N_o for V=0.2 m s^{-1} (left) and V=1.0 m s^{-1} (right) and T_o=213 (black) and 233 K (blue); for these simulations $D_{g,dry}$ was set to 40 nm and α_d to 0.1. In all cases of Figure 2.9, LP2005 and the adjusted parameterization show the best agreement with the parcel model results. Still, at T_o=213 K, V= 1.0 m s^{-1}, the adjusted parameterization underpredicts with respect to the numerical results, for N_o below 20 cm^{-3} whereas LP2005 overpredicts; in both cases the difference with the parcel model results is about ± 50 %, which is not critical as these very low N_o are atypical of cirrus forming conditions [i.e., 208]. In all cases of Figure 2.9, KL2002 predicts larger N_c than the parcel model, however the difference becomes much smaller at large N_o. In the same interval of N_o, SB2000 predicts N_c close to the average of the parcel model results at T_o=213 K; when T_o=233 K, SB2000 predicts N_c close to the parcel model results at large N_o. The theoretical parameterization shows the opposite tendency and tends to agree better with the parcel model results at low N_o. In most cases, the parcel model results can be reasonably well expressed in the form $N_c = aN_o^b$ where a and b are functions of T, V, $D_{g, dry}$ and α_d (also proposed in LP2005). The dependency of N_c on N_o generally increases when T and α_d decrease, and V increases. For the cases of Figure 2.9, b lies between 0.19 (T_o=233 K, V= 0.2 m s^{-1}) and 0.61 (T_o=213 K, V= 1 m s^{-1}). This is consistent with experimental and numerical studies that usually report an increase in N_c by a factor between 2 and 4 for a 10-fold increase in N_o [i.e., 85, 97, 228].
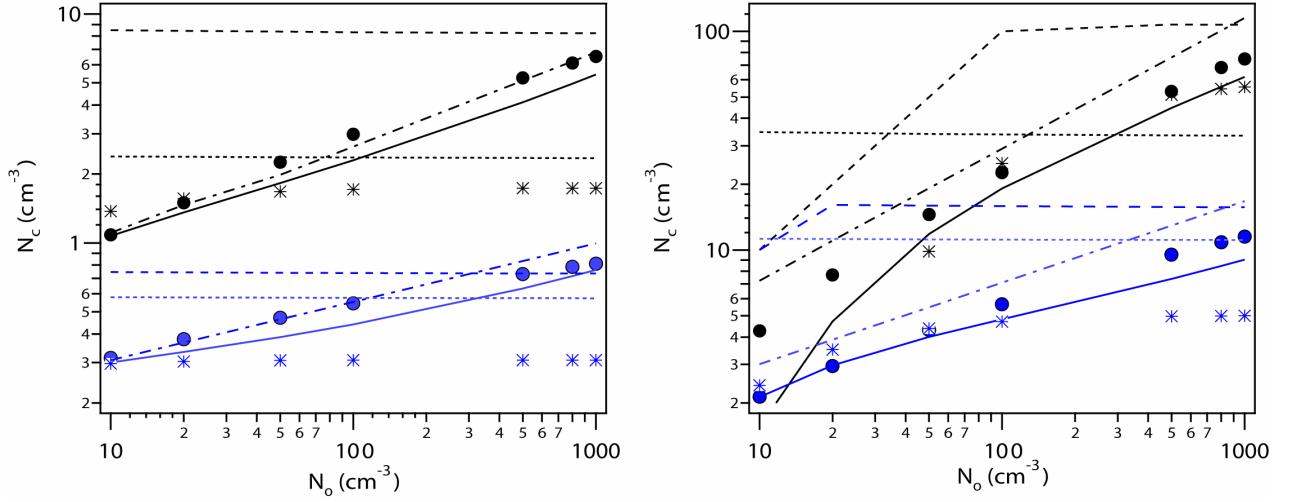
Figure 2.9. Ice crystal number concentration as a function of the aerosol number concentration. Symbols as in Figure 2.8. Results are shown for V= 0.2 m s^{-1} (left) and 1 m s^{-1} (right), and T=233 K, p=38812 Pa (blue) and T = 213 K, p=27350 Pa (black). α_d = 0.1, and $D_{g,dry}$ = 40 nm.

2.4.3.3 Dependency on $D_{g,\,dry}$

Figure 2.10 presents N_c as a function of $D_{g,\,dry}$ for T_o=213 K (left) and T_o=233 K (right), and α_d = 0.1 (black) and α_d = 1 (blue); for these simulations V=1.0 m s^{-1} and N_o = 200 cm^{-3}. To apply KL2002, $D_{g,\,dry}$ was converted into the volume-weighted mean diameter in equilibrium with $S_{i,max}$; however N_c results in Figure 2.10 are plotted using the original $D_{g,dry}$. In all conditions of Figure 2.10 parcel model results suggest N_c scales almost linearly with $D_{g,\,dry}$, which is also found by the combination of Eqs. (2.31) and (2.34). This was also observed in LP2005, and is a result of the increased P_f due to the larger volume of the liquid aerosol particles in equilibrium with the aerosol dry distribution (see section 2.3.3). This result is opposite to the tendency predicted by KL2002 ($N_c \propto \overline{D}_o^{-1}$),

44

and also by the theoretical parameterization (although with a much weaker dependence). In the latter, the effect of increased P_f is not accounted for due to the assumption of an infinite aerosol source (section 2.3.1). Although LP2005 does not take into account this dependency, it predicts N_c in agreement with parcel model results at $D_{g,\ dry} = 80$ nm, and $\alpha_d = 0.1$. SB2000 predicted N_c agrees with the parcel model results at $D_{g,\ dry} = 40$ nm and T_o=213, and at $D_{g,\ dry} = 120$ nm and T_o=233, when $\alpha_d = 0.1$. If a linear fit is adjusted to the cases shown in Figure 2.10 then its slope will decrease from 0.32 at T_o=213 and $\alpha_d = 0.1$ to 0.015 at T_o=233 and $\alpha_d = 1$, which suggests once more that these effects would be more important at low T and high V. In all cases of Figure 2.10, the adjusted parameterization closely reproduces the parcel model results. While the comparison of the different parameterizations was carried out over a comprehensive set of conditions, common values of $D_{g,\ dry}$ often ranges between 40-100 nm (and between 100-500 cm^{-3} for N_o) [e.g., 82, 64]. Figures 2.8-2.10 show that the effect of T and V variations on N_c is much stronger than that of $D_{g,\ dry}$ and N_o. The relative importance of each parameter remains to be assessed in global model studies.

2.5. Summary and Conclusions

To address the need for improved ice cloud physics in large scale models, we have developed a physically-based parameterization for cirrus cloud formation, which is robust, computationally efficient, and links chemical effects (e.g., water activity and uptake effects) with ice formation via homogenous freezing. This was accomplished by tracing back the growth of ice crystals to their point of freezing, in a given ice saturation profile, connecting their size to their freezing probability. Using this approach, an

expression for the crystal size distribution is derived, the integration of which yields the number concentration and size distribution of crystals.
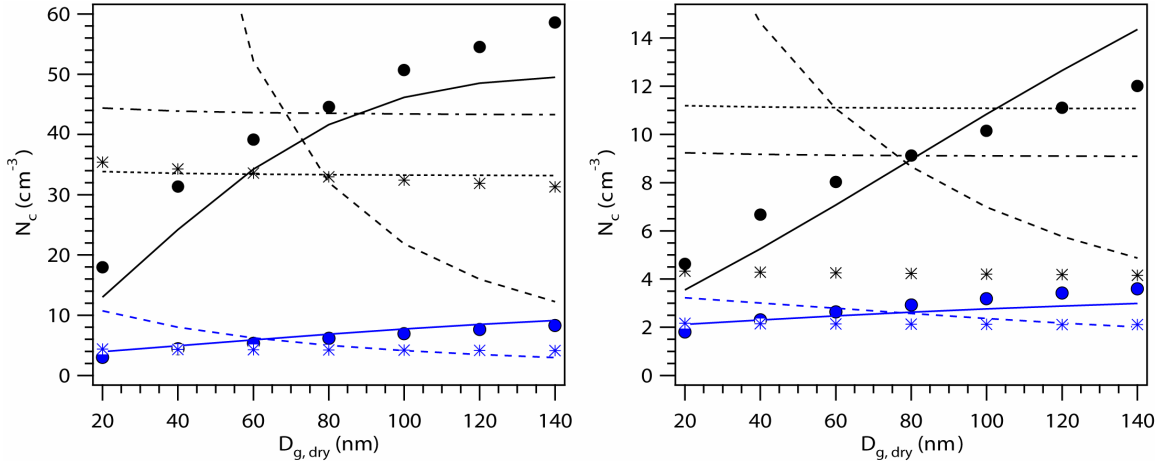
Figure 2.10. Ice crystal number concentration as a function of the aerosol mean dry diameter. Symbols as in Figure 2.8. Results are shown for T=233 K, p=34000 Pa (right) and T = 213 K, p=17000 Pa (left), and α_d = 0.1 (black) and α_d = 1.0 (blue). N_o=200 cm^{-3}, and V= 1 m s^{-1}.

The parameterization is evaluated against the predictions of a detailed numerical parcel model developed during this study. The parcel model equations were integrated using a Lagrangian particle tracking scheme; the evolution of the ice crystal size distribution is described by the superposition and growth of monodisperse crystal populations generated by the freezing of single classes (of same size and composition) of supercooled droplets.

Two versions of the parameterization are developed and evaluated; one based solely on theoretical arguments, and one with adjustments in the ice crystal growth rate using numerical parcel simulations. When compared against the predictions of the numerical parcel model over a broad set of conditions, the theoretically based parameterization for

N_c robustly reproduced the results of the parcel model within a factor of two and with an average relative error of about -15%. When numerical simulations are used to adjust the ice crystal growth rate, the relative error was reduced to $1 \pm 28\%$, which is remarkable given the simplicity of the final expression obtained for N_c, the broad set of conditions tested, and the complexity of the original parcel equations.

The new parameterization presented in this work offers an analytical and physically-based relationship between the parameters affecting cirrus ice formation via homogeneous freezing. The prediction skill of the parameterization is robust across a wide range of parameters (e.g., α_d, aerosol characteristics). As shown in Figure 2.7, the accuracy with which the parameterization reproduces the parcel model results, is independent of these parameters. In this regard, only the KL2002 parameterization shares this characteristic; the presented parameterization however *i)* explicitly links the variables that control the freezing time scale of the particles, and, *ii)* successfully reproduces the effect of the aerosol number on N_c.

The results given are applicable for cirrus formation on predominantly homogenous freezing conditions. Frequently, heterogeneous freezing and competition between multiple particle types can significantly impact cloud formation. Both the numerical model and the parameterization can be readily extended to include these processes, and will be the focus of the next chapters.

CHAPTER 3

PARAMETERIZING THE COMPETITION BETWEEN HOMOGENEOUS AND HETEROGENEOUS FREEZING IN CIRRUS CLOUD FORMATION - MONODISPERSE ICE NUCLEI[1]

In this study a parameterization of cirrus cloud formation that computes the ice crystal number and size distribution under the presence of homogeneous and heterogeneous freezing is developed. The parameterization is very simple to apply and is derived from the analytical solution of the cloud parcel equations, assuming that the ice nuclei population is monodisperse and chemically homogeneous. In addition to the ice distribution, an analytical expression is provided for the limiting ice nuclei number concentration that suppresses ice formation from homogeneous freezing. The parameterization is evaluated against the detailed numerical parcel model presented in Chapter 2, and reproduces numerical simulations over a wide range of conditions with an average error of $6 \pm 33\%$.

---

[1] This chapter appears as reference [13]: BARAHONA, D. and NENES, A. (2009). Parameterizing the Competition between Homogeneous and Heterogeneous Freezing in Cirrus Cloud Formation. Monodisperse Ice Nuclei. *Atmospheric Chemistry and Physics*, 9, 369-81.

3.1. Motivation

Cirrus clouds are key components of climate and can have a major impact on its radiative balance [145, 78, 153]. They can be affected by anthropogenic activities such as aircraft emissions in the upper troposphere [229, 195, 169, 237, 111], and from long range transport of pollution and dust [224, 61]. When studying ice-cloud-climate interactions, the key cloud properties that need to be computed are ice crystal concentration distribution, and ice water content [e.g., 143]; in large-scale models such parameters are either prescribed or computed with a parameterization. Due to the limited understanding of the physics behind ice nucleation, and the diversity and complexity of interactions between atmospheric particles during cirrus formation and evolution, the anthropogenic effect on cirrus clouds remains a major source of uncertainty in climate change predictions [e.g., 10].

Cirrus can form by either homogeneous or heterogeneous freezing. Homogeneous freezing occurs spontaneously from temperature and density fluctuations within a supercooled liquid phase [208]; whether it happens however largely depends on the temperature, droplet volume, and water activity within the liquid phase [27, 129, 40, 143]. The rate of formation of ice germs by homogeneous nucleation has been extensively studied and can be computed using a number of relationships based on experiments and theory [e.g., 44, 122, 129, 242]. Most cirrus clouds form at conditions favorable for homogeneous freezing, which is believed to be the primary mechanism of cirrus formation in pristine environments [e.g., 85, 23].

Heterogeneous freezing encompasses a group of nucleation "modes" (deposition, contact, immersion, and condensation) in which ice formation is mediated by insoluble

solids [208] or surfactant layers [260] that lower the energy barrier for the formation of an ice germ. Macroscopically, this can be expressed as a decrease in the freezing saturation threshold (or an increase in the freezing temperature) with respect the value for homogeneous freezing. Aerosol particles that contribute such surfaces and undergo heterogeneous freezing are termed ice nuclei (IN) [208]; the nature of IN is very diverse and not well understood. They can be composed of mineral dust [47, 224], sulfates [1], crustal material [263, 90], carbonaceous material [19, 38, 261], metallic particles (Al, Fe, Ti, Cr, Zn, and Ca) [28, 43], and biological particles [e.g., 172]. Sources of IN have been associated with long range transport of dust [47, 224], pollution [61], and direct aircraft emissions [195, 169]. Heterogeneous freezing saturation thresholds, S_h, depend primarily on the IN size, composition, and molecular structure, as well as on particle history [40, 171, 1]. Experimental studies have shown S_h ranging from 1.1 to 1.5 [e.g., 83, 43, 76, 5, 55, 205].

Field campaign data generally show that ice crystals collected at conditions favorable for homogeneous freezing contain a moderate fraction of insoluble material [i.e., 43, 205], which suggests the potential for interaction between homogeneous and heterogeneous freezing during cirrus formation. Therefore, a comprehensive understanding of ice formation requires a combined theory of homogeneous and heterogeneous freezing [e.g., 251, 110, 117, 262]. Modeling studies however suggest [110, 118, 147, 175] that at atmospherically relevant conditions, a single mechanism (i.e., homogeneous or heterogeneous) dominates the freezing process. This is largely because IN tend to freeze first, depleting water vapor, and inhibiting homogenous nucleation before it occurs [45]; only if IN concentration is low enough can homogeneous freezing

occur. Thus, IN and supercooled droplets may be considered separate populations that interact through the gas phase, but undergo heterogeneous or homogeneous freezing, respectively, at different stages during cloud formation [45]. This distinction may become less clear for heterogeneous freezing in the immersion mode for low concentration of immersed solid, or, if the solid is not an efficient ice nuclei (i.e., S_h is high, close to the value for homogeneous freezing) [117, 158]; we will assume for the rest of this study that we are far from such conditions, given that their importance for the atmosphere is not clear.

The presence of IN may drastically reduce the crystal concentration compared to levels expected for homogeneous freezing [44, 46], creating a potential anthropogenic indirect effect of IN on climate [45, 110]. Therefore, parameterizations of cirrus formation for use in climate models should explicitly resolve the interaction between homogeneous and heterogeneous freezing. Using a simplified approach to describe the growth of ice particles and box model simulations, Gierens [69] obtained a semi-analytical expression to estimate the limiting IN number concentration that would prevent homogeneous nucleation. Later, Ren and Mackenzi [216] derived analytical constraints for the effect of monodisperse IN on homogeneous freezing; these analytical constraints are not generally applicable to all cloud formation conditions. Liu and Penner [147] used parcel model simulations for combined homogeneous and heterogeneous freezing cases to obtain numerical fits relating N_c to T, V, and N_{IN}. Although based on simulations, these are limited by the particular choice of IN type, concentration, and freezing saturation thresholds, as well as assumptions made on crystal growth (i.e., deposition coefficient); conditions outside the simulation range could lead to deviations. The first comprehensive

physically-based parameterization of cirrus formation was presented by Kärcher, et al. [106] in which homogeneous and heterogeneous nucleation are considered. In this scheme, the competition between different freezing mechanisms is resolved by using numerical integration to calculate the size of ice crystals at different stages during the parcel ascent. Although accurate this method may be computationally expensive and does not analytically unravel the dependence of N_c on key properties of IN, like S_h and N_{IN}.

This study presents an analytical parameterization of cirrus formation that addresses the issues identified above and explicitly considers the competition between homogeneous and heterogeneous nucleation. We develop a novel method to account for the growth of the heterogeneously frozen ice crystals and incorporate their effect within the physically-based homogeneous nucleation framework of Barahona and Nenes [12, hereinafter BN08], presented in Chapter 2. The new parameterization explicitly resolves the dependency of N_c on dynamical conditions of cloud formation (i.e., temperature, pressure, and updraft velocity), aerosol number, size, the characteristics of IN and their effect on ice saturation ratio. To clearly present the approach used to unravel the interactions between IN and supercooled droplets, and develop the details of the parameterization, we assume IN are monodisperse and chemically uniform. The extension of the parameterization to polydisperse IN (in size and chemical composition) is presented in Chapter 4.

3.2. Parameterization Development

The parameterization is based on the ascending parcel conceptual framework. Contained within the cooling parcel is a population of supercooled droplets externally mixed with IN that compete for water vapor when their characteristic freezing threshold is met.

Heterogeneous and homogeneous freezing occur sequentially as the parcel water vapor saturation ratio over ice, S_i, increases during the cloud formation process. Homogeneous freezing is restricted to liquid droplets and described using the formulation of BN08. The IN population can be characterized by its number concentration, N_{IN}, and freezing threshold, S_h. Upon freezing, ice grows on the IN, depleting and redistributing the available water vapor between the homogeneously and heterogeneously frozen crystals (i.e., IN-frozen crystals) [e.g., 143, 216, 106]. Water vapor competition also affects the size distribution of homogeneously frozen crystals. To account for this competition effect, the change in homogeneous freezing probability due to the presence of IN-frozen crystals (i.e., the amount of water vapor condensed upon IN), and the size of the IN-frozen crystals at the homogenous freezing threshold, should be calculated. Both effects can be directly related to the impact of IN-frozen crystals on the rate of change of S_i [12]. A method to represent such interactions is presented below.

According to the homogeneous nucleation framework of BN08, the fraction of frozen droplets for a pure homogeneous pulse is given by (Chapter 2, Equation (2.31))

$$f_c = \frac{\rho_a}{\rho_i} \frac{[k_{\text{hom}}(T)]^{1/2}}{\beta N_o} \left[\frac{2\alpha V S_{\text{max}}}{\pi \overline{\Gamma}(S_{\text{max}} - 1)} \right]^{3/2} \tag{3.1}$$

Equation (3.1) was obtained under the assumption that homogeneously nucleated ice crystals do not substantially impact S_i, up to the point of maximum ice saturation ratio (in reality, S_i is affected, and is accounted for by adjusting the effective growth parameter $\overline{\Gamma}$ (Equation (2.26)) and setting S_{max} equal to the homogenous nucleation threshold).

The term $\alpha V S_{max}$ in Equation (3.1) represents an approximation to the rate of change of S_i at S_{max}. The presence of IN perturbs S_{max}, but Equation (3.1) can still be applied, provided that $\alpha V S_{max}$ is replaced with the (perturbed) rate of change of S_i at S_{max}, $\dot{S}_{max,IN}$ (calculated in Section 3.2),

$$ f_{c,IN} = \frac{\rho_a}{\rho_i} \frac{[k(T)]^{1/2}}{\beta N_o} \left[\frac{2\dot{S}_{max,IN}}{\pi \overline{\Gamma}(S_{max} - 1)} \right]^{3/2} \tag{3.2} $$

where $f_{c,IN}$ is the fraction of droplets frozen from homogeneous freezing in presence of IN (Equation (3.2) can be formally derived using the procedure presented in BN08, and Chapter 2). The use of Equation (3.2) implies that $\dot{S}_{max,IN}$ is almost constant during the homogeneous freezing pulse, even when IN are present. This is because, by the time homogeneous freezing occurs, the IN have reached large sizes (and grow very slowly); since the condensation rate is proportional to the available surface area (which can be considered constant over the timescale of S_{max}, which is around $10^{-3}V$ s, with V in m s⁻¹), $\dot{S}_{max,IN} \approx const.$

Dividing Eqs. (3.1) and (3.2) by parts we obtain,

$$ \frac{f_{c,IN}}{f_c} = \left[\frac{\dot{S}_{max,IN}}{\alpha V S_{max}} \right]^{3/2} \tag{3.3} $$

as all other terms in Eqs. (3.1) and (3.2) depend mainly on T (Chapter 2). Equation (3.3) expresses the impact of IN on the fraction of frozen droplets, which results from the redistribution of water vapor to IN-frozen crystals, and, the increase in the average size of the homogeneously frozen crystals due to a longer freezing pulse, which for the pure

homogeneous case (in s) is around $\dfrac{25}{V}$ (with V in m s^{-1}) [12]. Both of these effects tend to decrease $f_{c,IN}$ relative to f_c. When no IN are present, the freezing pulse is purely homogeneous and $f_{c,IN} = f_c$. If $f_{c,IN}$ is known, the number of crystals in the cirrus cloud, N_c, can be calculated as

$$N_c = N_o e^{-f_{c,IN}} (1 - e^{-f_{c,IN}}) + N_{IN} \tag{3.4}$$

where N_o is the liquid droplet number concentration in the parcel. The first term in Equation (3.4) is the contribution from homogeneously frozen droplets [12], while the second term is from heterogeneous freezing.

3.2.1. Calculation of the Size of the Heterogeneously Frozen Crystals at S_{max}

$\dot{S}_{max,IN}$ is required to find $f_{c,IN}$, and can be determined by solving a system of coupled ODEs that express the growth of heterogeneously frozen ice crystals and their impact on the parcel ice saturation ratio,

$$\frac{dS_i}{dt} = \dot{S}_i = \alpha V S_i - \beta \frac{dw_{IN}}{dt} \tag{3.5}$$

$$\frac{dw_{IN}}{dt} = \frac{\rho_i}{\rho_a} \frac{\pi}{2} N_{IN} D_{c,IN}^2 \frac{dD_{c,IN}}{dt} \tag{3.6}$$

$$\frac{dD_{c,IN}}{dt} = \frac{(S_i - 1)}{\Gamma_1 D_{c,IN} + \Gamma_2} \tag{3.7}$$

Equation (3.5) expresses the rate of change of parcel ice saturation ratio, which increases from cooling (first term of right hand side), and decreases from deposition on the growing IN (second term of right hand side). Equation (3.6) represents the rate of water

vapor deposition on IN-frozen crystals. Equation (3.7) expresses the rate of change of crystal size due to water vapor condensation.

Equation (3.5), evaluated at S_{max} provides $\dot{S}_{max,IN}$. If the initial conditions of the parcel are known, Eqs. (3.5) to (3.7) can be solved using numerical techniques, as their closed solution is challenging. If N_{IN} and S_h are such that $\left.\dfrac{dS_i}{dt}\right|_{S_{max}} = 0$, then Equations (3.5) to (3.7) become very stiff as $S_i \rightarrow S_{max}$, so even numerical integration of the system becomes difficult.

Although a general closed solution to Eqs. (3.5) to (3.7) is not possible, an approximation can be derived. Based on numerical simulations of Eqs. (3.5) to (3.7), and examining the impact of IN on S_i, $\dfrac{dS_i}{dt}$, and $\dot{S}_{max,IN}$, the behavior outlined in Figure 3.1 (top panel) is observed: (1) If $N_{IN} = 0$ (blue line), then $\dfrac{dS_i}{dt}$ vs. S_i is linear and $\dot{S}_{max,IN} = \alpha V S_{max}$. (2) If N_{IN} is low (green curve), IN-frozen crystals affect $\dfrac{dS_i}{dt}$ only after they grow substantially large; the resulting $\dot{S}_{max,IN}$ is slightly below its value at S_h, $\dot{S}_h = \alpha V S_h$, (shown as $\dot{S}_{max,IN}1$). (3) A similar behavior is obtained for higher N_{IN} (purple curve), however IN impact $\dfrac{dS_i}{dt}$ more quickly, and a lower $\dot{S}_{max,IN}$ is reached (point $\dot{S}_{max,IN}2$). (4) If N_{IN} is large enough, then the deposition rate on the ice crystals equals the rate cooling from expansion, so that $\left.\dfrac{dS_i}{dt}\right|_{S_{max}} = 0$, i.e., $\dot{S}_{max,IN} = 0$ (red curve) and corresponds to the inhibition of homogeneous nucleation due to IN freezing [69, 216].

The behavior outlined above can be described in terms of the following dimensionless variables,

$$x = \frac{S_i - S_h}{\Delta S_h} \tag{3.8}$$

where $\Delta S_h = S_{max} - S_h$, and

$$y = \frac{\dot{S}_h - \dfrac{dS_i}{dt}}{\dot{S}_h} \tag{3.9}$$

where, $\dot{S}_h = \alpha V S_h$, is the rate of change of S_i at the instant when IN freeze. x represents a normalization of S_i by the difference between homogeneous and heterogeneous freezing thresholds, and y represents a normalized $\dfrac{dS_i}{dt}$ with respect to its value at S_h. The relation between x, y, S_i, and $\dfrac{dS_i}{dt}$ is presented in Figure 3.1. If $N_{IN} = 0$ (blue line), x vs. y is linear and the value of y at $x = 1$ (termed "y_{max}") is equal to $-\dfrac{\Delta S_h}{S_h}$ (Equation (3.9)). Increasing N_{IN} is reflected by increase in y_{max} (y_{max1} and y_{max2}, for green and purple curves, respectively), in these cases the change in the sign of y (Figure 3.1, bottom panel) is related to the onset of significant depletion of water vapor, which impacts $\dfrac{dS_i}{dt}$.

$\dot{S}_{max,IN} = 0$ is represented as $y_{max} = 1$ (red curves); at this point S_i passes by a maximum at S_{max} so that there are at least two values of y for each value of x, one in the increasing branch of S_i and the second as S_i decreases (dashed red curves). Thus, at $x = y = 1$ the functional dependency between x and y ceases to be univocal and $\lim\limits_{y \to 1} \dfrac{dy}{dx} = \infty$, or,

57

$\lim\limits_{y \to 1} \dfrac{dx}{dy} = 0$. At this limit, IN impact $\dfrac{dS_i}{dt}$ very quickly after freezing, and y changes sign

at very low x.
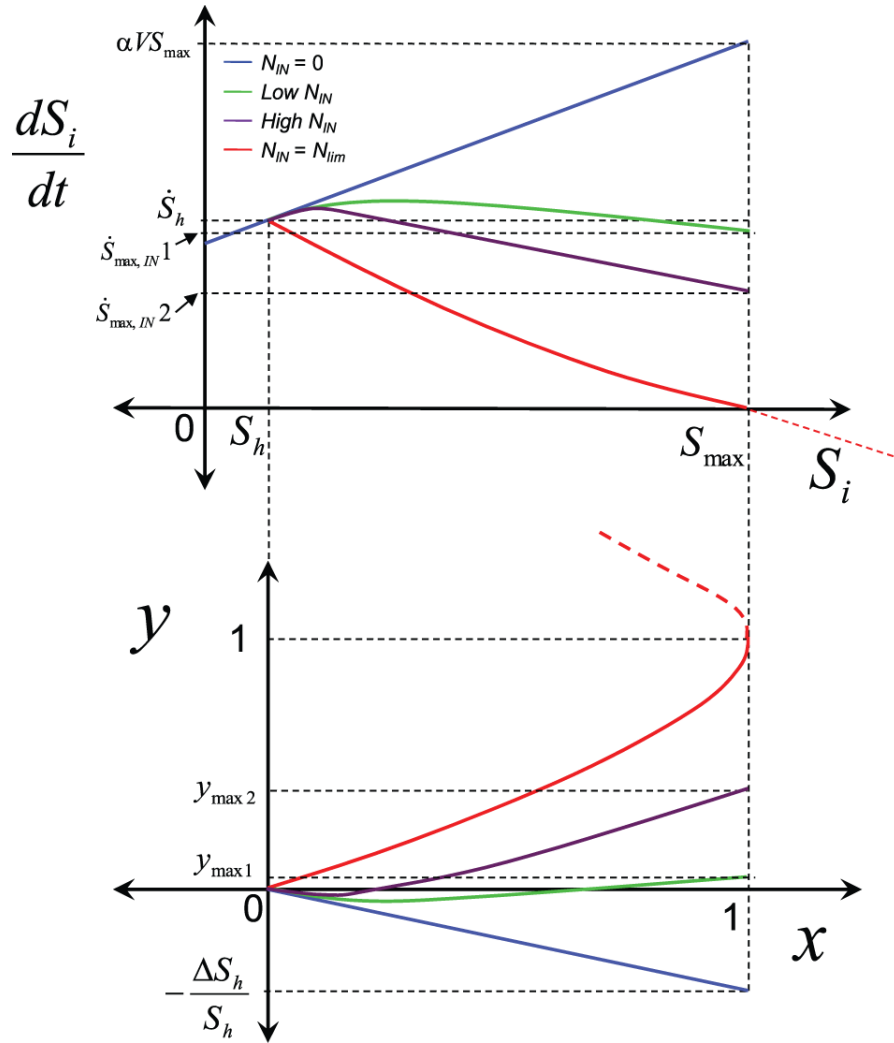
Figure 3.1. Schematic relation between x, y, S_i, and $\dfrac{dS_i}{dt}$.

Based on the above analysis an approximate mathematical relation can be obtained

between x and y. Since x is less than 1, together with $\left.\dfrac{dx}{dy}\right|_{y=1} = 0$, a Taylor series

expansion around $y = 1$ gives,

$$\left.\frac{d^2 x}{dy^2}\right|_{y=1} = -K + O(y, y^2, \ldots) \tag{3.10}$$

where K is a positive constant, and $O(y, y^2, \ldots)$ are higher order terms that are neglected

(the consequences of this assumption are discussed in section 3.3). Since to zeroth order,

the curvature around the point $y = 1$ is constant (equal to $-K$), x is related to y as,

$x = -Ky^2 + ay + b$ (being a and b integration constants). Since $x = 0$ when $y = 0$, and,

$\dfrac{dx}{dy} = 0$, for $y = 1$, then $b = 0$, $K = \dfrac{a}{2}$, and

$$A = y(y - 2) \tag{3.11}$$

where $A = -\dfrac{1}{a}$ is an arbitrary constant. As we desire x and y to be normalized, we select

A such that $x = 1$ when $y = y_{max}$, (Figure 3.1), or $A = y_{max}(y_{max} - 2)$. Substitution into

(3.11) and rearranging gives

$$y = 1 - \sqrt{1 + Ax} \tag{3.12}$$

Equation (3.12) represents an approximation of $\dfrac{dS_i}{dt}$ vs. S_i written in normalized form,

and expresses the dependency between $\dfrac{dS_i}{dt}$ and S_i considering, cooling from expansion,

and condensation of water vapor on ice crystals.

59

To find $\dot{S}_{max,IN}$, the rate of water vapor condensation on IN-frozen crystals at S_{max},

$\dfrac{dw_{IN}}{dt}\bigg|_{S_{max}}$, must be calculated (Eq. (3.5)); however, due the coupling between Eqs. (3.6)

and (3.7), this requires the calculation of the size of the IN-frozen crystals at S_{max}, $D_{max,IN}$.

Equation (3.12) combined with Eq. (3.7) can be used for the latter, as follows. First,

rearranging Eq. (3.7) and integrating from S_h to S_{max} we obtain

$$\frac{\Gamma_1}{2}D_{max,IN}^2 + \Gamma_2 D_{max,IN} - \Gamma(D_{o,IN}) = \int_{S_h}^{S_{max}} (S_i - 1)\,dt \tag{3.13}$$

in which $\Gamma(D_{o,IN}) = \dfrac{\Gamma_1}{2}D_{o,IN}^2 + \Gamma_2 D_{o,IN}$, and $D_{o,IN}$ is the initial size of the IN at the point of

freezing. In most cases, $\Gamma(D_{o,IN})$ in Eq. (3.13) can be neglected, since generally

$D_{max,IN} \gg D_{o,IN}$. From Eqs. (3.8) and (3.9), and using (3.12)

$$S_i = x\Delta S_h + S_h \tag{3.14}$$

and

$$\frac{dS_i}{dt} = \Delta S_h \frac{dx}{dt} = \dot{S}_h(1-y) = \dot{S}_h\sqrt{1+Ax} \tag{3.15}$$

substituting Eqs. (3.14) and (3.15) into Eq.(3.13), gives

$$\int_{S_h}^{S_{max}} (S_i - 1)\,dt = \frac{\Delta S_h^2}{\dot{S}_h}\int_0^1 \frac{x}{\sqrt{1+Ax}}\,dx + \frac{\Delta S_h(S_h - 1)}{\dot{S}_h}\int_0^1 \frac{1}{\sqrt{1+Ax}}\,dx \tag{3.16}$$

integrating Eq. (3.16), and after substituting $A = y_{max}(y_{max} - 2)$ and rearranging, gives

$$\frac{\Delta S_h^*}{\dot{S}_h} = \int_{S_h}^{S_{max}} (S_i - 1)\,dt = \frac{1}{\dot{S}_h}\frac{2\Delta S_h}{(2-y_{max})}\left[\frac{\Delta S_h(3-y_{max})}{3(2-y_{max})} + (S_h - 1)\right] \tag{3.17}$$

substituting Eq. (3.17) into (3.13), and solving for $D_{max,IN}$ gives,

$$D_{max,IN} = -\frac{\Gamma_2}{\Gamma_1} + \sqrt{\left(\frac{\Gamma_2}{\Gamma_1}\right)^2 + \frac{2}{\Gamma_1}\left[\frac{\Delta S_h^*}{\alpha V S_h} + \Gamma(D_{o,IN})\right]} \qquad (3.18)$$

where we have used $\dot{S}_h = \alpha V S_h$. Equation (3.18) uniquely defines $D_{max,IN}$, and represents an approximated solution of the ODE system Eqs. (3.5) to (3.7), at the point of maximum ice saturation ratio in the parcel; y_{max} can be computed after combining Eqs. (3.6) and (3.7) and using Eq. (3.15),

$$\frac{dS_i}{dt}\bigg|_{S_{max}} = \alpha V S_h(1 - y_{max}) = \alpha V S_{max} - \beta \frac{\rho_i}{\rho_a}\frac{\pi}{2} N_{IN} D_{max,IN}^2 \frac{(S_{max} - 1)}{\Gamma_1 D_{max,IN} + \Gamma_2} \qquad (3.19)$$

3.2.2. Limiting N_{IN}

Besides defining a maximum in S_i, the condition $\dfrac{dS_i}{dt}\bigg|_{S_{max}} = 0$, (red curves, Figure 3.1) also defines the maximum condensation rate that can be achieved right before homogeneous freezing is prevented; any increase in $\dfrac{dw_{IN}}{dt}$ beyond this value implies pure heterogeneous freezing [69]. Figure 3.1 shows that this condition is uniquely determined by $y_{max} = 1$; the limiting size of the ice crystals, D_{lim}, at the maximum water vapor deposition rate can then be computed from Equation (3.18) for ΔS_h^* calculated for $y_{max} = 1$,

$$D_{lim} = -\frac{\Gamma_2}{\Gamma_1} + \sqrt{\left(\frac{\Gamma_2}{\Gamma_1}\right)^2 + \frac{2}{\Gamma_1 \alpha V S_h}\left(\frac{4}{3}\Delta S_h^2 + 2\Delta S_h(S_h - 1)\right)} \qquad (3.20)$$

where $\Gamma(D_{o,IN})$ has been neglected because $D_{\text{lim}} \gg D_{o,IN}$.

Equation (3.20) can be used to compute the limiting number concentration of IN that will prevent homogeneous nucleation, N_{lim}, as follows. Since $\left.\dfrac{dS_i}{dt}\right|_{S_{\text{max}}} = 0$, Eqs. (3.5) and (3.6) can be combined to give

$$\beta \frac{\rho_i}{\rho_a} \frac{\pi}{2} N_{\text{lim}} D_{\text{lim}}^2 \frac{dD_{\text{lim}}}{dt} = \alpha V S_{\text{max}} \tag{3.21}$$

after substitution of Eqs. (3.20) and (3.7) into Eq. (3.21), N_{lim} can be obtained as

$$N_{\text{lim}} = \frac{\alpha V}{\beta} \frac{\rho_a}{\rho_i} \frac{2}{\pi} \left(\frac{S_{\text{max}}}{S_{\text{max}} - 1} \right) \left(\frac{\Gamma_1 D_{\text{lim}} + \Gamma_2}{D_{\text{lim}}^2} \right) \tag{3.22}$$

3.2.3. Calculation of $f_{c,IN}$

The set of Eqs. (3.15) to (3.19) represents a closed system that can be used to find $\dot{S}_{\text{max},IN}$ (hence $f_{c,IN}$). Although the dependence of $D_{\text{max},IN}$ on y_{max} suggests an iterative procedure for calculation of $\dot{S}_{\text{max},IN}$, a faster alternative (developed below) can be used. Assuming that $D_{\text{max},IN}$ is large enough so non-continuum effects can be neglected (i.e., $\Gamma_1 D_{\text{max},IN} \gg \Gamma_2$), Eq.(3.6), after substituting Eq. (3.7) and setting $S_i = S_{max}$, becomes

$$\left.\frac{dw_{IN}}{dt}\right|_{S_{\text{max}}} = \frac{\rho_i}{\rho_a} \frac{\pi}{2} \frac{(S_{\text{max}} - 1)}{\Gamma_1} N_{IN} D_{\text{max},IN} \tag{3.23}$$

rearranging Eq. (3.22), and assuming $\Gamma_1 D_{\text{lim}} \gg \Gamma_2$, gives

$$\frac{S_{max} - 1}{\Gamma_1} = \left(\frac{\beta}{\alpha V S_{max}} \frac{\pi}{2} \frac{\rho_i}{\rho_a} N_{lim} D_{lim} \right)^{-1} \tag{3.24}$$

after substituting Equation (3.24) into Eq. (3.23) we obtain

$$\left. \frac{dw_{IN}}{dt} \right|_{S_{max}} = \frac{\alpha V S_{max}}{\beta} \left(\frac{N_{IN}}{N_{lim}} \frac{D_{max,IN}}{D_{lim}} \right) \tag{3.25}$$

which after substituting into Eq. (3.7), at S_{max}, gives

$$\frac{\dot{S}_{max,IN}}{\alpha V S_{max}} = 1 - \left(\frac{N_{IN}}{N_{lim}} \frac{D_{max,IN}}{D_{lim}} \right) \tag{3.26}$$

Equation (3.26) can be used to determine $\dot{S}_{max,IN}$, if a relation is found between $D_{max,IN}$ and D_{lim}. Considering that at $N_{IN} = N_{lim}$ (hence $D_{max,IN} = D_{lim}$) the surface area of the crystal population is the largest, which follows from Eq. (3.18) since for all $N_{IN} < N_{lim}$, $y_{max} < 1$, then the total surface area of the crystal population at N_{IN} can be related to its value at N_{lim} by,

$$N_{IN} D_{max,IN}^2 + (N_{lim} - N_{IN})(D_{lim} - D_{max,IN})^2 = N_{lim} D_{lim}^2 \tag{3.27}$$

which after expanding the quadratic terms and rearranging, gives,

$$\frac{N_{IN}}{N_{lim}} = \frac{D_{max,IN}^2 - 2D_{lim} D_{max,IN}}{D_{lim}^2 - 2D_{lim} D_{max,IN}} \tag{3.28}$$

typically, by the time S_i reaches S_{max}, ice crystals have grown to sizes comparable to D_{lim}, i.e., $D_{max,IN} \sim D_{lim}$, and Eq. (3.28) can be approximated as,

$$\frac{N_{IN}}{N_{\mathrm{lim}}} \approx \frac{D_{\mathrm{max},IN}^2}{D_{\mathrm{lim}}^2} \tag{3.29}$$

Equation (3.29), when introduced into Eq. (3.26) gives,

$$\frac{\dot{S}_{\mathrm{max},IN}}{\alpha V S_{\mathrm{max}}} = 1 - \left(\frac{N_{IN}}{N_{\mathrm{lim}}} \left(\frac{N_{IN}}{N_{\mathrm{lim}}} \right)^{1/2} \right) \tag{3.30}$$

which can be solved for $\dot{S}_{\mathrm{max},IN}$ as,

$$\dot{S}_{\mathrm{max},IN} = \alpha V S_{\mathrm{max}} \left[1 - \left(\frac{N_{IN}}{N_{\mathrm{lim}}} \right)^{3/2} \right] \tag{3.31}$$

$\dot{S}_{\mathrm{max},IN}$ calculated from Eq. (3.31) can then be used into Eq. (3.3) to find $f_{c,IN}$. The restriction that $\dot{S}_{\mathrm{max},IN} > 0$ for all cases when homogeneous freezing is not prevented (e.g., Figure 3.1), implies that $f_{c,IN} = 0$, if $N_{IN} \geq N_{\mathrm{lim}}$.

3.2.4. Applying the Parameterization

The application of the parameterization is done as follows (Figure 3.2). First, D_{lim} is computed from Eq. (3.20) and used in Eq. (3.22) to calculate N_{lim}; if $N_{IN} \geq N_{\mathrm{lim}}$ then $f_{c,IN} = 0$. If $N_{IN} < N_{\mathrm{lim}}$, $\dot{S}_{\mathrm{max},IN}$ is then obtained from Eq. (3.31), which after substitution into Eq. (3.3) (using Eq. (3.1) to obtain f_c), gives $f_{c,IN}$. Equation (3.4) then is used to calculate N_c from combined heterogeneous and homogeneous freezing.

3.3. Results and Discussion

The parameterization was evaluated against the numerical parcel model developed in BN08 (Chapter 2) modified to include the effect of IN (by allowing the deposition of

water vapor onto the IN when S_i exceeds S_h). The performance of the parameterization

for pure homogeneous freezing conditions was discussed in BN08, so the evaluation here

is focused on the competition between homogeneous and heterogeneous freezing. The

conditions used for evaluation covered a wide range of T, V, α_d, S_h and N_{IN} (Table 1)

for a total of 800 simulations; initial p was estimated from hydrostatic equilibrium at T_o

using a dry adiabatic lapse rate. For simplicity, α_d was assumed to be the same for the

homogeneously frozen and IN-frozen ice crystal populations (although this assumption

can easily be relaxed).
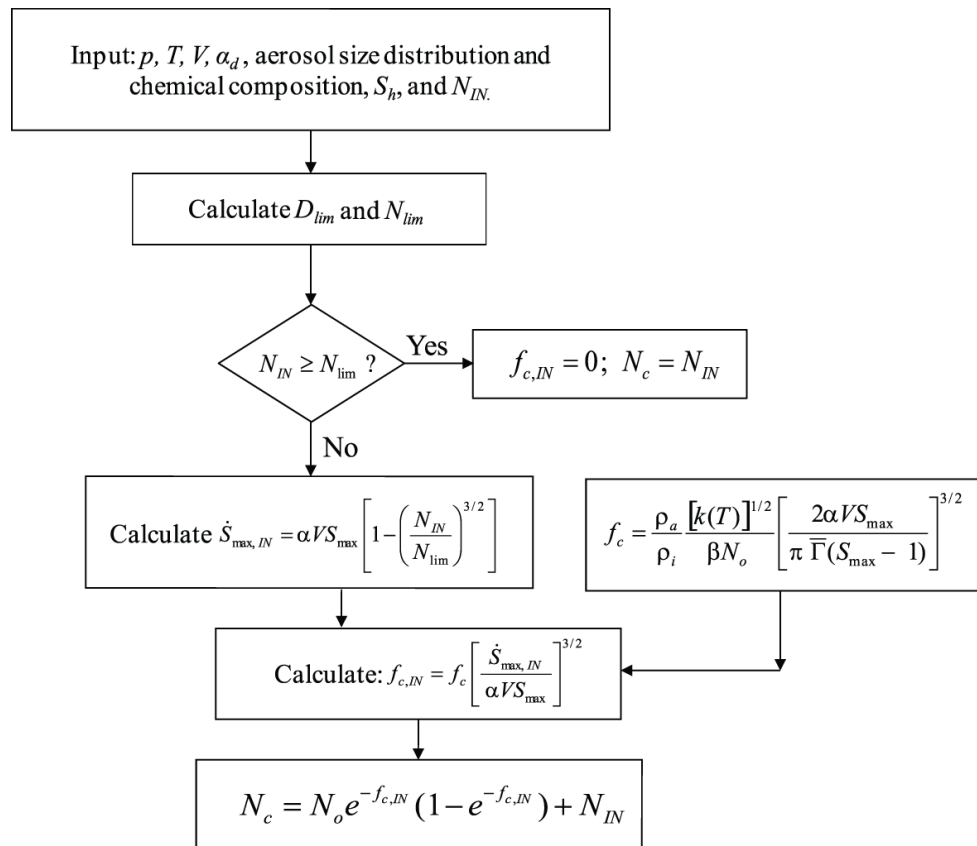
Figure 3.2. Parameterization algorithm.

65

3.3.1. Evaluation against Parcel Model

Figure 3.3 presents N_c versus N_{IN} using the parameterization (lines) and the parcel model (symbols), for all the simulations of Table 1. At low N_{IN} ($\sim$ less than 10^{-4} cm^{-3}), the impact of IN on N_c is minimal and N_c is close to the obtained under pure homogeneous freezing. As N_{IN} increases to about $0.1N_{\text{lim}}$, IN considerably impact N_c, so that N_c reduces proportionally to N_{IN} up to the prevention of homogeneous nucleation at $N_{IN} = N_{\text{lim}}$, at which a minimum $N_c = N_{\text{lim}}$ is reached. When N_{IN} is greater than N_{lim}, freezing is only heterogeneous and $N_c = N_{IN}$. Figure 3.3 shows that at high V and low T, large concentrations of IN ($N_{lim} \sim 1$ cm^{-3}) are required to impact homogeneous freezing, which is consistent with existing studies [e.g., 45]; given that high N_{IN} are rare in the upper troposphere [e.g., 64, 205], our results are consistent with understanding that homogeneous nucleation is the primary freezing mechanism at these conditions.

Table 3.1. Cloud formation conditions used in evaluation.

Property	Values
T_o (K)	215, 230
V (m s^{-1})	0.04-2
α_d	0.1, 1.0
$\sigma_{g, dry}$	2.3
N_o (cm^{-3})	200
$D_{g, dry}$ (nm)	40
S_h	1.1-1.4
N_{IN} / N_{lim}	0.01-3

Overall, the parameterization reproduces very well the parcel model results (Figure 3.3), and clearly captures the effect of N_{IN} on N_c. When calculating the error between parcel

model and parameterization, care should be taken to exclude points where homogeneous nucleation is prevented, as both the parameterization and the parcel model predict $N_c = N_{IN}$ (i.e., $f_{c,IN} = 0$ Eq. (3.31)). Including these points in the analysis would bias the error estimation towards low values. Omitting points where $N_c = N_{IN}$ (i.e., where homogeneous freezing does not occur), the average relative error for the calculation of N_c using the parameterization with respect to parcel model results for all the runs of Table 1, is about $6 \pm 33\%$.
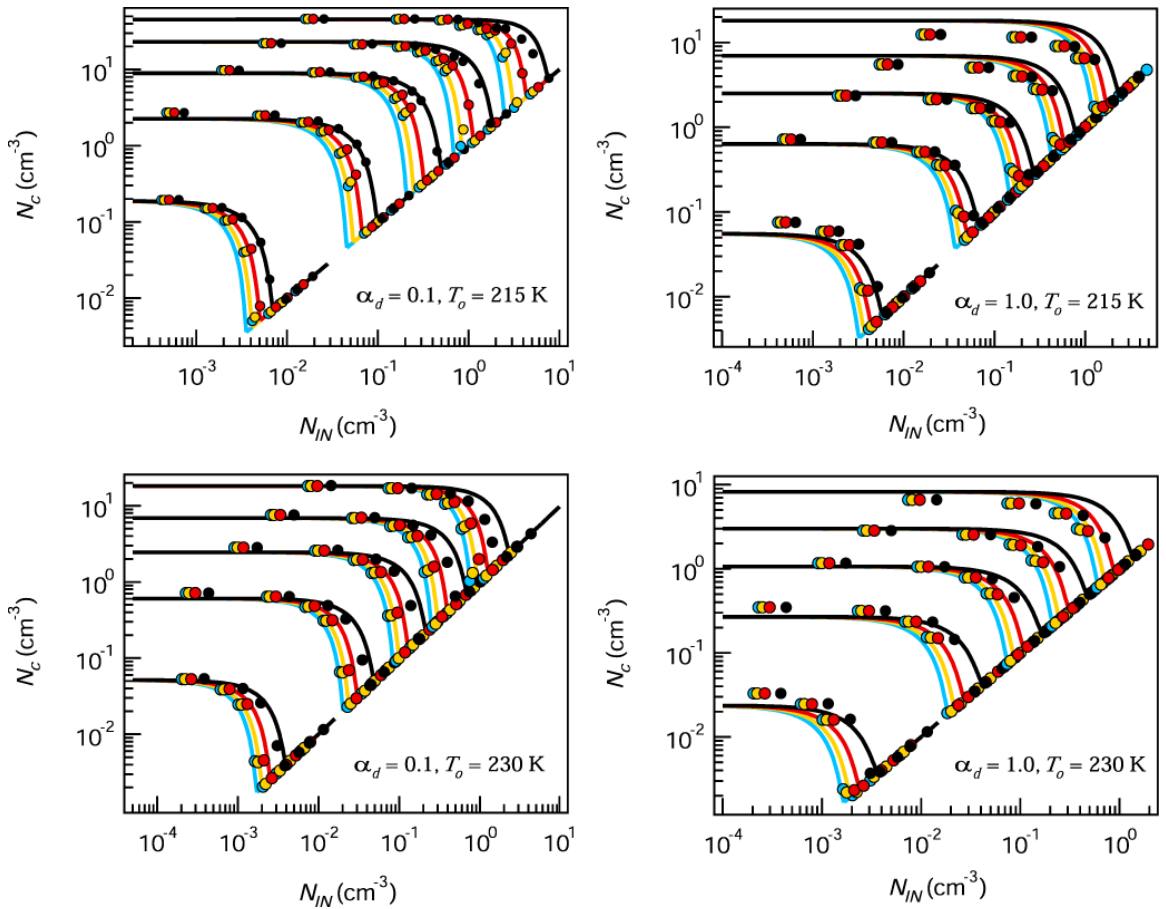
Figure 3.3. N_c vs. N_{IN} for all simulation conditions of Table 3.1. Lines represent parameterization results and symbols correspond to parcel model simulations. Symbols are colored by S_h, being 1.1 (blue), 1.2 (yellow), 1.3 (red), and 1.4 (black). V was set equal to 0.04, 0.2, 0.5, 1, and 2 m s^{-1}, from bottom to top lines in each panel, respectively.

The small value of the error indicates no significant systematic biases in the parameterization over the broad range of conditions considered. Still, some overprediction is found at N_c at $V = 2$ m s^{-1}, and a slight underprediction at $V = 0.04$ m s^{-1} and $T = 230$ K. The former bias is not critical as such high V are typically not encountered during cirrus formation. The latter can be attributed to the inherent error of the homogeneous framework of BN08 (1 ± 28 %), as a much better agreement is obtained if f_c (homogeneous) is replaced with the numerical solution.
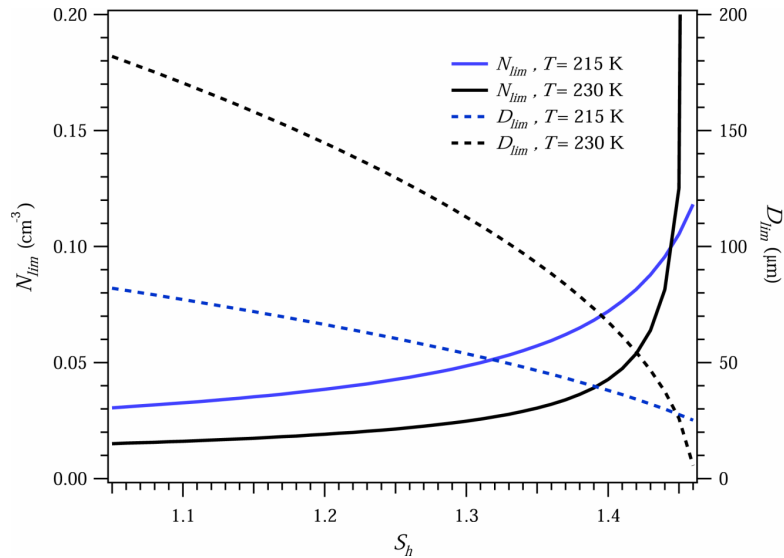
Figure 3.4. N_{lim} vs. S_h (solid line) and D_{lim} vs. S_h (dashed line) for $V = 0.2$ m s^{-1}, $\alpha_d = 0.1$.

The overestimation in N_{lim} at $S_h = 1.4$, however, is less pronounced at $T = 215$ K (Figure 3.3 upper panels); for these conditions $\Delta S_h > 0.1$, so the parameterization is insensitive to the error in S_{max}. It is also noticeable that at low V (< 0.2 m s^{-1}) the parameterized S_{max} does not introduce significant errors in N_{lim}.

3.3.2. Understanding Sources of Error

Discrepancy between the parameterization and the parcel model originate from (i) assumptions made in obtaining Eq. (3.31), which determines the shape of the curves N_c vs. N_{IN}, and, (ii) from errors in the calculation of N_{lim}, Eq. (3.22), which determines the minimum N_c. The relative contribution of each source of error can be assessed by calculating the average difference in N_c between the parcel model and the parameterization, normalized by the corresponding N_c (from parcel model results) obtained from pure homogeneous freezing (i.e., N_c for $N_{IN} \to 0$, Figure 3.3); which is about $1 \pm 10\%$ for all simulations of Table 3.1. This suggests that most of the discrepancy between parameterization and parcel model results occurs at low N_c (N_{IN} close to N_{lim}), therefore, most of the error in the parameterization should result from the calculation of N_{lim}. This is supported by the simulations in Figure 3.3, which show that the shape of the parameterized N_c vs. N_{IN} follows well the parcel model results, and discrepancy between the parameterization and parcel model mainly originates from slight "shifting" in N_{lim}.

Potential sources of error in the calculation of N_{lim} can be identified by analyzing Eq. (3.22). First, S_{max} has been assumed to remain constant during the homogeneous pulse. Although this is a good approximation for computing N_c from homogeneous nucleation, ΔS_h, which is dependent on S_{max} (Eq. (3.20)), maybe in error and bias the calculation of D_{lim} (hence N_{lim}). This is shown in Figure 3.4, which presents D_{lim} (dotted lines) and N_{lim} (solid lines) as a function of S_h, for $T = 215$ K ($S_{max} = 1.51$, blue lines) and $T = 230$ K ($S_{max} = 1.46$, black lines). At low S_h ($\Delta S_h > 0.1$), D_{lim} decreases almost linearly with S_h. For $\Delta S_h < 0.1$, the dependency of D_{lim} on S_h changes so that $D_{lim} \to 0$ when $S_h \to S_{max}$. As a

result, for $\Delta S_h > 0.1$, N_{lim} is almost linear in S_h (Eq. (3.22)) and insensitive to small errors in S_{max}. As $S_h \to S_{max}$, N_{lim} increases steeply and becomes very sensitive to errors in S_{max}. This is strongly evident for $T = 230$ K when $S_h > 1.4$ (Figure 3.4). At these conditions, $\Delta S_h < 0.06$, the parameterization becomes very sensitive to the value of S_{max} (Figure 3.3 for $S_h = 1.4$ and $T = 230$ K, i.e., black lines and circles), and tends to overestimate N_{lim} because the parameterized S_{max} is below S_{max} reached in the parcel model simulations. This effect is more pronounced at high V (Figure 3.3) as S_{max} tend to reach high values at such conditions.

Another potential source of error in the parameterization lies in neglecting the higher order terms in Eq. (3.10), $O(y, y^2, ...)$. Because of this, Eq. (3.12), will not predict a change in the sign of y (e.g., green line, Fig 3.1), and cannot describe the time "lag" before appreciable condensation rates are achieved upon the IN and the impact of ice crystals on $\dfrac{dS_i}{dt}$ becomes significant. Since Eq. (3.12) predicts an instantaneous effect of IN on $\dfrac{dS_i}{dt}$ (e.g., red line Figure 3.1), neglecting $O(y, y^2, ...)$ become less important when the impact of N_{IN} on $\dfrac{dS_i}{dt}$ is the highest, i.e., $N_{IN} = N_{lim}$. Moreover, the error introduced by neglecting $O(y, y^2, ...)$ is in general not critical to calculate $f_{c,IN}$, since at low N_{IN} the impact of IN on homogeneous nucleation is small.

Some bias may also be introduced when S_h is low. At these conditions, recently frozen crystals are exposed to low S_h therefore grow slowly, so even at $N_{IN} = N_{lim}$ there is a substantial time lag before they can impact ice saturation ratio. Since Eq. (3.12) does

not account for this, D_{lim} is slightly overpredicted and N_{lim} underpredicted (e.g., Figure 3.4). This "growth lag" effect is even stronger at low T and low α_d since condensation (growth) rates are further decreased. This is seen in the slight underprediction of the parameterization shown in Figure 3.3 at $S_h = 1.1$ and $T = 215$ K (upper panels, blue lines and circles).

3.3.3. Evaluation against Other Parameterizations

We first compare the new parameterization against the formulation of Kärcher et al. [106, referred to as K06]. K06 was developed for a polydisperse aerosol distribution, but it can be compared against the new parameterization provided that $S_{max} > S_h$ (for such conditions, the polydisperse population with a single freezing threshold can be well approximated by a chemically uniform and monodisperse IN with freezing threshold S_h). Simulations are carried out for $T_o = 210$ K (T= 206 K) and 230 K (T= 226 K), $p = 22000$ Pa, and $\alpha_d = 0.5$; N_{IN} was set to 1, 5, and 30 l^{-1} and S_h to 1.3. Results for K06 were obtained from [106]. Figure 3.5 shows the comparison between the two parameterizations; both formulations agree remarkably well. Slight discrepancies between the parameterization and K06 are found at $T_o = 210$ K and $N_{IN} = 1$ and 5 l^{-1}, which is explained by the differences in the homogeneous scheme of BN08 and K06, as analyzed in Barahona and Nenes [12]. very low V (< 0.03 m s^{-1}), $S_{max} < S_h$, and, comparison against K06 is not possible. Such conditions require a polydisperse formulation, and are addressed in the Chapter 4. Finally we compared Eq. (3.22) to the expressions provided for N_{lim} by Gierens [69, G03] and Liu and Penner [147, LP05]. LP05 (Figure 3.6, green circles) is based on detailed parcel model simulations and resolves the dependency of N_{lim} on T and V. G03 (Figure 3.6, stars) uses a semi-analytical

approach, where box model simulations are employed to fit the time scale of growth of the ice crystals; it resolves explicitly the dependency of N_{lim} on T, V, S_h and p.
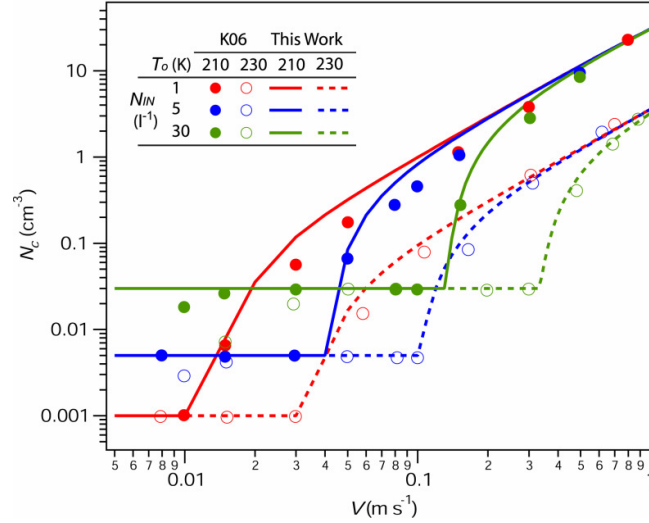
Figure 3.5. Comparison between the results of Kärcher et al. [106] and the parameterization in this work for $T_o = 210$ K ($T = 206$ K) and 230 K ($T=226$ K), $p = 22000$ Pa, and $\alpha_d = 0.5$.

Figure 3.6 presents the results of the three expressions as functions of T (left panel, $V = 0.1$ m s^{-1}) and V (right panel, $T = 215$ K), and $S_h = 1.3$ (blue) and 1.4 (black). Equation (3.22) is presented in Figure 3.6 for $\alpha_d = 0.1$ (dashed lines) and 1 (solid lines). At a given V (Figure 3.6, left panel), N_{lim} decreases almost exponentially with increasing T. The difference between N_{lim} predicted by G03 and Eq. (3.22) is the largest at $T = 200$ K, but is minimal at $T = 230$ K. The convergence at high T is likely from the large crystal size attained, which implies that the mass transfer coefficient is consistent with the approximation taken in G03 of neglecting kinetic effects. LP05 predicts N_{lim} about one order of magnitude lower than Eq. (3.22), potentially because they included both

deposition and immersion freezing in their simulations; deposition IN would act as a second population (with different S_h and N_{IN}) that would compete for water vapor with the existing crystals lowering N_{lim}. Equation (3.22) cannot currently represent such a case, but can be expanded to include it as shown in Chapter 4. At fixed T, G03 and Eq. (3.22) predict a $N_{lim} \sim V^{3/2}$ dependency (Figure 3.6, right panel). LP05 shows a higher order dependency, likely due to the effect of deposition IN depleting water vapor.
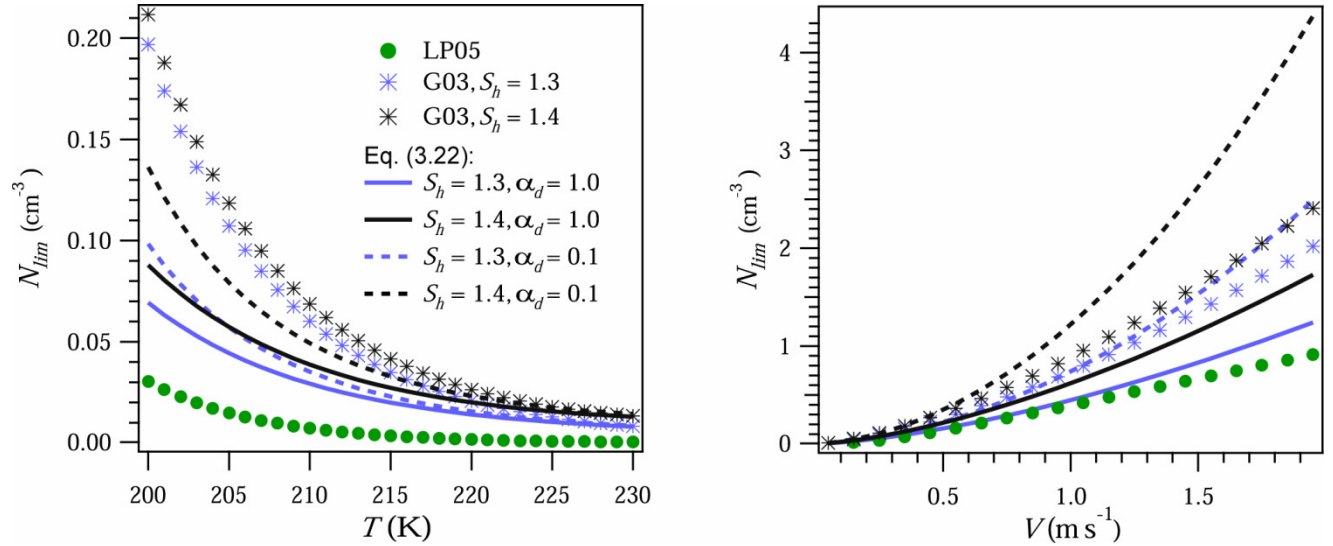
Figure 3.6. N_{lim} vs. T at $V = 0.1$ m s^{-1} (left panel) and N_{lim} vs. V at $T = 215$ K (right panel), calculated using the parameterizations of Gierens [69 , G03], Liu and Penner [147, LP05], and Eq. (3.22).

3.4. Summary and Conclusions

We developed an analytical parameterization for cirrus formation that explicitly considers the competition between homogeneous and heterogeneous nucleation. Using functional analysis of the crystal growth and ice saturation ratio evolution equations for a cloud

parcel, an expression relating $\dfrac{dS_i}{dt}$ to S_i was found, and used to calculate the limiting size

of the ice crystals, D_{lim}, and limiting concentration of IN that would prevent

homogeneous nucleation, N_{lim}. These two parameters were employed to obtain a simple,

yet accurate, expression to account for the reduction in $\dfrac{dS_i}{dt}$ due to the presence of

previously frozen crystals which, when incorporated within the physically-based

homogeneous nucleation framework of Barahona and Nenes [12], allows the calculation

of the number of crystals produced when heterogeneous and homogeneous freezing

mechanisms compete for water vapor during cirrus cloud formation.

Previous work, using numerical parcel simulations, determine "heterogeneously-

dominated" and "homogeneously-dominated" regimes and correlate them with cloud

formation conditions (V, T, and P). However, it was demonstrated that at conditions

where homogeneous freezing typically dominates (i.e., high V and low T), ice crystal

formation can be affected by IN, provided that N_{IN} is high enough. Thus, V and T cannot

uniquely define heterogeneously and homogeneously-dominated regimes, and,

parameterizations using such approaches are inherently limited. It was shown that the

contribution of each freezing mechanism to crystal number concentration, depends only

on $\dfrac{N_{IN}}{N_{lim}}$. By providing an expression for N_{lim}, the need for defining "dominant" regimes

of ice formation is eliminated.

When evaluated over a wide range of conditions, the new parameterization

reproduced the results of the detailed numerical solution of the parcel model equations,

with an average error of 6 ± 33%, which is remarkable low given the complexity and

nonlinearity of Eqs. (3.5) to (3.7). The approach presented here overcome common difficulties in including the competition between homogeneous and heterogeneous modes in large scale models. In this study we assumed a single type, monodisperse, chemically uniform, IN population. Multiple IN populations and freezing modes that reflect cirrus formation for atmospheric relevant aerosol is the focus of Chapter 4. Even though much work still remains to be done on the prediction of IN concentrations and freezing thresholds, this work offers a computationally efficient and rigorous approach to include such knowledge in atmospheric and cloud models, once available.

CHAPTER 4

PARAMETERIZING THE COMPETITION BETWEEN HOMOGENEOUS AND HETEROGENEOUS FREEZING IN ICE CLOUD FORMATION - POLYDISPERSE ICE NUCLEI[1]

This study presents a comprehensive ice cloud formation parameterization that computes the ice crystal number, size distribution, and maximum supersaturation from precursor aerosol and ice nuclei. The parameterization provides an analytical solution of the cloud parcel model equations and accounts for the competition effects between homogeneous and heterogeneous freezing, and, between heterogeneous freezing in different modes. The diversity of heterogeneous nuclei is described through a nucleation spectrum function which is allowed to follow any form (i.e., derived from classical nucleation theory or from observations). The parameterization reproduces the predictions of a detailed numerical parcel model over a wide range of conditions. The average error in ice crystal number concentration was -2.0 ± 8.5% for conditions of pure heterogeneous freezing, and, 4.7 ± 21% when both homogeneous and heterogeneous freezing were active. The formulation presented is fast and free from requirements of numerical integration.

---

[1] This chapter appears as referene [14]: BARAHONA, D. and NENES, A. (2009). Parameterizing the Competition between Homogeneous and Heterogeneous Freezing in Cirrus Cloud Formation. Polydisperse Ice Nuclei. *Atmospheric Chemistry and Physics*, 9, 5933-48.

4.1. Motivation

Ice clouds play a key role in rain production [e.g., 137], heterogeneous chemistry [196], stratospheric water vapor circulation [78], and the radiative balance of the Earth [145]. Representation of ice clouds in climate and weather prediction models remains a challenge due to the limited understanding of ice cloud formation processes [e.g., 143, 10], and the difficulties associated with the remote sensing of ice clouds [253]. Anthropogenic activities can potentially influence ice cloud formation and evolution by altering the concentration and composition of precursor aerosols [229, 195, 169, 111], which may result in a potentially important indirect effect [e.g., 110], the sign and magnitude of which however is highly uncertain.

Ice clouds form by homogeneous freezing of liquid droplets or heterogeneous freezing upon ice nuclei, (IN) [e.g., 208]. Observational data show that the two freezing mechanisms are likely to interact during cloud formation [43, 47, 76, 205]; their relative contribution is however a strong function of IN, aerosol concentration, and cloud formation conditions [69, 106, 13]. IN tend to freeze early during cloud formation, depleting water vapor supersaturation and hindering the freezing of IN with high freezing thresholds and the homogeneous freezing of liquid droplets [e.g., 45, 129]. Although numerous aerosol species have been identified as active IN, dust, soot, and organic particles are thought to be the most relevant for the atmosphere [43, 224, 5, 171, 55, 103, 198]. Assessment of the indirect effect resulting from perturbations in the background concentrations of IN requires a proper characterization of the spatial distribution of potential IN species and their freezing efficiencies (i.e., the aerosol freezing fraction). The large uncertainty in ice cloud indirect forcing is associated with incomplete

understanding of these factors which is evident by the large predictive uncertainty of aerosol-cloud parameterizations [198, 52].

Several approaches have been proposed to parameterize ice cloud formation in atmospheric models. Empirical correlations derived from field campaigns are most often employed to express IN concentrations [e.g., 166, 46] as a function of temperature, T, and supersaturation over ice, s_i. These expressions are simple but only provide the availability of IN over a limited spatial region. A more comprehensive expression was developed by Phillips et al. [198], who combined data from several field campaigns to estimate the contribution of individual aerosol species to the total IN concentration.

Empirical parameterizations are incomplete, as they provide only IN concentrations. Calculation of ice crystal number concentration, N_c, requires the knowledge of cloud supersaturation and therefore the usage of a dynamical framework. Liu and Penner [147] considered this, and used numerical solutions from a cloud parcel model to correlate N_c to cloud formation conditions (i.e., T, p, V) and the number concentration of individual aerosol species (dust, soot, and sulfate). Although a computationally efficient approach, these correlations are restricted to (largely unconstrained) assumptions regarding the nature of freezing (i.e., the estimation of freezing efficiencies), the size distributions of dust, soot, and sulfate, the mass transfer (i.e., deposition) coefficient of water vapor onto crystals, and, the active freezing mechanisms. Kärcher et al. [106] proposed a physically based approach to parameterize cirrus cloud formation combining solutions for the pure homogeneous freezing [108], and heterogeneous freezing [110] into a numerical scheme. Although this approach includes all known relevant factors that determine N_c, it may be computationally intensive; thus, its application is limited to cases where IN can be

characterized by a few, well defined, freezing thresholds. Although many cases of atmospheric aerosol can be described this way, it may not be adequate, as even single class aerosol populations usually exhibit a distribution of freezing thresholds [e.g., 166, 173, 158, 103, 198, 252, 255]. Barahona and Nenes [13] developed an analytical parameterization that combines homogeneous and heterogeneous freezing within a single expression. Although very fast and with low error (6 ± 33%), this approach is limited to cases where the IN population can be characterized by a single freezing threshold.

This work presents a new physically-based, analytical and computationally efficient framework to parameterize ice cloud formation. The new scheme allows the usage of both empirical and theoretical IN data in a simple dynamical framework, and can consider the spectral variability in aerosol and IN composition. The new parameterization builds upon the frameworks of Barahona and Nenes [12-13] that combine homogeneous and heterogeneous mechanisms of ice formation, and explicitly resolves the dependency of N_c on conditions of cloud formation (i.e., T, p, V), aerosol number and size, and the freezing characteristics of the IN.

4.2. Description of the Ice Nucleation Spectrum

Modeling of ice cloud formation requires a function describing the number concentration of crystals frozen from an aerosol population (i.e., the aerosol freezing fraction) at some temperature, T, and supersaturation, s_i. The function, known as the "nucleation spectrum", is closely related to the nucleation rate coefficient, J, and the freezing probability, P_f. Theoretical studies [e.g., 143, 120] and laboratory experiments [e.g., 241, 129, 89, 75-76] suggest that J becomes substantially large around some threshold T and s_i [208]. Decreasing T (or increasing s_i) beyond this level exponentially increases J so that

(unless s_i is depleted by water vapor deposition onto growing ice crystals) the probability of freezing, P_f eventually becomes unity [208, 143, 117, 175, 12]. Observations have confirmed this for homogeneous freezing of aqueous droplets, where the threshold s_i and T is confined within a very narrow range of values [85, 44, 208, 243, 27, 40, 117] and depends primarily on the water activity within the liquid phase [129].

Heterogeneous freezing is different from homogeneous freezing in that it exhibits a broad range of freezing thresholds, even for aerosol of the same type [e.g., 208, 263, 5, 1, 55, 173, 158, 51, 103, 120]. Field campaign data [166, 46] and laboratory studies [55, 173, 262, 255] show that for s_i values larger than the threshold s_i, the aerosol freezing fraction (i.e., P_f) is below unity, increasing with s_i much more slowly than suggested by theory [e.g., 118, 198, 52]. This discrepancy can be reconciled by assuming that the heterogeneous nucleation rate depends on the local conditions adjacent to individual nucleation sites, rather than on the average characteristics of the aerosol population (i.e., the "singular hypothesis" [e.g., 57, 251]). Freezing occurs instantaneously when a threshold s_i and T associated with a nucleation site are reached; thus a distribution of active nucleation sites on the aerosol particles would result in a distribution of freezing thresholds [158, 260, 252, 52, 120]. The aerosol freezing fraction is then related to the density of active nucleation sites (which generally depends on particle history and chemical composition [208, 1]) and to the surface area and number concentration of the aerosol population. Vali [251-252] have argued that $P_f < 1$ for each active nucleation site, which may arise if the active sites exhibit transient activity; this implies a temporal dependency of P_f which is however second order on the freezing threshold distribution [252, 120].

Experimental studies and field campaign data [e.g., 173, 198] show that at constant T, the aerosol freezing fraction is well represented by a continuous function of s_i, which results from the diversity of active nucleation sites that may be available in the insoluble aerosol population [208]. If sufficient time is allowed so that transient effects vanish (i.e., P_f is at its maximum), then the "nucleation spectrum" can be defined as,

$$n_s(s_i, T, p, ...) = \frac{\partial N_{het}(s_i, T, p, ...)}{\partial s_i}\bigg|_{T, p, ...} \tag{4.1}$$

where $N_{het}(s_i, T, p, ...)$ is the crystal number concentration produced by heterogeneous freezing. The subscripts on the right hand side of Eq. (4.1) indicate that all other state variables (T, p, aerosol concentrations) remain constant when the nucleation spectrum is measured or computed with theory. Therefore, for the remainder of this study, $N_{het}(s_i, T, p, ...)$ is represented as $N_{het}(s_i)$ ($n_s(s_i)$ in its differential form), assuming an implicit dependency on other state variables.

4.2.1. Empirical IN Spectra

Developing an ice formation parameterization requires the knowledge of the IN nucleation spectrum in its differential $n_s(s_i)$, or cumulative form, $N_{het}(s_i)$; these can be obtained empirically from field campaign data [166, 198], laboratory experiments [e.g., 173, 255] or from nucleation theory (section 4.2.2). The simplest form for $n_s(s_i)$ arises by assuming that IN concentrations depend solely on s_i; characteristic examples are the formulations of Meyers et al. [166, MY92, Table 1] and the background spectrum of Phillips et al. [199, PDG07, Table 1]. MY92 is derived from in-situ measurements of IN concentrations for T between 250 and 266 K and s_i between 2 and 25 %. PDG07 is

derived from MY92 (after applying an scaling factor to account for the height dependency of IN concentration) and the data of DeMott et al. [43]. A more comprehensive formulation, considering (in addition to s_i and T) the surface area contribution from different aerosol types (i.e., dust, organic carbon, and soot) and freezing modes (i.e., deposition and immersion), was presented by Phillips et al. [198, PDA08]. PDA08 is developed using IN and aerosol concentration measurements from several field campaigns.

4.2.2. IN spectra from Classical Nucleation Theory

Theoretical arguments can also be used to obtain an approximate form for the nucleation spectrum. Classical nucleation theory (CNT) suggests that the nucleation rate at two s_i thresholds can be related as [208, 117]

$$J(s_{i,1}) \approx J(s_{i,2}) \exp\left[-k(T)(s_{i,2} - s_{i,1})\right] \tag{4.2}$$

where $J(s_{i,1})$ and $J(s_{i,2})$ are the nucleation rate coefficients at $s_{i,1}$ and $s_{i,2}$ respectively; $k(T)$ is a proportionality constant depending on T. Using this, Barahona and Nenes [12] showed that for pure homogeneous freezing the nucleation spectrum, $N_{\text{hom}}(s_i)$, can be approximated as,

$$N_{\text{hom}}(s_i) \approx N_o \frac{J_{\text{hom}}(s_{\text{hom}})\overline{v}_o}{\alpha V\, k_{\text{hom}}} \frac{1}{(s_{\text{hom}} + 1)} \exp\left[-k_{\text{hom}}(s_{\text{hom}} - s_i)\right] \tag{4.3}$$

where $J_{\text{hom}}(s_{\text{hom}})$ is the homogenous nucleation rate coefficient at the homogeneous freezing threshold, s_{hom}; N_o and $\overline{v}_o$ are the number concentration and mean volume of the droplet population, respectively, and $k_{\text{hom}} = (s_{\text{hom}} - s_i)^{-1} \ln \dfrac{J_{\text{hom}}(s_{\text{hom}})}{J_{\text{hom}}(s_i)}$. Eq. (4.3) can be

extended to describe heterogeneous nucleation by replacing k_{hom} with a heterogeneous nucleation analog, $k(T)$ [e.g., 208, 117, 120],

$$k(T) = k_{hom} f_h \tag{4.4}$$

where $f_h \approx \frac{1}{4}(m^3 - 3m + 2)$, $m = \cos(\theta)$ and θ is the IN-water contact angle [56].

Replacing k_{hom} in Eq. (4.3) with $k(T)$ from Eq. (4.4), s_{hom} with the heterogeneous freezing threshold, $s_{h,j}$, and, generalizing to an external mixture of nsp IN populations, we obtain

$$N_{het}(s_i) \approx \sum_{j=1,nsp} \min\left\{ e_{f,j} N_{a,j} \exp\left[-k_{hom} f_{h,j}(s_{h,j} - s_i)\right], e_{f,j} N_{a,j} \right\} \tag{4.5}$$

where $s_{h,j}$ is the freezing threshold of the jth IN population, and, $N_{a,j}$ is the corresponding aerosol number concentration; $s_{h,j}$ is associated with the onset of large nucleation rates at which the aerosol freezing fraction reaches a maximum. $e_{f,j} \approx \left[C \frac{J_{h,j}(s_{h,j})\overline{\Omega}_j}{\alpha V\, k(T)} \frac{1}{(s_{h,j}+1)} \right]$ is the freezing efficiency of the jth population, where $J_{h,j}(s_{h,j})$ is the heterogeneous nucleation rate coefficient at $s_{h,j}$, and C depends on the mean surface area of the jth aerosol population, $\overline{\Omega}_j$.

Nucleation spectra based on CNT (and therefore on the stochastic hypothesis [208]) depend on t, which is evident on Eq. (4.5) as $e_{f,j} \propto \frac{J(s_{h,j})}{V}$. To be consistent with Eq. (4.1), it is required that $e_{f,j} \neq f(t)$, which implies that the temporal dependency in Eq. (4.5) should vanish. Assuming that enough time is allowed for heterogeneous freezing

during IN measurements (used to constrain the parameters of CNT), the stochastic component of CNT is small, and the resulting nucleation spectra would practically be time-independent, hence consistent with Eq. (4.1).

The exponential form of Eq. (4.5) is in agreement with experimental studies [e.g., 173]. Eq. (4.5) however requires the knowledge of $e_{f,j}$ which in this study is treated as an empirical parameter and used to constrain the maximum freezing fraction of the aerosol population (in reality $e_{f,j}$ is a function of T, aerosol composition and size, and is analyzed in a companion study). Values for $e_{f,j}$, $s_{h,j}$, and θ_j used in this study (section 4.4.1, Table 4.1) are selected from the literature. Complete characterization of the nucleation spectra using nucleation theory requires the usage of probability distributions for θ_j and $s_{h,j}$ [e.g., 158, 120]. Although this can in principle be included in Eq. (4.5), little is known on the formulation of such probability distributions and is not considered here.

4.3. Formulation of the Parameterization

The parameterization is based on the framework of an ascending Lagrangian parcel. At any height during the parcel ascent, supersaturation with respect to ice, s_i, develops and the ice crystal size distribution is determined by heterogeneous freezing of IN, homogeneous freezing of droplets, and growth of existing ice crystals. The solution when homogeneous freezing is the only mechanism active is presented in Barahona and Nenes [12]. The general solution for pure heterogeneous, and, combined homogeneous-heterogeneous freezing is presented in the following sections.

4.3.1. The Ice Parcel Equations

In the initial stages of cloud formation s_i increases monotonically due to cooling from expansion; growth of crystals, frozen either homogeneously or heterogeneously, increasingly depletes water vapor, up to some level where s_i reaches a maximum, s_{max} (because depletion balances the s_i increase due to cooling). At any given point in time, the state of the cloud is determined by the coupled system of equations [13]

$$w_i(t) = \frac{\rho_i}{\rho_a} \frac{\pi}{6} \int ... \int_X D_c^3 n_c(D_c, D_{IN}, m_{1,...,nx}, t) dD_c dD_{IN} dm_{1,...,nx} \tag{4.6}$$

$$\frac{ds_i}{dt} = \alpha V(1 + s_i) - \beta \frac{dw_i}{dt} \tag{4.7}$$

$$\frac{dw_i}{dt} = \frac{\rho_i}{\rho_a} \frac{\pi}{2} \int ... \int_X D_c^2 \frac{dD_c}{dt} n_c(D_c, D_{IN}, m_{1,...,nx}, t) dD_c dD_{IN} dm_{1,...,nx} \tag{4.8}$$

$$\frac{dD_c}{dt} = \frac{s_i}{\Gamma_1 D_c + \Gamma_2} \tag{4.9}$$

where $\dfrac{dw_i}{dt}$ is the rate of water vapor deposition on the ice crystals and V is the updraft velocity. D_c and D_{IN} are the volume-equivalent diameter of the ice crystals and IN, respectively (for homogeneous nucleation D_{IN} is replaced by the size of cloud droplets), $m_{1,...,nx}$ collectively represents the mass fractions of the nx chemical species present in the aerosol population. $n_c(D_c, D_{IN}, m_{1,...,nx}, t)$ is the number distribution of the ice crystals; therefore $n_c(D_c, D_{IN}, m_{1,...,nx}, t) dD_c dD_{IN} dm_{1,...,nx}$ represents the number concentration of ice crystals with sizes in the range $(D_c, D_c + dD_c)$, made from an aerosol particle in the size range $(D_{IN}, D_{IN} + dD_{IN})$, and with composition defined by the interval

$(m_{1,...,nx}, m_{1,...,nx} + dm_{1,...,nx})$. X in Eqs. (4.6) and (4.8) is the domain of integration and spans over all the values of D_c, D_{IN}, and $m_{1,...,nx}$ for which $n_c(D_c, D_{IN}, m_{1,...,nx}, t)$ is defined. The calculation of $w_i(t)$ and $\dfrac{dw_i}{dt}$ requires the knowledge of $n_c(D_c, D_{IN}, m_{1,...,nx}, t)$, therefore an equation describing the evolution of $n_c(D_c, D_{IN}, m_{1,...,nx}, t)$ should be added to Eqs. (4.7) to (4.9). The coupling between n_c, D_c, and s_i in Eqs. (4.7) to (4.9) precludes a closed analytical solution and are numerically integrated [e.g., 143 and references therein, 175, 12].

The main parameter of interest resulting from the solution of Eqs. (4.7) to (4.9) is the ice crystal number concentration, $N_c = N_{hom} + N_{het}$, where N_{hom} and N_{het} are the ice crystal number concentrations from homogeneous and heterogeneous freezing, respectively. N_{hom} can be treated using the analytical approach of Barahona and Nenes [12], while N_{het} is equal to N_{het} at s_{max}. Therefore, determining N_c requires the computation of s_{max}.

4.3.2. Simplifying the Supersaturation Balance

N_{het} and s_{max} are determined by solving for the root of Eq. (4.7). This is turn is accomplished by manipulating Eq. (4.7) so that the contribution of nucleation and growth to the evolution of the ice crystal population is decoupled. The root is then analytically determined for freezing of a monodisperse, chemically homogenous, ice crystal population based on the approach of Barahona and Nenes [13]. The monodisperse solution is then generalized for a polydisperse, heterogeneous IN population by introducing the characteristic freezing threshold and size of the ice crystal population.

The size of ice crystals after freezing and growth at any time during the parcel ascent is given by integration of Eq. (4.9), assuming negligible non-continuum effects on mass transfer; i.e., $\Gamma_1 >> \Gamma_2$ (Section 4.3.3), and, $\frac{dD_c}{dt} \approx \frac{s_i}{\Gamma_1 D_c}$ [12],

$$D_c(t, s_i) = \left(D_{IN}^2 + \frac{1}{\Gamma_1} \int_{s_o'}^{s_i} \frac{s}{ds/dt} ds \right)^{1/2} \qquad (4.10)$$

where D_{IN} is the initial size of the ice crystals at the moment of freezing, and, s_o' is their freezing threshold [12]. s_o' generally depends on composition and size (section 4.2). A chemically-heterogeneous, polydisperse IN population can thus be treated as the superposition of monodisperse, chemically-homogeneous IN classes, each with their respective s_o'; Eq. (4.10) can then be applied to each "IN class" of size and composition.

Equation (4.10) can be simplified assuming that $\frac{1}{\Gamma_1} \int_{s_o'}^{s_i} \frac{s}{ds/dt} ds >> D_{IN}^2$, which means that the growth experienced by crystals beyond the point of freezing is much larger than their initial size [e.g., 108, 189, 118, 175, 13], and is justified given that typical crystal sizes, $D_c > 20$ μm, are much larger than the typical $D_{IN} \sim 1$ μm found in the upper troposphere [e.g., 84, 64]. Eq. (4.10) is further simplified by considering that the thermodynamic driving force for ice crystal growth (i.e., the difference between s_i and the equilibrium supersaturation) is usually large (s_{max} generally above 20% [e.g., 143, 76]). This suggests that crystal growth rates would be limited by water vapor mass transfer rather than by s_i (confirmed by parcel model simulations). Therefore, D_c is a strong function of the crystal residence time in the parcel and weakly dependent on s_i. The

limits of the integral in Eq. (4.10) imply that the crystal residence time is mainly a function of the difference $s_i - s_o'$; Eq. (4.10) therefore can be rewritten as

$$D_c(t, s_i) \approx D_c(s_i - s_o') \tag{4.11}$$

where $D_c(s_i - s_o')$ signifies that D_c is a function of $s_i - s_o'$.

Equations (4.1) and (4.11) suggest that Eq. (4.6) can be written in terms of s_i and s_o',

$$w_i(s_i) = \frac{\pi}{6} \frac{\rho_i}{\rho_a} \int_0^{s_i} D_c^3(s_i - s_o') n_s(s_o') \, ds_o' = \frac{\pi}{6} \frac{\rho_i}{\rho_a} \left[D_c^3 \otimes n_s \right](s_i) \tag{4.12}$$

where $\otimes$ represents the half-convolution product [115]. Taking the derivative of Eq. (4.12) and substitution into Eq. (4.7) gives,

$$\frac{ds_i}{dt} = \alpha V(1 + s_i) - \beta \frac{\rho_i}{\rho_a} \frac{\pi}{2} \left[D_c^2 \frac{dD_c}{dt} \otimes n_s \right](s_i) \tag{4.13}$$

Equation (4.13) is a simplified supersaturation balance equation used in place of Eq. (4.7), the root of which (i.e., $\frac{ds_i}{dt} = 0$) gives s_{max},

$$\alpha V(1 + s_{max}) = \beta \frac{\rho_i}{\rho_a} \frac{\pi}{2} \left[D_c^2 \frac{dD_c}{dt} \otimes n_s \right](s_{max}) \tag{4.14}$$

4.3.3. Analytical Correction for Non-Continuum Effects

The solution of Eq. (4.14) requires the knowledge of $D_c^2 \frac{dD_c}{dt}$ at s_{max}, which is a highly nonlinear function of s_i (e.g., Eq. (4.10)); this however can be simplified as follows. The

lower limit for the size of an ice crystal ice crystal that freezes at supersaturation $s_o' = 0$

during the parcel ascent [216, 12], obtained assuming $\left. \dfrac{ds_i}{dt} \right|_{s_{max}} \approx \alpha V (s_{max} + 1)$, is given by

$$D_c (\Delta s, \alpha_d) = -\frac{\Gamma_2}{\Gamma_1} + \sqrt{\left(\frac{\Gamma_2}{\Gamma_1}\right)^2 + \frac{\Delta s^2}{\alpha V \Gamma_1}} \tag{4.15}$$

where $\Delta s = s_{max} - s_o'$ and it was assumed that $\Delta s - \ln\left(\dfrac{s_{max} + 1}{s_o' + 1}\right) \approx \dfrac{1}{2} \Delta s^2$. D_c depends on

α_d as $\Gamma_2 \propto \dfrac{1}{\alpha_d}$. Eq. (4.15) provides a lower limit for D_c and can be used to develop a

conservative (i.e., where mass transfer limitations to crystal growth are most significant)

correction for non-continuum mass transfer effects. Equation (4.15) can be rewritten as

$$D_c (\Delta s, \alpha_d) = \gamma \left[\sqrt{1 + (\lambda \Delta s)^2} - 1 \right] \tag{4.16}$$

where $\gamma = \dfrac{\Gamma_2}{\Gamma_1}$, $\lambda = \sqrt{\dfrac{1}{\alpha V \Gamma_1 \gamma^2}}$. After substituting Eq. (4.16) into Eq. (4.9) and

rearranging, the volumetric rate of change of an ice crystal at s_{max}, i.e.,

$$\frac{\pi}{2} D_c^2 \frac{dD_c}{dt} = \frac{\pi}{2} \frac{s_{max} D_c^2}{\Gamma_1 D_c + \Gamma_2}, \text{ can be written in the form}$$

$$\frac{\pi}{2} D_c^2 \frac{dD_c}{dt} = \frac{\pi}{2} \frac{s_{max}}{\Gamma_1} \frac{\gamma \left(1 - \sqrt{1 + (\lambda \Delta s)^2}\right)^2}{\sqrt{1 + (\lambda \Delta s)^2}} \tag{4.17}$$

Multiplying an dividing the right hand side of Eq. (4.17) by $\lambda \Delta s$ and rearranging gives,

$$\frac{\pi}{2} D_c^2 \frac{dD_c}{dt} = \left[\frac{\pi}{2} \frac{s_{\max} \gamma \lambda \Delta s}{\Gamma_1} \right] \left[\frac{\left(1 - \sqrt{1 + \left(\lambda \Delta s \right)^2} \right)^2}{\lambda \Delta s \sqrt{1 + \left(\lambda \Delta s \right)^2}} \right] \qquad (4.18)$$

It can be recognized that the first term in brackets in Eq. (4.18) is obtained from

$\frac{\pi}{2} D_c^2 \frac{dD_c}{dt} = \frac{\pi}{2} \frac{s_{\max} D_c^2}{\Gamma_1 D_c + \Gamma_2}$, taking into account Eq. (4.15), when $\Gamma_1 \gg \Gamma_2$, i.e., when non-

continuum effects on mass transfer can be neglected [cf. 12, section 3.3]. Thus, the

second term in brackets in Eq. (4.18) corresponds to a correction factor to $\frac{\pi}{2} D_c^2 \frac{dD_c}{dt}$ for

non-continuum mass transfer effects, which only depends on the product $\lambda \Delta s$. Eq. (4.11)

suggests that $\lambda s_{\max}$ is a characteristic value for $\lambda \Delta s$, therefore Eq. (4.18) can be rewritten

as

$$\frac{\pi}{2} D_c^2 \frac{dD_c}{dt} \approx \frac{\pi}{2} \frac{s_{\max} D_c (\Delta s)}{\Gamma_1} \frac{\left(1 - \sqrt{1 + \lambda^2 s_{\max}^2} \right)^2}{\lambda s_{\max} \sqrt{1 + \lambda^2 s_{\max}^2}} \qquad (4.19)$$

For $s_{\max} > 0.05$, Eq. (B5) can be approximated by

$$\frac{\pi}{2} D_c^2 \frac{dD_c}{dt} \approx \frac{\pi}{2} \frac{s_{\max} D_c (\Delta s)}{\Gamma_1} e^{-2/\lambda s_{\max}} \qquad (4.20)$$

4.3.4. Determining s_{max} and N_{het}

Combining Eqs. (4.9) and (4.20) e.g., $\frac{D_c^2 s_{\max}}{\Gamma_1 D_c + \Gamma_2} \approx \frac{s_{\max}}{\Gamma_1} e^{-2/\lambda s_{\max}} D_c$, and substitution into

Eq. (4.14) and rearranging gives,

$$\frac{\alpha V \Gamma_1}{\beta \dfrac{\rho_i}{\rho_a} \dfrac{\pi}{2}} \frac{1+s_{max}}{s_{max}} e^{2/\lambda s_{max}} = \left[D_c \otimes n_s\right](s_{max}) \tag{4.21}$$

Eq. (4.21) holds regardless of the form of $n_s(s_i)$, and can be applied to a monodisperse, chemically-homogeneous IN population, for which all ice crystals freeze at a characteristic threshold (e.g., Chapter 3), s_{char}. $n_s(s_i)$ is thus a delta function about s_{char}, $\delta(s - s_{char})$. Substitution into Eq. (4.21) gives

$$\frac{\alpha V \Gamma_1}{\beta \dfrac{\rho_i}{\rho_a} \dfrac{\pi}{2}} \frac{1+s_{max}}{s_{max}} e^{2/\lambda s_{max}} = N_{het}(s_{max}) \int_{s_{char}}^{s_{max}} D_c(s_{max} - s)\delta(s - s_{char})ds \tag{4.22}$$

Integration of (4.22) gives

$$\frac{\alpha V \Gamma_1}{\beta \dfrac{\rho_i}{\rho_a} \dfrac{\pi}{2}} \frac{1+s_{max}}{s_{max}} e^{2/\lambda s_{max}} = N_{het}(s_{max})D_c(\Delta s_{char}) \tag{4.23}$$

where $\Delta s_{char} = s_{max} - s_{char}$. Comparing Eqs. (4.21) and (4.23) gives,

$$\left[D_c \otimes n_s\right](s_{max}) = N_{het}(s_{max})D_c(\Delta s_{char}) \tag{4.24}$$

Equation (4.24) shows that the components describing nucleation and growth during the evolution of an ice crystal population can be separated; i.e., the nucleation spectrum can be determined independently of the dynamics of the parcel ascent. The same conclusion can be obtained by applying the identity $\int (f_1 * f_2)\,dx = \int f_1(u)\,du \int f_2(v)\,dv$ [115] to Eq. (4.14), e.g.,

$$\int_0^{s_{max}} \left[D_c^2 \frac{dD_c}{dt} \otimes n_s \right](s)\,ds = \left[\int_0^{s_{max}} n_s(s)\,ds \right]\left[\int_0^{s_{max}} D_c^2 \frac{dD_c}{dt}\,ds \right]$$
$$= N_{het}(s_{max}) \left[\int_0^{s_{max}} D_c^2 \frac{dD_c}{dt}\,ds \right] \tag{4.25}$$

which shows that nucleation and growth can be decoupled independently of the form of

$D_c^2 \dfrac{dD_c}{dt}$.

Equation (4.24) is a version of the mean value theorem, and physically means that the rate of change of surface area of a polydisperse ice crystal population can be described using the monodisperse approximation, provided that a suitable s_{char} is defined. Equation (4.24) is a Volterra equation of the first kind and can be solved using several analytically and numerical methods [e.g., 144]. For this, the functional form of $n_s(s_i)$ needs to be known in advance. To keep the parameterization as general as possible, an approximate solution is used instead. $D_c(\Delta s_{char})$ is expected to be of the order of the largest ice crystals in the population (since they dominate the ice crystal population surface area). As these crystals grow slowly, their size is to first order a linear function of $\Delta s = s_{max} - s_i$ [13]. Therefore, $D_c(\Delta s)$ and $D_c(\Delta s_{char})$ are related by

$$D_c(\Delta s) \approx D_c(\Delta s_{char}) \frac{\Delta s}{\Delta s_{char}} \tag{4.26}$$

Substituting Eq. (4.26) into Eq. (4.24), we obtain,

$$\left[n_s \otimes \Delta s \right](s_{max}) = N_{het}(s_{max})\Delta s_{char} \tag{4.27}$$

which after taking the derivative with respect to s_{max} gives [115],

$$\int_0^{s_{max}} n_s(s)ds = n_s(s_{max})\Delta s_{char} \tag{4.28}$$

Application of Eq. (4.1) to Eq. (4.28), and rearranging, gives,

$$\Delta s_{char} = \frac{N_{het}(s_{max})}{n_s(s_{max})} \tag{4.29}$$

If s_{max} is large enough, all IN are frozen and $n_s(s_{max}) \to 0$; this can lead to numerical instability as Δs_{char} becomes very large. However, a large Δs_{char} also implies that a significant fraction of crystals freeze during the early stages of the parcel ascent so that, $s_{char} \to 0$ hence, $\Delta s_{char} \to s_{max}$ and s_{max} is the upper limit for Δs_{char}. With this, Eq. (4.29) becomes,

$$\Delta s_{char} = \min\left(\frac{N_{het}(s_{max})}{n_s(s_{max})}, s_{max}\right) \tag{4.30}$$

$D_c(\Delta s_{char})$ is calculated considering the growth of a monodisperse population (Chapter 3) with freezing threshold, s_{char} [13],

$$D_c(\Delta s_{char}) = \sqrt{\frac{2\Delta s_{char}^*}{\alpha V \Gamma_1}} \tag{4.31}$$

with $\Delta s_{char}^* = \dfrac{\Delta s_{char}\left[\dfrac{4}{3}\Delta s_{char} + 2(s_{max} - \Delta s_{char})\right]}{(1 + s_{max} - \Delta s_{char})}$

4.3.4.1 Final Form for Pure Heterogeneous Freezing

$N_{het}(s_{max})$ is calculated from combination of Eqs. (4.23) and (4.31),

$$\frac{N_{het}(s_{max})}{N^*} = \frac{1}{\sqrt{\Delta s^*_{char}}} \frac{(1+s_{max})}{s_{max}} e^{\frac{2}{\lambda s_{max}}} \tag{4.32}$$

with $N^* = \sqrt{2}(\alpha V \Gamma_1)^{3/2} \left(\beta \frac{\pi}{2} \frac{\rho_i}{\rho_a} \right)^{-1}$. Eq. (4.32) is the solution of the s_i balance (Eq. (4.14)) for pure heterogeneous freezing and shows that $N_{het}(s_{max})$ depends only on s_{max}, N^*, λ, and Δs_{char}. N^* has dimensions of number concentration and represents the ratio of the rate of increase in s_i from expansion cooling to the rate of increase in the surface area of the crystal population. Δs_{char} is related to the steepness of $n_s(s_i)$ about s_{max}; a value of $\Delta s_{char} \to 0$ implies that most of the crystals freeze at s_i close to s_{max}. λ accounts for non-continuum effects; if the crystal concentration is low ($\sim$ less than 0.01 cm^{-3}) and $\Delta s_{char} \to s_{max}$ then size effects on $N_{het}(s_{max})$ can usually be neglected. Equation (4.32) is solved along with an expression for $N_{het}(s_{max})$ to find s_{max} (section 4.3.4, Figure 4.2).

4.3.5. Competition between Homogeneous and Heterogeneous Freezing

At T below 235 K, ice clouds form primarily from homogeneous freezing [e.g., 85, 43, 13]. If a significant concentration of IN is present, freezing of IN prior to the onset of homogeneous nucleation may inhibit droplet freezing [69, 13]. Eqs. (4.7) to (4.9) can be readily extended to account for this, for which a generalized nucleation spectrum is defined that includes contribution from homogeneous freezing of droplets. This is simplified if taken into account that homogeneous nucleation rates are very high, and, the nucleation spectrum is close to being a delta function about $s_i = s_{hom}$. Furthermore, since the number concentration of liquid droplets available for freezing is much greater than the concentration of IN (i.e., $N_o \gg N_{het}$), s_{max} is reached soon after homogeneous

freezing is triggered ($s_{max} \approx s_{hom}$) [109, 12]. IN freezing thresholds are generally lower than s_{hom}; homogeneous freezing can always be considered the last freezing step during ice cloud formation.

As the growth of previously frozen crystals reduces the rate of increase of s_i, (i.e., $\left.\dfrac{ds_i}{dt}\right|_{s_{hom}}$), the presence of IN tends to reduce the probability of homogeneous freezing and the ice crystal concentration (compared to a pure homogeneous freezing event). The droplet freezing fraction, f_c, in the presence of IN is proportional to the decrease in $\left.\dfrac{ds_i}{dt}\right|_{s_{hom}}$ [13] from the presence of IN, i.e.,

$$f_c = f_{c,hom} \left(\frac{\left.\dfrac{ds_i}{dt}\right|_{s_{hom}}}{\alpha V(s_{hom}+1)} \right)^{3/2} \tag{4.33}$$

where $\alpha V(s_{hom}+1)$ is an approximation to $\left.\dfrac{ds_i}{dt}\right|_{s_{hom}}$ when IN are not present, and, $f_{c,hom}$ is the droplet freezing fraction under pure homogeneous conditions, given by Barahona and Nenes [12]. Although Eq. (4.33) is derived for a monodisperse IN population, Eq. (4.27) suggests that the effect of the polydisperse IN population can be expressed as a monodisperse population, provided that a suitable characteristic freezing threshold, s_{char}, is defined. Extending the monodisperse IN population solution [13] to a polydisperse aerosol gives,

$$\frac{\frac{ds_i}{dt}\Big|_{s_{\text{hom}}}}{\alpha V(s_{\text{hom}}+1)} \approx 1-\left(\frac{N_{het}(s_{\text{hom}})}{N_{\text{lim}}}\right)^{3/2}$$ (4.34)

where $N_{het}(s_{\text{hom}})$ is calculated from the nucleation spectrum function (section 4.2), and N_{lim} is the limiting IN concentration that completely inhibits homogeneous freezing [13]. If $N_{het}(s_{\text{hom}})$ is such that $s_{\text{max}} = s_{\text{hom}}$, then all IN concentrations greater than $N_{het}(s_{\text{hom}})$ would result in $s_{\text{max}} < s_{\text{hom}}$ and prevent homogeneous freezing (i.e., heterogeneous freezing would be the only mechanism forming crystals). Conversely, if the IN concentration is lower than $N_{het}(s_{\text{hom}})$ and $s_{\text{max}} > s_{\text{hom}}$, homogeneous freezing is active. Thus, N_{lim} must be equal to $N_{het}(s_{\text{hom}})$ at $s_{\text{max}} = s_{\text{hom}}$, and is obtained by substituting $s_{\text{max}} = s_{\text{hom}}$ into Eq. (4.32), i.e.,

$$\frac{N_{\text{lim}}}{N^*} = \frac{1}{\sqrt{\Delta s_{char}^*\big|_{s_{\text{hom}}}}} \frac{(1+s_{\text{hom}})}{s_{\text{hom}}} e^{\frac{2}{\lambda s_{\text{hom}}}}$$ (4.35)

For very low N_{het}, Eq. (4.33) approaches the pure homogeneous freezing limit as the effect of IN is negligible; homogeneous freezing is prevented for $N_{het}(s_{\text{hom}}) \geq N_{\text{lim}}$ and $f_c \leq 0$. Thus, combination of Eqs. (4.32) and (4.33) provides the total crystal concentration, N_c, from the combined effects of homogeneous and heterogeneous freezing [13],

$$N_c = \begin{cases} N_o e^{-f_c}(1-e^{-f_c}) + N_{het}(s_{\text{hom}}) & f_c > 0 \text{ and } T < 235\,\text{K} \\ N_{het}(s_{\text{max}}) & f_c \leq 0 \text{ or } T > 235\,\text{K} \end{cases}$$ (4.36)

Equation (4.36) accounts for the fact that homogeneous freezing is not probable for $T > 235\,\text{K}$ [e.g., 208]; it is however restricted to cases in which the cloud environment remains subsaturated with respect to liquid water (i.e., ice cloud regime).

4.3.6. Implementation of the Parameterization

The generalized parameterization presented in this study is fairly simple to apply and outlined in Figure 4.1. Inputs to the parameterization are cloud formation conditions (i.e., p, T, V), liquid droplet and IN aerosol number concentration (i.e, N_o, N_{dust}, N_{soot}). Additional inputs (i.e., $s_{h,j}, \theta_j$) may be required depending on the expression used for the nucleation spectrum, $N_{het}(s_i)$. If $T < 235$ K, the procedure starts by calculating $N_{het}(s_{hom})$, N_{lim} (Eq.(4.35)) and then f_c (Eqs. (4.33) and (4.34)).
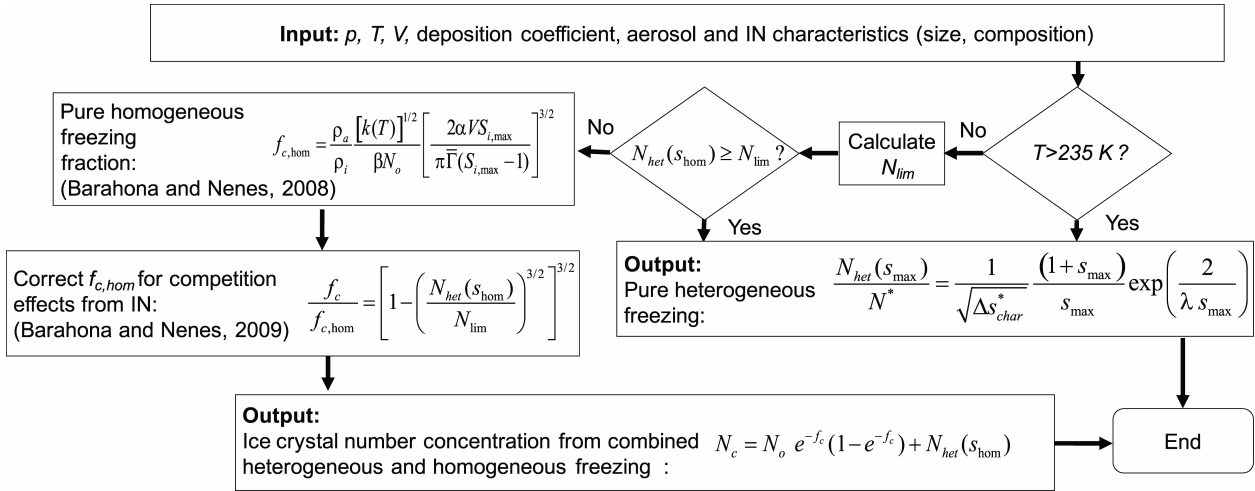
Figure 4.1. Parameterization algorithm

.

If $f_c > 0$, then N_c is given by the application of Eq. (4.36) with $f_{c,hom}$ from Barahona and Nenes [12]. If $f_c \leq 0$ or $T > 235$ K, heterogeneous freezing is the only mechanism active,

and $N_c = N_{het}(s_{\max})$, obtained by numerically solving Eq. (4.32). Alternatively, precalculated lookup tables or approximate explicit solutions to Eq. (4.32) can be used to avoid iterative solutions

4.4. Evaluation and Discussion

The parameterization is tested for all the nucleation spectra presented in Table 4.1. Only dust and black carbon aerosol is considered, as the contribution of organic carbon to the IN population is six fold lower than that of black carbon [198]. The total surface area of each aerosol population is scaled using the base size distributions of Phillips et al. [198].

Table 4.1. Cumulative freezing spectra considered in this study. The functions $H_{soot}(s_i, T)$ and $H_{dust}(s_i, T)$ for PDA08 are defined in Phillips et al. [198].

Spectrum	$N_{het}(s_i)$ (m^{-3})
Meyers et al. [166], MY92	$10^3 e^{-0.639+12.96 s_i}$
Phillips et al. [199], PDG07	$\begin{aligned} &60 e^{-0.639+12.96 s_i} \quad 243 < T < 268 \\ &10^3 e^{-0.388+3.88 s_i} \quad 190 < T \le 243 \end{aligned}$
Phillips et al. [198], PDA08	$\begin{aligned} &N_{dust}\left[1-\exp\left(-\frac{2}{3} H_{dust}(s_i, T)\frac{N_{het,PDG07}}{7.92\times10^4}\right)\right] \\ &+ N_{soot}\left[1-\exp\left(-\frac{1}{3} H_{soot}(s_i, T)\frac{N_{het,PDG07}}{1.04\times10^6}\right)\right] \end{aligned}$
Classical Nucleation Theory (section 4.2.2), CNT	$\begin{aligned} 0.05\Bigg[&\min\left(\frac{s_i}{0.2} N_{dust} e^{-0.0011 k_{hom}(0.2-s_i)}, N_{dust}\right) + \\ &\min\left(\frac{s_i}{0.3} N_{soot} e^{-0.039 k_{hom}(0.3-s_i)}, N_{soot}\right)\Bigg] \end{aligned}$

For the CNT spectrum a simple linear relation is employed to diagnose $e_{f,j}$, being about 0.05 for dust and soot aerosol particles at $s_i = s_h$ [208] and decreasing linearly for $s_i < s_h$

(Table 4.1). Freezing thresholds were set to $s_{h,dust} = 0.2$ [103] and $s_{h,soot} = 0.3$ [171]; θ_{dust} was set to 16° ($m_{dust} = 0.96$) and θ_{soot} to 40° ($m_{soot} = 0.76$) [26]. k_{hom} is calculated based on Koop et al. [129] using the fitting of Barahona and Nenes [12-13]; s_{hom} is obtained from the analytical fit of Ren and Mackenzie [216].

4.4.1. Comparison against Parcel Model Results

The parameterization was compared against the numerical solution of Eqs. (4.7) to (4.9) using the model of Barahona and Nenes [12-13], for all nucleation spectra of Table 4.1, and conditions of Table 4.2 (about 1200 simulations overall). To independently test the accuracy of Eqs. (4.32) and (4.36), simulations were made under conditions of pure heterogeneous and combined homogeneous-heterogeneous freezing.

Table 4.2. Cloud formation conditions and aerosol characteristic used in the parameterization evaluation.

Property	Values
T_o (K)	205-250
V (m s^{-1})	0.04-2
α_d	0.1, 1.0
$\sigma_{g,\,dry}$	2.3
N_o (cm^{-3})	200
$D_{g,\,dry}$ (nm)	40
N_{dust} (cm^{-3})	0.05-5
N_{soot} (cm^{-3})	0.05-5
θ_{dust}	16°
θ_{soot}	40°
$s_{h,dust}$	0.2
$s_{h,soot}$	0.3

Calculated N_c ranged from 10^{-4} to 10^2 cm^{-3}; s_{max} ranged (in absolute units) from 0.05 to 1 for pure heterogeneous freezing (i.e., homogeneous freezing deactivated) and from 0.05

to 0.6 for combined homogeneous-heterogeneous freezing, which covers the expected range of conditions encountered in a GCM simulation.

Figure 4.2 shows s_{max} (calculated solving Eq. (4.32)) vs. the parcel model results for conditions of pure heterogeneous freezing. The statistical analysis of the comparison is shown in Table 4.3 for all nucleation spectra of Table 4.1 and conditions of Table 4.2. The overall error with respect to parcel model results is $-1.68 \pm 3.42\%$, which is remarkably low, given the complexity of Eqs. (4.7) to (4.9), and the diversity of $N_{het}(s_i)$ expressions used (Table 4.1). Among the nucleation spectra tested, the largest variability was obtained when using the PDA08 ($-2.69 \pm 2.81\%$) and CNT ($-1.56 \pm 4.14\%$) spectra. This results from variations in the form of the $N_{het}(s_i)$ function; the distribution functions, $n_s(s_i)$, for MY92 and PDG07 are monotonically increasing and smooth (e.g., Figure 4.5) over the entire s_i range considered. PDA08 and CNT are characterized by abrupt changes in $N_{het}(s_i)$ which produces discontinuities in $n_s(s_i)$. This is evident for the CNT spectrum as the error in the calculation of s_{max} lowers (-1.7 ± 2.5 %) if only data with $s_{max} < s_{h,soot}$ is considered. CNT also shows a slight overestimation of s_{max} at high values caused by the assumption of $s_{h,char} = 0$ when $n_s(s_i) = 0$, Eq. (4.30); this however is not a source of uncertainty for N_{het} calculation (Figure 4.3) as crystal concentration is constant for $s_{max} > s_{h,soot}$ (Table 1). Another source of discrepancy is the small change in T (~ 4 K), from $s_i = 0$ to $s_i = s_{max}$ which is larger at high V and causes an slight underestimation of s_{max} at high values ($\sim s_{max} > 0.7$) for the PDG07 and MY92 spectra, which is however never outside of the $\pm 5\%$ range.
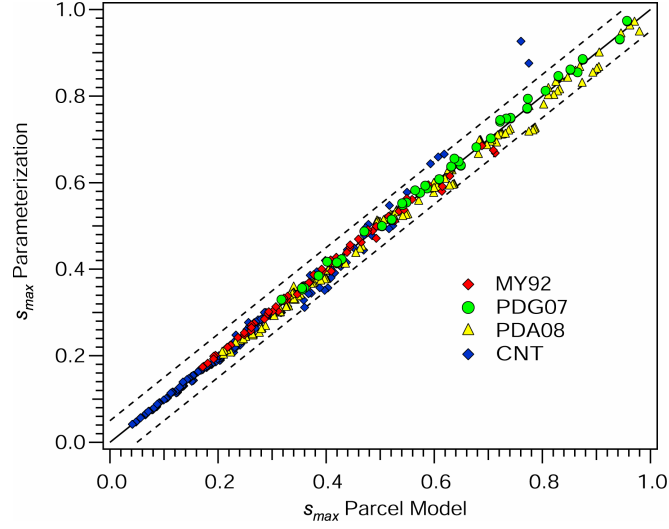
Figure 4.2. Comparison between s_{max} predicted by parameterization and parcel model for conditions of pure heterogeneous freezing. Dashed lines represent the $\pm 5\%$ difference.

Table 4.3. Average % relative error (standard deviation) of parameterized N_c and s_{max} against parcel model simulations. Results are shown for a) heterogeneous freezing is only active, and, b) homogeneous and heterogeneous nucleation are active. $N_{c,n}$, $N_{c,p}$, are ice crystal concentrations from parcel model and parameterization, respectively; similarly for maximum supersaturation, $s_{max,n}$, $s_{max,p}$.

Ice Formation Mechanism	Pure Heterogeneous		Homogeneous and Heterogeneous
Spectrum	$\dfrac{s_{max,p} - s_{max,n}}{s_{max,n}}$	$\dfrac{N_{c,p} - N_{c,n}}{N_{c,n}}$	$\dfrac{N_{c,p} - N_{c,n}}{N_{c,n}}$
MY92	0.43(2.29)	1.14(13.3)	2.95(21.2)
PDG07	0.63(1.56)	3.39(7.60)	-3.78(20.7)
PDA08	-2.69(2.81)	-3.26(8.32)	9.64(21.1)
CNT	-0.44(5.56)	-1.56(4.14)	3.26(22.6)
All combined	-1.68(3.42)	-2.08(8.58)	4.72(21.8)

Figure 4.3 shows that the error in N_{het} calculation is also quite low, -2.0 ± 8.5 %, which indicates no biases in the parameterization. The slightly larger error in N_c compared to the error in s_{max} originates from the sensitivity of $N_{het}(s_{max})$ to small variations in s_{max}. Figure 4.3 shows that the larger discrepancy in s_{max} (Figure 4.2) when using the CNT and PDA08 spectra does not translate into a large error in N_{het} which remains low for these cases (~5%). The largest variability (± 13.5%) was found using MY92 and is related to the slight underestimation of s_{max} at high V ($s_{max} > 0.7$). Δs_{char} for MY92 is around 0.07 (whereas for the other spectra of Table 1 it is generally above 0.2) which indicates that most crystals in the MY92 spectrum freeze at s_i close to s_{max} (Eq. (4.30)); therefore MY92 is most sensitive to the small underestimation in s_{max} at high V.
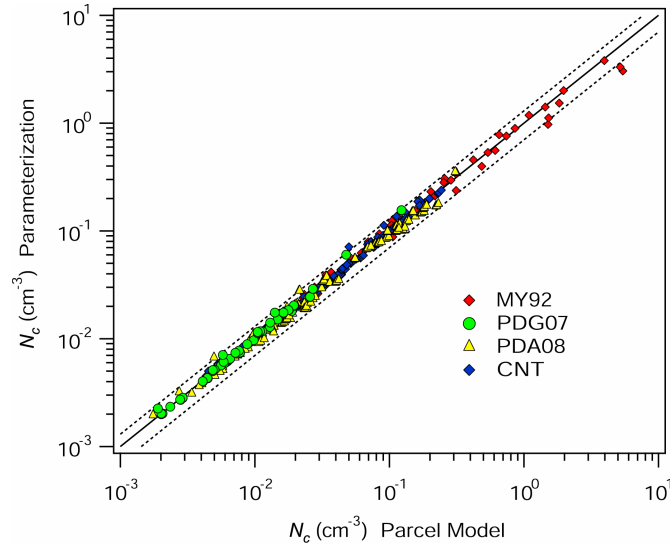
Figure 4.3. Comparison between N_{het} from pure heterogeneous freezing predicted by the parameterization and the parcel model for simulation conditions of Table 4.2 and freezing spectra of Table 4.1. Dashed lines represent the $\pm$ 30 % difference.

When competition between homogeneous and heterogeneous nucleation is considered (Figure 4.4), $s_{max} \approx s_{hom}$, and no explicit dependency of N_c on s_{max} is considered; this approximation however does not introduce substantial error in the calculation of N_c [12]. The overall error in N_c calculation for this case is $4.7 \pm 21\%$. Comparison of Figures 4.3 and 4.4 suggests that most of the error results from the inherent error of the homogeneous nucleation scheme ($1 \pm 28\%$, [12]). Figure 4.4 shows that the parameterization reproduces the parcel model results from the pure heterogeneous (i.e., $\frac{N_{het}}{N_{lim}} > 1$) to the

pure homogeneous (i.e., $\frac{N_{het}}{N_{lim}} \rightarrow 0$) freezing limit.
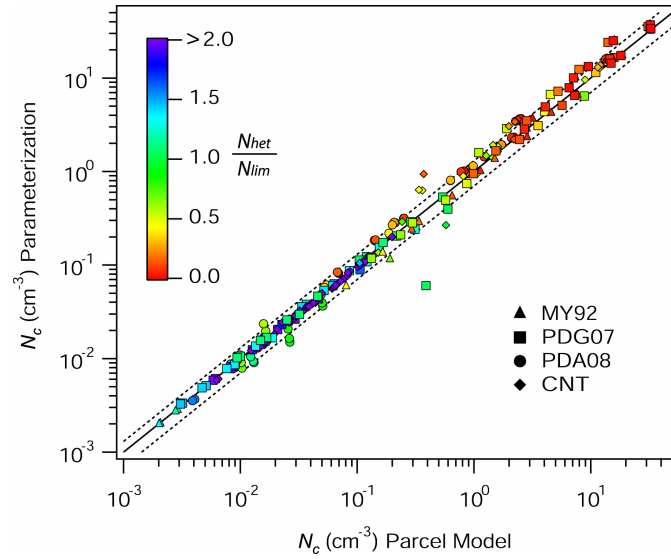
Figure 4.4. Comparison between N_c from combined homogeneous and heterogeneous freezing predicted by the parameterization and the parcel model for simulation conditions of Table 4.2 and freezing spectra of Table 4.1. Dashed lines represent the $\pm$ 30 % difference. Colors indicate the ratio $\frac{N_{het}}{N_{lim}}$.

The largest discrepancy ($-9.6 \pm 21\%$) occurs when the PDA08 spectrum is used, and is related to the complexity of the $N_{het}(s_i)$ function. Larger variations (mostly within a factor of 2) also occur when $N_{het}(s_{max}) \rightarrow N_{lim}$ and are caused by the high sensitivity of

N_c to $N_{het}(s_{max})$ for $\dfrac{N_{het}}{N_{lim}} \approx 1$ [cf., 13, Fig. 3].

4.4.2. Comparison against existing schemes

The new parameterization was compared against the schemes of Liu and Penner [147, LP05] and Kärcher et al. [106, K06], for all spectra of Table 4.1 and, for $T = 206 \text{K}$, $p = 22000 \text{ Pa}$, and, $\alpha_d = 0.5$.
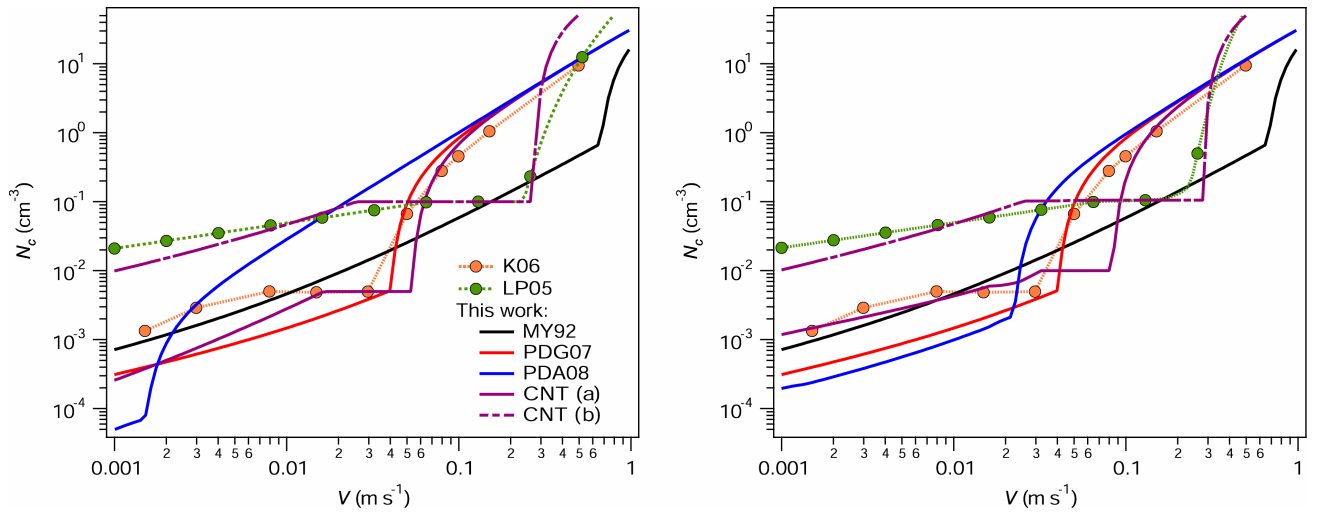
Figure 4.5. N_c vs. V calculated using the new parameterization for all freezing spectra of Table 4.1. Also shown are results taken from Kärcher et al. [106, K06] for $N_{IN} = 5 \times 10^{-3}$ cm^{-3} and, the parameterization of Liu and Penner [147]. Conditions considered were $T_o = 210$ K (T = 206 K), $p = 22000$ Pa, $\alpha_d = 0.5$. Left panel: $N_{soot} = 0.1$ cm^{-3}, $N_{dust} = 0$ cm^{-3} and no deposition freezing considered in LP05. Right panel: $N_{soot} = 0.1$ cm^{-3}, $N_{dust} = 0.1$ cm^{-3} and deposition freezing considered in LP05. For CNT(a) runs were made as presented in Tables 4.1 and 4.2 while for CNT (b) conditions were changed to $s_{h,soot} = 0.1$, $e_{f,soot} = 1.0$, and $\alpha_d = 0.1$.

Consistent with K06, the maximum number concentration of IN was set to 0.005 cm^{-3}, which for $e_{f,soot} = 0.05$ implies $N_{soot} = 0.1$ cm^{-3}. Cases with no dust present (i.e., $N_{dust} = 0$ and no deposition freezing in LP05) and with $N_{dust} = N_{soot}$ were considered.

For the "no-dust" case (Figure 4.5, left) K06 and the new parameterization (Eq. (4.36), using the CNT, MY92, and PDG07 spectra), agree within a factor of two at the pure heterogeneous limit ($\sim V < 0.01$ m s^{-1}). Homogenous freezing in these cases is triggered (i.e., $N_{\lim} > N_{het}$) between 0.03 and 0.07 m s^{-1} except when using MY92 where $V > 0.7$ m s^{-1} is needed to allow homogeneous freezing. When using Eq. (4.36) and PDA08, a much lower N_{het} is predicted over the entire V range considered, and homogeneous freezing is triggered at very low $V \sim 0.002$ m s^{-1} (i.e., heterogeneous freezing has a negligible effect on N_c).

LP05 predicts N_{het} about two orders of magnitude larger than the application of Eq. (4.36) to the PDG07 and CNT spectra. This discrepancy may result from the high $e_{f,soot} \sim 1$ (which is evident for $V > 0.04$ m s^{-1} as $N_{het} \approx N_{soot}$) implied in this parameterization compared to the other freezing spectra considered. LP05 also predicts complete inhibition of homogeneous freezing up to $V \sim 0.3$ m s^{-1} (Figure 4.5, right) which is much larger than the range between 0.03 and 0.07 m s^{-1} found by application of Eq. (4.36). The discrepancy between LP05 and the other schemes in Figure 4.5 is due to differences in the values of $s_{h,soot} = 0.2$ and $\alpha_d = 0.1$ used in generating the LP05 parameterization. In fact, the results of LP05 can be approximately reproduced by setting $e_{f,soot} = 1.0$ and $s_{h,soot} = 0.1$ in the CNT profile and by changing the value of α_d to 0.1,

as shown in the CNT(b) curves of Figures 4.5 and 4.6. The lower value of $s_{h,soot} = 0.1$

required to reproduce LP05, compared to the one used by Liu and Penner (2005),

$s_{h,soot} = 0.2$, results from the smoother freezing pulse in the CNT model as opposed to

the step function implied by the model of Liu and Penner [147].
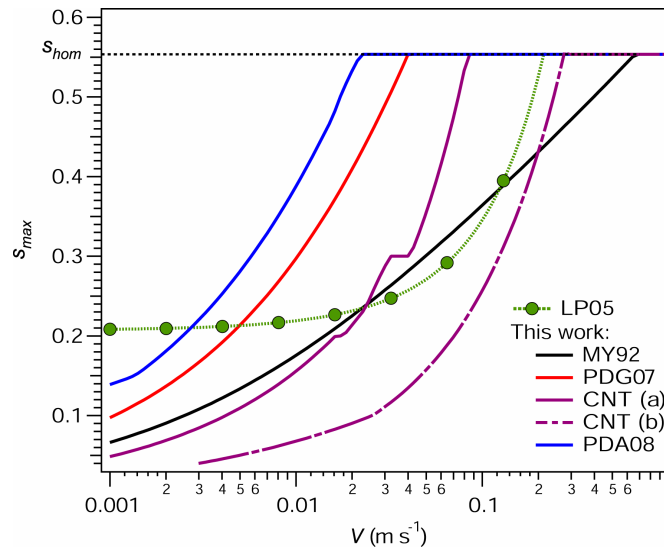
Figure 4.6. s_{max} vs. V calculated using the parameterization of Liu and Penner [147] and the new parameterization for all freezing spectra of Table 4.1 and. Conditions considered are similar to Figure 4.5 and $N_{soot} = N_{dust} = 0.1$ cm⁻³. For CNT (b) $s_{h,soot} = 0.1$, $e_{f,soot} = 1.0$, and $\alpha_d = 0.1$.

When similar concentrations of dust and soot are considered (Figure 4.5 right), Eq. (4.36)

with PDA08 come much closer to simulations using CNT and PDG07. K06 (maintaining

$N_{IN} = 0.005$ cm⁻³) still lies within a factor of two from the results obtained with Eq.

(4.36) and the CNT, PDA08, and PDG07 spectra. By including dust, the onset of

homogeneous nucleation is triggered at slightly higher V, compared to the case with no dust (CNT). For PDA08 the change is more pronounced, indicating that the maximum $e_{f,dust}$ implied by PDA08 is substantially larger than $e_{f,soot}$ for the same spectrum, i.e., most of the crystals in this case come from freezing of dust. At the pure homogeneous freezing limit ($V \sim 1$ m s^{-1}), IN effects on N_c are unimportant, and, N_c for all spectra agree well with K06 [12]. At this limit, LP05 predicts a twofold higher N_c due to the different set of parameters used in developing LP05 [147]. The discrepancy between LP05 and the CNT profile can be reconciled by setting $e_{f,soot} = 1$, $s_{h,soot} = 0.1$, and $\alpha_d = 0.1$.

A comparison of predicted s_{max} between the new parameterization and LP05 was also carried out. The curves of Figure 4.6 can be used to explain the profiles of Figure 4.5, as homogeneous freezing is prevented if $s_{max} < s_{hom}$ [69, 13]. When dust is not included, s_{max} calculated using PDA08 approaches s_{hom} at very low V, therefore allowing homogeneous nucleation to take place in almost the entire range of V considered (not shown). When dust is included, s_{max} calculated using Eq. (4.36) and the PDG07, PDA08 and CNT spectra approaches s_{hom} for V between 0.02 and 0.06 m s^{-1}. When using MY92, s_{max} is below s_{hom} for almost the entire range of V considered, and, explains why homogeneous freezing is prevented for most values of V. LP05 predicts a very different s_{max} profile, being constant ($s_{max} \sim 0.2$) at low V, then a steep increase in s_{max} around $V \sim 0.1$ m s^{-1} which reaches s_{hom} at $V \sim 0.3$ m s^{-1}. In this case, setting $e_{f,soot} = 1$, $s_{h,soot} = 0.1$, and

$\alpha_d = 0.1$ reduces the discrepancy between LP05 and CNT (curve CNT (b)) for

$s_{max} \sim s_{hom}$ and $V \sim 0.2$-0.3 m s^{-1}. The two schemes however still diverge at $V < 0.1$ m s^{-1}.

4.5. Summary and Conclusions

We present an ice cloud formation parameterization that calculates N_c and s_{max} explicitly considering the competition between homogeneous and heterogeneous freezing from a polydisperse (in size and composition) aerosol population. Heterogeneous freezing is accounted for by using a nucleation spectrum that could have any functional form. Analytical solution of the parcel model equations was accomplished by reformulating the supersaturation balance and by introducing the concepts of characteristic freezing threshold and characteristic size of a polydisperse ice crystal population. The approach presented here successfully decouples the nucleation and growth factors in the solution of the supersaturation balance, and together with the work of Barahona and Nenes [12-13], provides a comprehensive parameterization for ice cloud formation. The parameterization was tested with a diverse set of published IN spectra (Table 4.1), which includes a formulation introduced here derived from classical nucleation theory.

When evaluated over a wide set of conditions and IN nucleation spectra the parameterization reproduced detailed numerical parcel model results to -1.6 ± 3.4 % and -2.0 ± 8.5%, for the calculation of s_{max} and N_{het} from pure heterogeneous freezing, respectively, and 4.7 ± 21% for the calculation of N_c from combined homogeneous and heterogeneous freezing. Comparison against other formulations over a limited set of conditions showed that the freezing efficiency of the different IN populations (i.e., dust and soot) is the main factor determining the effect of heterogeneous freezing on the total

ice crystal concentration, N_c. The variability of N_c shown in Figure 4.6 is however much lower than reported by Phillips et al [198], who compared several nucleation spectra at fixed s_i; this emphasizes the importance of using a proper dynamic framework in comparing nucleation spectra.

During the development of the parameterization (section 4.3) it was implicitly assumed that the cloudy parcel is initially devoid of ice crystals. If cirrus persist beyond the time step of the host model, then the effect of preexisting ice crystals should be accounted for in the parameterization by including an additional water vapor depletion term at the left hand side of Eq. (4.14) (see Chapter 7, [18]). This effect however may be small as crystals with large sizes tend to fall out of the nucleation zone (i.e., the zone with highest supersaturation in the cloud) during the evolution of the cirrus cloud [234]. If the heterogeneously nucleated ice crystals fall out however from the nucleation zone before $s_{\max}$ is reached, the effect of IN on homogeneous nucleation may be reduced. Theoretical studies [114, 234] suggest that deposition effects may be significant at low V (< 0.05 m s^{-1}) and low N_{het} (<0.01 cm^{-3}). Deposition effects can be included in Eq. (4.14) by adding a "fallout" term [114] to the supersaturation balance, Eq. (4.7).

The parameterization presented in this work is suitable for large-scale atmospheric models that cannot resolve ice supersaturation at the scale of cloud formation (~50 m [208]). It is computationally efficient and analytically unravels the dependency of ice crystal concentration on cloud formation conditions (T, p, V), deposition coefficient, the size and composition of the droplet population, and insoluble aerosol (i.e., IN)

concentrations. It provides a framework in which new ice nucleation data can easily be incorporated in aerosol-cloud interaction studies.

CHAPTER 5

SENSITIVITY OF THE GLOBAL DISTRIBUTION OF CIRRUS ICE CRYSTAL CONCENTRATION TO HETEROGENEOUS FREEZING[1]

This study presents the sensitivity of ice crystal number concentration, N_c, that would occur in global cirrus to heterogeneous ice nuclei (IN) spectra derived from field campaign data and theoretical considerations. Simulations are carried out with NASA Global Modeling Initiative (GMI) chemical and transport model coupled to an analytical ice microphysics parameterization. When competition between homogeneous and heterogeneous freezing is considered, global mean N_c vary by factor of 20 depending on the heterogeneous freezing spectrum used. Ice nuclei effects on N_c strongly depend on dust and black carbon concentrations, and, most important under conditions of weak updraft and high temperature. Regardless of the heterogeneous spectrum used, dust is an important contributor of IN over large regions of the northern hemisphere. Black carbon however exhibits appreciable effects on N_c when the freezing fraction is greater than 1%. Compared to in situ observations, N_c is overpredicted at temperatures below 205 K. Assuming cirrus formation is forced by weak updraft addressed this overprediction but

---

promoted heterogeneous freezing effects to the point where homogeneous freezing is inhibited even for IN concentrations as low as 1 L^{-1}. It was found only cloud formation scenarios where competition between homogeneous and heterogeneous freezing is the dominant feature would result in maximum supersaturation levels consistent with observations.

5.1. Motivation

The role of cirrus clouds in a changing climate system constitutes a major source of uncertainty in anthropogenic climate change assessment and prediction [229, 23, 10]. Cirrus clouds form by homogeneous freezing of deliquesced aerosol and heterogeneous freezing of ice nuclei (IN) [208]. Analysis of ice crystal residues from field campaigns shows that both freezing mechanisms interact during cirrus formation [e.g., 43, 76, 205], suggesting that IN can strongly affect cloud ice crystal concentration and size distribution [44, 69, 110, 13, 234].

Global modeling studies have shown that heterogeneous IN emissions can impact the global distribution of ice crystal concentration, N_c, resulting in a potentially large climatic effect. *Lohmann et al.* [153] performed simulations considering either pure homogeneous (from deliquesced sulfate aerosol) or pure heterogeneous freezing (from dust and black carbon freezing) as limits of variability induced from heterogeneous IN effects. Compared to homogeneous freezing, heterogeneous freezing resulted in lower N_c, higher precipitation rates, and smaller ice water paths. *Hendricks, et al.* [80] studied the effect of aircraft emissions of black carbon on N_c, assuming that the freezing mechanism shifted from homogeneous to heterogeneous when the grid-cell black carbon

concentration, N_{bc}, exceeded a threshold value (around 0.5 cm^{-3}); considering IN effects reduced N_c between 10 and 40% at the midlatitudes of the northern hemisphere. A similar approach was used by *Lohmann et al.* [154] to study the effect of IN from dust on N_c; it was found that considering IN effects decreased the shortwave cloud forcing associated with cirrus clouds by 2.7 W m^{-2}. Competition between homogeneous and heterogeneous freezing of dust and black carbon IN during cloud formation was considered by *Penner, et al.* [194] using parameterizations of *Liu and Penner* [147] and *Kärcher, et al.* [106] to describe freezing. The aerosol indirect forcing from black carbon IN emissions ranged between -0.72 and 0.038 W m^{-2}.

At atmospherically-relevant conditions, dust, soot, and biogenic particles can act as IN [43, 61, 204, 206, 250]. The large seasonal and geographical variability of aerosol and the limited understanding of heterogeneous nucleation challenges the prediction of IN concentrations [143, 23, 10, 253]. Most of the uncertainty in predicting the impact of aerosol emissions on cirrus clouds is associated with estimating the fraction of the aerosol that freezes heterogeneously, i.e., the IN concentration, N_{IN} [143, 23, 10]. Typically, heterogeneous freezing is treated as an extension of homogeneous nucleation [110], or using classical nucleation theory, herein referred to as CNT [117]. Empirical correlations [e.g., 166, 46, 198] are also heavily used.

Cloud studies have shown that N_c can be very sensitive to the assumptions made in the calculation of N_{IN} [e.g., 80, 14, 52]. *Lin et al.* [143] compared N_c from several parcel models using different parameterizations for N_{IN}, leading to two orders of magnitude difference amongst models. *Monier et al.* [175] used several empirical

expressions [166, 45-46] and CNT methods to describe heterogeneous nucleation within the same cloud parcel model. It was found that a factor of 10 variation in N_{IN} translated into a factor of 3 difference in calculated N_c from the combined effects of homogeneous and heterogeneous freezing. A similar approach was followed by *Eidhammer et al.* [52] who found several orders of magnitude variation in N_c when empirical parameterizations and CNT-derived approaches where used to calculate N_{IN}.

The large sensitivity of N_c to N_{IN} reported in parcel model studies has not been reflected in global circulation model studies to date. This is largely because cirrus formation parameterizations used in GCM studies [e.g., 147, 106] are highly constrained, considering specific N_{IN} parameterizations with a prescribed dependency on T, p, s_i, and aerosol concentration. This limitation can be relaxed using the *Barahona and Nenes* [12-14] framework, which predicts N_c using any form of N_{IN} parameterization (theoretical or experimental) and unravels the dependency of N_c on thermodynamic, chemical and dynamic factors that drive cloud formation. In this study, this parameterization is incorporated within the NASA Global Modeling Initiative (GMI) framework [221, 150] to study the sensitivity of N_c that would from in cirrus clouds using several common parameterizations of N_{IN}. The sensitivity of our findings to the meteorological features is also considered, by carrying out simulations using meteorological fields from the NASA Goddard Institute for Space Studies GCM (GISS) and the NASA former Global Data Assimilation Office (DAO) GCMs.

114

5.2. Model Description

The Global Modeling Initiative (GMI) is a state-of-the-art modular 3-D chemical and transport model developed for assessment calculations of anthropogenic effects on climate [221, 148]. GMI utilizes off-line meteorological fields to calculate advective and convective transport of chemical species, transformation, and removal by wet and dry deposition [221]. Here we use fields derived from the NASA Goddard Institute for Space Studies (GISS) and from the former NASA Data Assimilation Office (DAO) GCMs. Each of the archived data sets spans over one year and represents the period from March 1997 to February 1998 archived as 6-hour averages. The GISS field has a resolution of 23 vertical levels, from the surface to 0.02 mb [218]. DAO has a vertical resolution of 46 vertical levels which extent from the surface to 0.15 mb. The horizontal resolution in both meteorological fields is $4° \times 5°$.

Table 5.1. Dry number size distributions for sulfate, dust, and black carbon aerosol [143, 148, 194]. D_g and σ_g are the geometric mean diameter and standard deviation, respectively.

Aerosol	Number Fraction	D_g (μm)	σ_g	Density (g cm^{-3})
Sulfate	1	.04	2.3	1.7
Dust	0.152	0.02	2.3	2.6
	0.727	0.09	1.6	
	0.121	0.55	2.5	
Black carbon (Fuel and biomass burning)	1	0.14	1.5	1.5

The GMI aerosol module is coupled to the GMI-CTM advection core and includes primary emissions, chemical production of sulfate, gravitational sedimentation, dry deposition, wet scavenging, and hygroscopic growth [150, 148]. Anthropogenic and natural aerosol and precursor emissions include SO_2, organic matter, black carbon,

oceanic DMS, dust and sea-salt. Model prognostic variables include dimethylsulfide, sulfur dioxide, sulfate aerosol, hydrogen peroxide, black carbon (biomass burning and fossil fuel) and organic matter. Mineral dust and sea salt are predicted in four size bins: 0.01-0.63 µm, 0.63-1.26 µm, 1.26-2.5 µm, and 2.5-10 µm [148]. Explicit aerosol microphysics is not considered and aerosol size distributions are assumed to follow those derived from observations (shown in Table 5.1).

5.2.1. Ice Crystal Number Concentration Parameterization

The number concentration of ice crystals that would nucleate in cirrus is calculated using the analytical framework of *Barahona and Nenes* [12-14] referred hereinafter as BN09. Competition effects between homogeneous and heterogeneous freezing is explicitly considered, while the dependency of N_c on the conditions of cloud formation (i.e., T, p), updraft velocity, deposition coefficient, and soluble and insoluble aerosol concentrations is resolved. N_c is given by

$$N_c = \begin{cases} N_{hom} + N_{het}(s_{hom}) & ; \ N_{het}(s_{hom}) < N_{lim} \\ N_{het}(s_{max}) & ; \ N_{het}(s_{hom}) \geq N_{lim} \end{cases} \tag{5.1}$$

where s_{max} is the maximum supersaturation that develops in the cirrus, and N_{hom}, N_{het} are the number of ice crystals forming from homogeneous and heterogeneous freezing, respectively. N_{lim} is the IN concentration that completely inhibits homogenous nucleation (calculated below), and, sets the limit between combined heterogeneous and homogeneous, and pure heterogeneous freezing. N_{lim} is given by

$$N_{lim} = \frac{N^*}{\sqrt{\Delta s^*_{char}\big|_{s_{hom}}}} \frac{(1+s_{hom})}{s_{hom}} e^{\frac{2}{\lambda s_{hom}}} \tag{5.2}$$

where N^* and λ are functions of cloud formation conditions (i.e., T, p, V, and deposition coefficient) defined in the symbols and abbreviation section, and

$$\Delta s^*_{char}\Big|_{s_i} = \frac{\Delta s_{char}\left[\dfrac{4}{3}\Delta s_{char} + 2(s_i - \Delta s_{char})\right]}{(1 + s_i - \Delta s_{char})} \tag{5.3}$$

where $\Delta s_{char} = \min\left[\left(\dfrac{d\ln N_{het}(s_i)}{ds_i}\right)^{-1}, s_i\right]$ is a characteristic of the IN population related

to the slope of the IN spectrum at supersaturation s_i.

For the special case of a monodisperse IN population with freezing threshold, $s_{h,mono}$, Eq. (5.2) simplifies to [13],

$$N_{\lim} = \frac{\alpha V}{\beta}\frac{\rho_a}{\rho_i}\frac{2}{\pi}\left(\frac{s_{hom}+1}{s_{hom}}\right)\left(\frac{\Gamma_1 D_{\lim} + \Gamma_2}{D_{\lim}^2}\right) \tag{5.4}$$

where $D_{\lim} = -\gamma + \sqrt{\gamma^2 + \dfrac{2}{\Gamma_1\alpha V}\Delta s^*_{char}\Big|_{s_{hom}}}$, and $\gamma = \dfrac{\Gamma_2}{\Gamma_1}$, and $\Delta s_{char} = s_i - s_{h,mono}$.

For $N_{het}(s_{hom}) < N_{\lim}$, s_{max} is equal to the homogeneous freezing threshold, s_{hom} [129]. For $N_{het}(s_{hom}) \geq N_{\lim}$, s_{max} is below s_{hom} and homogeneous freezing does not occur (s_{max} for this case is calculated below). The heterogeneous contribution to N_c is equal to $N_{het}(s_{max})$ when only heterogeneous nucleation is active, and, equal to $N_{het}(s_{hom})$ when homogeneous and heterogeneous freezing are both active. The functional form of $N_{het}(s_i)$ is discussed in section 5.2.2 The homogeneous contribution to N_c is given by

$$
N_{\text{hom}} = \begin{cases} N_o e^{-f_c}(1-e^{-f_c}) & f_c < 0.6 \\ N_o\left[1+\exp\left(\dfrac{9-2f_c}{7}\right)\right]^{-1} & f_c \geq 0.6 \end{cases} \tag{5.5}
$$

where f_c is the droplet freezing fraction for cirrus clouds formed in-situ [12-13] and is calculated below. The second term in Eq. (5.5) (for $f_c \geq 0.6$) is added to the result of *Barahona and Nenes* [c.f., 12, equation 30], to account for high homogeneous freezing fractions where N_{hom} is limited by the available sulfate aerosol concentration. It is derived assuming a sigmoidal form for $\dfrac{N_{\text{hom}}(f_c)}{N_o} > 0.6$ based on published observations for convective clouds and parcel model results [199, 12]. f_c depends on the active freezing mechanism and is calculated below.

When homogeneous and heterogeneous freezing are active, heterogeneously frozen crystals deplete water vapor [44, 106, 13] and weaken the homogeneous freezing pulse. In this case, $s_{\text{max}} \approx s_{\text{hom}}$, $N_{IN} = N_{het}(s_{\text{hom}})$, and, f_c depends on N_{IN} and the freezing characteristics of the IN population as,

$$
f_c = f_{c,\text{hom}}\left\{1-\left(\frac{N_{het}(s_{\text{hom}})}{N_{\text{lim}}}\right)^{3/2}\right\}^{3/2} \tag{5.6}
$$

where $f_{c,\text{hom}} = \dfrac{\rho_a}{\rho_i}\dfrac{k_{\text{hom}}^{1/2}}{\beta N_o}\left[\dfrac{2\alpha V(s_{\text{hom}}+1)}{\pi\bar{\Gamma}s_{\text{hom}}}\right]^{3/2}$ is the droplet freezing fraction in absence of IN, i.e., for pure homogeneous freezing [12]. Other symbols are defined in the symbols and abbreviations section..

If N_{IN} is high enough, heterogeneously frozen crystals may deplete enough water vapor so that $s_{max} < s_{hom}$, inhibiting homogeneous freezing [69, 13]. In this regime, $N_c = N_{het}(s_{max})$ (Eq. (5.1)), and s_{max} is given by the solution of

$$\frac{N_{het}(s_{max})}{N^*} = \frac{1}{\sqrt{\Delta s_{char}^*\big|_{s_{max}}}} \frac{(1+s_{max})}{s_{max}} e^{\frac{2}{\lambda s_{max}}}$$
(5.7)

where $\lambda = \dfrac{\Gamma_1}{\Gamma_2}\sqrt{\dfrac{1}{\alpha V \Gamma_1}}$. Other symbols are defined in the list of symbols section.

5.2.2. Heterogeneous IN Spectra

The freezing spectrum function $N_{het}(s_i)$ gives the number concentration of IN at conditions of T, p, and s_i, accounting for the contribution of individual insoluble aerosol species and different freezing modes [14]. $N_{het}(s_i)$ can be obtained from theoretical considerations, field campaign and laboratory data [e.g., 166, 55, 173, 198, 14, 120, 255]. BN09 is developed so that any expression for $N_{het}(s_i)$ (experimental or theoretical) can be used without loss of accuracy.

Table 5.2. Heterogeneous nucleation spectra used in this study

$N_{het}(s_i)$	Description	Type
HOM	No heterogeneous freezing allowed	Theoretical
MONO	Monodisperse IN with $s_{h,mono} = 0.3$ (Eq. (5.8))	Theoretical
CNT-BN	Equation (5.9) with $s_{h,dust} = 0.2$, $s_{h,bc} = s_{i,sat}$, $f_{h,dust} = 0.011$ (θ_{dust} =16°), $f_{h,bc} = 0.039$ (θ_{bc} =40°) [26], and k_{hom} from Barahona and Nenes [12]	Semi-empirical
MY	Meyers et al. [166]	Empirical
BKG	Phillips et al. [199]	Empirical
PDA	Phillips et al. [198]	Empirical

Table 5.2 describes the heterogeneous freezing spectra used in this study. Three empirically derived expressions are used: the spectra of *Meyers et al.* [166, MY], *Phillips et al.* [199, BKG], and *Phillips et al.* [198, PDA] (Figure 5.1). MY and BKG depend only on s_i and have a similar functional form. BKG yields about tenfold lower N_{IN} than MY for the same s_i; this is because MY is derived from surface measurements and therefore represents an upper limit in N_{IN}. PDA is derived from several field campaign datasets; apart from s_i and T, the contribution of individual aerosol species (dust, black carbon and organics) and freezing modes (i.e., immersion and deposition) to $N_{het}(s_i)$ is provided. PDA uses BKG as a "background" IN spectrum from which the individual contribution of dust, black carbon, and organic aerosol species are scaled according their surface area distribution. In this study, PDA is applied assuming the *Phillips, et al.* [198] background size distribution for dust and black carbon.
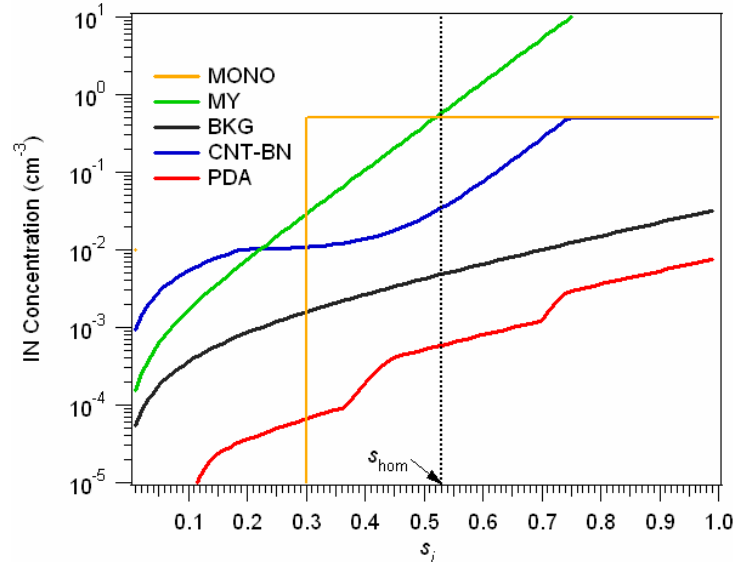
Figure 5.1: Examples of heterogeneous freezing spectra used in this study (presented in Table 5.2). Conditions considered were $N_{dust} = 0.01$ cm^{-3}, $N_{bc} = 0.5$ cm^{-3}, $T = 210$ K, and $p = 22000$ hPa. The vertical line represents the onset of homogeneous freezing.

Theoretically-derived $N_{het}(s_i)$ are also used in this study. The simplest $N_{het}(s_i)$ scheme is the so-called "monodisperse IN" (MONO) approximation, in which IN are assumed to be monodisperse and chemically homogeneous [13]. $N_{het}(s_i)$ is then a step function at a pre-specified freezing threshold, $s_{h,mono} < s_{hom}$,

$$N_{het}(s_i) = \begin{cases} (N_{dust} + N_{bc}), & s_i \geq s_{h,mono} \\ 0 & , & s_i < s_{h,mono} \end{cases} \tag{5.8}$$

where N_{dust}, N_{bc} are the number concentrations of BC and dust, respectively. The steep increase in $N_{het}(s_i)$ about $s_{h,mono}$ is a behavior predicted by classical nucleation theory (CNT) [117, 120]; it is also obtained by generalizing expressions derived for homogeneous nucleation [110]. The "monodisperse approximation" is the main type of IN parameterization currently implemented in GCMs [e.g., 153, 149, 194] with $s_{h,mono}$ typically treated as a free parameter constrained by observations. *Lohmann, et al.* [153] assumed $s_{h,mono} = 0.3$, based on reported measurements of black carbon freezing [42]. *Liu and Penner* [147] did not directly assume a value for $s_{h,mono}$, but rather used prescribed parameters as input to a CNT expression [117] which effectively results in $s_{h,mono} \sim 0.2$ for black carbon [14]. Laboratory studies [e.g., 55, 173, 51, 255] suggest that most dust freeze in the deposition mode around $s_i \sim 0.1 - 0.3$. Theoretical studies show that for $s_{h,mono}$ between 0.1 and 0.3 the effect of IN on N_c is not very sensitive to $s_{h,mono}$ [69, 13]. Based on these considerations, $s_{h,mono} = 0.3$ is assumed in this study (Table 5.2).

Experimental observations [e.g., 55, 198, 52, 255] suggest that $N_{het}(s_i)$ is an smooth function of s_i, and, the freezing fraction varies between aerosol species (generally less than unity for black carbon) [e.g., 166, 198, 52]. These features are at odds with the assumption of a monodisperse, single type IN [52]. In a polydisperse, chemically heterogeneous aerosol, each aerosol size and composition type would freeze at a characteristic s_i threshold. Based on this and other theoretical considerations, *Barahona and Nenes* [14] proposed that for polydisperse IN, the relative concentration of monodisperse IN classes is approximately equal to the ratio of their heterogeneous nucleation rates at s_i (calculated using CNT [117]). This results in a semi-empirical freezing spectrum derived from CNT (referred to as CNT-BN) but constrained with observations. When applied to dust and black carbon, it takes the form

$$N_{het}(s_i) \approx \min\left\{\frac{s_i}{s_{h,dust}}\exp\left[-k_{hom}f_{h,dust}(s_{h,dust}-s_i)\right],1\right\}N_{dust} + \\ \min\left\{\frac{s_i}{s_{h,bc}}\exp\left[-k_{hom}f_{h,bc}(s_{h,bc}-s_i)\right],1\right\}N_{bc}$$

(5.9)

where $s_{h,dust}$ and $s_{h,bc}$ are the values of s_i at which the dust and black freezing fraction is unity, respectively, and can be constrained using measurements of nucleation rate [e.g., 26]. Based on published laboratory studies, we assume $s_{h,dust}=0.2$ [e.g., 55, 173, 51, 255]. As black carbon tends to freeze in both the immersion and deposition modes, $s_{h,bc}$ is highly variable and depends on the IN concentration, the water activity in the deliquesced aerosol, and the particle history [171, 50, 111, 203, 262]. Laboratory results however indicate that when water saturation is reached, black carbon is an active IN in

the condensation mode [42, 50]. Thus it is assumed that $s_{h,bc} = s_{i,sat}$, where $s_{i,sat}$ is the supersaturation with respect to ice at liquid water saturation (e.g., $s_{h,bc} = 0.51$ at $T = 230$ K, and $s_{h,bc} = 0.85$ at $T = 200$ K).

5.2.3. Implementation of ice crystal concentration parameterization within GMI

In this study we assume that N_c that can form in cirrus is equal to the nucleated ice crystal concentration calculated by BN09. This gives the maximum sensitivity of N_c to N_{IN} since crystal sedimentation and sublimation are not considered. Calculation of N_c using the BN09 parameterization requires the knowledge of T, p, V, and the concentration of individual aerosol species (i.e., deliquesced droplets, dust, and black carbon). T and p were assumed to be those of the grid cell (sub-grid cell fluctuation in cooling rate is also considered as described below). N_c is calculated only for $T < 235$ K (i.e., the cirrus cloud regime). Following *Chen and Penner* [29] (and references therein), the total number of deliquesced aerosol available for homogeneous freezing, N_o, is assumed equal to the sulfate aerosol number (calculated from the sulfate mass by using a prescribed lognormal size distribution function; Table 1). Since N_{hom} is rarely limited by the available aerosol (i.e., $N_{hom} \ll N_o$) [109, 228] this assumption is not expected to introduce a significant bias in N_c. A similar approach is used to calculate N_{dust} and N_{bc}; prescribed dust and black carbon size distribution functions are shown in Table 1 (the consequences of assuming a fixed size distribution for dust and black carbon is assessed in section 4). In agreement with theoretical studies and field campaign data, the vapor-to-ice deposition coefficient, α_d, was set to 0.1 [e.g., 64, 86, 147, 121, 175, 12, 95].

5.2.3.1 Dynamical Forcing

The cloud-scale updraft velocity, V, sets the rate of expansion cooling during cloud formation, and is considerably different from the grid-scale value resolved in a large-scale model. Subgrid-scale variations in V are associated with turbulence and gravity waves [152, 112, 125, 74, 86, 36, 101], the effect of which on N_c can be accounted for by averaging over the probability distribution function (PDF) of updraft velocities $P_V(V)$,

$$N_c = \frac{\displaystyle\int_{V_{min}}^{V_{max}} N_c(V) P_V(V) dV}{\displaystyle\int_{V_{min}}^{V_{max}} P_V(V) dV} \qquad (5.10)$$

PDF averaging is also applied to calculate grid-cell average s_{max} and N_{lim}. According to Eq. (5.10), the grid cell in-cloud N_c results from a weighted average of cirrus formation events where homogeneous and heterogeneous freezing take place (Figure 5.2). Thus, for a given N_{IN}, there are always a fraction of cirrus formation events (associated with the lowest updrafts) for which homogeneous freezing is completely inhibited.

In this study, $P_V(V)$ is assumed to be a normal distribution with zero mean and standard deviation, σ_V, of 25 cm s^{-1} [64], reflective of the gravity wave activity and small scale turbulence in the upper troposphere [112, 74, 92-93]. The sensitivity of N_c to σ_V is addressed by assuming that it varies with temperature from 25 cm s^{-1} at 238 K to 1 cm s^{-1} at 198 K [254], suggesting that the influence of gravity wave motion on cirrus formation decreases with altitude and is driven by large-scale dynamics (and therefore weak

updrafts) at the tropopause level [e.g., 121, 95, 235]. V_{min} and V_{max} were set to 1 and 50 cm s^{-1} respectively, in agreement with field measurements [121, 36, 138].
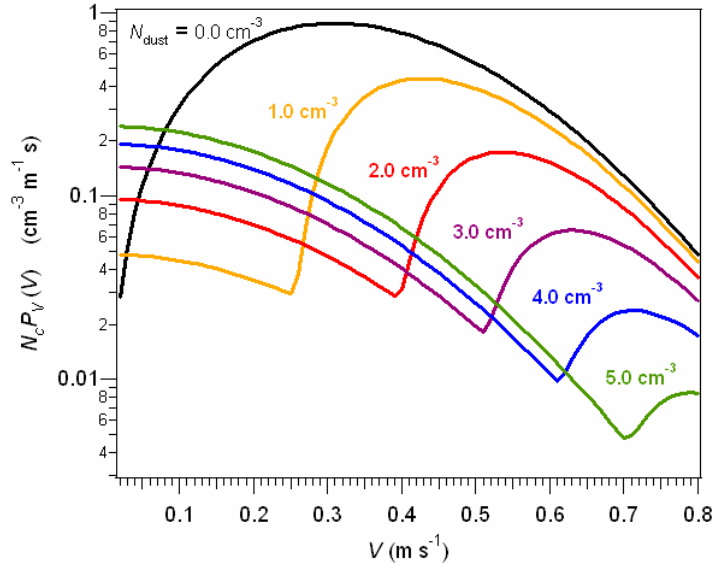
Figure 5.2. Example of N_c calculated over a distribution of updraft velocities using the BN09 parameterization [14, 13] and the PDA heterogeneous freezing spectrum [198]. The minimum in each curve defines the transition between "pure heterogeneous" and "combined homogeneous-heterogeneous" freezing regimes. Conditions considered were $N_{bc} = 1$ cm^{-3}, $T = 230$ K, and $p = 34000$ hPa.

5.3. Results and Discussion

5.3.1. Global Distribution of IN concentration

Figure 5.3 shows the annual zonal average of N_{IN}, calculated as $N_{het}(s_{max})$, for the different IN spectra of Table 5.2. The spatial distribution of N_{IN} depends strongly on the freezing spectra employed to describe heterogeneous freezing. The lowest global mean N_{IN} was found for BKG and PDA (~ 3 L^{-1}) and the highest for MONO (~ 2.4 cm^{-3}). As MY and BKG do not account for the spatial variation of dust and black carbon

concentration, N_{IN} is quite uniform across the globe and only increases near the tropical

tropopause level in response to an increase in s_{max} associated with decreasing T.
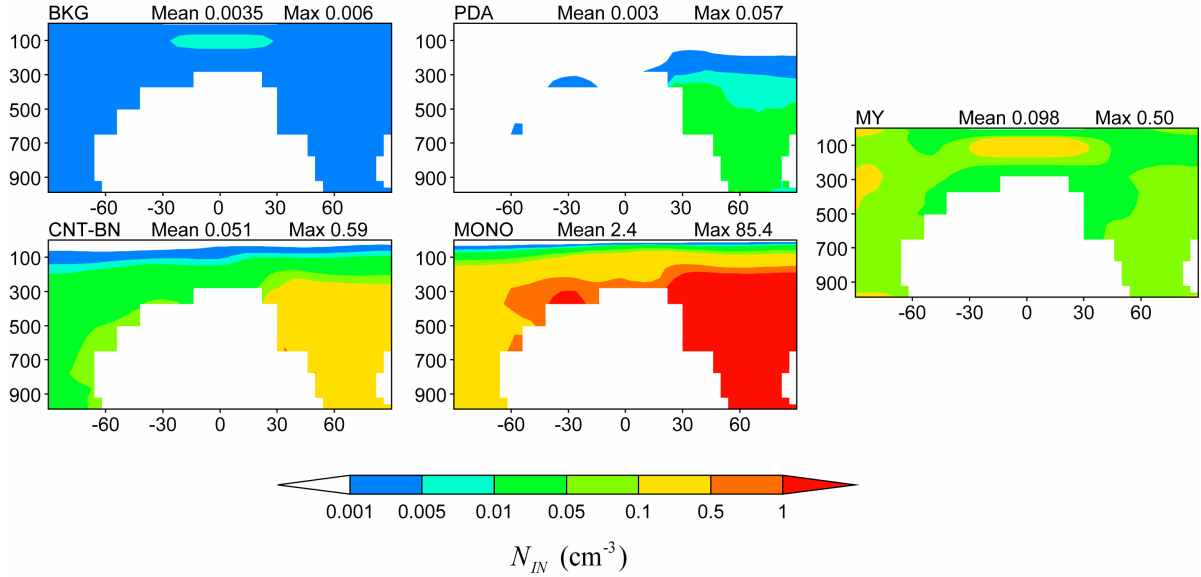
Figure 5.3. Annual zonal mean average N_{IN} (equal to $N_{het}(s_{max})$) using the heterogeneous freezing spectra of Table 5.2. Only in-cloud N_{IN} is considered so that events with $T > 235$ K and $N_c = 0$ are excluded from the average.

The dependency of N_{IN} on the dust and black carbon concentration is considered using

the MONO, PDA, and CNT-BN spectra (section 5.2.2). For levels below 300 hpa, N_{IN} is

larger in the Northern than in the Southern hemisphere, decreasing with altitude. The

PDA spectrum yields N_{IN} below 10^{-3} cm^{-3} for most of the upper troposphere, being even

lower than with the BKG spectrum. This is likely because N_{dust} and N_{bc} predicted by the

GMI model [148] are below the background levels assumed by *Phillips, et al.* [198].

When using the MONO spectrum, black carbon is the predominant IN precursor (as N_{bc}

is typically much higher than N_{dust} [148]). CNT-BN and PDA however predict a much higher freezing fraction for dust than for black carbon, and in some regions (around 30° North) N_{dust} dominates N_{IN}; these features are further analyzed in section 5.3.4.

5.3.2. Global Distribution of Ice Crystal Number Concentration

The variation in N_{IN} from application of the freezing spectra of Table 5.2 results in a factor of 20 variation in global mean N_c (Figure 5.4). Considering only homogeneous freezing (HOM) produces high N_c (greater than 10 cm^{-3}) near the tropical tropopause level (TTL) which decreases with increasing T. When heterogeneous freezing is considered, usage of the MY spectrum results in the lowest N_c (0.12 cm^{-3}) whereas the MONO spectrum gives the highest N_c (2.5 cm^{-3}). Apart from the CNT-BN spectrum, N_c is generally higher in the northern than in the southern hemisphere (especially for $p > 300$ hpa).

All the spectra presented in Table 5.2 (except for MONO) resulted in average N_c below the level for pure homogeneous freezing (HOM); this means that competition between homogeneous and heterogeneous freezing could occur globally. The MONO spectrum resulted in global mean N_c higher than in HOM, suggesting that N_{IN} is high enough to completely prevent homogeneous freezing over large regions of the globe. Using BKG and PDA resulted in global mean N_c close the HOM case (0.58 cm^{-3}), whereas using CNT-BN resulted in a global mean N_c about 35% below HOM.
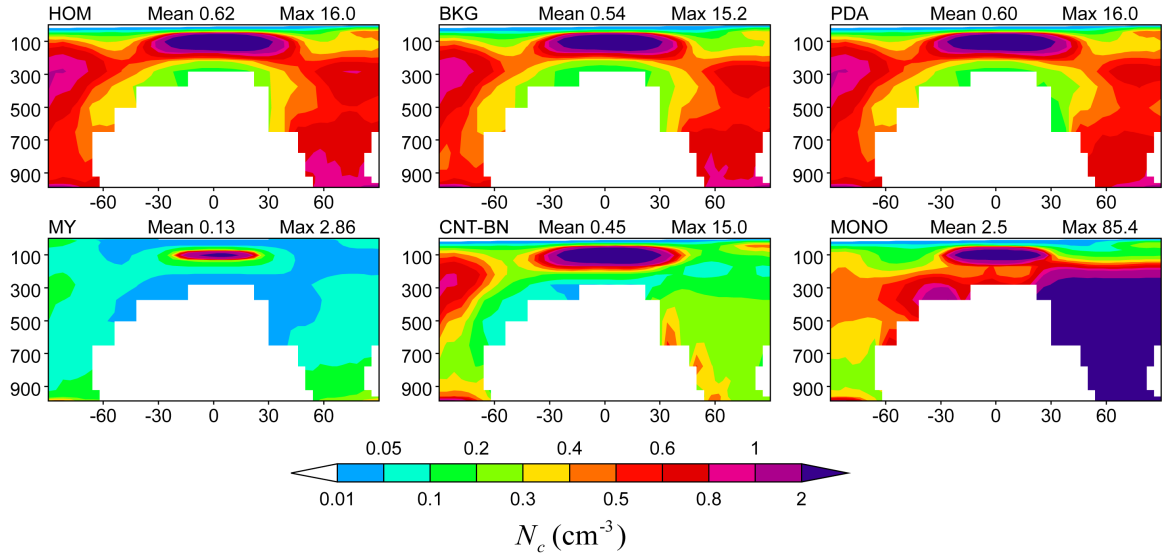
Figure 5.4. Annual zonal average N_c that would form in cirrus clouds obtained for the heterogeneous nucleation spectra of Table 5.2. Only in-cloud N_c is considered so that events with $T > 235$ K and $N_c = 0$ are excluded from the average.

It is important to identify regions of the globe where cirrus could be susceptible to competition effects from IN. This is shown in Figure 5.5, which shows the global maps of N_c normalized with N_c from pure homogeneous freezing, $N_{c,HOM}$. At the 281 hPa level, competition effects from IN on N_c are strongest, as this is the minimum height where cirrus could form (i.e., T is less than 235 K over the entire year) and aerosol concentrations (i.e., N_{IN}) are highest. $\dfrac{N_c}{N_{c,HOM}}$ at $p = 171$ hPa exhibits less pronounced IN competition, a consequence of decreasing aerosol concentration with height. Figure 5.5 also presents isolines of the visible cirrus optical depth (COD) obtained from ISCCP climatology [220]. COD is about 0.8 to 1 in the northern midlatitudes and in the

128
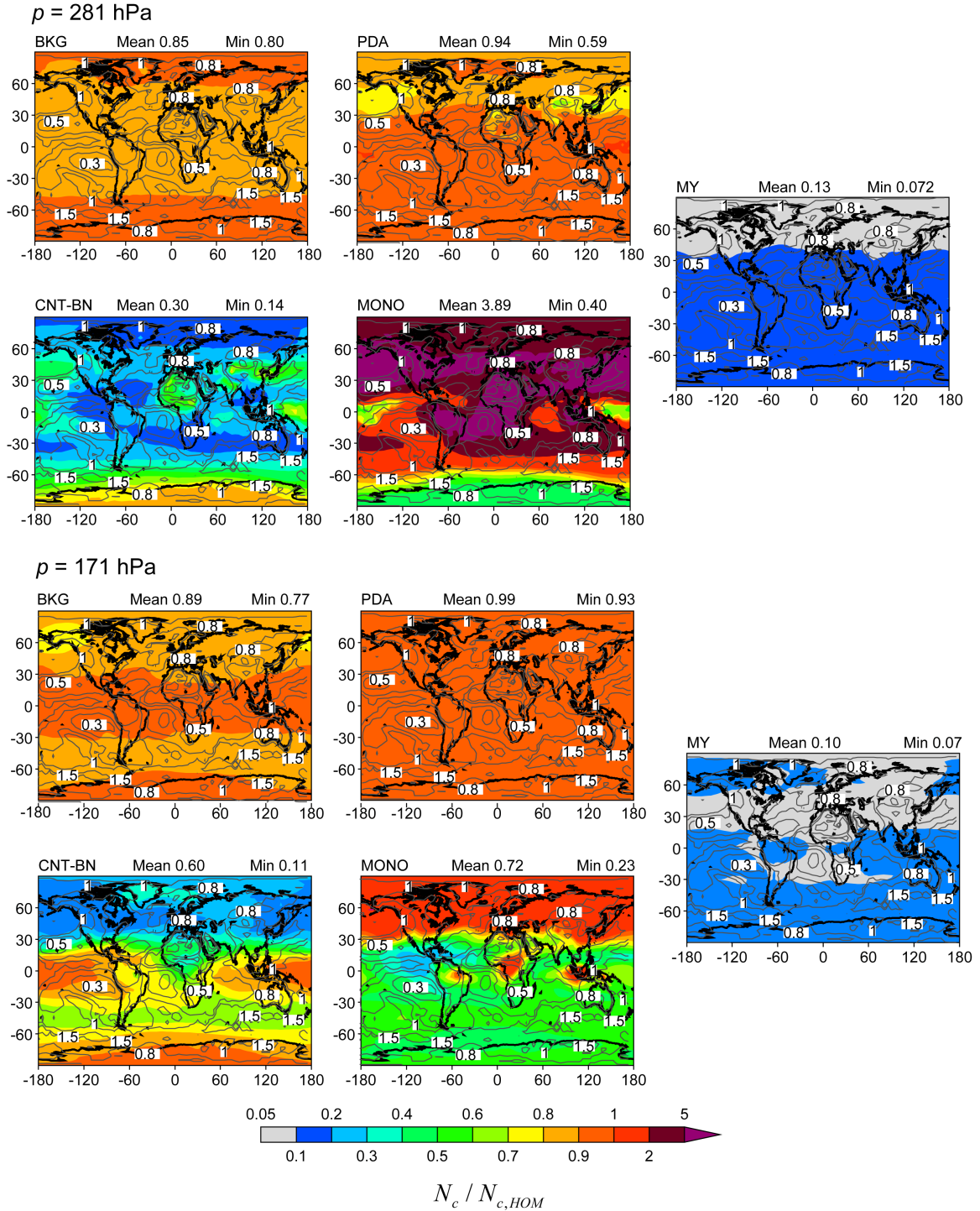
Figure 5.5. Annual average ice crystal concentration obtained in the GMI model at p =281 hPa (top panels) and 171 hPa (bottom panels), normalized with N_c from pure homogeneous freezing (HOM). Isolines are cirrus optical depth obtained from the ISCCP climatology [220].

Southernmost latitudes of the Southern Hemisphere, and slightly lower in the tropics and the midlatitudes of the Southern Hemisphere (~0.3-0.5). These characteristics are consistent with cirrus formed in situ at lower levels and high temperatures (between 210 and 235 K [146]) in the Northern Hemisphere and at high altitudes (i.e., low T) in the tropics and the midlatitudes of the Southern Hemisphere. Cirrus are more frequently observed in the tropics and Northern Hemisphere midlatitudes [48, 220] than in the midlatitudes of the Southern Hemisphere. Based on this, we conclude that cirrus formed in the northern hemisphere would be more prone to heterogeneous IN than in other regions of the globe.

Usage of empirical IN spectra that only depend on s_i (BKG and MY) predict a uniform global distribution of $\dfrac{N_c}{N_{c,HOM}}$ with slight variations occurring from variations in T (e.g., Figure 5.5). N_c for the CNT-BN, PDA, and MONO spectra is controlled by the spatial distribution of dust and black carbon concentration (e.g., Figures 5.3 and 5.8). For the PDA spectrum, heterogeneous effects are confined to the midlatitudes of the northern hemisphere and are strongest ($\dfrac{N_c}{N_{c,HOM}} \sim 0.5$) in regions of high dust concentration at South East Asia, north of Africa, and the west coast of North America (N_{dust} between 0.1 and 0.5 cm^{-3} [148]). Similar features are evident when using the CNT-BN spectrum, being $\dfrac{N_c}{N_{c,HOM}}$ around 0.6 in the same regions. For CNT-BN, the high N_{bc} over the Caribbean, Central America, and the remote Pacific ocean would result in very low $\dfrac{N_c}{N_{c,HOM}}$ [148]. Given that low-level cirrus are scarce in these regions (e.g., Figure 5.5),

competition effects are not expected to be important. The strongest effect of IN on N_c is found with the MONO spectrum, where $\dfrac{N_c}{N_{c,HOM}} > 1$ over most of the Northern hemisphere. $\dfrac{N_c}{N_{c,HOM}}$ for MONO is however close to unity over large areas of the southern hemisphere and the tropics, where complete inhibition of homogeneous freezing tend to give N_{IN} close of $N_{c,HOM}$.

Comparison between the $\dfrac{N_c}{N_{c,HOM}}$ contours at the 281 hPa and 171 hPa vertical levels (Figure 5.5) show that $\dfrac{N_c}{N_{c,HOM}}$ increases with height for the PDA and CNT-BN spectra, and, decreases for the MONO, MY and BKG spectra. For PDA and CNT-BN this results from a decrease in N_{dust} and N_{bc} with height that limits competition effects. With the MONO spectrum, the predominance of heterogeneous freezing results in a direct correlation of N_c (hence $\dfrac{N_c}{N_{c,HOM}}$) with N_{IN}. The decrease in $\dfrac{N_c}{N_{c,HOM}}$ with height seen with the MY and BKG spectra results from a slightly higher N_{IN} caused by the lower T (and higher s_{max}) at the 171 hPa level (Figure 5.3). Only the MONO and MY spectra result in an appreciable effect of IN emissions on N_c in the Southern Hemisphere and the tropics; for other spectra of Table 5.2, N_{IN} is too low to impact N_c, which is agreement with in-situ observations [76]. This would indicate that IN spectra that predict high black carbon freezing fractions would overestimate IN effects at the high levels of the upper troposphere.
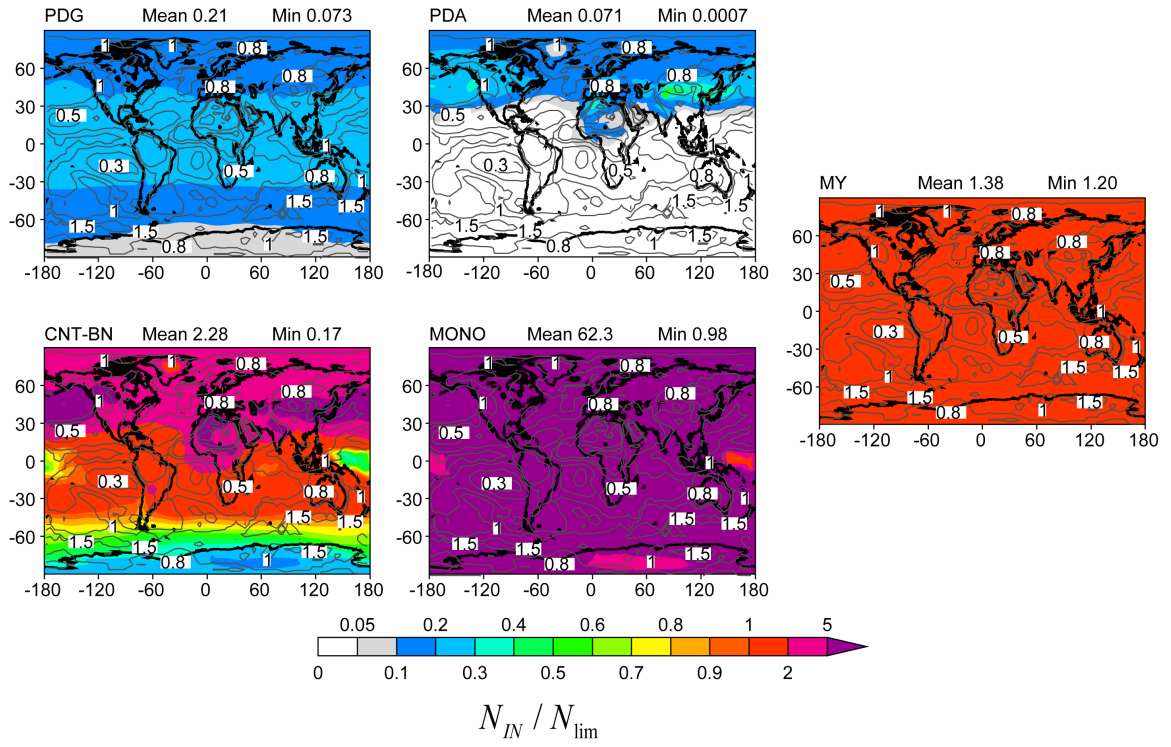
Figure 5.6. Annual average N_c / N_{lim} maps corresponding to the $p = 281$ hPa level. Isolines are cirrus optical depth obtained from the ISCCP climatology [220].

The active freezing mechanisms can be revealed by the ratio $\dfrac{N_{IN}}{N_{\text{lim}}}$. When $\dfrac{N_{IN}}{N_{\text{lim}}} < 1$, homogeneous and heterogeneous freezing actively contribute to N_c; when $\dfrac{N_{IN}}{N_{\text{lim}}} > 1$, only heterogeneous freezing takes place (Eq. (5.6)). Figure 5.6 presents the annual average $\dfrac{N_{IN}}{N_{\text{lim}}}$ for the spectra of Table 5.2 at the $p = 281$ hpa level. For the MONO spectrum, $\dfrac{N_{IN}}{N_{\text{lim}}} > 1$, which indicates that N_{IN} is high enough to inhibit homogeneous freezing over

most of the globe. Figure 5.3 indicates that this is the case up to very high levels in the atmosphere. If MONO reflected atmospheric IN, cirrus would show a marked difference in N_c between the northern and the southern hemisphere. This behavior was seen in the global modeling study of *Penner, et al.* [194], whom used an IN framework derived from classical nucleation theory. For the CNT-BN spectrum, $\dfrac{N_{IN}}{N_{lim}} > 1$ in the northern hemisphere (although lower than for MONO). In the southern hemisphere however, $\dfrac{N_{IN}}{N_{lim}} \sim 1$ and $\dfrac{N_c}{N_{c,HOM}} \ll 1$, indicating strong competition between homogeneous and heterogeneous freezing; however heterogeneous IN impacts would not manifest given the low frequency of low level cirrus in these regions [220]. At higher levels, N_{IN} predicted by the CNT-BN spectrum decreases and competition effects vanish in the southern hemisphere and the tropics ($\dfrac{N_{IN}}{N_{lim}} < 0.2$, not shown). As N_{IN} predicted by the PDA and BKG spectra is generally low (Figure 5.3), competition effects are weak over most of the globe (i.e., $\dfrac{N_{IN}}{N_{lim}} \ll 1$) except near dust sources in the northern hemisphere; PDA results in $\dfrac{N_{IN}}{N_{lim}}$ up to 0.4, depleting N_c to about half of the homogeneous freezing value ($\dfrac{N_c}{N_{c,HOM}} \sim 0.5$). Competition effects are very strong for the MY spectrum being $\dfrac{N_{IN}}{N_{lim}} \sim 1$ around the globe, which results in very low $\dfrac{N_c}{N_{c,HOM}}$ (about 0.1 - 0.2, Figure 5.5).

5.3.3. The Role of Dust and Black Carbon as IN Precursors

As dust and black carbon emissions originate from different sources [148], it is important to distinguish their relative contribution to the IN population. Figure 5.7 shows $N_c / N_{c,HOM}$ for the CNT-BN and PDA spectra considering either only black carbon ($N_{dust} = 0$) or dust ($N_{bc} = 0$) as IN precursor. Generally, dust freezes at a lower s_i and has a higher freezing fraction than black carbon (i.e., it is a more "efficient" IN). Therefore lower N_{dust} than N_{bc} is needed to impact homogeneous freezing. The number concentration of black carbon is however higher in the upper troposphere ($N_{bc} \gg N_{dust}$) [148] so, even if it is not a very efficient IN, heterogeneous freezing of black carbon still contribute appreciably to N_{IN}.

Using CNT-BN and assuming dust as the only IN precursor produces a global annual mean N_{IN} around 0.05 cm^{-3}, about 0.1 cm^{-3} in most of the northern hemisphere and as high as 0.3 cm^{-3} near dust sources (not shown). The spatial variability of dust concentration results in near pure homogeneous freezing in Tropical cirrus ($\frac{N_c}{N_{c,HOM}} \sim 1$ and $\frac{N_{IN}}{N_{\lim}} \ll 1$) and strong competition between freezing mechanisms in the Northern midlatitudes ($\frac{N_c}{N_{c,HOM}} \sim 0.1$ and $\frac{N_{IN}}{N_{\lim}} \sim 1$). Regions of $\frac{N_c}{N_{c,HOM}} \sim 0.5$ result from dominant heterogeneous freezing ($N_{IN} > N_{\lim}$) near dust sources in the northen hemisphere, and, partially inhibited homogeneous freezing ($N_{IN} < N_{\lim}$) in the midlatitudes of the Southern hemisphere. Using the PDA spectrum results in mean N_{IN} around 0.001 cm^{-3} (with an

upper limit of 0.01 cm^{-3}). Given the simulated $N_{dust} \sim 0.1$ cm^{-3} at $p = 281$ hpa (not shown), PDA on average predicts that about 1% of dust freezes (as opposed to $\sim 100\%$ predicted by CNT-BN). Thus, only in regions of high N_{dust} (around 0.5 cm^{-3}) are IN numerous enough to impact N_c.
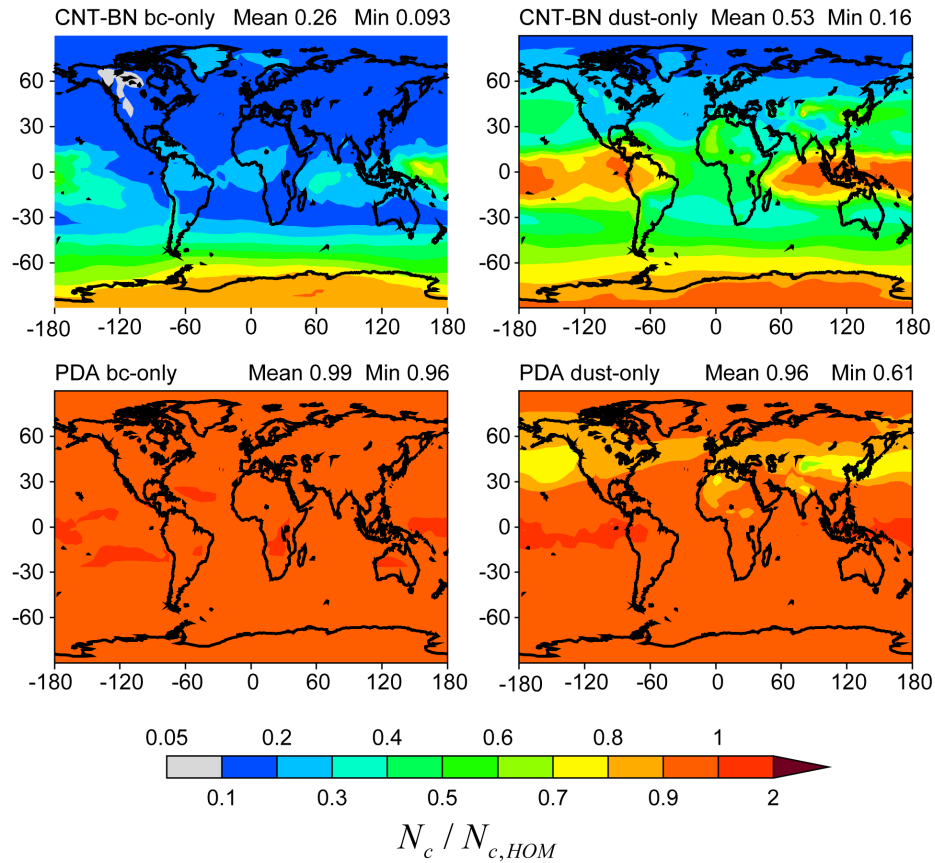
Figure 5.7. Annual average ice N_c at $p = 281$ hPa normalized with N_c from pure homogeneous freezing (HOM). Results shown assuming only dust ($N_{bc} = 0$, "dust-only") or black carbon ($N_{dust} = 0$, "bc-only") contribute IN.

If black carbon is assumed to be the only precursor of IN ($N_{dust}= 0$, Figure 5.7, "bc-only") the CNT-BN spectrum predicts N_{IN} around 0.04 cm^{-3} and up to 0.07 cm^{-3} in the midlatitudes of the Northern hemisphere. As $N_{IN} \sim N_{\lim}$, there is strong competition between freezing mechanisms, resulting in very low N_c over most of the northern hemisphere. Using the PDA spectrum for this case gives a mean N_{IN} around 0.001 cm^{-3} (up to 0.01 cm^{-3}) and black carbon freezing fraction around 0.01% , which is too low to impact freezing (i.e., $\dfrac{N_c}{N_{c,HOM}} \sim 1$ and $\dfrac{N_{IN}}{N_{\lim}} < 0.1$).

Comparison of Figures 5.4 and 5.7 shows that the combined effect of dust and black carbon on N_c is not additive, and depends on their relative freezing characteristics. For CNT-BN, there are enough IN from black carbon alone to strongly reduce N_c from pure homogeneous freezing concentrations (Figure 5.7, "bc-only"), most of the black carbon however does not freeze in the presence of dust (Figure 5.4) because s_{max} does not exceed its freezing threshold; therefore sufficient amounts of dust prevent the freezing of supercooled droplets and black carbon. In the southern hemisphere, N_{dust} is very low and black carbon is the dominant factor controlling N_c, leading to competition between homogeneous and heterogeneous freezing (which however is not significant at high altitudes, section 3.2). This is not the case in PDA, as the black carbon freezing fraction is too small to have an appreciable impact on N_c and dust is the only significant source of IN. However, the presence of low dust concentration may reduce the N_{bc} required to have an appreciable effect on N_c; the very small black carbon freezing fractions

predicted by the PDA spectrum may thus exert a noticeable effect of IN on N_c. This is

illustrated by the values of $\dfrac{N_c}{N_{c,HOM}}$ at the northern latitudes of the Atlantic Ocean (around

50°); for both the dust-only and bc-only cases, $\dfrac{N_c}{N_{c,HOM}} \approx 1$ (Figure 5.7, PDA), but

$\dfrac{N_c}{N_{c,HOM}} \approx 0.8$ when both dust and black carbon act as IN precursors (Figure 5.5, PDA).

5.3.4. Sensitivity to dynamical forcing

When σ_V is assumed to decrease with temperature (Figure 5.8) N_c near the tropical

tropopause level (TTL, $p \sim 100$ hpa) is much lower ($N_c \sim 1$ cm^{-3}) than when using a fixed

σ_V ($N_c \sim 10$ cm^{-3}). In terms of the global annual mean N_c for the whole atmosphere, this

variation in σ_V leads to about a threefold decrease for all the spectra of Table 5.2,

primarily because reductions in updraft velocity decreases N_{hom} [109, 12], which

inevitably limits N_c. However, small values of σ_V also exacerbate the effect of IN on N_c

because N_{lim} decreases with decreasing V (i.e., fewer IN are required to perturb

homogeneous freezing) [13]. For the CNT-BN, MONO and PDA spectra, N_{IN} decreases

with height (as N_{dust} and N_{bc} decrease); if σ_V decreases with T, N_{lim} also drops,

allowing for significant heterogeneous effects even at very low N_{IN} (~ 1 L^{-1}; Figure 5.3).

Because of this, using the BKG and MY spectra, where N_{IN} does not depend on aerosol

concentration (therefore does not decrease with height), leads to the predominance of

heterogeneous freezing at low T. This behavior is further analyzed in sections 5.3.5 and

5.3.6.
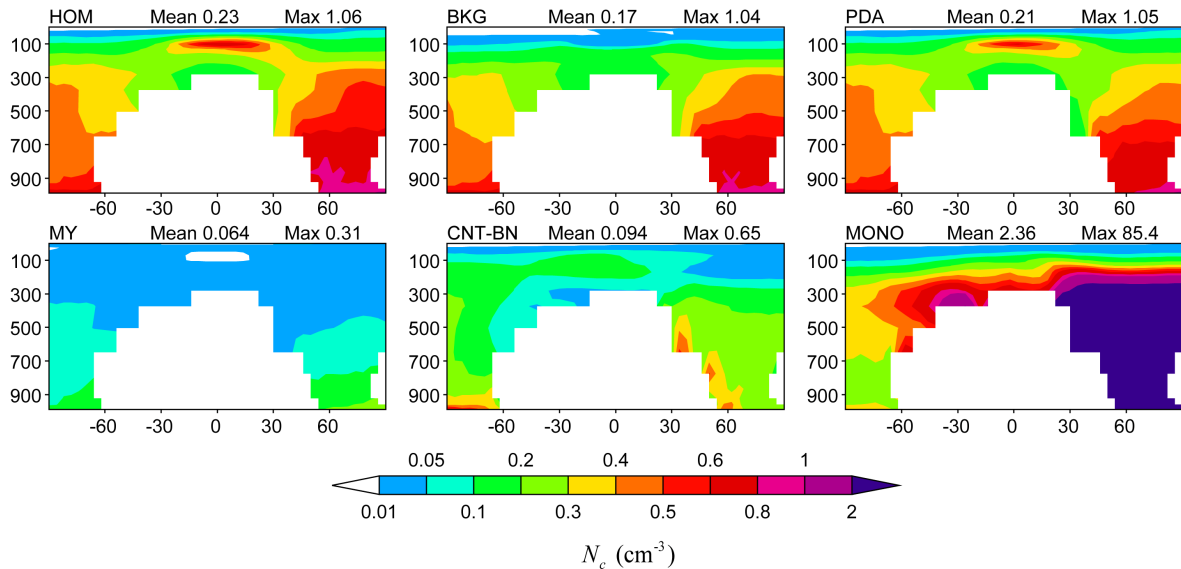
Figure 5.8. Similar to Figure 5.3 with σ_V decreasing from 25 cm s^{-1} (at 238 K) to 1 cm s^{-1} (at 198 K).

5.3.5. Effect of Temperature on N_c

As N_{IN} is limited by the available aerosol concentration, N_c in cirrus formed by heterogeneous freezing is less sensitive to changes in T than clouds where homogeneous freezing dominates [154, 13]. Figure 5.9 compares the results of the GMI model for the runs of Table 5.2 against in situ data reported by *Krämer, et al.* [132]. Agreement to within a factor of two with observations is obtained for $T > 205$ K for all IN spectra except MY (which underpredicts N_c). For $T < 205$ K, and assuming a fixed σ_V (Figure 5.9, left panel), the model largely overestimates N_c by at least tenfold, even in cases where heterogeneous effects are the strongest (e.g., MONO and MY). Assuming a decreasing σ_V decreases N_c at low T (section 5.3.3), giving a much better agreement

138

with observations (although using BKG and MY underestimate N_c, from an overestimation of N_{IN} at high altitudes). For $T > 205$ K, the CNT-BN, BKG, HOM, and MONO spectra display roughly similar N_c (mostly within a factor of 3). However, similar N_c may result from very different interactions between homogeneous and heterogeneous freezing (Figures 5.4 and 5.5; section 5.3.2). The distribution of s_{max} that results from application of each IN spectrum considered in this study can help elucidate whether lowering σ_V with altitude is consistent with other available cirrus microphysical characteristics.
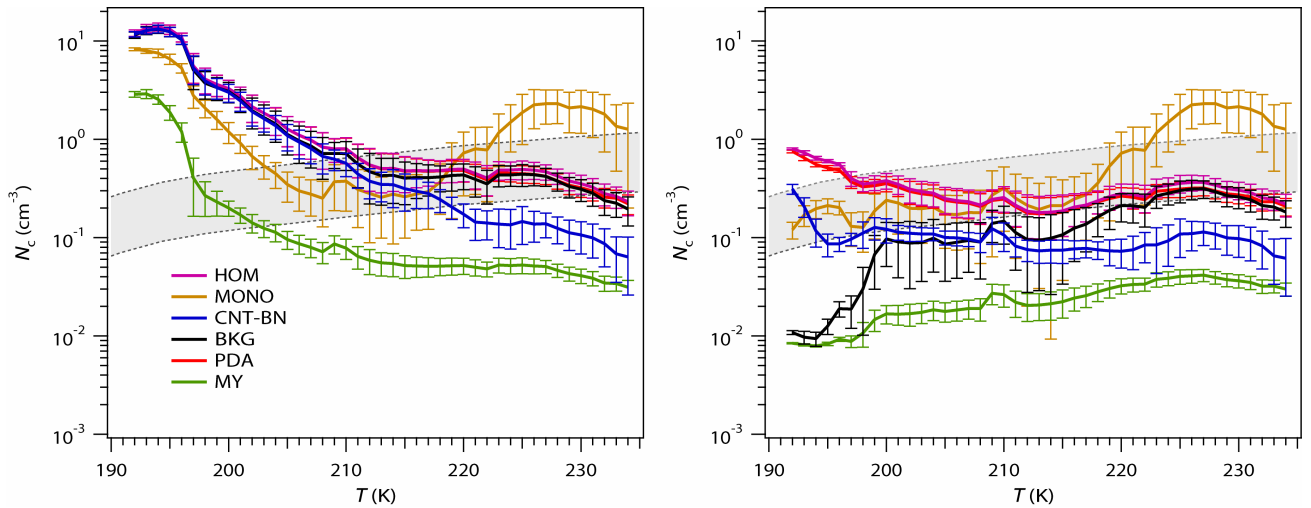
Figure 5.9. Ice crystal concentration against grid-cell temperature using the spectra of Table 2. Results shown assuming $\sigma_V = 25$ cm s^{-1} (left panel) and σ_V decreasing from 25 cm s^{-1} (at 238 K) to 1 cm s^{-1} (at 198 K) (right panel). Error bars represent one standard deviation about the mean N_c. The shaded area corresponds to a factor of two from the mean N_c observed in-situ [132].

5.3.6. Maximum supersaturation statistics

The frequency distribution of maximum supersaturation achieved during cloud formation, $P(s_{max})$ is shown in Figure 5.10, for fixed σ_V (right panel) and for σ_V decreasing with T (left panel). As homogeneous freezing occurs over a very narrow s_i interval [109, 12], $P(s_{max})$ for HOM is insensitive to σ_V and depends only on T; s_{max} ranges mostly between 0.4 and 0.65 with a mean around 0.5. Predominance of pure heterogeneous freezing for MONO and MY is expressed by a shift in $P(s_{max})$ toward low s_{max} (mean around 0.2 to 0.3). Competition between homogeneous and heterogeneous freezing (e.g., BKG and CNT-BN) results in a broad $P(s_{max})$ with a maximum about the homogeneous freezing threshold ($s_{max} \sim 0.5$) extending to low s_{max}. Assuming a T-dependent σ_V exacerbates IN effects on s_{max}; $P(s_{max})$ therefore resides mostly below the homogeneous freezing threshold for all the IN spectra (except in PDA where N_{IN} is too low to significantly impact s_{max}).

Observations can be used to diagnose s_{max} as it is related to the upper limit of the relative humidity distribution in recently formed clouds [83, 76]. Field campaign data consistently show s_{max} near the homogeneous freezing threshold [e.g., 85, 83, 76, 64, 36, 132]. *Haag, et al.* [76] have shown however that in some regions of the northern hemisphere, s_{max} can be lower (~ 0.3) due to heterogeneous freezing, which is also consistent with theoretical considerations [110, 14]. To be consistent with these observations, $P(s_{max})$ should exhibit a mean around $s_{max} \sim 0.5$, with a broad tail toward lower s_{max} values. Figure 5.10 shows that these features cannot be reconciled assuming

weak dynamical forcing (a T-dependent σ_V; Figure 5.10, right panel), or when heterogeneous IN completely inhibits homogeneous freezing during cloud formation (i.e., MY and MONO spectra). Indeed, only cloud formation scenarios where competition between homogeneous and heterogeneous freezing is the dominant feature (e.g., CNT-BN, BKG) would result in $P(s_{max})$ consistent with observations. Thus, simulations that prescribe a weakening of dynamical forcing (σ_V) with height provide N_c predictions that are closer to observations, but for the wrong reason.
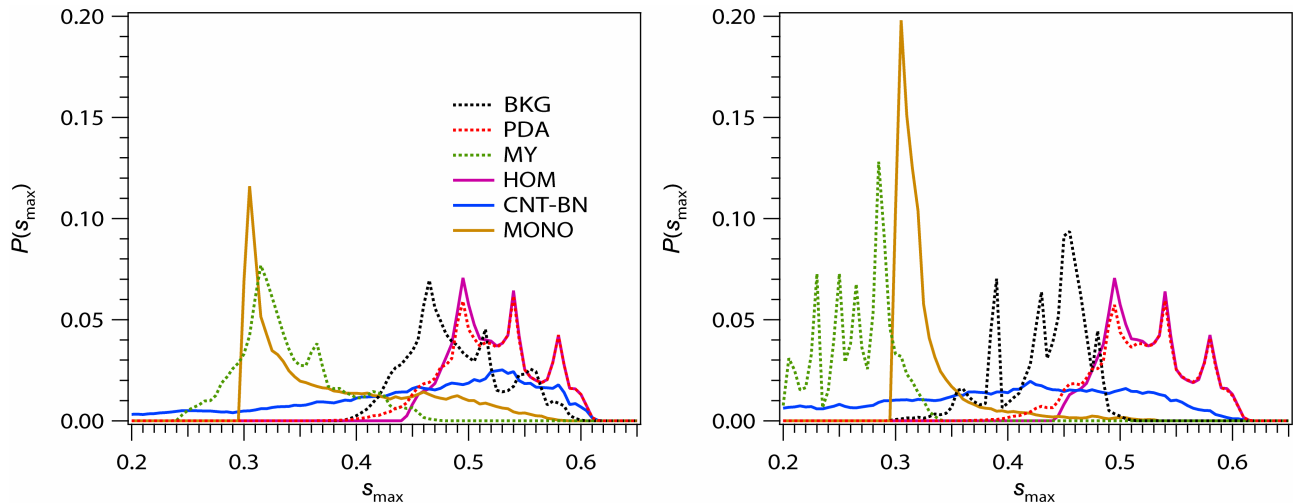
Figure 5.10. Global annual average probability distribution of s_{max} calculated by the BN09 parameterization, for the different heterogeneous freezing spectra of Table 5.2. σ_V was assumed constant equal to 25 cm s^{-1} (left panel), or, decreasing from 25 cm s^{-1} at 238 K to 1 cm s^{-1} at 198 K (right panel).

5.3.7. Sensitivity of N_c distributions to meteorological field

The global distribution of temperature, as well as of aerosol concentration, can be greatly affected by the meteorological field employed to drive the aerosol simulation [148]. To

study how this sensitivity would affect the global distribution of N_c, GMI runs were carried out using the DAO meteorological field for the HOM, CNT-BN, and PDA spectra (Figures 5.11 and 5.12). When no heterogeneous effects are considered (HOM) the global annual mean N_c obtained with the DAO field (0.60 cm^{-3}) is very close to obtained using GISS (0.62 cm^{-3}), although the spatial distribution of N_c differs. Upper tropospheric ($p <$ 200 hpa) N_c is generally larger in DAO than in GISS and vice versa at lower levels. This results from a weaker vertical transport in DAO (compared to GISS), producing lower high-altitude temperatures in the former [148].
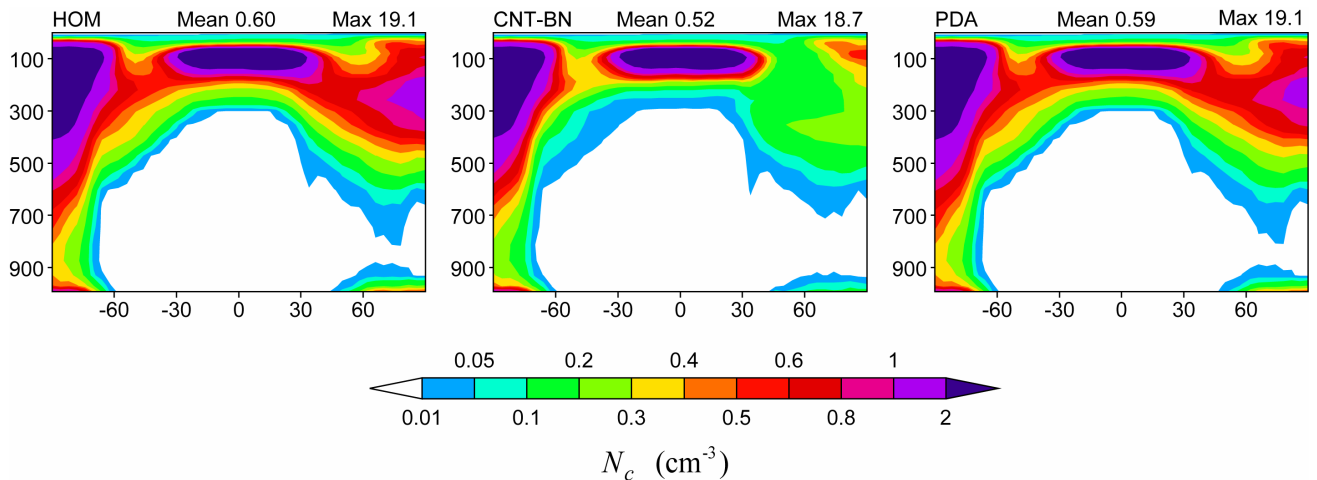
Figure 5.11. Annual zonal average N_c that would form in cirrus clouds for the spectra of Table 5.2. Simulations are carried out using the DAO meteorological field. Only in-cloud N_c is considered so that events with T > 235 K and $N_c = 0$ are excluded from the average.

For the CNT-BN spectra, N_c in the northern hemisphere ($p >$ 300 hpa) is much lower using the DAO field than obtained with the GISS field. For simulations with the PDA spectrum, the DAO field results in even weaker IN effects on N_c than obtained with the

GISS field (Figure 5.4). These features originate from differences in predicted N_{dust} and

N_{bc} (therefore different interaction between homogeneous and heterogeneous freezing)

and can be understood in terms of $\dfrac{N_c}{N_{c,HOM}}$ and $\dfrac{N_{IN}}{N_{lim}}$.

The spatial distribution of $\dfrac{N_c}{N_{c,HOM}}$ at the $p = 258$ hpa level obtained with the DAO

field is shown in Figure 5.12 for the PDA (right panel) and CNT-BN (left panel) spectra.

Compared to simulations with the GISS meteorological field (Figure 5.4), the CNT-BN

spectrum generally results in lower N_c around the globe. The opposite occurs for the

PDA spectrum where $\dfrac{N_c}{N_{c,HOM}} \sim 1$ (and $\dfrac{N_{IN}}{N_{lim}} \ll 1$) is considerable different that

simulations with the GISS ($\dfrac{N_c}{N_{c,HOM}} \sim 0.5$ near dust sources, section 5.3.2). These

differences result from weaker dust transport to the upper troposphere in the DAO

(compared to the GISS field). Indeed, the mean upper-level N_{dust} and N_{bc} predicted with

DAO (0.05 and 0.8 cm^{-3}, respectively) are about a factor of two lower than for GISS (0.1

and 1.17 cm^{-3}, respectively). Thus, N_{IN} is insufficient to prevent freezing of black carbon

when using the CNT-BN spectrum with the DAO field. This implies that instead of pure

heterogeneous freezing ($\dfrac{N_{IN}}{N_{lim}} > 1$) caused by dust for the GISS field, there is competition

between freezing mechanisms ($\dfrac{N_{IN}}{N_{lim}} \sim 1$) when using the DAO field.
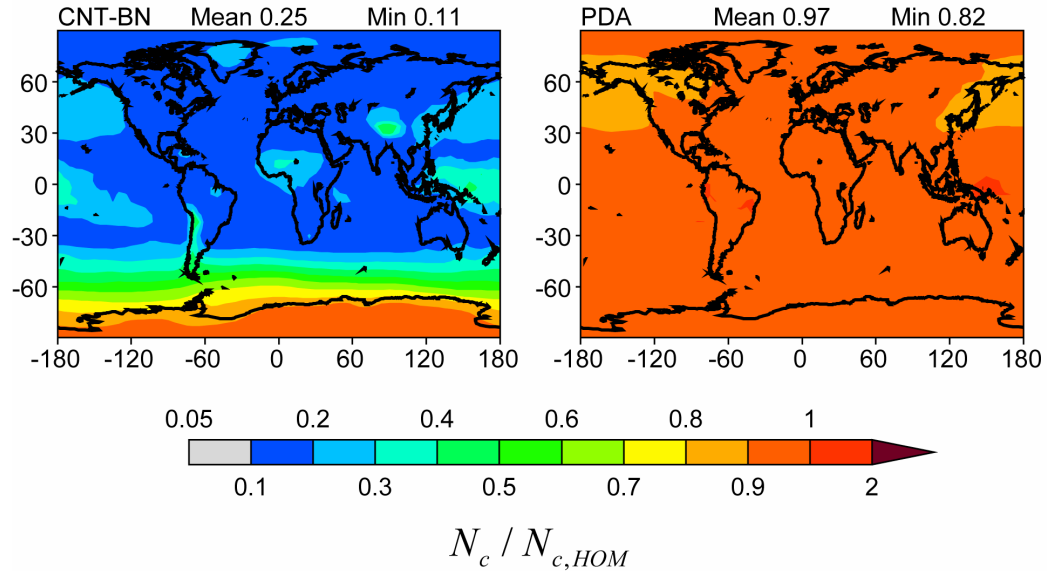
Figure 5.12. Annual average ice crystal concentration at $p = 258$ hPa, normalized with N_c from pure homogeneous freezing (HOM). Simulations obtained using the DAO meteorological field.

Lower N_{dust} with DAO winds also resulted in lower N_{IN} when using PDA, therefore a weaker impact of dust on N_c ($\frac{N_c}{N_{c,HOM}} \approx 1$) that simulated with GISS. Despite these differences, both the DAO and GISS meteorological fields consistently show high N_c at the TTL (Figure 5.4) and a significant contribution of dust to N_{IN} in the Northern hemisphere.

5.4. Summary and Conclusions

A parameterization of cirrus cloud formation that accounts for competition between homogeneous and heterogeneous freezing was implemented in the Global Modeling Initiative (GMI) chemical and transport model. Simulations were then carried out to

study the sensitivity of ice crystal number concentration to dust and black carbon aerosol concentrations. Ammonium sulfate was assumed to deliquesce and contribute supercooled droplets that freeze homogeneously. Dust and black carbon were assumed to heterogeneously freeze, using spectra derived from empirical data (PDA, BKG, and MY) and theory (CNT-BN and MONO). The global annual mean N_{IN} predicted by these formulations varied between 0.003 and 2.4 cm^{-3}. When included into the cirrus formation framework, this variation resulted in up to a factor of 20 difference (0.13-2.5 cm^{-3}) in the predicted global mean N_c. For low N_{IN} (PDA spectrum), homogeneous freezing was predominant and vice-versa for high N_{IN} (MONO spectrum), giving N_c even higher than for pure homogeneous freezing. The lowest N_c resulted when strong competition between homogeneous and heterogeneous freezing ($\frac{N_{IN}}{N_{\lim}} \sim 1$) was predominant (MY spectrum).

The sensitivity of N_c to IN is a strong function of the heterogeneous IN spectrum. Empirical parameterizations that only depend on supersaturation (BKG and MY) predicted a uniform N_{IN} around the globe and little variation of N_{IN} with height. Explicitly accounting for the dependency of dust and black carbon concentration (MONO, CNT-BN, and PDA) resulted in a highly variable spatial distribution of N_{IN}. In the latter, heterogeneous effects on N_c were the strongest at the lowest levels of cirrus formation ($T \sim 230$ K) in the midlatitudes of the northern hemisphere, mostly near regions impacted by transport of dust and black carbon. In the tropics and Midlatitudes of the Southern hemisphere, it was found that IN would affect cirrus formation only if the

freezing fraction of black carbon is close to unity. In general, heterogeneous effects were less significant at low temperatures as dust and black carbon concentration were low and the N_{IN} needed to impact homogeneous freezing (i.e., $N_{\lim}$) was higher than at warmer levels. Dust was found to be an important contributor of IN over large regions of the northern hemisphere. The effect of black carbon as heterogeneous IN is still controversial, as it is depends on the functional form of the freezing spectrum. The simulations carried out in this study suggest that at least 1% of black carbon aerosol should freeze at cirrus levels in the Northern hemisphere to have an appreciable effect on N_c.

The sensitivity of the global distribution of N_c to large scale meteorological features was tested by running the GMI model using two different meteorological data sets (GISS and DAO). Differences in the vertical transport of dust and black carbon to the upper troposphere lead to significant variation in N_{dust} and N_{bc} (therefore on N_{IN} and N_c). The largest sensitivity to the meteorological field resulted in regions where $N_{IN} \sim N_{\lim}$ (midlatitudes of the Northern hemisphere and near the tropics). For such conditions, a factor of two decrease in N_{dust} and N_{bc} at cirrus levels may change the predominant freezing regime from pure heterogeneous ($\frac{N_{IN}}{N_{\lim}} > 1$) to competition between homogeneous and heterogeneous freezing ($\frac{N_{IN}}{N_{\lim}} < 1$), and therefore the predicted response of cirrus to increased IN emissions. Despite this, runs with DAO and GISS

meteorological fields consistently show high N_c at the TTL (Figure 5.4) and a significant contribution of dust to N_{IN} in the Northern hemisphere.

Comparison of N_c predicted with the GMI model against reported observations [132] showed agreement for $T > 205$ K for most of the freezing spectra tested. However, at least a tenfold overprediction in N_c for $T < 200$ K where N_c was as high as 10 cm^{-3}, resulting from a high fraction of sulfate freezing homogeneously a low temperature. It was shown that if cirrus formation at low temperature forms in weak updrafts, N_c is in much better agreement with observations. This however magnifies the sensitivity to heterogeneous nuclei, so that N_{IN} as low as 1 L^{-1} was enough to affect homogeneous freezing. This results in s_{max} distributions that are in strong disagreement with available observations. Since s_{max} largely controls the steady-state size of the ice crystals and ice water content [131], incorrect predictions of $P(s_{max})$ will likely lead to biases in predicted cirrus ice crystal size distribution. Thus, even if the bias of N_c can be addressed by reducing σ_V, this would likely introduce other biases in the effective radius of ice crystals and ice water path with potentially important implications for radiative forcing. Altogether this reveals a fundamental weakness in the "classical" theory of cirrus formation at low T, the resolution of which would likely require considering ice sedimentation and transport effects [235], and the existence of other sources of IN (e.g., solid ammonium sulfate) at the TTL [1, 94].

The results presented in this work must be interpreted as the potential of IN to alter N_c whenever a cirrus cloud is formed. Cirrus cloud fraction was not calculated explicitly

(i.e., grid-cell cloud fraction was unity for $T < 235$ K). Although regions where IN effects are expected to be important can be determined by focusing on areas with high cirrus optical depth (using climatological data from ISCCP). Another assumption made in this work was to consider N_c at its maximum, i.e., no sedimentation or sublimation effect were accounted for. Sedimentation may structure the cirrus cloud layer and reduce the ice crystal concentration, particularly at low updraft velocity [235]. Sublimation may impact the ice crystal concentration in dry regions at high temperatures ($T > 235$ K) [104]. Although important, these effects are not expected to introduce N_c variability comparable to the variability introduced by N_{IN} and will not modify the conclusions of these study. However, the ice crystal concentrations presented in Figures 5.4, 5.7 and 5.9, may have a positive bias, particularly at warmer temperatures where sedimentation and evaporation are more significant. Nevertheless, the comparison of N_c with available measurements ($T > 205$ K) suggests that they are usually within a factor of two of predictions.

The size distribution of different aerosol species was assumed to follow prescribed functions as presented in Table 5.1. This is not expected to introduce a bias for homogeneous freezing however may introduce errors in N_{dust} and N_{bc}. Nevertheless, the plethora of IN treatments is placed for the first time within the same global modeling dynamical framework. Despite the very large variability in IN concentration and relative contribution of freezing seen, ice crystal number concentrations are less variable that we had initially anticipated. However, the large sensitivity of s_{max} to the prevailing

mechanism clearly points out that it too needs to be sufficiently constrained for cirrus optical properties and climate forcing to be correctly represented in climate models.

CHAPTER 6

THE TWO FACES OF CIRRUS CLOUDS[1]

Cirrus clouds play a key role in climate, and are thought to form mainly by large-scale dynamics forcing the homogeneous freezing of deliquesced aerosol. Low ice crystal concentration and sustained in-cloud supersaturation, commonly found in cloud observations at low temperature [63, 132], challenge this view [197]. Heterogeneous freezing [1] from effloresced ammonium sulfate, glassy aerosol [183], dust and black carbon are often proposed to cause these phenomena; this however requires very slow updrafts to produce the observed cirrus features and is at odds with the ubiquitous presence of gravity waves in the upper troposhere [226, 9, 92]. Instead, background temperature fluctuations can establish a "dynamical equilibrium" between ice production and sedimentation loss that explains low temperature cirrus properties. This newly-discovered state is favored at low temperatures, does not require heterogeneous nuclei to occur, and is insensitive sensitive to their presence. Our understanding of cirrus clouds and their role in anthropogenic climate change is reshaped, as the type of dynamical forcing will set these clouds in one of two "preferred" microphysical regimes with very different susceptibility to aerosol.

---

[1] This chapter appears are reference [15]: BARAHONA, D. and NENES, A. (In review). The Two Faces of Cirrus. *Nature*.

6.1. Motivation

Cirrus clouds are composed of ice crystals that form at high altitudes and temperatures typically below 235 K [208]. They play a key role in climate by modulating the planetary radiative balance [145] and heat transport in the upper troposphere [213]. They strongly impact water vapor transport across the tropopause level [92] and play an important role in lower stratospheric chemistry [196]. Cirrus may be affected by aircraft emissions [229] and long range transport of pollutants [61], and are an important (but highly uncertain) component of anthropogenic climate change. A key microphysical parameter required for understanding the climate impact of cirrus is their concentration of ice crystals, N_c. It is known that at temperatures between 200 and 235 K cirrus ice crystals form primarily by homogenous freezing of supercooled deliquesced aerosol [85, 43], which occurs if the saturation ratio with respect to ice, S, (i.e., the ratio of water vapor partial pressure to its equilibrium value over ice) reaches a characteristic threshold value, S_{hom} [129]. Heterogeneous freezing of water upon existing aerosol particles (termed "ice nuclei", IN) can also occur (at S lower than S_{hom}) and contribute to ice crystal concentrations [43, 62]. The level of water vapor supersaturation (i.e., $S - 1$) is the thermodynamic driver for ice formation, and is generated by expansion of air parcels forced by large scale dynamics, gravity waves, and small scale turbulence [125].

At temperatures below 200 K, the simple conceptual model for cirrus presented above is at odds with observations [197, 132, 94]. Temperature fluctuations from mesoscale gravity waves are common at high altitudes [9, 92] and can produce localized vertical motion with updraft velocity as large as 1 m s^{-1}. Homogeneous freezing driven by this motion would produce high ice crystal number concentration, N_c, between 1 and 10

cm^{-3} near the tropopause (Figure 6.1). Such high concentrations however are not observed; N_c remains low, sometimes even lower (0.005 - 0.2 cm^{-3}) than concentrations observed in weak updraft zones at cold temperatures [138, 132]. This "low N_c" paradox is accompanied by other unexplained phenomena, such as low supersaturation relaxation times [132], which in turn leads to sustained supersaturation levels inside clouds (i.e., "the supersaturation puzzle" [63]), high clear-sky supersaturation [96], and broad ice crystal size distributions (i.e., large crystal sizes [95]). These phenomena occur despite the strong dynamical forcing and the ample amounts of deliquesced aerosol available for homogeneous freezing. Suppressed freezing by organics [181], slow water vapor transfer to the ice phase [63, 156], and freezing to cubic instead of hexagonal ice [182], have been proposed to explain these features. These mechanisms however only act under specific conditions and cannot explain the low N_c and high S coexisting in low temperature cirrus clouds [197]. Lacking the predictive understanding of such phenomena hinders the ability of climate models to capture the climate effects of cirrus clouds and their response to anthropogenic perturbations.

6.2. Heterogeneous Freezing at Low Temperature

Recently, heterogeneous freezing of IN as the main path of cirrus formation has been proposed to explain the features of cirrus clouds at low temperature [1, 94]. Owing to their ability to freeze at much lower supersaturation than homogeneous freezing requires, IN can deplete water vapor, reduce supersaturation and inhibit homogeneous freezing; this can drastically reduce the number of ice crystals that forms in the cirrus [13]. Much of the anthropogenic impact on cirrus clouds and climate is thought to occur through this IN-N_c feedback mechanism [151]. The impact however of IN on N_c depends on their

concentration, N_{IN}. If too low ($N_{IN} < 1 \times 10^{-4}$ cm^{-3}), a negligible impact is seen on N_c, as too few (heterogeneously-frozen) ice crystals form to quench supersaturation below the homogeneous freezing threshold [13]. When N_{IN} approaches a characteristic "limiting" concentration (which depends on updraft velocity, the IN freezing threshold and size), $N_{\lim}$, supersaturation is quenched, homogeneous freezing is depressed, and N_c decreases steeply [13]. For $N_{IN} \geq N_{\lim}$, homogeneous nucleation is inhibited and $N_c = N_{IN}$. Thus, $N_{\lim}$ is the minimum N_c that can form in an active nucleation zone in a freshly-formed cirrus cloud [13] and presents the maximum reduction in N_c possible from IN.
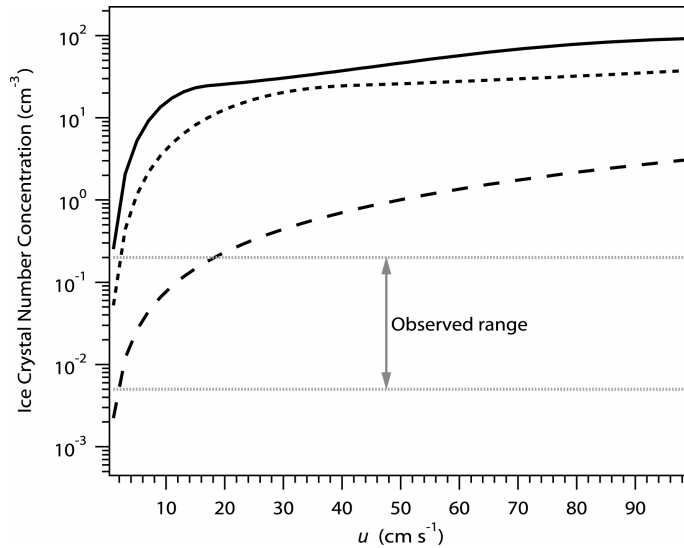
Figure 6.1. Ice crystal concentration, N_c, as a function of updraft velocity, u. Cloud was assumed to form at $T = 185$ K and p $= 100$ hPa (details provided in Section 6.5). Low values of u correspond to cloud formation driven primarily by large scale dynamics, whereas $u > 50$ cm s^{-1} is characteristic of cirrus developing in the vicinity of convective systems with intense gravity wave breaking [125]. Solid lines indicate N_c calculated for pure homogeneous freezing, dashed lines for $N_{IN} = N_{\lim}$, and dotted for $N_{IN} = 0.75 N_{\lim}$. For $N_{IN} = N_{\lim}$, N_c lies close to the observed values for $u < 50$ cm s^{-1} [132] but is very sensitive to small fluctuations in N_{IN}.

153

Simulations show that if N_{IN} is always very close to N_{lim}, competition between homogeneous and heterogeneous freezing could yield N_c close to observations (Figure 6.1). This requires $N_{IN} \sim 0.1$ cm^{-3}, which is 20-fold higher than typically measured dust concentrations ($\sim .005$ cm^{-3}) at the tropopause level [62]. Ammonium sulfate aerosol is present at much higher concentrations than dust, and can serve as IN [1] if a fraction of them is effloresced (which is possible, given that it deliquesces at ~90% relative humidity [59]).
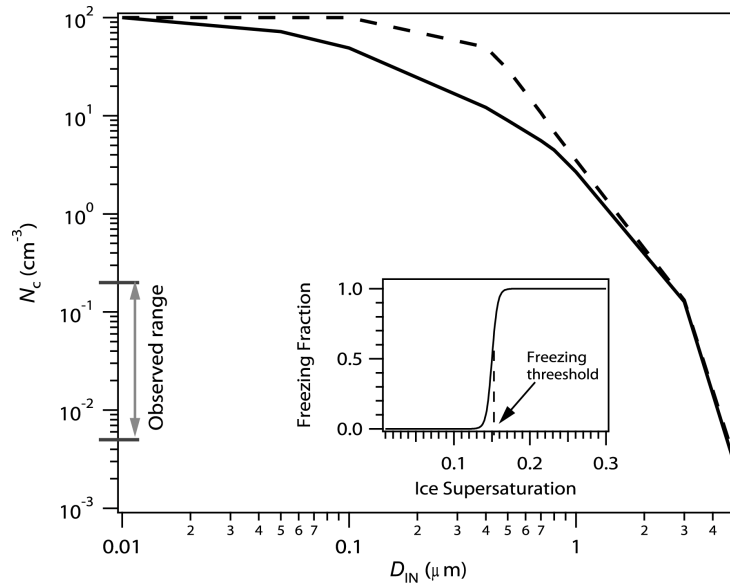
Figure 6.2. Simulations of ice crystal concentration by pure heterogeneous freezing using the "conventional" model of cirrus formation (i.e., fluctuations in S and u from fluctuations in temperature are neglected). N_c is presented as a function of the initial size of the ice nuclei. Conditions [138] used were $T = 185$ K, $p=100$ hPa, $\alpha_d =0.07$ (dashed line), and 1.0 (solid line). The IN population was assumed to be monodisperse with total number concentration of 100 cm^{-3} [138]. Simulations were carried out with a numerical parcel model that considers the competition between homogeneous and heterogeneous freezing [12]. Consistent with published studies[1], freezing of solid ammonium sulfate was assumed to occur in a "burst" around the heterogeneous freezing threshold described by sigmoidal freezing spectrum with inflection point $s_{het} = 15\%$, where 99% of the aerosol freeze within a 2% supersaturation interval about s_{het} (inset plot).

154
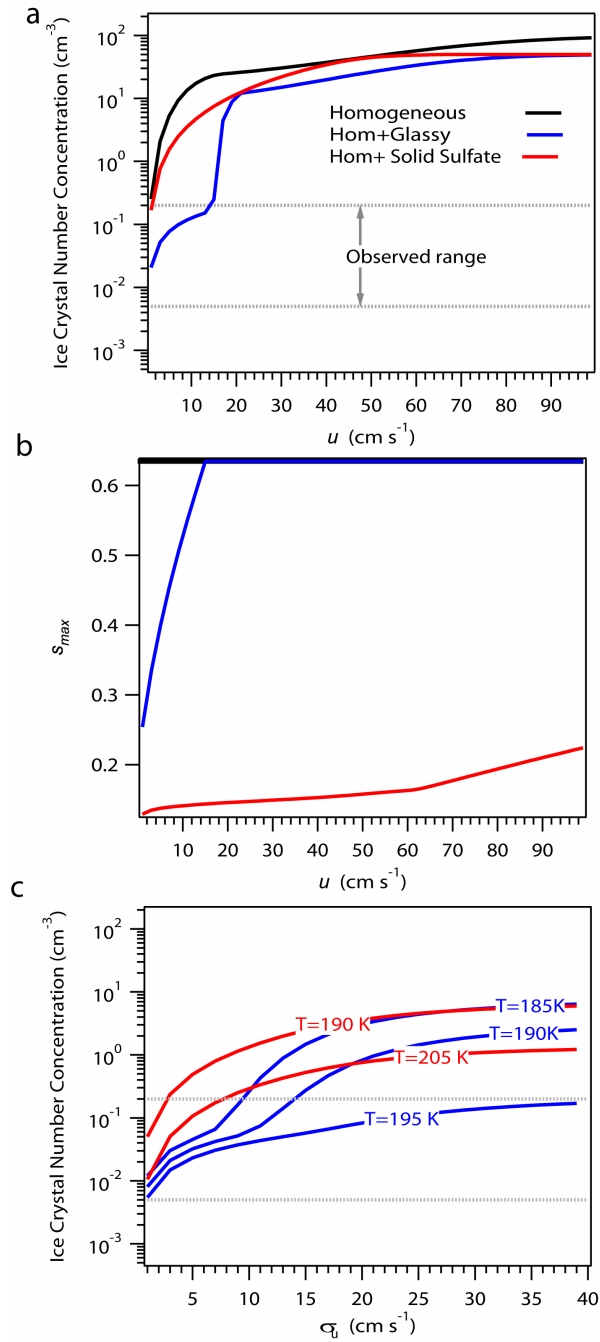
Figure 6.3. Comparison between heterogeneous effects from solid ammonium sulfate [1] and glassy citric acid aerosol [183], using the analytical model of Barahona and Nenes [14] for homogeneous and heterogeneous freezing. (a) Maximum ice crystal concentration as a function of updraft velocity for a single freezing event. (b) Maximum supersaturation achieved for a single freezing event. (c) Ice crystal concentration averaged over a normal distribution of updraft velocities with zero mean and standard deviation σ_u. The gray lines represent the range of N_c typically observed [132].

To inhibit homogeneous freezing and reproduce observations of N_c, the concentration of ammonium sulfate IN needs to be within 10% of N_{lim}; if concentrations fall below $0.9N_{lim}$, predicted N_c is significantly above observations (Figure 6.1).

If higher concentration than N_{lim} is present, homogeneous freezing is completely suppressed, but too many crystals still form [12]. In fact, N_c from heterogeneous freezing of ammonium sulfate and pure homogeneous freezing are always comparable (Figure 6.2), because crystals formed from ammonium sulfate IN are very small (with size close to the dry aerosol; 0.02-0.05 µm [62]) and grow too slowly to quench supersaturation before a large fraction of the aerosol freezes heterogeneously. N_c is within observed values only if the average size of crystals at the point of freezing is 2 µm or larger (Figure 6.2), which is too large for upper tropospheric aerosol [62]. Hence, with the exception of a remarkably constant concentration of ammonium sulfate IN (0.1 ± 0.01 cm^{-3}) or exceptionally large concentration of dust, heterogeneous IN cannot explain the low N_c observed at high-level cirrus. The freezing fraction of organic glassy aerosol is much lower than that of ammonium sulfate and N_{IN} is close to N_{lim} (maintaining low N_c, Figure 6.3a, b) up to 15 cm s^{-1} [183], after which homogeneous freezing is triggered producing high N_c. The onset of homogeneous freezing occurs at even lower u for colder temperatures (Figure 6.3).; therefore this mechanism alone cannot explain all the cirrus features in the presence of T fluctuations.

6.3. Dynamical Equilibrium during Cirrus Evolution

Ice falling though active freezing zones (typically located at the top of the cirrus layer [235]) in clouds consume water vapor and can inhibit homogeneous freezing much like IN do. Their effectiveness depends on their residence time in freezing zones, hence depends on their size. Large ice crystals tend to quickly fall out of freezing zones and have limited effect on new ice formation events; small crystals (typically those with terminal velocity, u_{term}, less or equal to the mean updraft $\bar{u}$ of the cirrus layer) fall slowly and can remain long enough in the upper part of the cloud to affect new freezing events. This suggests that at low temperatures preexisting (and typically small [132]) ice crystals may locally dehydrate the freezing zone sufficiently to inhibit the formation of new ice. The rate of crystal production is not uniform through the freezing zone, as "local" saturation ratio, S, and updraft velocity, u (defined at the scale of individual cloud "parcels" ~ 50 m [208]) may be affected by fluctuations in wind speed and temperature induced by gravity waves [125, 105]. These internal S variations are usually neglected in cirrus cloud studies on the basis that the long-term evolution of the cloud is determined by the mean values of S and u. However, we show that accounting for them can profoundly impact the state and microphysical evolution of the cirrus cloud.

The main processes affecting the evolution of N_c and mean saturation ratio, S_o, within a cirrus layer are the freezing of new ice, the sedimentation of existing ice crystals, the lifting of air masses (which generates supersaturation), and the relaxation (i.e., mass transfer) of water vapor to/from the ice phase. The magnitude of each process can be expressed in terms of a characteristic timescale, i.e., τ_{fr}, τ_{sed}, τ_{lift}, and τ_{rel} for freezing, sedimentation, lifting, and relaxation, respectively (Table 6.1). Fluctuations in S and u

157

can have a strong impact on all cloud processes; we therefore represent them in terms of a probability distribution centered about the cirrus-average saturation ratio, S_o, and vertical velocity, $\bar{u}$. The width of these probability distributions is largely determined by the mean amplitude of temperature fluctuations, δT [9, 86, 104]. If homogeneous freezing is the only ice production mechanism considered, the rate of ice production is given by the frequency with which S exceeds the homogeneous freezing threshold [104] times the length and intensity of each freezing event (hence τ_{fr}) [208, 12]. The same fluctuations also affect the local mass transfer rate between the ice and vapor phases, so that when averaged over the cloud, water deposition/sublimation occurs at an "effective" saturation ratio, S_{eff}, that may differ from S_o (Table 6.1). From these considerations, simple equations can be derived that represent the evolution of N_c, S_o in the cirrus (Table 6.1 and Section 6.5.1). The influence of T and u fluctuations is accounted for in the probability distribution of S, which is then used to determine S_{eff} and τ_{fr}.

Table 6.1. Equations describing the evolution of ice crystal concentration, N_c, and mean saturation ratio, S_o, in a cirrus cloud. Processes considered include ice crystal production (subscript "fr"), sedimentation (subscript "sed"), expansion cooling (subscript "uplift"), and condensation/evaporation of water vapor on ice (subscript "evap/cond"). S_{eff} is the local, effective saturation ratio defined to take into account the effect temperature fluctuations (from gravity wave motion) on S. The derivation of equations is described in Section 6.5.1.

$$\frac{dN_c}{dt} = \frac{dN_c}{dt}\bigg|_{fr} + \frac{dN_c}{dt}\bigg|_{sed} = \frac{N_o P_S (S > S_{\text{hom}}) H_v(u)}{\tau_{fr}} - \frac{N_c}{\tau_{sed}}$$

$$\frac{dS_o}{dt} = \frac{dS_o}{dt}\bigg|_{cooling} + \frac{dS_o}{dt}\bigg|_{evap/cond} = \frac{S_o}{\tau_{uplift}} - \frac{S_{\text{eff}} - 1}{\tau_{rel}}$$

where $\tau_{sed} = H\,u_{term}^{-1}$, $\tau_{fr} = \left[\overline{v}_o J(S_{\max}) \exp\left(-\int_0^t \overline{v}_o J(S) dt \right) \right]^{-1}$ [12], $\tau_{uplift} = (\alpha\,\overline{u})^{-1}$ [208],

$\tau_{rel} = (\beta\,N_c \overline{D}_c)^{-1}$ [131], and $\quad S_{\text{eff}} = \dfrac{\displaystyle\int_a^b S\,\dfrac{dP_s(\delta T, S_o)}{dS}\,dS}{P_s(b) - P_s(a)}$

with $a = \begin{cases} 1 & u > 0 \\ 0 & u \le 0 \end{cases}$ and $\quad b = \begin{cases} S_{\text{hom}} & u > 0 \\ 1 & u \le 0 \end{cases}$

Nomenclature: $H \equiv$ Cirrus layer thickness; $H_v \equiv$ Heaviside function; $u_{term} \equiv$ Ice crystal terminal velocity; $\overline{v}_o \equiv$ Average volume of the deliquesced aerosol; $N_o \equiv$ Number concentration of deliquesced aerosol; $J \equiv$ Homogeneous nucleation rate [129]; $S \equiv$ Local Saturation Ratio; $S_{\max} \equiv$ Maximum local saturation ratio during ice crystal freezing [12-13]; $\overline{u} \equiv$ Average updraft velocity; $u \equiv$ Parcel updraft velocity; $\overline{D}_c \equiv$ mean sphere-equivalent ice crystal diameter; $S_o \equiv$ Mean saturation ratio; $S_{\text{hom}} \equiv$ Homogeneous freezing threshold [129]; $\dfrac{dP_s}{dS} \equiv$ Probability distribution of S [105]; $\delta T \equiv$ Standard deviation of temperature fluctuations; $\alpha \approx \dfrac{0.5473}{T} \text{-}1.402 \times 10^{-3}$ m^{-1}; $\beta \approx -6.44 \times 10^{-8} T^2 + 2.85 \times 10^{-5} T - 2.75 \times 10^{-3}$ m^{-3} Kg with T in K [13].
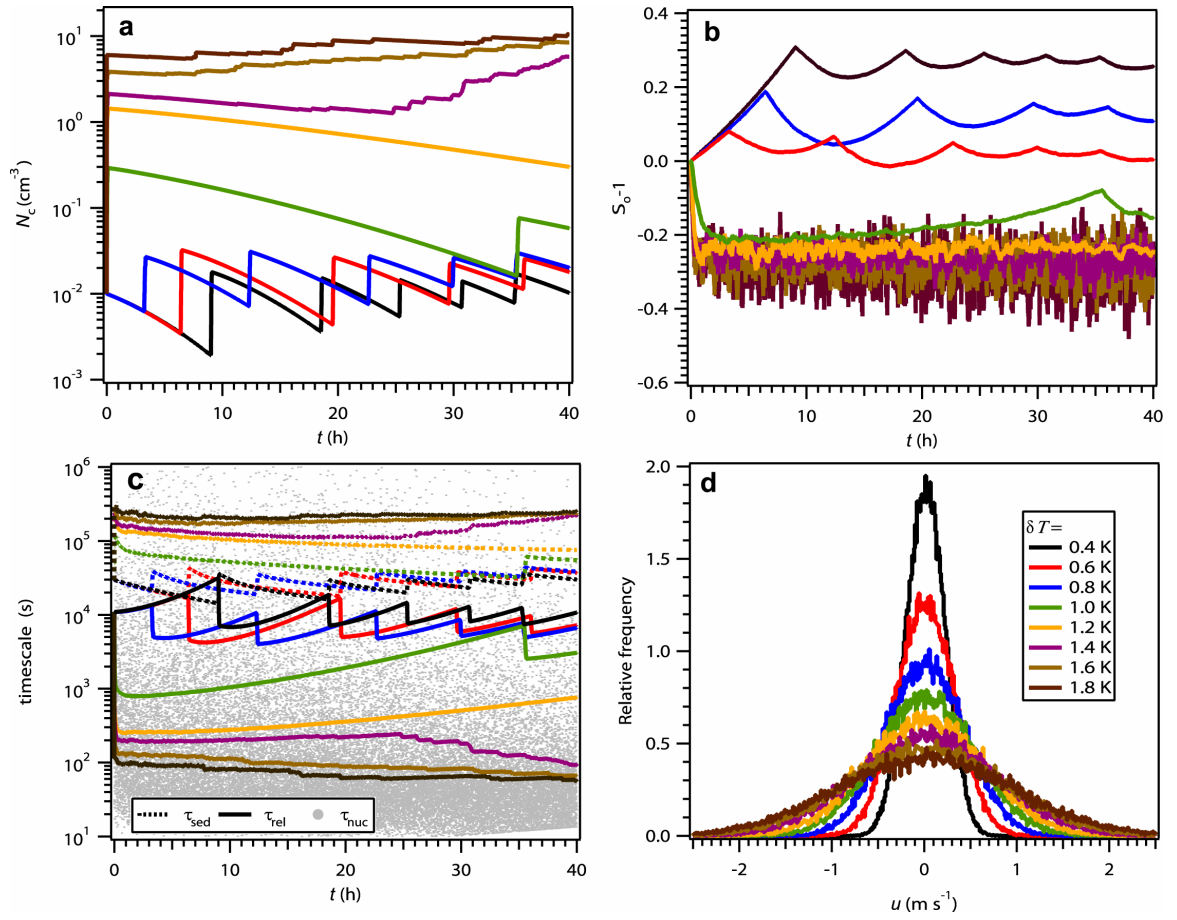
Figure 6.4. Evolution of a cirrus cloud lifting at 1 cm s^{-1} with initial T = 195 K and cloud thickness, H = 500 m, and using a water vapor to ice deposition coefficient equal to 1. Shown are (a) the ice crystal number concentration, (b) mean supersaturation, (c) characteristic timescales of freezing (gray dots), relaxation (solid lines), and sedimentation (dotted lines), and, (d) frequency distribution of vertical velocity, for different values of the mean amplitude temperature fluctuations, δT. For large fluctuations ($\delta T > 1$ K) most ice crystals form during the initial stage of cloud formation and the cloud slowly decays over time. For smaller fluctuations ($\delta T < 1$ K) a dynamic equilibrium states establishes where ice losses by sedimentation is compensated by production of new ice crystals, maintaining low N_c and high S_o over time.

Figure 6.4 presents the evolution of a cirrus layer subject to gravity-wave fluctuations with an initial average temperature of 195 K and lifting at $\bar{u} = 1$ cm s^{-1}. For values of $\delta T > 1$ K, the cloud initially experiences a strong homogeneous nucleation pulse, so that N_c initially increases steeply (Figure 6.4a); the consumption of water vapor by crystal growth decreases S_o (Figure 6.4b) which prevents any new freezing events. N_c slowly decreases from sedimentation loss; only after enough ice crystals sediment out of the cloud layer, S_o increases (e.g., $\delta T = 1$ K, green lines) and new freezing events occur. For $\delta T > 1.4$ K (purple lines) this is possible even if the layer remains on average subsaturated ($S_o < 1$) because the probability distribution of S is broad enough for a non-negligible probability with $S > S_{\text{hom}}$. This "pulse-decay" behavior is characterized by $\tau_{sed} \gg \tau_{rel}$ so ice crystals reside long enough in the cloud to relax supersaturation (Figure 6.4c); this behavior is also consistent with the parcel model concept of cirrus (where high N_c and low S_o coexist within the parcel). The subsaturation levels (Figure 6.4b) achieved in this state are in agreement with in situ observations of relative humidity in dissipating clouds [63, 132].

The cirrus evolution is however quite different when δT is small; the distribution of S is narrow, and substantial ice production is only possible after supersaturation (i.e., S_o) builds up in the cloudy layer to allow a non-negligible probability where $S > S_{hom}$. Thus, freezing events producing large N_c (associated with large u fluctuations; Figure 6.4d) are less frequent. Low N_c allows the formation of large ice crystals (Figure 6.8) which sediment out of the layer before substantially depleting supersaturation, leading to new freezing events. This "dynamic equilibrium" between ice production and loss is a

previously unidentified microphysical regime of cirrus, characterized by $\tau_{sed} \sim \tau_{rel}$ (Figure 6.4c); it maintains low N_c and high S_o in the cloudy layer (Figure 6.4a,b) and is consistent with observations of low-temperature cirrus. Clouds in "dynamic equilibrium" also exhibit broad crystal size distribution, because large ice crystals coexist with freshly-formed (small) crystals in the cloud.
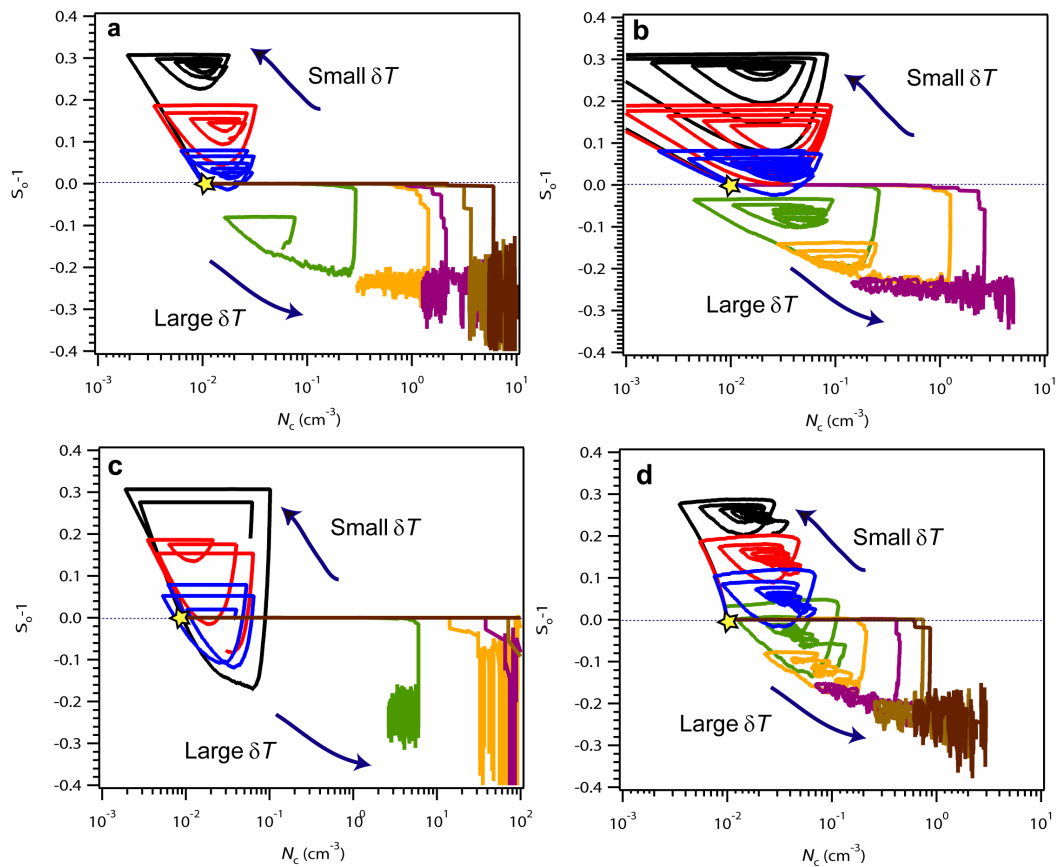
Figure 6.5. Sensitivity of N_c and S_o evolution to cloud formation conditions for different values of δT (color scheme same as in Figure 6.3); (a) same conditions as in Figure 6.4, (b) cloud thickness, $H = 100$ m (increased ice crystal removal rate), (c) deposition coefficient equal to 0.006 [156] (slow water vapor transfer), and (d) initial temperature 225 K and cloud lifting at 5 cm s^{-1}. The yellow star in each panel indicates initial conditions. The integration time was 40 h cases, except in (d) were it was 15 h.

When simulations (such as those of Figure 6.4) are placed on a "state diagram" of N_c vs. S_o, the two microphysical regimes described above clearly emerge. Examples are presented in Figures 6.5 and 6.6 for a range of initial conditions (presented as stars on the plots) and a variety of δT (lines of distinct color). Progression towards a "dynamic equilibrium" is favored when supersaturation replenishes quickly (i.e., at high τ_{sed}) and high $\bar{u}$; vice-versa for "pulse-decay" behavior. Figures 6.5 and 6.6 also show that the "dynamic equilibrium" state occurs spontaneously when δT goes below a characteristic transition value (which depends on $\bar{u}$ and T). It can also be reached after a cloud initially resides in a "pulse-decay" state, if δT is close to the characteristic value ($\delta T \sim 1$ K in Figure 6.4). Clouds in the "dynamic equilibrium" regime are also much less sensitive to the presence of IN and to slow water vapor deposition (e.g., Figure 6.5c). When maximum N_c and time-averaged S_o are presented on the state diagram for all simulations considered, the conditions of δT that separate "pulse-decay" and "dynamic equilibrium" regimes seem to be universal (Figure 6.7).

From the discussion above, cold cirrus clouds will reside in the "dynamic equilibrium" regime if δT is below the characteristic threshold. High-amplitude, orographically-generated gravity waves are ubiquitous [125] but often lose intensity with altitude, weakening their contribution to the background spectrum of temperature fluctuations. Thus δT can decrease enough at high altitude for cirrus to transition from a "pulse-decay" to a "dynamic equilibrium" regime (Figures 6.3 to 6.5). This would explain why low N_c and high S_o are observed at low temperatures near the tropopause.
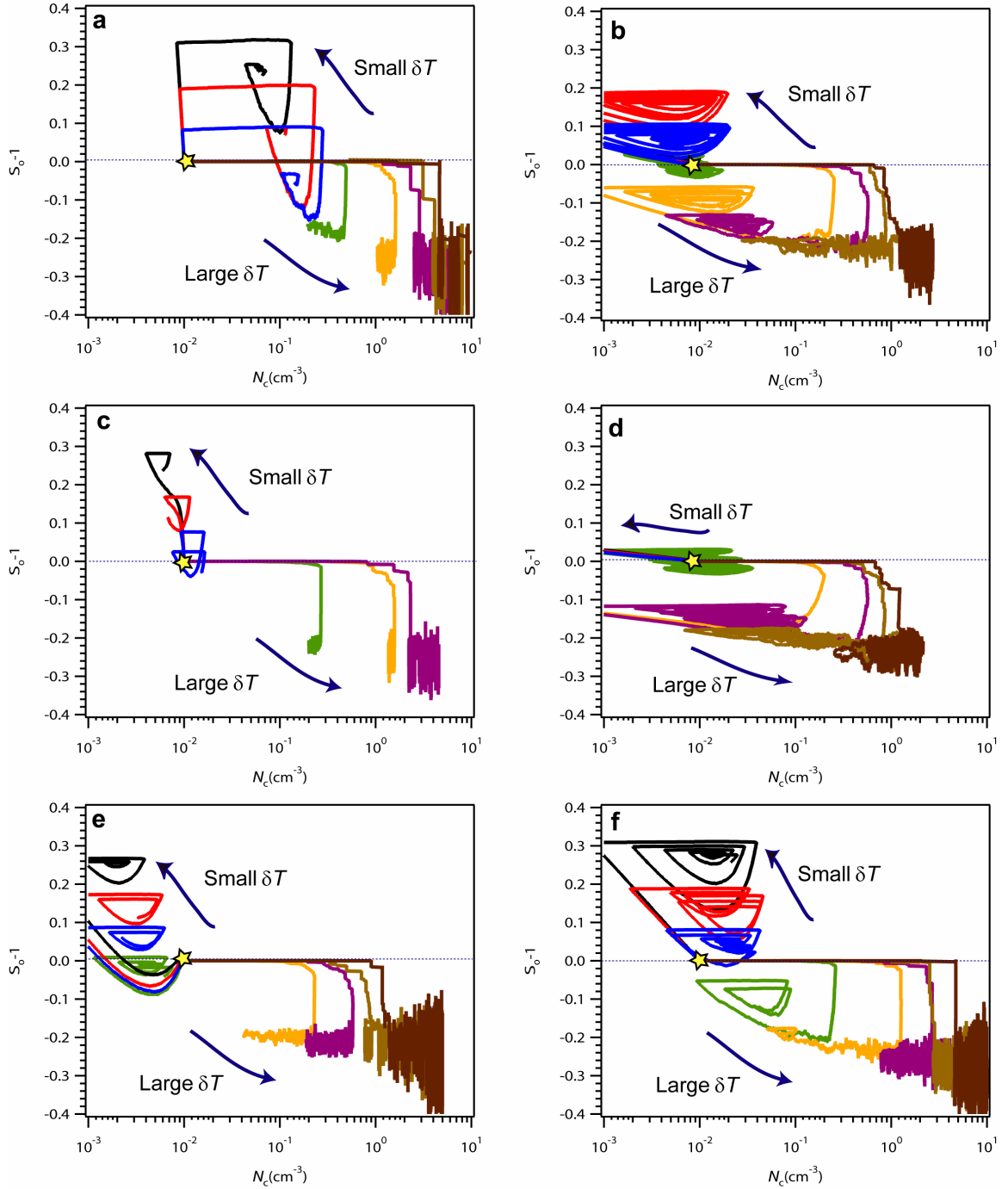
Figure 6.6. Similar to Figure 6.5, but varying cloud mean vertical velocity, $\overline{u}$, initial layer temperature, T_o, cloud thickness ,H, and mean ice crystal terminal velocity, u_{term} . (a) $\overline{u}$ = 5 cm s^{-1}, H = 500 m, T_o =195 K; (b) $\overline{u}$ = 1 cm s^{-1}, H = 500 m, T_o =225 K; (c) $\overline{u}$ =1 cm s^{-1}, H = 5000 m, T_o =195 K; (d) $\overline{u}$ =1 cm s^{-1}, H = 100 m, T_o =225 K; (e) $\overline{u}$ =1 cm s^{-1}, H = 5000 m, T_o =225 K; (f) $\overline{u}$ =1 cm s^{-1}, H = 500 m, T_o =195 K, and u_{term} multiplied by 2.   The yellow star in each plot indicates initial conditions. The integration time was 40 h in for $\overline{u}$ =1 cm s^{-1} and 15 h for $\overline{u}$ =5 cm s^{-1}.

Dynamical equilibrium is also possible at warmer conditions (particularly for high $\bar{u}$; Figure 6.5d) but require small δT; given that high amplitude fluctuations are widespread at lower altitudes [86], cirrus clouds are likely forced to always follow a pulse-decaying behavior.
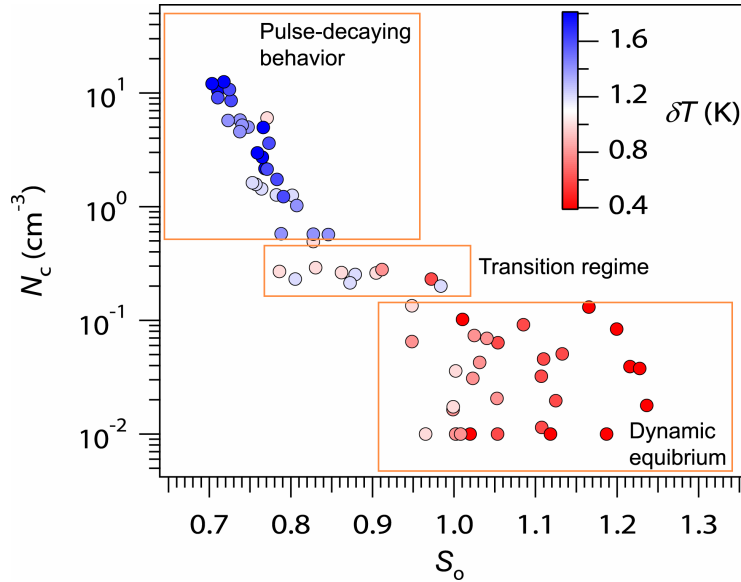
Figure 6.7. Maximum ice crystal concentration obtained during the cloud evolution simulations against the time-averaged mean saturation ratio. Results presented for all simulations carried out in this study. Integration time varied between 15 and 40 h. Symbols are colored by the value of δT used. Regions where the cloud spontaneously transitions to a "pulse-decay" and "dynamic equilibrium" state are noted; the "transitional" region marks where the cloud generally initially exhibited "pulse-decay" behavior over few hours and then transitioned to a "dynamic equilibrium" regime.

6.4. Implications

In summary, cirrus clouds at low temperature exhibit characteristics (e.g., low N_c and high saturation ratios) that cannot be explained with the simple "conventional" picture of homogeneous freezing driven by expansion cooling. The prevailing hypothesis of heterogeneous freezing requires that only weak vertical movement (lower than 10 cm s^{-1})

force the formation of cirrus clouds in the upper troposphere, and therefore cannot alone explain the observed cirrus features in the presence of T fluctuations. We show that small-scale fluctuations from the action of gravity waves can switch a cloud into a previously unknown "dynamic equilibrium" regime, with sustained levels of low N_c and high saturation ratios consistent with "puzzling" characteristics observed in low temperature cirrus. With this study, a new understanding for cirrus clouds emerges, where the "unperturbed" microphysical state is one of dynamical equilibrium with low crystal number and high supersaturation. Only when the mean amplitude of temperature fluctuations exceeds a threshold value ($\delta T > 1$ K at cold temperatures), cirrus exhibit the well-known "pulse-decay" microphysical state. Throughout much of the atmosphere, the latter state dominates, simply because δT is larger than the characteristic threshold value. In the TTL, δT is still remarkably large (0.6-0.8 K) [9, 92], but does not systematically exceed the threshold for "pulse-decay" behavior, so cirrus regress to their "unperturbed" dynamic-equilibrium state. The structure and responses of cirrus to dynamical and microphysical forcing can also be portrayed. For example, cirrus formed in the region of convective anvils might exhibit "pulse-decay" state until gravity-wave fluctuations decay to below the δT threshold and transition to a dynamic-equilibrium state. For the same reasons, IN impacts on cirrus properties can be strong for clouds in pulse-decay state, but not for clouds in dynamic equilibrium. In summary, the discovery of dynamic equilibrium states reshapes our understanding of cirrus clouds and their role in anthropogenic climate change, as the type of dynamical forcing will set these clouds in one of two "preferred" microphysical regimes with very different susceptibility to anthropogenic aerosol.

6.5. Methods

Competition between homogeneous and heterogeneous freezing : Calculation of ice crystal number concentration, N_c in in-situ cirrus from combined homogeneous and heterogeneous freezing in Figure 6.1 is done using an analytical parameterization developed for in situ formed cirrus clouds and freezing fractions below 0.6 [13]. When the calculated freezing fraction exceeds 0.6, a sigmoidal increase in N_c is assumed, in agreement with parcel model simulations and field observations [43, 12]. For combined homogeneous and heterogeneous freezing, it was assumed that the IN freeze instantaneously at a supersaturation freezing threshold, s_{het}, of 15%, typical of deposition mode IN [1] with a 0.1 μm diameter at freezing [62].

Vertical velocity: A spectrum of vertical velocity fluctuations was generated by superimposition of gravity waves from different sources [9, 92] expressed in the form $u = \bar{u} + \sum_j A(\varpi_j) \cos(\varpi_j t + mH + \phi)$ where m is the vertical wave number, H is the cloud thickness, and ϖ_j, $A(\varpi_j)$, and ϕ, are the wave frequency , phase , and amplitude, respectively. For each simulation a time series of u was generated over the frequency interval $\varpi = [3.35 \times 10^{-7}, 9.44 \times 10^{-4}]$ [92] Hz, using randomly generated ϕ and m. $A(\varpi_j)$ was calculated using a power spectrum scaling law of -1.85 for $\varpi_j > 1 \times 10^{-5}$ Hz and of -0.5 for $\varpi_j \leq 1 \times 10^{-5}$ Hz [92]. This procedure resulted in a normal distribution of u (Figure 6.3d) centered around $\bar{u}$. The maximum amplitude was assumed to occur at $\varpi_j = 1 \times 10^{-3}$ Hz [92] as it reproduces the results of Gayet et al. [64] (Figure 6.4 green

line) which give positive u around 0.23 m s^{-1} for $\delta T = 1$ K (i.e., $A(1 \times 10^{-3}) \approx 2.1 \delta T$).

Representative time series for $u(t)$ are presented in Figure 6.8.
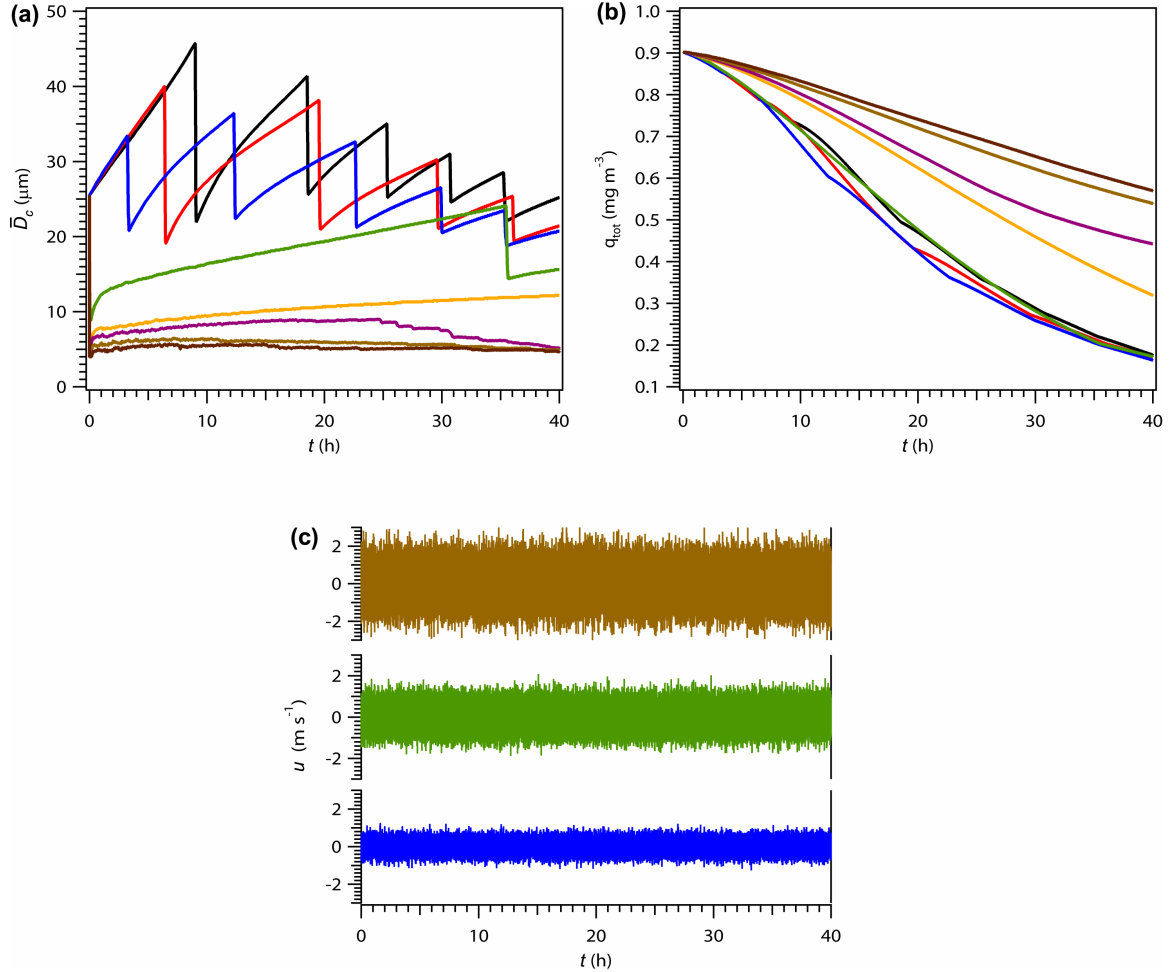
Figure 6.8. Time series of mean ice crystal diameter, $\bar{D}_c$, total water content, q_{tot}, and updraft velocity, u, for the conditions presented in Figure 6.4.

Ice crystal freezing: The freezing timescale, τ_{nuc}, was calculated using the parameterization of *Barahona and Nenes* [12]. Precursor aerosol was assumed to be composed of ammonium sulfate, lognormally distributed with dry mean geometric diameter of 40 nm, geometric dispersion of 2.3, and number concentration of 100 cm^{-3}

168

[138]. To account for possible compositional impacts on crystal growth kinetics, the water-vapor deposition coefficient was varied between 0.006 [156] and 1.0. Homogeneous freezing is described using the parameterization of *Koop et al.* [129]. The term $P_s(S > S_{hom})$ in Table 6.1 is the probability of finding S above S_{hom}, and is introduced to account for the threshold behavior of homogeneous freezing [129, 104]. The effect of preexisting ice crystals on freezing was accounted for by allowing a fraction of N_c to deplete water vapor and increase τ_{nuc} [13]. The fraction of preexisting crystals remaining in freezing zones was calculated as, $f_{ps} = \dfrac{1}{N_c} \displaystyle\int_{D_{min}}^{D_{term}} n(D_c)dD_c$ where $n(D_c)$ is the ice crystal size distribution, D_{min} is the minimum pre-existing crystal size, and D_{term} is the crystal size for which its terminal velocity, u_{term}, is equal to the uplift velocity of the cirrus later, $\bar{u}$. u_{term} was calculated assuming ice crystals have columnar shape with maximum dimension equal to $\bar{D}_c$ [81]. Following *Heymsfield and Platt* [84] it was assumed $n(D_c) = AD_c^{-3.15}$; the parameters A and D_{min} were calculated from the moments of $n(D_c)$: $N_c = \displaystyle\int_{D_{min}}^{\infty} n(D_c)dD_c$ and $\bar{D}_c = \dfrac{1}{N_c} \displaystyle\int_{D_{min}}^{\infty} D_c n(D_c)dD_c$. The calculation of $\bar{D}_c$ is described below. Integration of equations of Table 6.1 was accomplished using a fixed time step of 2 s. Initial values for $N_c = 0.01$ cm^{-3} and $S_o = 1.0$ were set. Using different initial values affected the time required to establish dynamic equilibrium (by a few hours) but did otherwise not affect the simulations.

Ice crystal sedimentation: The rate of ice crystal sedimentation over the cloud scale, H, was assumed proportional to the terminal velocity of the mean crystal size $\bar{D}_c$. (Eq.

(6.26)). Other removal processes (ice crystal sublimation and detrainment) are neglected; H however was varied over a wide interval (100 to 5000 m) to account for the uncertainty associated with neglecting these processes. $\bar{D}_c$ was calculated so that the total water vapor in the layer was partitioned between ice and vapor phases, i.e.,

$$\bar{D}_c = \left(\frac{6q_{ice}}{\pi\rho_i N_c}\right)^{1/3} \text{ where } q_{ice} = q_{tot} - \frac{p^o S_o M_w}{RT} \text{ , } \rho_i \text{ is the ice density [208], } R \text{ is the}$$

universal gas constant, M_w is the molecular mass of water, and p^o is the saturation water vapor pressure over ice [179]. Loss of total water content, q_{tot}, from the cloudy layer is also accounted for by solution of $\dfrac{dq_{tot}}{dt} = -\dfrac{\pi}{6}\rho_i \bar{D}_c^3 \dfrac{dN_c}{dt}\bigg|_{sed}$. Time profiles of $\bar{D}_c$ and q_{tot} are presented in Figure 6.8.

Water vapor deposition and sublimation: Exchange of water vapor between the ice and vapor phases is controlled by the distribution of local saturation ratio, $\dfrac{dP_S\left[S(\delta T, T)\right]}{dS}$ (with upper limit $S = S_{\text{hom}}$), which can be derived from the distribution of temperature fluctuations [105], and by the instantaneous vertical velocity, $u(t)$. The effective saturation ratio, S_{eff}, for condensation/evaporation, was defined using a "Lagrangian trajectory ensemble" approach (Section 6.5.1). From the ensemble averaging of the parcel solutions it was found that sublimation takes place when $u(t) < 0$ and deposition when $u(t) > 0$. S_{eff} is then calculated by averaging $S\dfrac{dP_S}{dS}$ between 1 and S_{hom} for $u(t) > 0$ and between 0 and 1 for $u(t) < 0$ (Table 6.1). The timescale of relaxation, τ_{rel}, was calculated using N_c and $\bar{D}_c$ of the cloud layer.

170

6.5.1. Derivation of the cirrus evolution equations

Supersaturation and crystal number in the cirrus cloud is determined using a "Lagrangian trajectory ensemble" approach. This involves determining the time-dependant state of i homogeneous adiabatic Lagrangian "parcels" that move with a (time-dependant) vertical velocity, u_i; ensemble averaging of the parcel solutions (outlined below) give approximate equations that describe the time-dependant properties for the whole cirrus.

6.5.1.1 Evolution of Saturation Ratio

In the absence of ice nucleation, the rate of change of saturation ratio, S, within the ith Lagrangian parcel is given by [208]

$$\frac{dS_i}{dt} = \alpha u_i S_i - \gamma \int_{D_{min}}^{\infty} D_{c,i}^2 \frac{dD_{c,i}}{dt} n_{c,i}(D_c)dD_c \tag{6.1}$$

where $\alpha = \dfrac{g\Delta H_s M_w}{c_p R T^2} - \dfrac{gM_a}{RT}$ and $\gamma = \dfrac{\rho_i}{\rho_a}\dfrac{\pi}{2}\dfrac{M_a p}{M_w p_i^o}$, ΔH_s is the latent heat of sublimation of water, g is the acceleration of gravity, c_p is the heat capacity of air, p_i^o is the ice saturation vapor pressure at T [179], p is the ambient pressure, M_w and M_a are the molar masses of water and air, respectively, and R is the universal gas constant, ρ_i and ρ_a are the ice and air densities, respectively, and D_c is the volume-equivalent diameter of an ice particle (assuming spherical shape); $n_{c,i}(D_c)$ is the ice crystal size distribution in the ith parcel, and

$$\frac{dD_{c,i}}{dt} = \frac{G(S_i - 1)}{D_{c,i}} \tag{6.2}$$

where $G \approx \left[\dfrac{\rho_i RT}{4 p_i^o D_v' M_w} + \dfrac{\Delta H_s \rho_i}{4 k_a T} \left(\dfrac{\Delta H_s M_w}{RT} - 1 \right) \right]^{-1}$, k_a is the thermal conductivity of air,

D_v is the water vapor diffusion coefficient from the gas to ice phase. Substituting (6.2)

into (6.1) provides after evaluation of the integral,

$$ \frac{dS_i}{dt} = \alpha u_i S_i - \frac{(S_i - 1)}{\tau_{rel,i}} \tag{6.3} $$

where $\tau_{rel,i} = \left(\beta N_{c,i} \bar{D}_{c,i} \right)^{-1}$ is the relaxation time scale in the ith parcel, $\beta = \gamma G$, and, $N_{c,i}$,

$\bar{D}_{c,i}$ are the concentration and mean size of ice crystals in the ith parcel, respectively.

Equation (6.3) provides the supersaturation "state" for every Lagrangian parcel

considered in the ensemble. Knowledge of the distribution of u_i (from the spectrum of

gravity waves in the cirrus) can then be used to "drive" the parcels in the ensemble to

find the resulting distribution of S_i. Averaging is carried out first over all parcels

reaching a given cloud level with vertical velocity u_j (referred to as the "j^{th} cloud

velocity state"), and then averaging over all cloud states. Based on this, the average

saturation ratio, S_o, of the cloud over a time interval Δt is

$$ S_o(t) = \frac{\displaystyle\int_{U(t)} \int_{X(t)} \int_{t-\Delta t/2}^{t+\Delta t/2} S_i(u, \tilde{x}, \tau) P(u, \tilde{x}, \tau) \, du \, d\tilde{x} \, d\tau}{\displaystyle\int_{U(t)} \int_{X(t)} \int_{t-\Delta t/2}^{t+\Delta t/2} P(u, \tilde{x}, \tau) \, du \, d\tilde{x} \, d\tau} \tag{6.4} $$

where u is the vertical velocity, $\tilde{x}$ is a vector that denotes the position in the cloud,

$P(u, \tilde{x}, \tau)$ is the probability at time τ of finding a parcel between position $\tilde{x}$ and $\tilde{x} + d\tilde{x}$

(where $d\tilde{x} = dx\,dy\,dz$), with vertical velocity within u and $u + du$. $U(t)$ and $X(t)$ are the domains of u and $\tilde{x}$, respectively.

Equation (6.4) can be simplified, by considering that fluctuations generated by gravity waves are random in nature (i.e., follow a Gaussian distribution, Figure 6.4d), the distribution of which does not vary with space and time. Hence $P(u,\tilde{x},\tau) \simeq P(u)$ and Eq. (6.4) simplifies to

$$S_o(t) = \frac{\int_{U(t)} \int_{t-\Delta t/2}^{t+\Delta t/2} \int_{X(t)} P(u) S_i(u,\tilde{x},\tau) d\tilde{x}\,d\tau\,du}{V \bar{u} \Delta t} \qquad (6.5)$$

where V, $\bar{u}$ are the volume and average vertical velocity of the cirrus layer, respectively.

Equation (6.5) assumes that S_o is affected by processes that act throughout the volume of the cirrus cloud. Other processes, like entrainment and radiative cooling, are neglected. Although this will not affect the conclusions of our study, they could be included in future studies indirectly through appropriate modification of the vertical velocity distribution [e.g., 11]

Defining $\quad \bar{S}_j = \dfrac{\int_{X(t)} S_i(u = u_j, \tilde{x}, \tau) d\tilde{x}}{\int_{X(t)} d\tilde{x}} = \dfrac{1}{V} \int_{X(t)} S_i(u_j, \tilde{x}, \tau) d\tilde{x} \quad$ as the average

supersaturation of parcels in the "j" velocity state, and assuming that the cloud volume does not change over the interval Δt, Eq. (6.5) can be rewritten as

$$S_o(t) = \frac{\int_{U(t)} \int_{t-\Delta t/2}^{t+\Delta t/2} P(u) \frac{1}{V} \int_{X(t)} S_i(u = u_j, \tilde{x}, \tau) d\tilde{x} d\tau du}{\bar{u} \Delta t}$$

$$= \frac{\int_{U(t)} P(u_j) \int_{t-\Delta t/2}^{t+\Delta t/2} \bar{S}_j d\tau du_j}{\bar{u} \Delta t}$$

(6.6)

the time derivative of which gives,

$$\frac{dS_o}{dt} = \frac{d}{dt} \left\{ \frac{\int_{U(t)} P(u_j) \int_{t-\Delta t/2}^{t+\Delta t/2} \bar{S}_j d\tau du_j}{\bar{u} \Delta t} \right\}$$

(6.7)

$$= \frac{\int_{U(t)} P(u_j) \frac{d}{dt} \left\{ \frac{1}{\Delta t} \int_{t-\Delta t/2}^{t+\Delta t/2} \bar{S}_j d\tau \right\} du_j}{\bar{u}} \simeq \frac{\int_{U(t)} P(u_j) \frac{d\bar{S}_j}{dt} du_j}{\bar{u}}$$

where $\bar{S}_j$ was assumed to vary little over Δt, so that $\frac{1}{\Delta t} \int_{t-\Delta t/2}^{t+\Delta t/2} \bar{S}_j d\tau \simeq \frac{\bar{S}_j}{\Delta t} \int_{t-\Delta t/2}^{t+\Delta t/2} d\tau = \bar{S}_j$.

Based on the definition of $\bar{S}_j$,

$$\frac{d\bar{S}_j}{dt} = \frac{d}{dt} \left\{ \frac{1}{V} \int_{X(t)} S_i(u_j, \tilde{x}, t) d\tilde{x} \right\} \simeq \frac{1}{V} \int_{X(t)} \frac{dS_i(u_j, \tilde{x}, t)}{dt} d\tilde{x}$$

(6.8)

substitution of Equation (6.3) into above provides

$$\frac{d\bar{S}_j}{dt} = \frac{1}{V} \int_{X(t)} \left\{ \alpha u_j S_i - \frac{(S_i - 1)}{\tau_{rel,j}} \right\} d\tilde{x}$$

$$\simeq \alpha u_j \left(\frac{1}{V} \int_{X(t)} S_i d\tilde{x} \right) - \frac{1}{\tau_{rel,j}} \left(\frac{1}{V} \int_{X(t)} (S_i - 1) d\tilde{x} \right)$$

(6.9)

174

where $\tau_{rel,j}$ is assumed to vary much more slowly over space than $\bar{S}_j$, and replaced with

the average relaxation timescale of the jth state. With the above, equation (6.10) becomes

$$\frac{d\bar{S}_j}{dt} = \alpha u_j \bar{S}_j - \frac{(\bar{S}_j - 1)}{\tau_{rel,j}} \tag{6.11}$$

Substituting (6.11) into (6.7) gives,

$$\frac{d\bar{S}_o}{dt} = \frac{1}{\bar{u}} \int_{U(t)} P(u_j) \left\{ \alpha u_j \bar{S}_j - \frac{(\bar{S}_j - 1)}{\tau_{rel,j}} \right\} du_j =$$

$$= \frac{\alpha \int_{U(t)} P(u_j) u_j \bar{S}_j du_j}{\bar{u}} - \frac{\frac{1}{\tau_{rel}} \int_{U(t)} P(u_j) \frac{(\bar{S}_j - 1)}{\tau_{rel,j}} du_j}{\bar{u}} \tag{6.12}$$

$$= \alpha \langle u_j \bar{S}_j \rangle - \left\langle \frac{\bar{S}_j - 1}{\tau_{rel,j}} \right\rangle$$

where quantities in the brackets denote the averages over $P(u_j)$. The first term in

the right hand side of Eq. (6.12) is equal to $\bar{u}S_o$, as in the absence of

deposition/sublimation, S_o in the layer increases exponentially with time [208]. The

second term in the right hand side of Eq. (6.12) can be simplified by considering that

$\tau_{rel,j}$ responds much more slowly to changes in updraft than $\bar{S}_j$ [131],

$$\frac{dS_o}{dt} = \alpha \bar{u} S_o - \frac{\langle \bar{S}_j \rangle - 1}{\langle \tau_{rel,j} \rangle} = \frac{S_o}{\tau_{lift}} - \frac{S_{eff} - 1}{\tau_{rel}} \tag{6.13}$$

where $\tau_{lift} = (\alpha \bar{u})^{-1}$ and S_{eff} is an "effective" saturation ratio for deposition/sublimation

processes, and $\tau_{rel} = (\beta N_c \bar{D}_c)^{-1}$ where N_c and $\bar{D}_c$ ice crystal number concentration and

mean ice crystal size in the cloud layer at time t, respectively. The equality

$$\frac{\langle \overline{S}_j \rangle - 1}{\langle \tau_{rel,j} \rangle} = \frac{S_{eff} - 1}{\tau_{rel}}$$ in Eq. (6.13) is valid if the time step for integration is much smaller

than τ_{lift} $(\sim 10^3\,\mathrm{s})$, which is usually the case.

To estimate S_{eff} in Eq. (6.13) the properties of the different parcels reaching the

cloud layer at t must be considered. For example, if S_i in the ith parcel is a pseudo-steady

state, $\dfrac{dS_i}{dt} \sim 0$ [131] and from Eq. (6.3),

$$S_{i,ss} = \frac{\tau_{lift,i}}{\tau_{lift,i} - \tau_{rel,i}} \tag{6.14}$$

where $\tau_{lift,i} = (\alpha u_i)^{-1}$ and $S_{i,ss}$ is the steady state saturation ratio in the ith parcel. If

$\tau_{lift,i} < 0$ then $S_{i,ss} < 1$, and vice-versa. Thus, if $u_j < 0$, the layer would be instantaneously

subsaturated and vice-versa. Thus, depending on the sign of u_j there is net

deposition/sublimation of water vapor in the cloud layer. Not all parcels however reach

steady state; therefore the degree of saturation/subsaturation associated with the jth state

depends on the probability distribution of saturation within the cloudy layer,

$P_s(S, S_o, \delta T)$, which is a function of S_o and the average amplitude of temperature

fluctuations, δT. Thus, S_{eff} for $u_j < 0$ is found by averaging over all states that would lead

to subsaturation, i.e., $P_s(S, \delta T, S_o)$ for which $S < 1$. Similarly, when $u_j > 0$, the

supersaturated ($S > 1$) region of $P_s(S, \delta T, S_o)$ is used,

$$S_{eff} = \dfrac{\displaystyle\int_a^b S \dfrac{dP_s(S,\delta T,S_o)}{dS} dS}{\displaystyle\int_a^b \dfrac{dP_s(S,\delta T,S_o)}{dS} dS} \tag{6.15}$$

where $a = \begin{cases} 1 & u > 0 \\ 0 & u \le 0 \end{cases}$ and $b = \begin{cases} S_{hom} & u > 0 \\ 1 & u \le 0 \end{cases}$. The homogeneous freezing threshold,

S_{hom}, is set as the upper limit of $P_s(\delta T, S_o)$ as ice crystal production quickly removes

supersaturation above S_{hom} [85, 105]. Table 6.1 summarizes the main equations

describing the evolution of S_o within the cloud layer.

6.5.1.2 Evolution of Ice Crystal Number Concentration

The evolution of the number concentration within a cloudy layer is given by

$$\frac{dN_c}{dt} = \frac{dN_c}{dt}\bigg|_{fr} + \frac{dN_c}{dt}\bigg|_{sed} \tag{6.16}$$

where $\dfrac{dN_c}{dt}\bigg|_{fr}$ is the rate production of ice crystals within the layer, and $\dfrac{dN_c}{dt}\bigg|_{sed}$ is their

sedimentation rate. Ice crystal freezing is a local process and occurs within single parcels

when $S_i > S_{hom}$ and $u_i > 0$. The maximum ice crystal concentration frozen within the ith

parcel is given by [208]

$$N_{c,i} = N_o \left\{ 1 - \exp\left(-\int_0^{t_{max,i}} \overline{v}_o J(S_i) dt \right) \right\} \tag{6.17}$$

where $t_{max,i}$ is the time at which crystal freezing stops, and J is the homogeneous

nucleation rate coefficient and N_o, $\overline{v}_o$ are the deliquesced aerosol number concentration

and average volume, respectively. Taking the time derivative of Eq. (6.17) gives,

$$\left.\frac{dN_{c,i}}{dt}\right|_{fr} = N_o \bar{v}_o J(S_i) \exp\left(-\int_0^{t_{max,i}} \bar{v}_o J(S_i)dt\right) \tag{6.18}$$

which can be approximated by [12]

$$\left.\frac{dN_{c,i}}{dt}\right|_{fr} \approx N_o \bar{v}_o J_{max,i} \exp\left(-\frac{\bar{v}_o}{\alpha u_i}\int_0^{S_{max,i}} J(S_i)dS_i\right) \tag{6.19}$$

where $J_{max,i} = J(S_{max,i})$. $S_{max,i}$ is the maximum saturation ratio reached in the ith parcel, calculated by setting $\frac{dS_i}{dt} = 0$ in Eq. (6.1),

$$S_{max,i} = \frac{\gamma}{\alpha u_i}\int_{\bar{D}_o}^{\infty} D_{c,i}^2 \frac{dD_{c,i}}{dt} n_{i,nuc}(D_c)dD_c \tag{6.20}$$

where $n_{i,nuc}(D_c)$ is the size distribution of the recently nucleated ice crystals, and, $\bar{D}_o$ is the mean size of the deliquesced aerosol. Equation (6.20) assumes that only recently nucleated ice crystals are contained within the parcel. In reality, a fraction of preexisting crystals remain in nucleation zones (typically located near the cloud top [235]) inhibiting the homogeneous freezing of ice. Ice crystals experience gravitational settling, hence only those crystals with terminal velocity, u_{term}, below $\bar{u}$ would be found at the cloud top. Adding the consumption of water vapor from preexisting crystals to the right hand side of Eq. (6.20) gives

$$S_{max,i} = \frac{\gamma}{\alpha u_i}\left[\int_{\bar{D}_o}^{\infty} D_{c,i}^2 \frac{dD_{c,i}}{dt} n_{i,nuc}(D_c)dD_c + \int_{D_{min}}^{D_{term}} D_c^2 \frac{dD_c}{dt} n_c(D_c)dD_c\right] \tag{6.21}$$

where $n_c(D_c)$ is the cloud ice crystal size distribution, D_{term} is the size of the crystal for which $u_{term} = \bar{u}$, and D_{min} is the minimum size of the preexisting crystals in the cloud. Equation (6.21) can be combined with Eq. (6.2) to obtain

$$S_{max,i} = \frac{\gamma}{\alpha u_i}\left[\int_{\bar{D}_o}^{\infty} D_{c,i}^2 \frac{dD_{c,i}}{dt} n_{i,nuc}(D_c, S_{max,i})dD_c + GN_c\bar{D}_c f_{ps}(S_{max,i}-1)\right] \qquad (6.22)$$

where, $f_{ps} = \dfrac{1}{N_c\bar{D}_c}\displaystyle\int_{D_{min}}^{D_{term}} D_c n_c(D_c)dD_c$, is the fraction of preexisting ice crystals remaining in nucleation zones. The analytical solution of Eq. (6.22) is presented elsewhere [13].

The rate of ice crystal production in cloud velocity state j^{th} is given by the concentration of nucleated crystals over the freezing timescale,

$$\left.\frac{dN_{c,j}}{dt}\right|_{fr} = \frac{P_s(S > S_{hom})N_o}{\tau_{fr,j}}H_v(u_j) \qquad (6.23)$$

where $\tau_{fr,j}^{-1} = \bar{v}_o J_{max,j}\exp\left(-\dfrac{\bar{v}_o}{\alpha u_j}\displaystyle\int_0^{S_{max}} J(S_j)dS_j\right)$, $H_v(u_j)$ is the Heaviside function, and $P_s(S > S_{hom})$ represents the fraction of parcels for which $S > S_{hom}$. Using the same averaging procedure as for the saturation equation, we obtain

$$\left.\frac{dN_c}{dt}\right|_{fr} = P_s(S > S_{hom})N_o\left\langle\frac{H_v(u)}{\tau_{fr}}\right\rangle \qquad (6.24)$$

If the time step of integration is much smaller than τ_{fr} (τ_{fr} is usually greater than 10^2 s, Figure 6.3c), then Eq. (6.24) can be approximated by

$$\frac{dN_c}{dt}\bigg|_{fr} \approx P_s(S > S_{\text{hom}})N_o\frac{H_v(u)}{\tau_{fr}} \tag{6.25}$$

Sedimentation processes are not very sensitive to fluctuations in u and a bulk approach can be used. Thus,

$$\frac{dN_c}{dt}\bigg|_{sed} = \frac{1}{H}\int_{D_{\text{min}}}^{\infty} u_{term}(D_c)n(D_c)dD_c \tag{6.26}$$

where H is the cloud layer thickness. As $u_{term} \sim D_c$ [81], Eq. (6.26) can be further simplified to

$$\frac{dN_c}{dt}\bigg|_{sed} = \frac{N_c\bar{u}_{term}}{H} = \frac{N_c}{\tau_{sed}} \tag{6.27}$$

where $\bar{u}_{term} = u_{term}(\bar{D}_c)$.

CHAPTER 7

COMPREHENSIVELY ACCOUNTING FOR THE EFFECT OF GIANT CCN IN CLOUD ACTIVATION PARAMETERIZATIONS[1]

Large cloud condensation nuclei (CCN) (e.g., aged dust particles and sea salt) cannot attain their equilibrium size during the typical timescale of cloud droplet activation. Cloud activation parameterizations applied to aerosol with a large fraction of large CCN often do not account for this limitation adequately and can give biased predictions of cloud droplet number concentration (CDNC). Here we present a simple approach to address this problem that can easily be incorporated into cloud activation parameterizations. This method is demonstrated with activation parameterizations based on the "population splitting" concept of Nenes and Seinfeld (2003); it is shown that accounting for large CCN effects eliminates a positive bias in CDNC where the aerosol dry geometric diameter is greater than 0.5 μm. The method proposed here can also be extended to include the water vapor depletion from pre-existing droplets and ice crystals in global and regional atmospheric models.

---

[1] This chapter appears as reference [18]: BARAHONA, D., WEST, R. E. L., STIER, P., ROMAKKANIEMI, S., KOKKOLA, H. and NENES, A. (2010). Comprehensively Accounting for the Effect of Giant Ccn in Cloud Droplet Activation Parameterizations. *Atmospheric Chemistry and Physics*, 10, 2467-73.

7.1. Motivation

Cloud droplet activation is the direct microphysical link between aerosol and clouds, and its accurate description is essential for studying aerosol indirect climate effects. Sophisticated parameterizations are currently used for describing activation in global circulation models, based on solutions to the coupled mass and energy balance for a Lagrangian cloud parcel [e.g., 2, 34, 189, 58, 168]. Depending on the formulation, effects of the aerosol composition [e.g., 2, 58], adsorption activation [135], mixing and entrainment [11], and mass transfer limitations on droplet growth [58, 168] can explicitly be accounted for.

In accordance with Köhler theory, cloud condensation nuclei (CCN) activate into cloud droplets when the ambient supersaturation is above the global maximum of their equilibrium curve (termed "critical supersaturation") and sufficient time is allowed for their wet size to exceed their critical diameter [230]. Most often, the timescale of equilibration of CCN (up to the point of activation) is shorter than the rate of change of supersaturation in ambient clouds; this gives rise to the assumption that CCN instantaneously equilibrate with their environment. However, droplet growth may be subject to a variety of kinetic limitations, one of which is the so-called "inertial mechanism" [188]. Due to their large dry size, inertially-limited particles, although having very low critical supersaturation, cannot attain their critical size within the timescale typically associated with activation in clouds. Despite this, these particles are comparable in size to strictly activated droplets and can still contribute substantial amounts of liquid water content (LWC) and surface area, particularly in polluted clouds where the supersaturation is very low [25]. Therefore, assuming that all droplets exceed

their equilibrium size at the point of maximum supersaturation tends to overestimate their liquid water content and surface area [32, 188]; parameterizations that neglect these kinetic limitations underestimate cloud droplet number concentration (CDNC) [200].

Including the contribution of inertially-limited CCN in cloud droplet activation parameterizations is not trivial. Ming et al. (2006) proposed the usage of a semi-empirical power law to express growth; although effective, its application in existing parameterization frameworks may not be straightforward. Nenes and Seinfeld (2003) used the concept of "population splitting" to differentiate between particles that activate and those that are inertially-limited. The approach of Twomey (1959) is used for the latter, which works for most atmospheric aerosol and presumes the size of droplets at cloud base is negligible compared to the growth experienced up to the level of maximum supersaturation in the cloud [e.g., 246, 2, 189]. This assumption is subject to increasingly-large error as the dry particle size increases and can lead to significant underestimation in droplet size and surface area if giant CCN are present. Under such conditions, the condensation rate of water vapor is underestimated, which leads to overestimation in maximum supersaturation, s_{max}, and droplet number [11, 135].

This work proposes a new approach to account for the contribution of initially-limited CCN to the condensation surface area in the water vapor balance equations. The application of this method does not require reformulation of a parameterization, and is illustrated using the parameterizations of Nenes and Seinfeld [189] and Fountoukis and Nenes [58].

7.2. Development of the Inertial Effect Correction

Every physically-based droplet formation parameterization conceptually consists of two steps, one involving the determination of the "CCN spectrum" (i.e., the number of CCN that can activate at a given level of supersaturation computed by e.g., Köhler or adsorption activation theory) and one determining the maximum supersaturation, s_{max}, that develops in the ascending parcel. The droplet number concentration is then just the value of the CCN spectrum at s_{max}. The supersaturation in the ascending parcel is determined from [230, 189, 11],

$$\frac{ds}{dt} = \alpha V \left(1 - \frac{e}{e_c}\right) - \gamma \frac{dW}{dt} \tag{7.1}$$

where $\dfrac{dW}{dt}$ is the rate of condensation of liquid water onto the drops, V is the updraft velocity, $\alpha = \dfrac{gM_w \Delta H_v}{c_p RT^2} - \dfrac{gM_a}{RT}$, $\gamma = \dfrac{pM_a}{p^s(T)M_w} + \dfrac{M_w \Delta H_v^2}{c_p RT^2}$, ΔH_v is the latent heat of vaporization of water, g is the acceleration due to gravity, T and T' are the parcel and ambient temperature, respectively, c_p is the heat capacity of air, $p^s(T)$ is the water saturation vapor pressure (over a flat surface) at T, p is the ambient pressure, M_w and M_a are the molar masses of water and air, respectively, and R is the universal gas constant. Homogeneous mixing of dry air is accounted for by using a fractional entrainment rate, e, (for an adiabatic parcel, mixing effects are negligible, i.e., $e = 0$);

$e_c \approx \alpha \left[(1 - RH) - \dfrac{\Delta H_v M_w}{RT^2}(T - T')\right]^{-1}$, is the critical entrainment rate at which

supersaturation is no longer generated in the parcel [11] and RH is the ambient relative humidity. The maximum supersaturation, s_{max}, is found from Eq. (7.1) by setting $\dfrac{ds}{dt} = 0$.

When large CCN are not contributing to droplet number, $\dfrac{dW}{dt}$ at the point of maximum supersaturation in the cloud ascent is denoted as $\left.\dfrac{dW}{dt}\right|_{ps}$, and computed using the parameterization of interest. When inertially-limited CCN dominate $\dfrac{dW}{dt}$, then droplets do not substantially change size from cloud base to the level of s_{max}; the condensation rate in this limit is denoted as $\left.\dfrac{dW}{dt}\right|_{ie}$. When both activated and inertially-limited CCN contribute to condensation, $\dfrac{dW}{dt}$ at the point of maximum supersaturation can be written as

$$\frac{dW}{dt} = \left.\frac{dW}{dt}\right|_{ie} + \left.\frac{dW}{dt}\right|_{ps} \tag{7.2}$$

$\left.\dfrac{dW}{dt}\right|_{ie}$ can be computed from the liquid water content at cloud base in equilibrium with the aerosol particles that would eventually become droplets, i.e.,

$$W|_{ie} = \frac{\pi}{6}\frac{\rho_w}{\rho_a}\left[\int_{\ln D_{p\,min}}^{\infty} D_p^3 n(\ln D_p)\,d\ln D_p\right] \tag{7.3}$$

where $n(D_p)$ is the droplet size distribution, and D_p is their size at saturation. If the aerosol is assumed to follow classical Köhler theory, D_p can be shown to be,

185

$$D_p = \frac{2}{3\sqrt{3}} \frac{A}{s_c}$$
(7.4)

where $A = \dfrac{4\sigma M_w}{RT\rho_w}$, σ is the surface tension of the droplet at saturation, and s_c is the droplet critical supersaturation. D_{pmin} in Eq. (7.3) is the equilibrium diameter, at saturation, of the smallest particle that activates (i.e., for which $s_c = s_{max}$), i.e.,

$$D_{p\min} = \frac{2}{3\sqrt{3}} \frac{A}{s_{\max}}.$$

$\left.\dfrac{dW}{dt}\right|_{ie}$ is calculated taking the time derivative of Eq. (7.3), assuming that the droplet growth rate is given by $\dfrac{dD_p}{dt} = \dfrac{Gs}{D_p}$ [e.g., 189] and the diameter does not change between cloud base and s_{max},

$$\left.\frac{dW}{dt}\right|_{ie} = \frac{\pi}{2} \frac{\rho_w}{\rho_a} Gs \left[\int_{\ln D_{p\min}}^{\infty} D_p n(\ln D_p) d\ln D_p \right]$$
(7.5)

with

$$G = \frac{4}{\dfrac{\rho_w RT}{p^s(T)D_v' M_w} + \dfrac{\Delta H_v \rho_w}{k_a T}\left(\dfrac{\Delta H_v M_w}{RT} - 1\right)}$$
(7.6)

where k_a is the thermal conductivity of air, and D_v' is the water vapor mass transfer coefficient from the gas to droplet phase corrected for non-continuum effects, computed as suggested by Fountoukis and Nenes [2005].

7.2.1. Calculating the Wet Size Distribution of Inertially-Limited CCN

Expressing the critical supersaturation in terms of the dry aerosol properties, Eq. (7.4) can be expressed in terms of the dry size, d_s, as

$$D_p = \left(\frac{B}{A}\right)^{1/2} d_s^{3/2}$$
(7.7)

where $B = \dfrac{\varepsilon_s v M_w}{M_s \rho_w}\left(\dfrac{\varepsilon_s}{\rho_s} + \dfrac{1-\varepsilon_s}{\rho_u}\right)^{-1}$, v is the effective van't Hoff factor, ε_s is the mass fraction of soluble material, and ρ_s and ρ_u are the densities of the soluble and insoluble fractions of the dry particle, respectively. Using Eq.(7.7), the wet size distribution at saturation can be expressed in terms of the dry size distribution as

$$n(\ln D_p) = \frac{dN_d}{d \ln D_p} = \frac{dN_d}{d \ln d_s}\frac{d \ln d_s}{d \ln D_p} = \frac{2}{3}\frac{dN_d}{d \ln d_s}$$
(7.8)

where $N_d = \displaystyle\int_{D_{p\,\min}}^{\infty} n(D_p)dD_p$ is the droplet number concentration.

For a lognormal aerosol representation,

$$\frac{dN_a}{d \ln d_s} = \sum_{i=1}^{n_m} \frac{N_i}{\sqrt{2\pi}\,\ln \sigma_i}\exp\left[-\frac{\ln^2\left(d_s / d_{g,i}\right)}{2\ln^2 \sigma_i}\right]$$
(7.9)

where $d_{g,i}, \sigma_i$ are the geometric mean diameter and standard deviation of mode i, respectively, n_m is the number of lognormal modes, N_a the total aerosol concentration, and N_i is the aerosol concentration of mode i. Substituting Eqs. (7.7) and (7.8) into Eq. (7.9) gives

$$\frac{dN_d}{d \ln D_p} = \sum_{i=1}^{n_m} \frac{2}{3} \frac{N_i}{\sqrt{2\pi} \ln \sigma_i} \exp\left[-\frac{4}{9} \frac{\ln^2\left(D_p / D_{g,i}\right)}{2\ln^2 \sigma_i}\right] \tag{7.10}$$

where $D_{g,i}$ is the equilibrium size of $d_{g,i}$ at saturation given by Eq. (7.7). Substitution of

Eq. (7.10) into Eq. (7.5) gives the condensation rate of inertially-limited CCN at s_{max},

$$\left.\frac{dW}{dt}\right|_{ie} = \frac{\pi}{2} \frac{\rho_w}{\rho_a} Gs_{max} \sum_{i=1}^{n_m} \frac{N_i}{2} D_{g,i} \exp\left(\frac{9}{8} \ln^2 \sigma_i\right) \times$$
$$\text{erfc}\left[\frac{2}{3\sqrt{2}} \frac{\ln(D_{p\min} / D_{g,i})}{\ln \sigma_i} - \frac{3}{2\sqrt{2}} \ln \sigma_i\right] \tag{7.11}$$

Alternatively, Eq. (7.11) can be written in terms of the mean droplet

diameter, $\bar{D}_p = \frac{1}{N_d} \int\limits_{\ln D_{p\min}}^{\infty} D_p n(\ln D_p) d \ln D_p$, as

$$\left.\frac{dW}{dt}\right|_{ie} = \frac{\pi}{2} \frac{\rho_w}{\rho_a} Gs_{max} N_d \bar{D}_p . \tag{7.12}$$

For a sectional aerosol representation,

$$\frac{dN_a}{d \ln d_s} \cong \frac{\Delta N_m}{\Delta \ln d_{s,m}} = \frac{\Delta N_m}{\ln d_{s,m} - \ln d_{s,m-1}} \tag{7.13}$$

where ΔN_m is the number concentration of particles in section m, and, $d_{s,m}$ and $d_{s,m-1}$ are

the "upper" and "lower" dry diameters of the section m, respectively [189]. Substituting

Eqs. (7.7) and (7.8) into (7.13) gives

$$\frac{dN_d}{d \ln D_p} \cong \frac{\Delta N_m}{\Delta \ln D_{p,m}} = \frac{\Delta N_m}{\ln D_{p,m} - \ln D_{p,m-1}} \tag{7.14}$$

where $D_{p,m}$ and $D_{p,m-1}$ are the droplet diameters in equilibrium with $d_{s,m}$ and $d_{s,m-1}$,

respectively. Substitution of Eq. (7.14) into Eq. (7.5) gives,

$$\left.\frac{dW}{dt}\right|_{ie} = \frac{\pi}{2}\frac{\rho_w}{\rho_a}Gs_{max}\sum_{m=i_{max}}^{n_{sec}}D_{p,m}\frac{\Delta N_m}{\Delta \ln D_{p,m}}\Delta \ln D_{p,m} \tag{7.15}$$

where n_{sec} is the total number of sections and $D_{p,m}$ is averaged within section m, and i_{max} is the section that contains s_{max}. Defining the average droplet diameter at the limit where all are kinetically limited as $\bar{D}_p = \frac{1}{N_d}\sum_{m=i_{max}}^{n_{sec}}D_{p,m}\frac{\Delta N_m}{\Delta \ln D_{p,m}}\Delta \ln D_{p,m}$, the condensation rate

$\left.\frac{dW}{dt}\right|_{ie}$ for sectional aerosol can also be expressed in the form of Eq. (7.12).

7.3. Implementing Inertially-Limited CCN Effects: Demonstration for "Population Splitting" Activation Frameworks.

Using the "population splitting" approach of Nenes and Seinfeld [189], $\left.\frac{dW}{dt}\right|_{ps}$ at s_{max} can be written as the sum of two terms,

$$\left.\frac{dW}{dt}\right|_{ps} = \frac{\pi}{2}\frac{\rho_w}{\rho_a}Gs_{max}\left[I_1(0,s_{part}) + I_2(s_{part},s_{max})\right] \tag{7.16}$$

The functions $I_1(0,s_{part})$ and $I_2(s_{part},s_{max})$ are given in Nenes and Seinfeld [189] (hereafter NS03) and Fountoukis and Nenes [58] for sectional and lognormal aerosol representations, respectively. The partition supersaturation, s_{part}, separates two CCN populations, one (expressed by I_2) for which droplets experience negligible growth beyond the critical diameter ($s_c \approx s_{max}$), and one (expressed as I_1) for which droplet growth is much larger than the critical diameter ($s_c \ll s_{max}$). In reality, the large kinetically-limited CCN is a third population, as they have low s_c, but do not reach their critical diameter at the point of s_{max}. Nenes and Seinfeld [189] recognized this, and

postulated (guided by numerical simulations) that the growth experienced by these particles is still substantially larger than their dry diameter, hence can be approximated with I_1. This approximation may not apply for very large and giant CCN; as suggested by Eq. (7.2), a third term, $\left.\dfrac{dW}{dt}\right|_{ie}$, must be added to Eq. (7.16) to account for their effect on the condensation rate.

Combining Eqs. (7.16) , (7.2), and Eq. (7.12) gives for the supersaturation balance at s_{max},

$$\frac{\dfrac{\pi}{2}\dfrac{\rho_w}{\rho_a}Gs_{max}}{\dfrac{\alpha V}{\gamma}\left(1-\dfrac{e}{e_c}\right)}\left\{I_1(0,s_{part})+I_2(s_{part},s_{max})+N_a\left.\overline{D}_p\right|_{s_{part}}\right\}-1=0 \qquad (7.17)$$

$\left.\overline{D}_p\right|_{s_{part}}$ is calculated at s_{part} instead of s_{max} (i.e., $D_{p,min}=\dfrac{2}{3\sqrt{3}}\dfrac{A}{s_{part}}$ in Eqs. (7.11) and (7.15)). This is justified as s_{part} represents the limit between particles that experienced significant growth after activation and those that are kinetically limited [189]. Equation (7.17) constitutes the extension of the population-splitting droplet activation parameterization to include the inertially-limited CCN effects. It is solved iteratively to find s_{max}; cloud droplet number concentration is then calculated from the cumulative CCN spectrum, $F^s(s)$, at s_{max}, [189].

7.4. Comparison against Parcel Model Results

The modified population-splitting activation parameterization is evaluated by comparing predictions of s_{max} and droplet number against simulations with a comprehensive cloud

parcel model (Nenes et al., 2001) for a wide range of updraft velocities and aerosol size distribution characteristics. Initial parcel temperature and pressure were 290 K and 100 kPa, respectively, and the water uptake coefficient was set to 0.06, following the suggestions of Fountoukis et al. (2007). All aerosol particles are assumed to be initially in equilibrium with the surrounding environment at RH = 80%. Consistent with other studies [e.g., 200], using a higher initial RH would result in slightly lower CDNC (mostly within 10%) for updraft velocities lower than 0.1 m s^{-1}. However, varying the initial RH between 60 and 90% causes little CDNC variability (not shown).
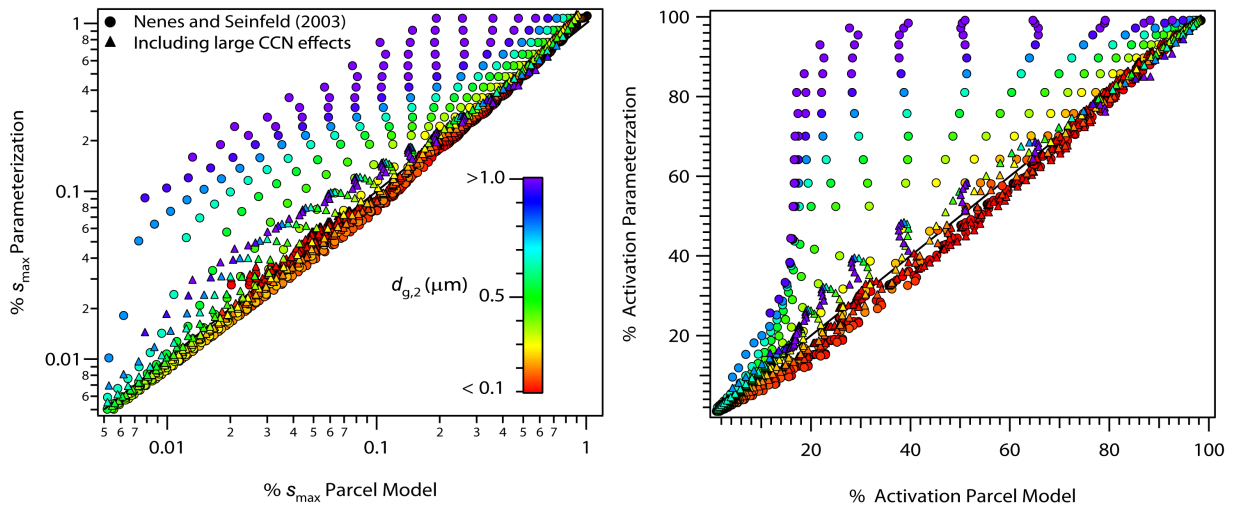
Figure 7.1. Maximum supersaturation (left) and aerosol activation fraction (right) for a bimodal aerosol distribution. Results are from application of the Nenes and Seinfeld [189] parameterization neglecting (circles) and considering (triangles) the effect of kinetic limitations on large CCN. Conditions considered are $N_1 = 2000$ cm^{-3} and $N_2 = 400$ cm^{-3}, $\sigma_1 = \sigma_2 = 1.59$, $d_{g,1} = 0.08\,\mu$m, $T = 290$ K, $p = 100$ kPa, and $\alpha_c = 0.06$. Color coding varies with the geometric mean diameter of the coarse mode. Symbols within the same color vary with updraft speed.

Entrainment reduces supersaturation generation from expansion cooling and reduces s_{max}. Given the wide range of s_{max} seen in the simulations (from the variation in V and aerosol characteristics) varying e is unnecessary; we therefore set $e = 0$ in all simulations presented. After s_{max} is reached, entrainment effects may substantially modify the droplet size distribution [e.g., 209, 141, 238] but these are beyond the scope of this work.

The aerosol is assumed to be pure ammonium sulfate and composed of two lognormal modes, with number concentration $N_1 = 2000$ cm^{-3} and $N_2 = 400$ cm^{-3}, respectively. The geometric dispersion for both modes is set to $\sigma_1 = \sigma_2 = 1.59$; $d_{g,1}$ is set to 0.08 μm. These values were selected as representative of atmospheric aerosol [230]; section 7.5 presents sensitivity runs using different sets of parameters. V was varied over conditions expected in GCM simulations (0.01 to 10 m s^{-1}), and $d_{g,2}$ was varied between 0.005 and 5 μm to represent typical values of recently nucleated particles (< 0.01 μm) and/or giant CCN (> 1 μm) [208].

Parcel model results indicate that at high V (> 5 m s^{-1}) and moderate $d_{g,2}$ (less than 0.1 μm) the activation fraction reaches high values as the s_{max} is sufficient (~ 1%) to activate most CCN. As $d_{g,2}$ increases, significant water vapor depletion by droplets in the coarse mode decreases s_{max}, therefore reducing the activation fraction (mostly in the fine mode). As $d_{g,2}$ becomes substantially large (> 0.5 μm), the activation fraction approaches 16 % (i.e., $N_1/(N_1+N_2)$) as all particles in the coarse mode are activated (i.e., they have $s_c < s_{max}$) but virtually none in the fine mode. At this limit, underestimating the surface area from large CCN overpredicts s_{max} and the activation fraction hence the

droplet concentration, especially for $d_{g,2} > 0.5$ µm (Figure 7.1). This is in agreement with the results of Phinney et al. [200] who showed that neglecting the effect of inertially-limited particles would result in an overestimation in CDNC (as opposed to assuming equilibrium conditions which results in underestimation of CDNC). Accounting for depletion effects from inertially-limited CCN largely corrects this bias (Eq. (7.17)) producing results that are in agreement with the parcel model. Figure 7.1 shows that for $d_{g,2} > 0.5$ µm, significant deviations between the parameterization and the parcel model occur (depicted by circles); which are to a large extent reduced at lower $d_{g,2}$. Application of the large CCN correction for $d_{g,2} > 0.5$ µm significantly reduces the difference in s_{max} between the parameterization and the parcel model (triangles).

7.5. Sensitivity Tests

The sensitivity of the parameterization results to N_1, N_2, σ_2, and the aerosol soluble fraction, ε_s, is presented in 7.2. Repeating the simulations of Figure 7.1 for "clean" conditions, i.e., $N_1 = 100$ cm^{-3} and $N_2 = 50$ cm^{-3} (Figure 7.2, top left panel), tests the robustness of the large CCN correction to aerosol number concentration. NS03 tends to slightly overestimate CDNC [189, 11], particularly at low V (< 0.1 m s^{-1}, hence low activation fractions); the overestimation being larger for $d_{g,2} > 0.5$ µm. Including the effects of large CCN corrects this and CDNC remains mostly within a 10% from the parcel model results.

The sensitivity of CDNC predictions to aerosol composition was assessed by reducing the coarse mode sulfate fraction to 0.4 (Figure 7.2, top right panel). CDNC

predicted by NS03 is within 20% from the parcel model results (with a slightly higher underestimation for $V < 0.1$ m s^{-1}); for $d_{g,2} > 0.5$ μm, NS03 largely overpredicts CDNC. Including large CCN effects corrects this, however, significant overprediction ($> 50\%$) may still result for $d_{g,2} > 1$ μm and $V \sim 0.1$ m s^{-1}, which results from neglecting the contribution of the insoluble core to the saturated wet size , D_p, in Eq. (7.7). Using a modified version of Köhler theory [119] can account for this issue.

Sensitivity tests were carried out for $d_{g,2} = 0.12$ μm, and varying N_2 between 50 and 5×10^4 cm^{-3} (all other conditions similar to Figure 7.1). At low $N_2 \sim 100$ cm^{-3}, an increase in the activation fraction from 10 % to 80% was produced when V increased from 0.1 to 1 m s^{-1} (not shown); at high $N_2 > 10^4$ cm^{-3}, significant activation fractions were found only for $V > 0.5$ m s^{-1}. At these conditions, however, the effect of large CCN was not significant and the NS03 parameterization reproduced the results of the parcel model with a slight underprediction for $N_2 > 1000$ cm^{-3}. Therefore the effect of giant CCN is expected to be negligible, as the surface area of the aerosol particles at cloud base is negligible compared to the surface area of activated droplets; thus significant droplet growth after activation occurs, and the equilibrium size at cloud base is negligible compared to the size after activation. Indeed, no change in CDNC is seen when the inertial correction is included (Figure 7.2, bottom left panel).
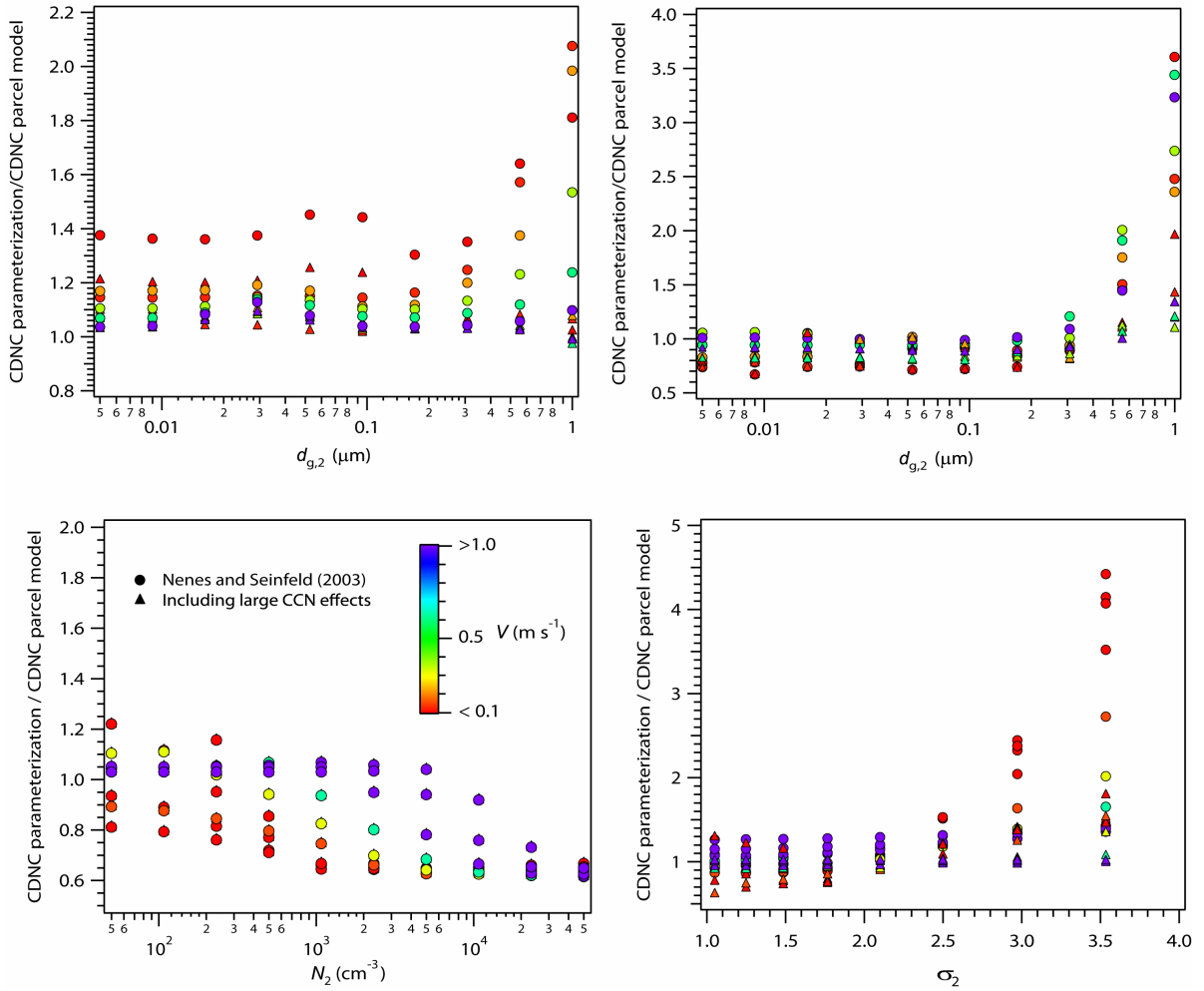
Figure 7.2. CDNC predicted by the parameterization over CDNC predicted by the parcel model as a function of the geometric mean diameter (top panels), aerosol number concentration (bottom left panel) and the geometric dispersion (bottom right panel) of the coarse mode, for a bimodal aerosol distribution. Simulations were performed for $N_1 = 100\,\mathrm{cm^{-3}}$ and $N_2 = 50\,\mathrm{cm^{-3}}$ (top, left panel), $\varepsilon_s = 0.4$ (top, right panel), $d_{g,2} = 0.12$ μm, $\sigma_1 = \sigma_2 = 1.59$ (bottom, left panel), $d_{g,1} = 0.08$ μm, $d_{g,2} = 0.12$ μm, $\sigma_1 = 1.59$ (bottom, left panel). All other conditions are similar to Figure 7.1. Color coding varies with updraft speed.

A final sensitivity test was carried out for $d_{g,2} = 0.12$ μm, $N_2 = 400$ cm^{-3} and varying σ_2

between 1.05 and 3.5 (all other conditions similar to Figure 7.1). Including the effect of

kinetically-limited CCN for $\sigma_2 > 2.5$ significantly reduces the activated fraction (Figure 7.2, bottom right panel) (since a substantial fraction of aerosol are giant CCN) and the predicted CDNC shows good agreement with parcel model results. In all sensitivity tests, the effects of kinetically-limited CCN were much more pronounced when $d_{g,2}$ was increased to values over 0.5 µm, which is also evident in Figure 7.1.

The CDNC assessment was repeated for the lognormal aerosol activation parameterization of Fountoukis and Nenes [58], using Eq. (7.11) to calculate $\left.\overline{D}_p\right|_{s_{part}}$; the calculated activated fraction was within 1% of the results using the sectional formulation of Nenes and Seinfeld [189]. Finally, for all the runs carried out in this study, including the correction for kinetically-limited CCN had a minor impact on computational time (2% and 7% increase for the sectional and lognormal versions of the parameterization, respectively).

7.6. Conclusions

When a significant fraction of large CCN are present during cloud formation (i.e., droplets which at the point of maximum supersaturation in a cloud updraft have not experienced significant growth compared to cloud base), their contribution to the droplet surface area must correctly be accounted for in parameterizations to avoid biases in maximum supersaturation and droplet number. A general correction is proposed for droplet activation parameterizations, where the condensation upon inertially-limited droplets is added to the "default" expression in the parameterization of interest. The correction was incorporated into the Nenes and Seinfeld [189] and Fountoukis and Nenes [58] parameterizations and tested for a wide range of conditions. Results show that

196

incorporation of the correction greatly improved the parameterization performance for conditions where inertially-limited CCN dominate droplet formation, without significant impact on the computational burden of the parameterization. The approach outlined here can easily be extended to include adsorption activation of mineral dust (Kumar et al., 2009). It can also be applied to account for the water vapor depletion from pre-existing droplets and ice crystals during secondary activation events in convective updrafts, by appropriately modifying the growth constant and size distribution in Eq. (7.12) [e.g., 14]. The approach outlined here is a simple way to account for some of the prediction biases in regions strongly influenced by dust [e.g., 207] and large sea salt particles [e.g., 190].

CHAPTER 8

PARAMETERIZATION OF CLOUD DROPLET FORMATION IN LARGE SCALE MODELS: INCLUDING EFFECTS OF ENTRAINMENT[1]

This work offers for the first time a comprehensive parameterization suitable for large scale models which is robust, computationally efficient, and from first principles links chemical effects, aerosol heterogeneity and entrainment with cloud droplet formation. The parameterization is based on the entraining ascending parcel model framework; mixing of outside air is parameterized in terms of a per-length entrainment rate. The integration of the droplet growth is done using the "population splitting" concept of Nenes and Seinfeld. Formulations for lognormal and sectional aerosol representations are given, as well as simplifications that allow the treatment of entrainment with high computational efficiency without loss of accuracy. The concept of "critical entrainment", a value beyond which droplet activation is not favored, is introduced and shown that it is important for defining *i*) whether or not entrainment effects have an impact on droplet formation, and, *ii*) the characteristic temperature and pressure for cloud droplet formation. The performance of the parameterization was evaluated against a detailed numerical parcel model over a comprehensive range of droplet formation conditions. The

---

agreement is always very good (mean relative error 2.3% ± 21%); errors tend to increase as entrainment approaches the critical value, but are never above 40%.

8.1. Motivation

Atmospheric aerosols strongly impact the radiative balance of the earth. They can either scatter and absorb thermal and solar radiation ("direct effect") or alter the radiative properties and global distribution of clouds ("indirect effect") [248, 4, 3, 151]. The increase in cloud albedo from increases in cloud condensation nuclei, CCN, is commonly termed the "first indirect" or "Twomey" effect [248]. Assessment of the first indirect effect requires the detailed description of the droplet formation process by activation of precursor aerosols (CCN). The ability of an aerosol to act as a CCN is controlled by its physicochemical properties [208]; thus, the aerosol size distribution and mixing state, the solubility and hygroscopicity of the aerosol components, the presence of soluble gases, the formation of surfactant layers that can change surface tension and water vapor uptake rate, as well as other mass transfer limitations (such as dissolution kinetics [7]) play an important role in the formation of new droplets [160]. Besides these factors, the dynamical (e.g., updraft velocity, mixing and cooling by entrainment) and thermodynamical state (temperature, pressure, relative humidity) of the cloudy air mass profoundly impact the droplet formation process [208].

Cloud droplet formation is simulated by solving a system of ordinary differential equations that represent the condensational growth of CCN coupled with conservation of heat and water vapor mass in an ascending air parcel [e.g., 208, 188, 232]. Although this theory is well established, the computational burden associated with its solution precludes its application in large-scale general circulation models (GCMs). Instead, droplet

activation is calculated from computationally efficient parameterizations whose sophistication ranges from empirical correlations (relating aerosol mass or number concentration and cloud droplet number concentration) [21, 73] to physically-based prognostic representations of the activation physics [53, 2, 34, 189, 58, 168].

All physically-based parameterizations developed to date rely on the assumption that the droplet formation is an adiabatic process (with the exception of Feingold and Heymsfield [53] who discuss how to include entrainment); thus conditions at cloud base uniquely determine the number of CCN that activate. Adiabaticity considerably simplifies the equations for cloud droplet formation so they can be solved analytically (or approximated by semi-empirical correlations). However, entrainment during the parcel ascent may influence its temperature and cloud liquid water content; entrainment decreases cloud droplet number relative to adiabatic conditions [209, 202, 100]. After activation, the droplet spectra can be further modified by evaporation and mixing, with important implications for the cloud characteristics [191, 219, 201, 100, 208, 238]. The importance of entrainment is corroborated by in-situ observations which mostly show that the liquid water content measured is lower than expected by adiabaticity [192, 22, 232, 37, 67, 165, 193]. Neglecting entrainment may therefore lead to an overestimation of in-cloud droplet number and an underestimation of droplet spectral width, which if used in large scale models, may bias indirect effect assessments. Despite its complexity, developing a physically-based prognostic parameterization that can explicitly treat entrainment would be a powerful tool to study aerosol-cloud interactions within large-scale models, and is the objective of this study. The new parameterization is based on the frameworks of Nenes and Seinfeld [189] and Fountoukis and Nenes [58], where kinetic

limitations, slow water vapor accommodation, and "chemical effects" are explicitly treated. Two formulations are presented, one for sectional and one for lognormal aerosol representation.

8.2. Description of the Parameterization

Calculation of cloud droplet number concentration is accomplished in three steps. First, the critical entrainment rate, e_c, (the entrainment required to completely prevent activation), and the characteristic temperature and pressure for droplet formation are computed. Afterwards, aerosol size distribution/chemical composition information is used to compute the "CCN spectrum" (the concentration of CCN as a function of cloud maximum supersaturation, s_{max}). Then s_{max} and droplet number, N_d, are computed.

8.2.1. Representation of the CCN Spectrum

Two representations of the aerosol size distribution and chemical composition are used to represent the CCN spectrum: the "sectional" and "lognormal" representations. The first is a "sectional representation", in which the aerosol size distribution is divided into an arbitrary number of size classes (sections) each with a uniform profile of aerosol number concentration and chemical composition between its boundaries [189]. Using Köhler theory [230], the aerosol size distribution is mapped onto supersaturation space to obtain the critical supersaturation distribution function, $n^s(s)$,

$$n^s(s) = \frac{dN}{ds} = \frac{N_i}{s_{c,i} - s_{c,i-1}} \qquad s_{c,i} < s < s_{c,i-1} \qquad (8.1)$$

where N_i is the aerosol number concentration of section i, s is supersaturation, and $s_{c,i}$ and $s_{c,i-1}$ represent the lower and upper bounds of each supersaturation bin, respectively. The "CCN spectrum", $F^s(s)$, is obtained by integration of Eq. (8.1) from $s'=0$ to $s'=s$

$$F^s(s) = \sum_{l=1}^{k} \int_0^s n_l^s(s') ds' = \sum_{l=1}^{k} \left[\sum_{j=1}^{i(l)-1} N_{j,l} + N_{i(l),l} \left(\frac{s - s_{c,i(l)-1}^l}{s_{c,i(l)}^l - s_{c,i(l)-1}^l} \right) \right] \tag{8.2}$$

where $s_{c,i}^l$ and $s_{c,i-1}^l$ are the critical supersaturations for the boundaries of section i, and population l. The sectional representation provides the most general description of the aerosol size distribution, as it can describe the presence of externally or internally mixed aerosol populations [189].

In the "lognormal representation", we assume each lognormal population mode has a uniform chemical composition and the aerosol follows a lognormal size distribution. Following Nenes and Fountoukis [58], $n^s(s)$ and $F^s(s)$, are given by,

$$n^s(s) = \frac{dN}{ds} = \sum_{i=1}^{n_m} \frac{2 N_i}{3 s \sqrt{2\pi} \ln \sigma_i} \exp \left[-\frac{\ln^2 \left(s_{g,i} / s \right)^{2/3}}{2 \ln^2 \sigma_i} \right] \tag{8.3}$$

$$F^s(s) = \int_0^s n^s(s') ds' = \sum_{i=1}^{n_m} \frac{N_i}{2} erfc \left[-\frac{2 \ln \left(s_{g,i} / s \right)}{3\sqrt{2} \ln \sigma_i} \right] \tag{8.4}$$

where σ_i is the geometric standard deviation for lognormal mode i, $s_{g,i}$ is the critical supersaturation of a particle with a diameter equal to the geometric mean diameter of the mode i, and n_m is the number of lognormal modes in the population.

If the maximum supersaturation, s_{max}, in the cloud parcel is known, then the maximum activated droplet number N_d, is given by

$$N_d = F^s(s_{max})$$
(8.5)

8.2.2. Calculation of s_{max}

The rate of change of water vapor supersaturation, s, in a homogenously mixed entraining parcel ascending with constant velocity V, can be written as [230]

$$\frac{ds}{dt} = \alpha V + \gamma \frac{dw}{dt} + eV\left(\frac{\Delta H_v M_w}{RT^2}\right)\left[\frac{\Delta H_v}{c_p}(w - w') + (T - T')\right]$$
(8.6)

where, $\alpha = \dfrac{gM_w \Delta H_v}{c_p RT^2} - \dfrac{gM_a}{RT}$, $\gamma = \dfrac{pM_a}{p^s(T)M_w} + \dfrac{M_w \Delta H_v^2}{c_p RT^2}$, ΔH_v is the latent heat of vaporization of water, g is the acceleration of gravity, T and T' are the parcel and ambient temperatures, respectively, c_p is the heat capacity of air, $p^s(T)$ is the water saturation vapor pressure at T, p is the ambient pressure, M_w and M_a are the molar masses of water and air, respectively, e is the entrainment rate (m^{-1}), w and w' are the water vapor mixing ratios in the parcel and in the ambient, respectively, and R is the universal gas constant. The water mass balance in the entraining parcel is [208, 230]

$$\frac{dw}{dt} = -\frac{dW}{dt} - eV(w + W - w')$$
(8.7)

where W is the liquid water mixing ratio in the parcel, and $\dfrac{dW}{dt}$ is the rate of condensation of liquid water onto the drops. Using Eq. (8.7) and assuming $1+s \approx 1$, Eq. (8.6) can be written as

$$\frac{ds}{dt} = \alpha V - \gamma \left[\frac{dW}{dt} + eVW \right] + eV \left[\frac{\Delta H_v M_w}{RT^2} (T - T') - (1 - RH) \right] \qquad (8.8)$$

where *RH* is the ambient fractional relative humidity. The first term in the right hand side of Eq. (8.8) represents the tendency of supersaturation to increase from expansion (cooling); the second term expresses the decrease of supersaturation from depletion of water vapor by condensational growth of water droplets and by entrainment of liquid water during the parcel ascent. The third term is the combined effect of entraining dry air, where cooling from mixing at *T'* tends to increase the supersaturation, and mixing with subsaturated dry air decreases *s*.

The use of the entrainment rate to parameterize mixing implies a constant aerosol mixing ratio during the parcel ascent where the entrained aerosol have the same properties of the pre-cloud aerosol; the short time scale of cloud formation precludes significant transformation or ageing of the aerosol during the activation event [238]. Although a simplification, it is more realistic than adiabatic activation (which is what all current physically-based parameterizations employ). The extension of our formulation to include such as chemistry and vertically heterogeneous aerosol mixing is certainly possible, but beyond the scope of this manuscript.

By definition, the liquid water mixing ratio, *W*, is [208]

$$W = \frac{\pi}{6} \frac{\rho_w}{\rho_a} \int_0^{s_{max}} D_p^3 \, n(s') ds' \qquad (8.9)$$

where ρ_w and ρ_a are the liquid water and air densities, respectively, and D_p is the droplet wet diameter. From Eq. (8.9), the rate of water condensation on the droplet population is obtained,

$$\frac{dW}{dt} = \frac{\pi}{2}\frac{\rho_w}{\rho_a}\int_0^{s_{max}} D_p^2 \frac{dD_p}{dt} n(s')ds' \tag{8.10}$$

neglecting curvature effects, Eq. (8.10) can be written as [246, 189]

$$\frac{dW}{dt} = \frac{\pi}{2}\frac{\rho_w}{\rho_a}Gs_{max}\int_0^{s_{max}}\left(D_p^2(\tau) + 2G\int_\tau^{t_{max}} s(t)dt \right)^{1/2} n(s')ds' \tag{8.11}$$

with

$$G = \frac{4}{\dfrac{\rho_w RT}{p^s(T)D_v'M_w} + \dfrac{\Delta H_v \rho_w}{k_a T}\left(\dfrac{\Delta H_v M_w}{RT} - 1 \right)} \tag{8.12}$$

where k_a is the thermal conductivity of air, D'_v is the water vapor mass transfer coefficient from the gas to droplet phase corrected for non-continuum effects, computed as suggested by Fountoukis and Nenes[58], τ represents the time at which the parcel supersaturation exceeds the CCN critical supersaturation; for CCN that instantaneously activate, $D_p(\tau)$ is equal to the CCN critical diameter, $D_c = \dfrac{A}{s_c}$ (where $A = \dfrac{4\sigma M_w}{\rho_w}$, and σ is the surface tension of the droplet at the point of activation [188]). The maximum supersaturation, s_{max}, controls the total number of droplets that can form and is computed from Eq. (8.8) by setting $\dfrac{ds}{dt} = 0$. Integrating Eq. (8.11) and substituting in Eq. (8.8) one obtains at s_{max},

$$\frac{\alpha V + eV\left[\dfrac{\Delta H_v M_w}{RT^2}(T - T') - (1 - RH) \right]}{\gamma \dfrac{\pi}{2}\dfrac{\rho_w}{\rho_a}} - I_e(0, s_{max}) = 0 \tag{8.13}$$

where the second term in Eq. (8.13) is known as the "condensation integral" [189],

$$I_e(0, s_{max}) = Gs_{max} \int_0^{s_{max}} \left(D_p^2(\tau) + 2G \int_\tau^{t_{max}} s(t)dt \right)^{1/2} n(s')ds' +$$
$$\frac{eV}{3} \int_0^{s_{max}} \left(D_p^2(\tau) + 2G \int_\tau^{t_{max}} s(t)dt \right)^{3/2} n(s')ds' \tag{8.14}$$

If $I_e(0, s_{max})$ is known, Eq. (8.13) can be solved for s_{max}.

The condensation integral, Eq. (8.14), can be simplified, as the term eVW in Eq. (8.8) in many cases can be neglected. Simulations suggest (not shown) that this simplification can be applied when in-cloud $s_{max} < 0.8\%$ and $e < 0.1e_c$; Eq. (8.8) then reduces to

$$\frac{ds}{dt} = \left\{ \alpha + e \left[\frac{\Delta H_v M_w}{RT^2}(T - T') - (1 - RH) \right] \right\} V - \gamma \left[\frac{dW}{dt} \right] \tag{8.15}$$

and $I_e(0, s_{max})$ would simplify to:

$$I_e(0, s_{max}) = Gs_{max} \int_0^{s_{max}} \left(D_p^2(\tau) + 2G \int_\tau^{t_{max}} s(t)dt \right)^{1/2} n(s')ds' \tag{8.16}$$

This simplified representation of entrainment is equivalent to using the adiabatic formulation of the parameterization after modifying the factor α in the expansion cooling term to include entrainment effects, i.e.,

$$\alpha = \frac{gM_w \Delta H_v}{c_p RT^2} - \frac{gM_a}{RT} + e \left[\frac{\Delta H_v M_w}{RT^2}(T - T') - (1 - RH) \right].$$

8.2.3. Computing the Condensation Integral $I_e(0, s_{max})$

The "population splitting" concept of Nenes and Seinfeld [2003] can be used to approximate $I_e(0, s_{max})$ as the sum of two terms,

$$I_e(0, s_{max}) = I_{e,1}(0, s_{part}) + I_{e,2}(s_{part}, s_{max}) \tag{8.17}$$

where $I_{e,1}(0, s_{part})$ represents the growth of CCN that either do not strictly activate or experience significant growth beyond their critical diameter [189], so that $D_p^2(\tau) << 2G\int_\tau^{t_{max}} s(t)dt$; $2G\int_\tau^{t_{max}} s(t)dt$ can be evaluated using Twomey's lower bound [246] which after substitution gives for $I_{e,1}(0, s_{part})$,

$$I_{e,1}(0, s_{part}) = \left(\frac{G}{\alpha V}\right)^{1/2} \int_0^{s_{part}} \left(s_{max}^2 - s^2\right)^{1/2} \left(Gs_{max} + \frac{eG}{3\alpha}\left(s_{max}^2 - s^2\right)\right) n(s')ds' \quad (8.18)$$

$I_{e,2}(s_{part}, s_{max})$ represents the growth of CCN that are recently activated and have not grown significantly beyond their critical diameter, i.e., $D_p^2(\tau) >> 2G\int_\tau^{t_{max}} s(t)dt$. With this, and assuming $D_p(\tau) = D_c$, $I_{e,2}(s_{part}, s_{max})$ can be written as

$$I_{e,2}(s_{part}, s_{max}) = \frac{2}{3} \int_{s_{part}}^{s_{max}} \frac{A}{s} \left(Gs_{max} + \frac{eV}{3}\left(\frac{2A}{3s}\right)^2\right) n(s')ds' \quad (8.19)$$

The "partitioning critical supersaturation", s_{part}, separates the two CCN populations expressed by Eq. (8.17), and is calculated using the "descriminant criterion"[189], i.e., the sign of $\Delta = \left(s_{max}^4 - \frac{16A^2\alpha V}{9G}\right)$. $\Delta > 0$ indicates a droplet growth regime primarily free from kinetic limitations, and $\Delta < 0$ a regime where kinetic limitations are dominant [189].

When $\Delta \geq 0$, s_{part} is given by $s_{part} = s_{max}\left\{\frac{1}{2}\left[1 + \left(1 - \frac{16A^2\alpha V}{9Gs_{max}^4}\right)^{1/2}\right]\right\}^{1/2}$; when $\Delta < 0$, s_{part} is

calculated using $s_{part} = s_{max} \min\left\{\frac{2\cdot 10^7 A}{3} s_{max}^{-0.3824}, 1.0\right\}$ [189].

8.2.3.1 $I_e(0, s_{max})$ for lognormal aerosol

For lognormal aerosol, substitution of Eq.(3) into equations (16) and (17), and approximating $\left(1 - s_{g,i} \middle/ s_{part}\right)^{1/2} \approx \left(1 - \frac{1}{2}\frac{s_{g,i}}{s_{part}}\right)$ gives,

$$I_{e,1}(0, s_{part}) = \left(\frac{G}{\alpha V}\right)^{1/2}\frac{N_i}{2}\left\{Gs_{max}\left[erfc(u_{part}) - \frac{1}{2}\left(\frac{s_{g,i}}{s_{max}}\right)^2\exp\left(\frac{9\ln^2\sigma_i}{2}\right)erfc\left(\frac{3}{\sqrt{2}}\ln\sigma_i + u_{part}\right)\right] + \right.$$
$$\left(\frac{eG}{3\alpha}\right)\left[s_{max}^2 erfc(u_{part}) + \frac{1}{2}s_{g,i}^2\left(\frac{s_{g,i}}{s_{max}}\right)^2\exp\left(\frac{27\ln^2\sigma_i}{2}\right)erfc(3\sqrt{2}\ln\sigma_i + u_{part}) - \right.$$
$$\left.\left. s_{g,i}^2 erfc\left(\frac{3}{\sqrt{2}}\ln\sigma_i + u_{part}\right)\left(Gs_{max} + \frac{eGs_{max}^2}{3\alpha} + \frac{1}{2}\right)\right]\right\}$$

$$(8.20)$$

$$I_{e,2}(s_{part}, s_{max}) = \frac{N_i A_i}{3s_{g,i}}\left\{Gs_{max}\exp\left(\frac{9\ln^2\sigma_i}{8}\right)\left[erf\left(u_{part} - \frac{3\ln\sigma_i}{2\sqrt{2}}\right) - erf\left(u_{max} - \frac{3\ln\sigma_i}{2\sqrt{2}}\right)\right] + \right.$$
$$\left.\left(\frac{eV}{3}\right)\left(\frac{2A_i\ln^2\sigma_i}{3s_{g,i}}\right)^2\exp\left(\frac{81\ln^2\sigma_i}{8}\right)\left[erf\left(u_{part} - \frac{9\ln\sigma_i}{2\sqrt{2}}\right) - erf\left(u_{max} - \frac{9\ln\sigma_i}{2\sqrt{2}}\right)\right]\right\}$$

$$(8.21)$$

where,

$$u_{part} = \frac{\ln\left(s_{g,i}\middle/ s_{part}\right)^2}{3\sqrt{2\ln\sigma_i}}, \qquad u_{max} = \frac{\ln\left(s_{g,i}\middle/ s_{max}\right)^2}{3\sqrt{2\ln\sigma_i}} \qquad (8.22)$$

If no entrainment is present, (i.e. $e=0$) the parcel is adiabatic and Eqs. (8.20) and (8.21) reduce to the solution of Fountoukis and Nenes [58].

8.2.3.2 $I_e(0, s_{max})$ for sectional aerosol

For the sectional representation, Eq. (8.1) is substituted in Eqs. (8.18) and (8.19), to obtain

$$I_{e,1}\left(0, s_{part}\right)=\left(\frac{G}{\alpha V}\right)^{1/2}\sum_{j=1}^{i_{part}}\frac{N_j}{s_{c,j}-s_{c,j-1}}\left\{\frac{Gs_{max}}{2}\left[x\left(s_{max}^2-x^2\right)+s_{max}^2\sin^{-1}\left(\frac{x}{s_{max}}\right)\right]+\right.$$
$$\left.\left(\frac{eG}{24\alpha}\right)\left[x\left(5s_{max}^2-2x^2\right)\left(s_{max}^2-x^2\right)^{1/2}+3s_{max}^4\sin^{-1}\left(\frac{x}{s_{max}}\right)\right]\right\}\bigg|_{x=s_c^{j-1}}^{x=s_c^j}$$

(8.23)

$$I_{e,2}\left(s_{part}, s_{max}\right)=\sum_{j=i_{part}}^{i_{max}-1}\left[\frac{2Gs_{max}}{3}\ln\left(\frac{s_{c,j}}{s_{c,j-1}}\right)\left(\frac{N_j A_j}{s_{c,j}-s_{c,j-1}}\right)+\frac{4eV}{81}\left(\frac{1}{s_{c,j-1}^2}-\frac{1}{s_{c,j}^2}\right)\left(\frac{N_j A_j^3}{s_{c,j}-s_{c,j-1}}\right)\right]+$$
$$\frac{2Gs_{max}}{3}\ln\left(\frac{s_{max}}{s_{c,i_{max}-1}}\right)\left(\frac{N_{i_{max}} A_{i_{max}}}{s_{c,i_{max}}-s_{c,i_{max}-1}}\right)+\frac{4eV}{81}\left(\frac{1}{s_{c,i_{max}-1}^2}-\frac{1}{s_{max}^2}\right)\left(\frac{N_{i_{max}} A_{i_{max}}^3}{s_{c,i_{max}}-s_{c,i_{max}-1}}\right)$$

(8.24)

where i_{part} and i_{max} are the sections that bound s_{part} and s_{max}, respectively. When no entrainment is considered, Eqs. (8.23) and (8.24) reduce to the solution of Nenes and Seinfeld [189] for adiabatic conditions. Depending on the aerosol formulation used, s_{max} is calculated by substituting Eqs. (8.20) and (8.21), or (8.23) and (8.24), in Eq. (8.17) and then into Eq. (8.13), which is then solved using the bisection method. Using s_{max}, N_d is computed from Eq. (8.5).

8.2.4. Critical Entrainment Rate

Entrainment reduces s_{max} (hence, N_d) achieved during cloud formation. Therefore, a "critical entrainment rate", e_c, must exist, above which mixing of outside air prevents supersaturation and cloud droplet formation. If e is below e_c, supersaturation develops and CCN activate into cloud droplets. e_c is therefore a bound between two regions: one that forms a cloud, (where $s > 0$ and there is a maximum in the supersaturation profile for

finite time), and another where $s < 0$ and no maximum supersaturation is reached. For $e >$ e_c, s is always negative; at e_c, $s_{max} = 0$ and $\frac{ds}{dt} = 0$ are reached at a finite time (Figure 8.1).
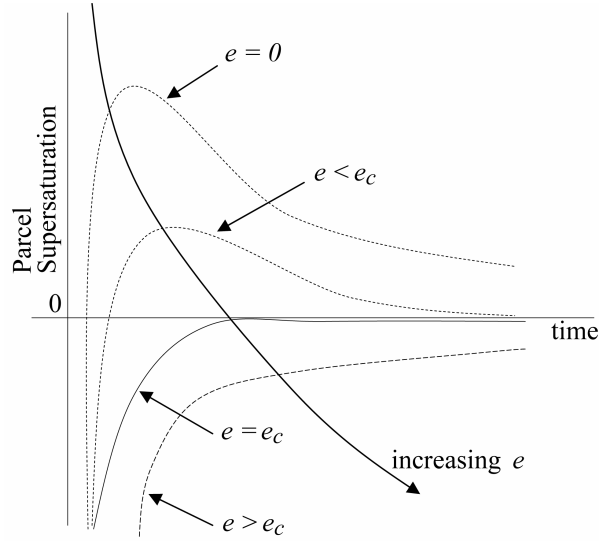
Figure 8.1. Sketch of parcel supersaturation vs. time for different values of e.

The critical entrainment rate can be calculated from Eq. (8.8). Since at e_c, $s_{max} = 0$, then neglecting any water vapor condensation from the aerosol particles before supersaturation gives $\frac{dW}{dt} \approx 0$. At these conditions, $\frac{ds}{dt} = 0$ is reached when water availability from cooling via expansion and mixing at T', balance the depletion from mixing with subsaturated air. With this, Eq. (8.8) can be solved for e_c to give

$$e_c = \frac{\alpha}{(1-RH) - \frac{\Delta H_v M_w}{RT^2}(T-T') + \gamma W} \tag{8.25}$$

Consistent with existing studies [191-192, 211, 71], e_c is a strong function of the parcel thermodynamic state and its environment, (i.e, T, RH, T'). W in Eq. (8.25) is the mass

mixing ratio of water just before supersaturation (RH=1.0). An order of magnitude analysis of the terms in the denominator of Eq. (8.25) (not shown) suggests that γW is of the order of 10^{-4} to 10^{-3} and is in most of the cases much smaller than the other terms (of order 10^{-2}), so can be neglected

$$e_c = \frac{\alpha}{(1-RH) - \dfrac{\Delta H_v M_w}{RT^2}(T - T')} \qquad (8.26)$$

Eq. (8.26) is an excellent approximation of Eq. (8.25) except in very polluted environment (aerosol mass > 10^2 µg m^{-3}) and ambient conditions close to saturation (RH > 0.95 and T-T' < 0.3 °C); in such cases neglecting the term γW would introduce some bias in the calculation of e_c and Eq. (8.25) should be used.

8.2.5. Characteristic T and p for Droplet Formation

To calculate s_{max} and N_d, it is necessary to define "characteristic" conditions for droplet formation. Cloud base conditions (those at the lifting condensation level) are typically used since most of the droplets activate during the first stages of cloud formation [208, 188]. Entrainment affects cloud base conditions by mixing of ambient (dry) air, so they become a function of the entrainment rate. It would however be desirable (and computationally efficient) to define characteristic T and p for droplet formation that does not depend on e. We choose T and p at e = 0.98e_c, (since by definition, cloud base is not defined at e =e_c) as small temperature variations exert a large influence on s_{max} as e becomes closer to e_c (shown below), whereas their influence on s_{max} at adiabatic conditions is much lower. Selecting "characteristic" cloud formation conditions at e = 0.98e_c closely approximates the actual cloud base p and T for high e, where its influence on s_{max} is more important.

Cloud base conditions are computed from conservation of energy and water vapor mass for an unsaturated entraining parcel [230],

$$-\frac{dT}{dz} = \frac{g}{c_p} + e(T - T')$$ (8.27)

$$\frac{dw}{dz} = e\left(\frac{M_w p^s(T')}{M_a p} RH - w\right)$$ (8.28)

The water mass and energy balances should be solved simultaneously with Eq. (8.25) or (8.26) (depending on the liquid water content and ambient conditions, section 8.2.4), to obtain e_c and the characteristic T and p for droplet formation. If the difference between the parcel and the ambient temperatures, T-T', is constant during the parcel ascent (constant lapse rate) then the ambient air will remain subsaturated assuring that other effects i.e., secondary activation due to isobaric mixing [130], or mixing with supersaturated environments [202] are second order.

8.2.6. Application of the parameterization

Application of the parameterization is presented in Figure 8.2. The input consists of the aerosol distribution characteristics, the physicochemical properties of the aerosol population (i.e., density, composition, solubility, surfactant characteristics), the initial temperature, T_o, and pressure, p_o, entrainment rate, e, the ambient temperature, T', and relative humidity, RH, and the water vapor uptake coefficient, α_c. Initial conditions T_o and p_o are used to calculate the characteristic T and p of the cloud and the critical entrainment rate, e_c, by solving simultaneously Eqs. (8.26) to (8.28). After e_c is determined, the CCN spectrum is computed using either Eq. (8.2) or (8.6). s_{max} is computed from Eq. (8.13); the condensation integral is computed depending on the size

distribution type, and, if the simplified treatment for entrainment is desired (Section 8.2.3). Eq. (8.5) is then used to calculate N_d.
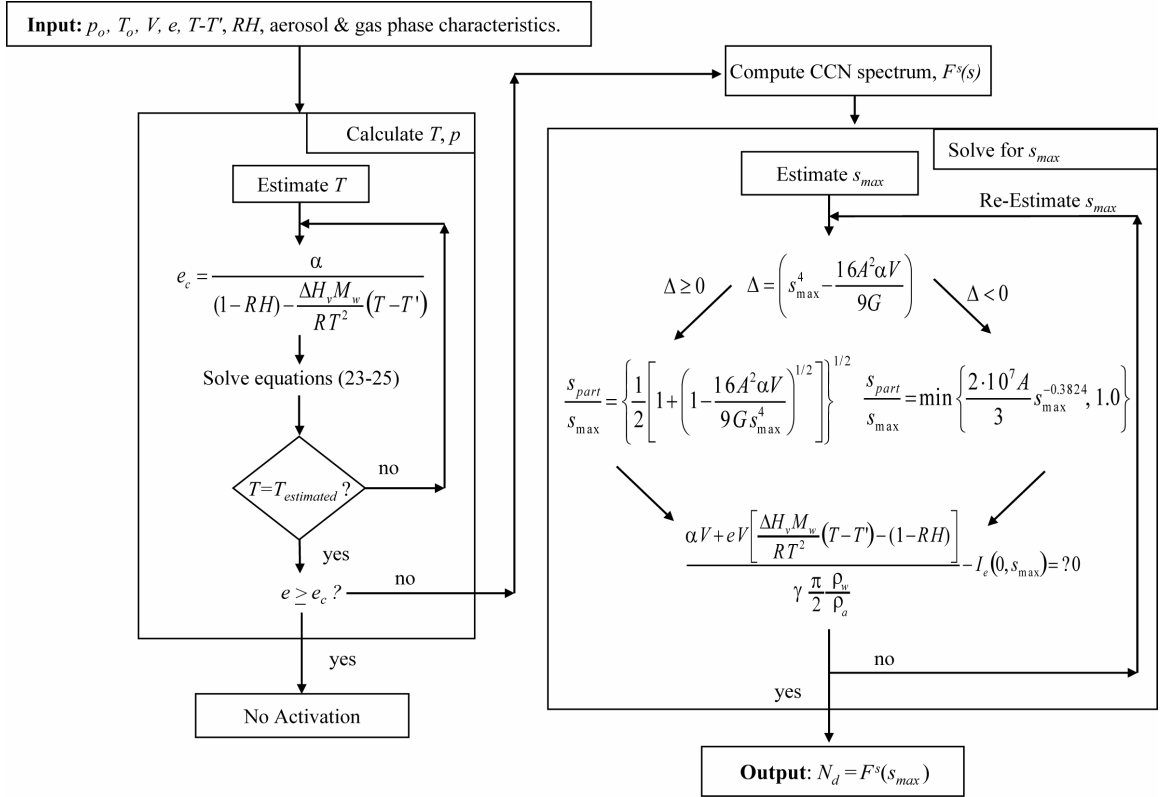
Figure 8.2. Parameterization algorithm

8.3. Evaluation of the Parameterization

8.3.1. Conditions Considered

The sectional and the lognormal formulations of the parameterization were evaluated against the numerical solution of a detailed numerical parcel model [188] with explicit treatment of entrainment, Eqs. (8.6) to (8.12) [230]. Four tri-modal aerosol size distributions were selected (Table 8.1) that represent characteristic types of global aerosol

(urban, clean continental, background and marine). The aerosol in all simulations is assumed to be composed of 50% by volume ammonium sulfate, and 50% insoluble material. In all numerical simulations, the aerosol is initially in equilibrium with the ambient relative humidity, *RH*. *T-T'* and *RH* were kept constant through the simulations. Initial parcel pressure and temperature were 1.013 kPa and 290 K, respectively. The water vapor mass uptake coefficient, α_c, was set to 0.06 as suggested by Meskhidze, et al. [165] and Fountoukis et al. [60] to represent growth kinetics of ambient aerosols; runs were also done using $\alpha_c = 1.0$.

Table 8.1. Aerosol lognormal distributions used in this study [256]. D_g is the modal diameter (μm), N_i is the number of dry particles (cm^{-3}), and σ is the geometric standard deviation. The size distributions refer to dry size with 50 % insoluble fraction.

Aerosol type	Nuclei Mode			Accumulation Mode			Coarse Mode		
	D_g	σ	N_1	D_g	σ	N_2	D_g	σ	N_3
Marine	0.010	1.6	340	0.070	2.0	60	0.62	2.7	3.1
Continental	0.016	1.6	1000	0.068	2.1	800	0.92	2.2	0.72
Background	0.016	1.7	6400	0.076	2.0	2300	1.02	2.16	3.2
Urban	0.014	1.8	106000	0.054	2.16	32000	0.86	2.21	5.4

The performance of the parameterization under adiabatic conditions has been extensively studied and evaluated against parcel model and in-situ observations [188, 165, 60], therefore the evaluation will be focused on entraining conditions, over a wide range of *e*, *RH*, *T-T'*, and *V*. Values for the entrainment rates were varied between 10^{-8} m^{-1} and $0.9e_c$ (Table 8.2). A summary of the evaluated conditions is shown in Table 8.3; ambient and initial *RH* was varied between 60% and 97%. Updraft velocity is varied from 0.1 to 5.0 ms^{-1}. The selected values represent typical conditions encountered in low level cumulus and stratocumulus clouds of marine and continental origin [202, 37, 165, 193]. In total, 2100 conditions were considered in the evaluation. s_{max} ranged from 0.01% to 5%, and N_d

ranged from 0.1 to 10^4 cm^{-3}; this covers the broad range of conditions expected in a GCM simulation. The evaluation in Sections 8.3.2 to 8.3.5 use the comprehensive formulation (based on Eq. (8.15)); the impact of the simplifications introduced by using Eq. (8.16) is assessed in Section 8.3.6.

8.3.2. Evaluation of Lognormal vs. Sectional Formulation

The lognormal and sectional formulations of the parameterization should give the same answer provided that the same cloud formation conditions and aerosol (i.e., same chemical composition and adequate number of sections to reproduce lognormal distributions) are used as input. This was tested by comparing predictions of droplet number between formulations for all conditions in Table 8.3 and lognormal distributions of Table 8.1; 200 sections per lognormal mode were used in computing droplet number with the sectional representation. The two formulations of the parameterization produced effectively identical results, agreeing in calculated droplet number within 1% (not shown).

Table 8.2. Critical entrainment rate, e_c, and characteristic T and p for cloud droplet formation. *RH* and *T-T'* are assumed constant during parcel ascent. Initial temperature and pressure of the parcel are 290 K and 101325 Pa, respectively.

RH (%)	*T-T'* (K)	e_c (m^{-1})	*p* (Pa)	*T* (K)
60	1.0	1.69×10-3	75760	263.1
70	1.0	2.21×10-3	84360	272.0
80	1.0	3.55×10-3	91880	279.2
90	1.0	11.6×10-3	98640	285.2
80	0.0	2.45×10-3	88210	278.7
90	0.0	4.66×10-3	95100	284.8
70	2.0	3.05×10-3	88570	272.4
80	2.0	6.45×10-3	95890	279.6
97	0.3	3.62×10-2	100567	288.7
98	0.3	1.78×10-1	101171	289.2

Table 8.3. Cloud formation conditions used in evaluation.

Property	Values
RH (%)	60, 70, 80, 90, 97
T-T' (K)	0, 0.3, 1, 2
V (ms^{-1})	0.1, 1.0, 5.0
α_c	0.06, 1.0
e (m^{-1})	10^{-8} - $0.9e_c$

8.3.3. Critical Entrainment Rate

Adiabatic conditions ($e = 0$) set the upper limit for s_{max} in the ascending parcel; as $e \rightarrow e_c$, $s_{max} \rightarrow 0$. The point at which $s_{max} = 0$ is calculated using Eq. (8.26); an example of the resulting s_{max} vs. e profiles is shown in Figure 8.3. It can be seen that e_c does not depend explicitly on V (although e may [192, 100]) or of the type of aerosol considered (Eq. (8.26)). Figure 8.3 shows that the calculation of e_c (Eq. (8.26)) is in good agreement with the extrapolation of the s_{max} vs. e curve from numerical results, to the point where $s_{max} = 0$ (hence $e=e_c$). However, obtaining a solution with the parcel model for $e \sim e_c$ becomes numerically challenging (owing to the stiffness of the system of Equations (8.6) to (8.12) under such conditions); therefore comparisons are made for $e \leq 0.9e_c$. The parameterization does not exhibit such numerical issues and solutions are smooth up to $0.99e_c$. All simulations performed in this work show that most of the variation on s_{max} and N_d from entrainment occurs for $e > 0.1e_c$ (Figure 8.3).

8.3.4. Effects of RH and *T-T'*

It is important to evaluate the parameterization for a wide range of *RH* and *T'*. In all simulations (Table 8.3), the parameterization closely reproduced the results of the parcel model. Figure 8.4 shows s_{max} vs. e (left panel) and N_d vs. e (right panel) profiles for *T-T'*

equal 0 and 1 °C. Increasing T-T' tends to increase e_c because cooling from mixing with ambient air increases s (therefore a larger e is required to prevent supersaturation), and offsets the effect of mixing with subsaturated air (which decreases s). Similarly, increasing ambient RH increases e_c because a larger mixing rate is required to prevent supersaturation (not shown). Regardless of RH and T-T', Figures 8.3 and 8.4 clearly show that entrainment becomes important when $e > 0.1e_c$. The tendency of the parameterization to overpredict s_{max} is discussed in section 8.3.5.
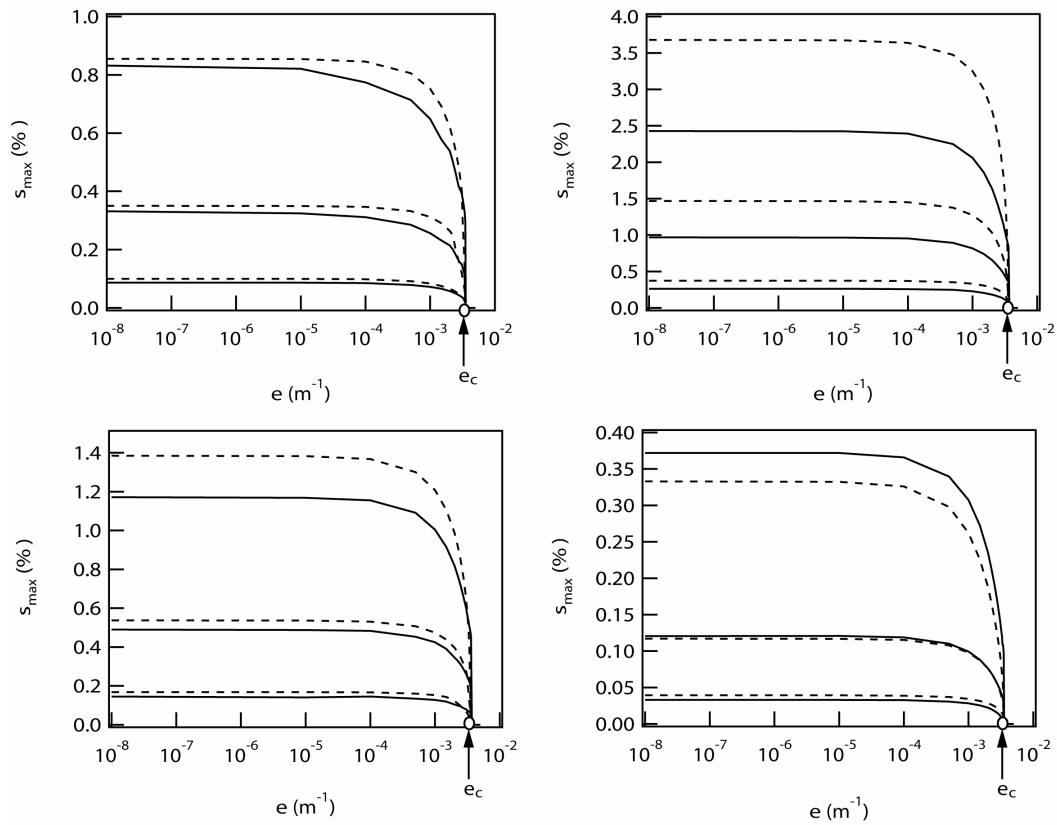
Figure 8. 3. s_{max}-e profiles for background (upper left), marine (upper right), continental (lower left), and urban (lower right) aerosols. Parcel model results are represented as solid lines, parameterization results given as dashed lines. RH=80%, T-T'=1.0, V=0.1 ms^{-1} (lower lines), 1.0 ms^{-1} (middle lines) and 5.0 ms^{-1}(upper lines). e_c for this set of runs is equal to 3.55×10^{-3} m^{-1}.
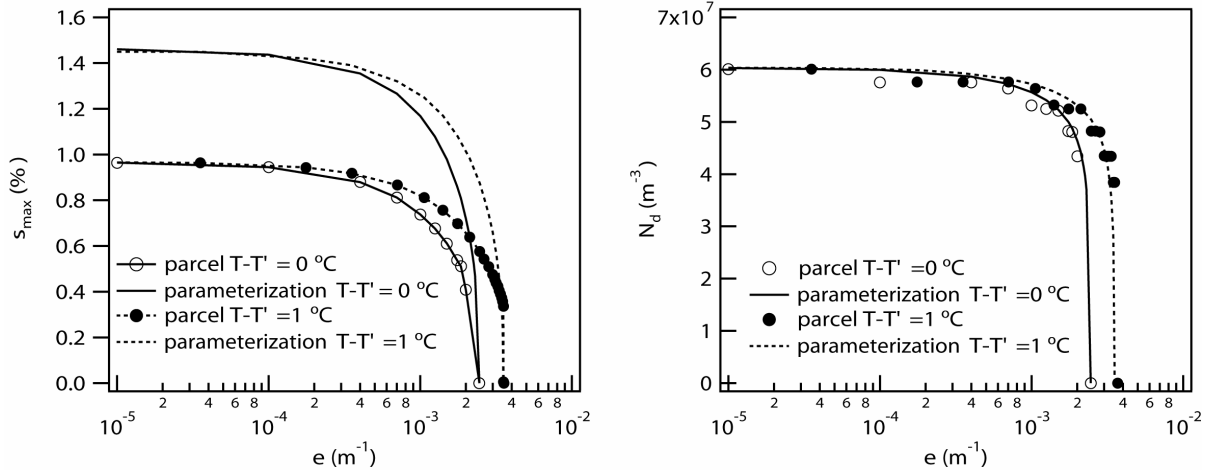
Figure 8.4. s_{max} (right panel) and N_d (left panel) for marine aerosol. T-T'= 1 °C, RH= 80%, V= 1.0 ms^{-1} [11].

8.3.5. Evaluation of s_{max} and N_d predictions

Figure 8.5 presents s_{max} calculated by the parcel model and the parameterization, for the four tri-modal aerosol populations of Table 8.1 and conditions of Table 8.3. The parameterization closely reproduces the results of the parcel model (average error 26%, standard deviation 36%). The agreement is best for background aerosol at high RH (80 and 90 %) whereas for marine and continental aerosols, an overprediction of above 25% can be found, which increases as RH decreases. This systematic overprediction is attributed to the expression used for representing droplet growth kinetics. Equation (8.18) for population 1 (in which $D_p^2(\tau) << 2G\int_{\tau}^{t_{max}} s(t)dt$) tends to underestimate the size of droplets [189]. When most of the activated CCN are composed of such drops (e.g., where most CCN at the point of activation are either far above or way below their D_c) there is an underestimation of surface area for water vapor condensation. This means the

218

condensation integral $I_e(0, s_{max})$ is underestimated; to compensate, s_{max} must increase (i.e.

be overestimated) to satisfy Eq. (8.13). For marine aerosols, this occurs when most of the

CCN are activated (i.e., s_{max} is large) so overestimation of s_{max} does not significantly

impact N_d. However, for polluted urban aerosol, where s_{max} is low, most of the CCN are

not activated, so overestimation in s_{max} will lead to some overestimation in $\underline{N_d}$.
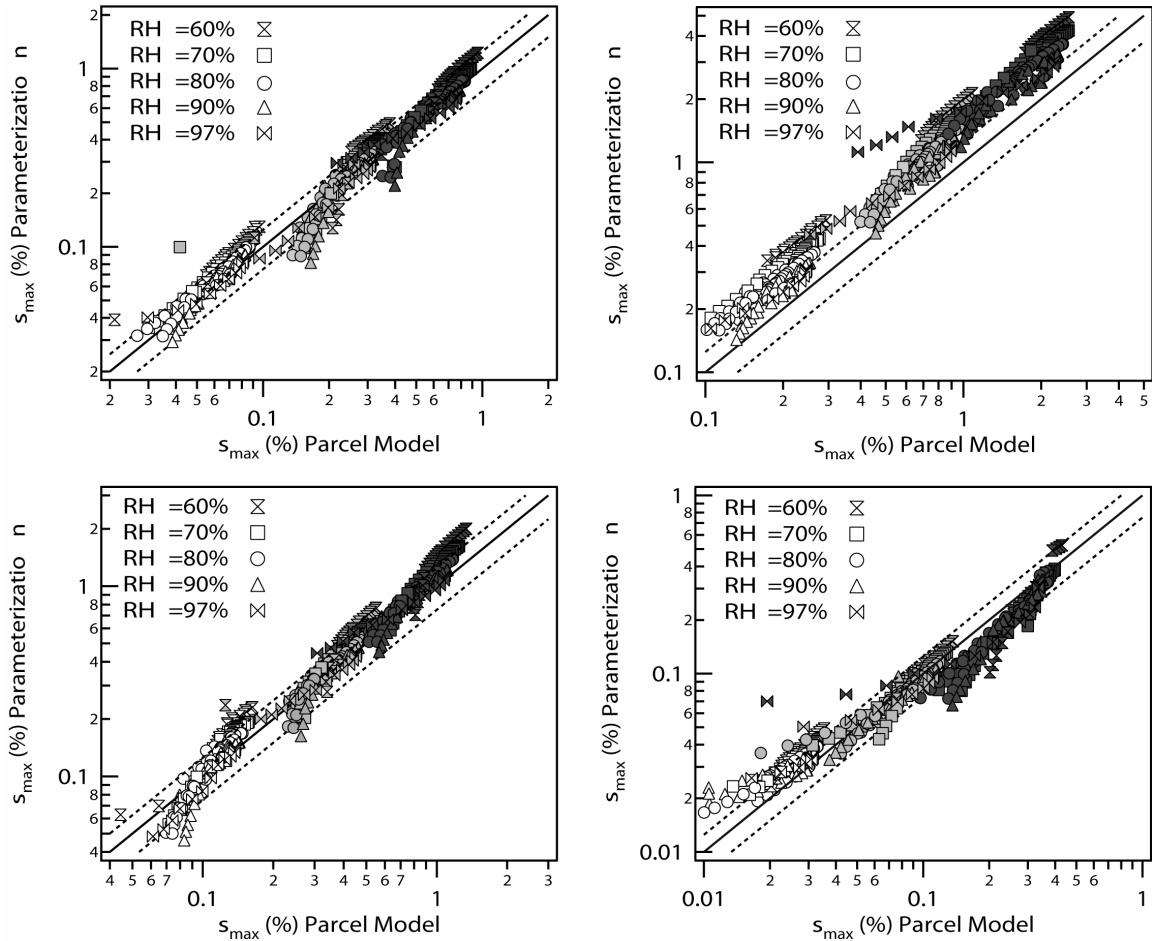
Figure 8.5. s_{max} as predicted by the parameterization vs. the parcel model. Simulations presented are for background (upper left panel), marine (upper right panel), continental (lower left panel), and urban (lower right panel) aerosols. V=0.1 ms^{-1} (white), V=1.0 ms^{-1} (gray), and V=5.0 ms^{-1} (dark gray). T, T-$T', RH,$ and p are presented in Tables 8.2 and 8.3. Dashed lines represent ±25% deviation.

The parameterization closely reproduces the parcel model predictions at high V and RH, and low to moderate entrainment (i.e., high to moderate s_{max}). When entrainment strongly impacts s_{max} (s_{max} is low, i.e., low RH, high $T\text{-}T'$, e close to e_c), the parameterization tends to overpredict N_d which is more noticeable for the background and urban aerosols (Table 8.4). This is depicted in Figure 8.6; for low e values, most points fall around the 1:1 line, whereas for e values close to e_c, N_d is slightly overestimated. Figures 8.6 and 8.7 show that the difference between N_d calculated by the parameterization by the parcel model is usually the largest (above 25%) when RH is low (60 %) and $T\text{-}T'$ (2 °C) is high. It can be noticed as well in Figure 8.7 that overprediction in s_{max} found at high updraft velocities for marine aerosol (Figure 8.5) does not correspond to a N_d overprediction. Increasing the temperature difference $T\text{-}T'$, will offset these effects; however the influence of RH dominates over the mixing at T'.

The small value of the mean relative error (with reference to the parcel model results, Table 8.4) in parameterized N_d (2.3%), suggests that there are no significant systematic biases for droplet calculation. The standard deviation of the relative error is about 20% which is remarkably small given the diverse set of conditions considered in the evaluation, and the numerically challenging nature of entrainment.

All simulations up to this point were done for a "basecase" value of $\alpha_c = 0.06$. We repeated the assessment for $\alpha_c = 1.0$, the results of which are shown in Figure 8.6. Increasing α_c intensifies water vapor condensation onto the drops; competition for water vapor increases, hence s_{max} and N_d decrease [58]. As expected, the general decrease in s_{max} slightly increases N_d error (-16 ± 9%) compared to the basecase.
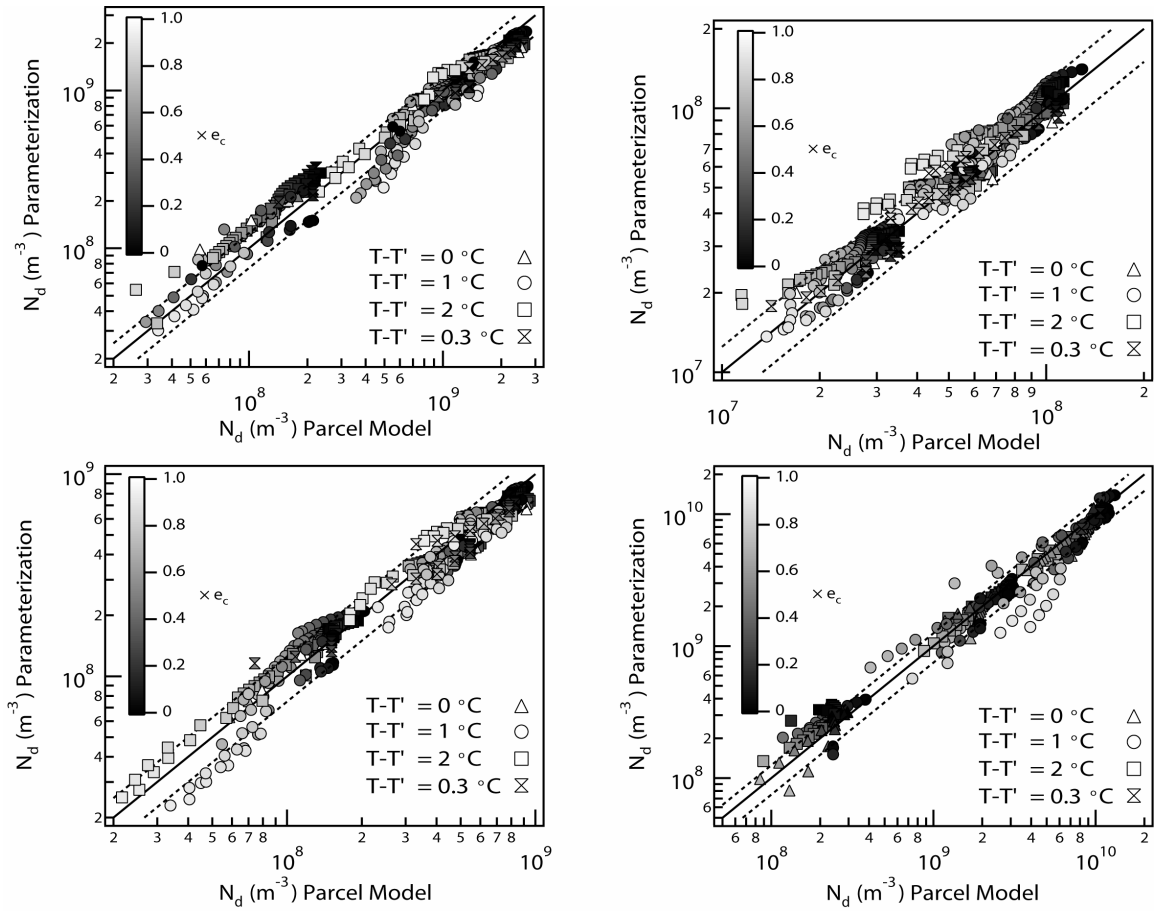
Figure 8.6. Cloud droplet number concentration as predicted by the parameterization and the parcel model. Simulations presented are for background (upper left panel), marine (upper right panel), continental (lower left panel), and urban (lower right panel) aerosols. Gray scale indicates the entrainment rate as a fraction of e_c. $V = 0.1$, 1.0, and 5.0 ms^{-1}. *T, T-T', RH,* and *p* are presented in Tables 8.2 and 8.3. Dashed lines represent ±25% deviation.

Table 8.4. Average error (standard deviation) of parameterized N_d versus parcel model N_d for $e <$ $0.9e_c$.

Aerosol type	Relative error (%)			Absolute error (cm^{-3})		
	All data	$\Delta < 0$	$\Delta > 0$	All data	$\Delta < 0$	$\Delta > 0$
Background	4.1(23.4)	-8.0(9.8)	22.7(22.6)	138(148)	193(133)	50(28)
Marine	6.8(16.4)	4.7(11.7)	N/A	5(6)	6(5)	N/A
Continental	-4.0(15.7)	-3.8(12.8)	4.8(19.0)	44(49)	51(42)	17(10)
Urban	6.5(22.8)	6.1(9.08)	3.6(23.7)	688(714)	984(669)	410(560)
All aerosol	2.3(21.8)	-1.3(12.8)	9.4(24.4)	136(354)	81(171)	265(471)
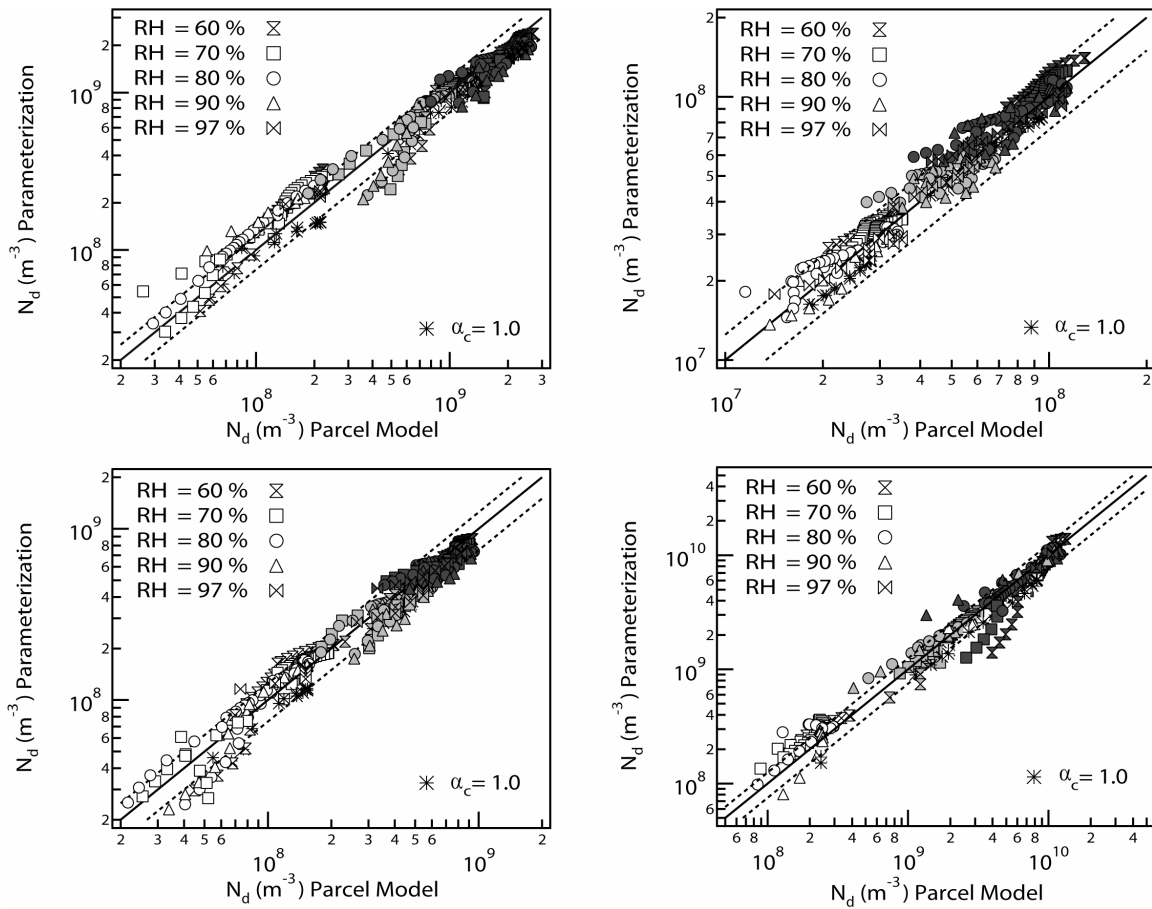
**Figure 8.7**. Cloud droplet number concentration as predicted by the parameterization and the parcel model. Simulations presented are for background (upper left panel), marine (upper right panel), continental (lower left panel), and urban (lower right panel) aerosols. Nomenclature and conditions same as in Figure 8.5.

Further insight into the influence of kinetic limitations on the parameterization performance can be gained by analyzing the descriminant criterion, Δ. Figure 8.8 shows that in most cases tested for marine and continental aerosols, the droplet growth is free from kinetic limitations ($\Delta > 0$) whereas for background and urban aerosols the growth regime is generally kinetically limited ($\Delta < 0$). Table 8.4 shows larger average error in N_d for kinetic limited regimes; however, the difference in errors between the two regimes is

not statistically significant (Table 8.4).
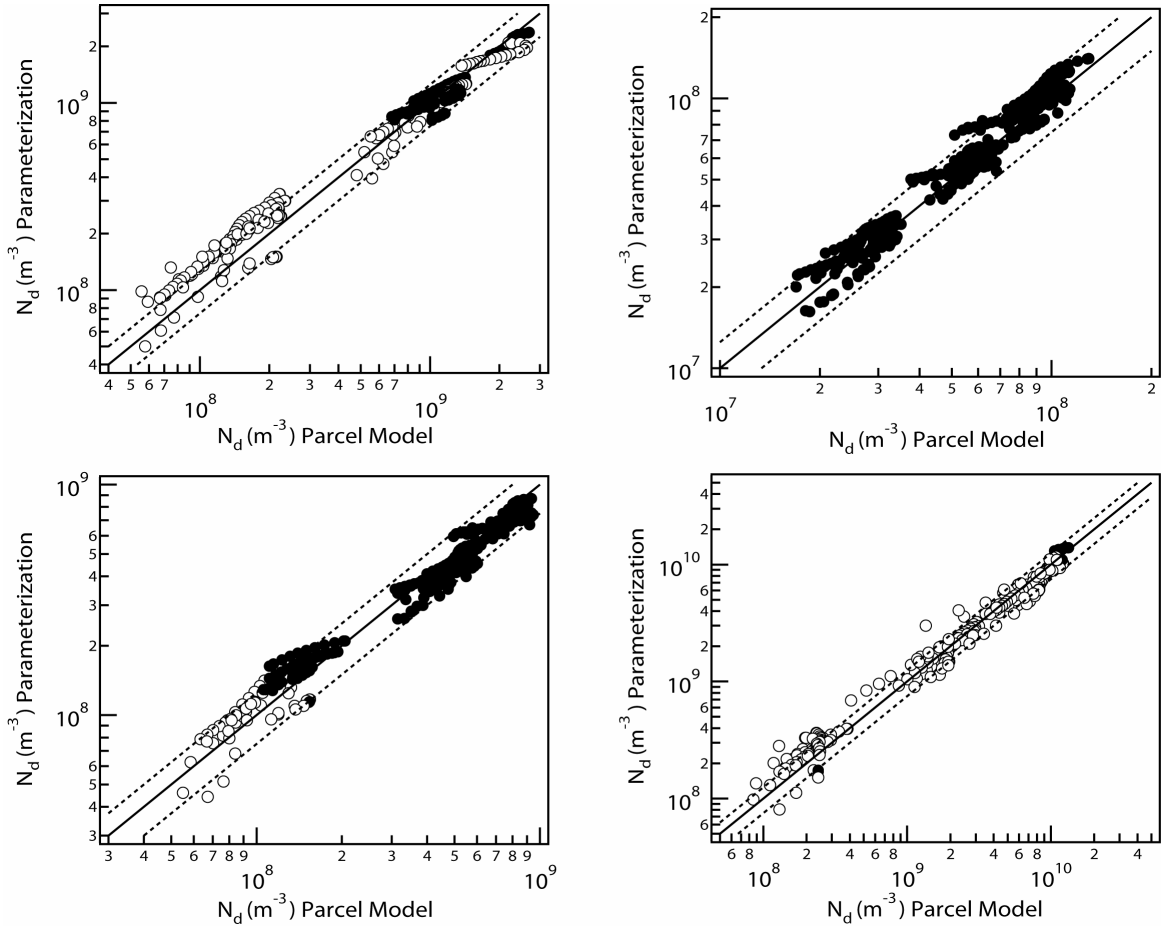
Figure 8.8. Same as Figure 8.7 but classified according to the descriminant criterion and e < $0.75e_c$. Open symbols are for $\Delta < 0$ (kinetically limited regime), and filled symbols are for $\Delta \geq 0$ (lack of significant kinetic limitations).

Δ is essentially a function of s_{max} (hence, e), therefore it is important to investigate if N_d error will be correlated with s_{max} (Figure 8. 9). It is noticeable that although there is no correlation between s_{max} and the average relative error in N_d, the dispersion in the error is higher for low s_{max}. In all simulations shown in Figure 8.9, the threshold s_{max} for dominantly kinetically limited CCN activation ($\Delta = 0$) ranges between 0.1% - 0.3% depending of the aerosol type, so it is clear that a larger discrepancy between the

223

parameterization and the parcel model (although below 40%) may be expected for kinetically limited regimes. Figure 8.6 supports this, as most of the points outside the 25% deviation interval correspond to $e > 0.6e_c$.
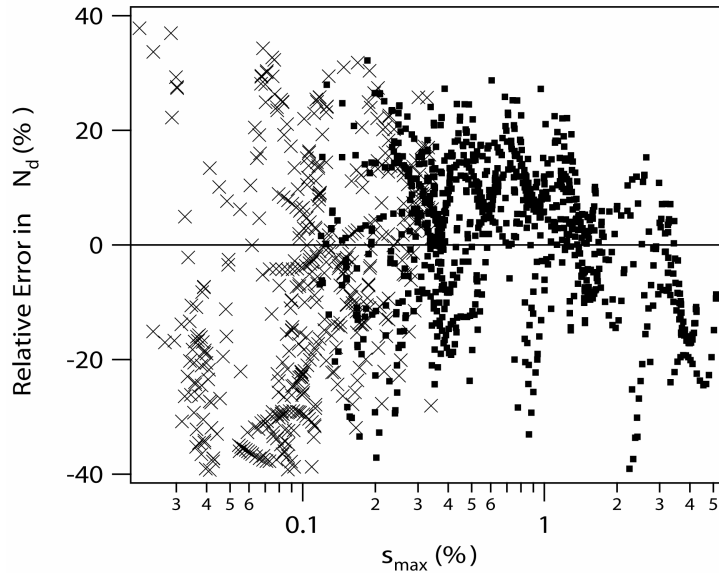
Figure 8.9. Relative error in cloud droplet number concentration as function of s_{max}, for the data presented in Figures 8.7 and 8.5 ($e < 0.75ec$). Crosses indicate kinetically limited regimes ($\Delta < 0$) and dots denote lack of significant kinetic limitations ($\Delta \geq 0$).

The parameterization was also assessed for systematic biases with respect to activation fraction (i.e., the fraction of aerosol that activate into droplets). This is an important test, as the CCN spectrum shape changes considerably from low to high activation ratios. Most of the results reside close to 1:1 line (not shown) for all aerosol types, a larger parcel model - parameterization discrepancy results at $V = 0.1$ ms^{-1}, low RH (60 and 70 %), and high e, (i.e., low activation fractions). The dispersion of the data at low V was about the same for the different kinds of aerosol considered, which suggested that the parameterization is not biased with respect to activation fraction.

224

8.3.6. Comprehensive vs. Simplified Parameterization

We assess the simplified version of the parameterization (based on using Eq. (8.16)) by comparing its predictions of droplet number with that of the comprehensive formulation (based on Eq. (8.14)). The assessment is done for all the cloud drop formation conditions shown in Tables 8.1 to 8.3; in addition we also included a set of simulations for ambient RH=98% and $T\text{-}T' = 0.3$. The results of the formulation intercomparison are shown in Figure 8.10, which shows $N_d/N_{d,\text{adiabatic}}$ predicted by the comprehensive formulation vs. $N_d/N_{d,\text{adiabatic}}$ from the simplified parameterization. When $N_d/N_{d,\text{adiabatic}} < 0.4$, the difference between the two formulations is negligible (not shown); for higher values of $N_d/N_{d,\text{adiabatic}}$, the simplified parameterization tends to overestimate N_d when V (*i.e.*, s_{max}) and ambient RH are high (Figure 8.10). This bias is not surprising, as neglecting the eVW term in Eq. (8.8) eliminates the effects of entrained water, and affects s_{max}. The simulations suggest that the simplified parameterization can safely be used when s_{max} does not exceed 0.8%.

8.3.7. Computational Requirements of Parameterization

The computational efficiency of the new parameterization is assessed by the CPU time required relative to the Fountoukis and Nenes [58] parameterization; the latter is selected because the equations, code structure and algorithm are very similar to the new formulation. We compare the two parameterizations, for all the cases in Tables 8.1 to 8.3 which have $e = 0$. The inclusion of entrainment increased the CPU time by about 30%, most of which arises from the increased complexity of the equations (section 8.2.3), whereas the calculation of e_c and characteristic T and p (section 8.2.5) has a minor impact.
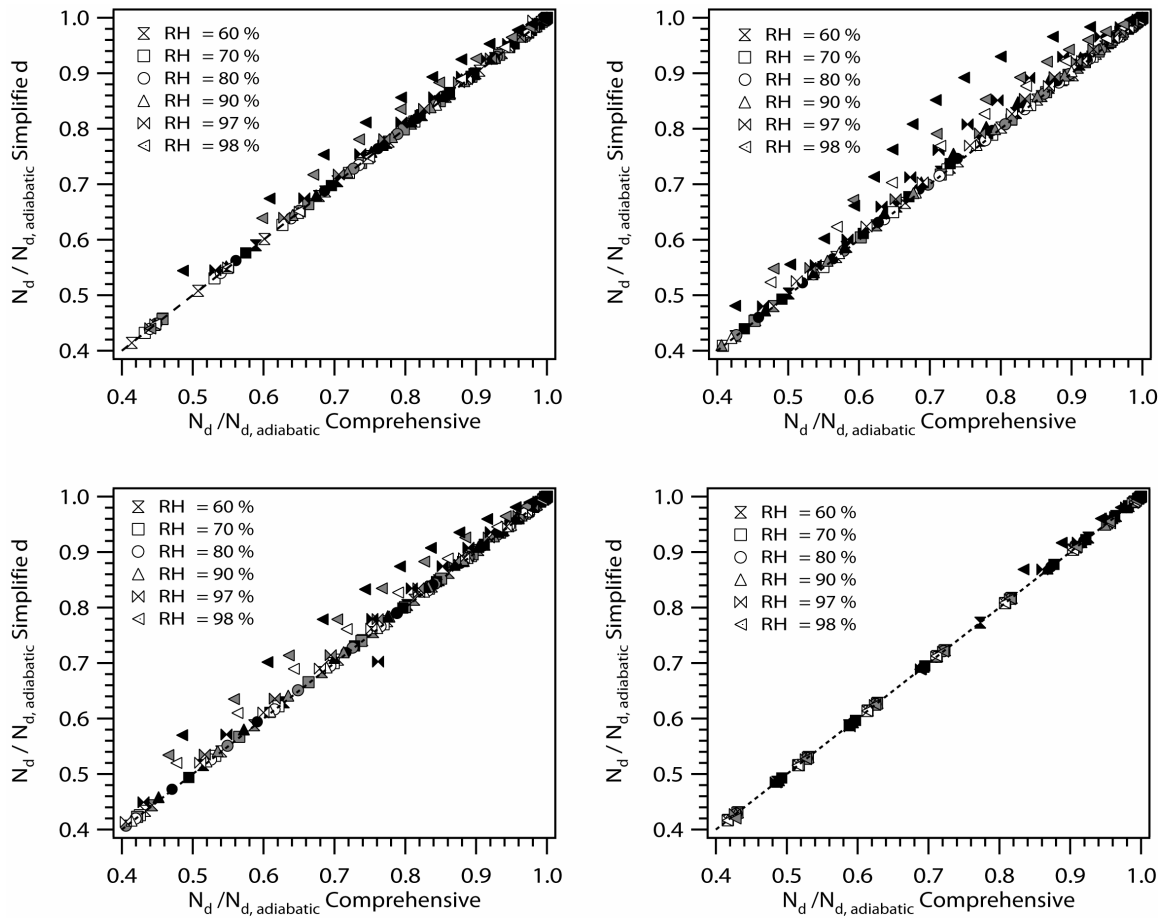
Figure 8.10. Comparison between the simplified and comprehensive parameterizations. Simulations presented are for background (upper left panel), marine (upper right panel), continental (lower left panel), and urban (lower right panel) aerosols. V=0.1 ms^{-1} (white), V=1.0 ms^{-1} (gray), and V=5.0 ms^{-1} (dark gray). All other conditions presented in Tables 8.2 and 8.3.

Compared to the parcel model, the parameterization is orders of magnitude faster; the difference becomes even larger as e approaches e_c (where a numerical solution becomes increasingly difficult). The CPU time of the simplified parameterization is about the same as the adiabatic formulation of Fountoukis and Nenes [58]; this is expected as the two parameterizations share the same expression for the condensation integral (section 8.2.3).

226

8.4. Conclusions and Summary

This study presents a physically-based prognostic parameterization of droplet formation in which entrainment effects are explicitly considered. The parameterization is the first of its kind and it extents the works of Nenes and Seinfeld [189] and Fountoukis and Nenes [58]. The concept of "population splitting" [189] was used to obtain a closed solution for maximum supersaturation and cloud droplet number. Two formulations are presented, one for sectional and one for lognormal aerosol size distribution. Entrainment of ambient air is parameterized in terms of a per-length entrainment rate which implicitly assumes that all mixing processes occur homogeneously, at a time scale much faster than that of activation. Therefore, the model presented here implies a lateral mixing mechanism, and instantaneous mixing of the entrained air. Since this work is an extension of the Nenes and Seinfeld [189] and Fountoukis and Nenes [58] parameterizations, by design it can treat the effects of externally mixed aerosol, CCN containing surfactants and slowly-growing droplets (expressed by changes in the water vapor mass transfer coefficient). Even slightly soluble compounds can easily be accounted for during the computation of $F^s(s)$, and $n^s(s)$.

We also introduced the concept of critical entrainment rate, a value at which mixing completely prevents activation. The critical entrainment rate was shown to largely influence the characteristics of parcels experiencing intense mixing, and it is useful to determine whether or not entrainment effects are important for droplet number calculations. The critical entrainment rate is also useful for determining the characteristic T and p for cloud droplet formation.

The new parameterization was extensively tested against a detailed entraining numerical parcel model. The evaluation was considered for a wide range of relative humidity, entrainment rate, updraft velocity, water vapor uptake coefficient, ambient temperature, and aerosol characteristics. The parameterization closely followed the parcel model results with a mean relative error below 3% and mostly within 20%. The new parameterization requires approximately 30% more CPU time than the adiabatic formulation.

Finally, we also have proposed simplified version of the parameterization which for most conditions of cloud droplet formation, predict droplet with the same accuracy as the comprehensive formulation. This simplified formulation requires effectively the same CPU time as the Fountoukis and Nenes [58]and Nenes and Seinfeld [189] adiabatic droplet formation parameterizations.

In summary, the new parameterization framework offers for the first time a comprehensive and computationally efficient treatment of cloud droplet formation that can couple complex chemical effects on aerosol activation together with entrainment. The parameterization is ideally suited for large scale regional and global models, with explicit aerosol-cloud interactions.

CHAPTER 9

ENTRAINMENT EFFECTS ON CLOUD DROPLET FORMATION: AN EXPLORATORY GCM STUDY[1]

This study presents a global assessment of the sensitivity of droplet activation to entrainment and its potential impact on indirect forcing and autoconversion. Simulations were carried out with the NASA Global Modeling Initiative (GMI) atmospheric and transport model. Cloud droplet number concentration (CDNC) is calculated using a physically-based prognostic parameterization that explicitly includes entrainment effects on droplet formation. It is shown that the ratio of the entrainment rate, e, to its critical value, e_c (defined as the value of e that prevents activation), controls the extent to which entrainment affects CDNC. It was found that for a typical value of $e = 3 \times 10^{-3}$ m^{-1} (global mean $e/e_c \approx 0.48$), neglecting entrainment may bias global mean CDNC, indirect forcing, and autoconversion rate by -20%, -36%, and +70%, respectively. Regionally, entrainment effects can be stronger and most significant in regions of moderate CCN concentrations (100 to 300 cm^{-3}). Considering the correlation of e with updraft velocity for atmospherically-relevant conditions dampens the sensitivity of CDNC to cloud dynamics,

and suggests that CDNC calculation based on diabatic activation is less sensitive to errors in estimated updraft velocity.

9.1. Motivation

Cloud droplet number concentration (CDNC) depends on the size distribution and composition of the precursor aerosol, and, on the thermodynamical and dynamical (i.e., updraft velocity, mixing rates) state of the cloudy air during its formation [230]. At constant liquid water content (LWC), increasing the precursor aerosol number concentration may lead to a decrease in cloud effective radius and therefore to an increase in cloud albedo, i.e., the first aerosol indirect effect [248]. The limited ability of general circulations models (GCMs) to explicitly represent aerosol – cloud interactions motivated the development of physically-based representations parameterizations of the cloud droplet formation process [e.g., 2, 189, 58, 168, 134]. State-of-the-art parameterizations are capable of relating effects of the aerosol composition, such as the role of organic surfactants and solutes [186, 136, 160], adsorption activation [134] and kinetic and mass transfer limitations on droplet formation [32, 188, 58, 7].

Besides an explicit relation between aerosol concentration and CDNC, estimation of the indirect forcing requires the knowledge of macroscale cloud characteristics (i.e., liquid water content and path, cloud fraction), which are usually derived from large-scale circulation and thermodynamic fields [e.g., 133]. The relevant scale for cloud activation is however much smaller than the characteristic size of the cloud, and large-scale dynamic fields are not suitable to describe droplet formation [208]. Thus, cloud droplet formation parameterizations are typically used in the calculation of CDNC and the cloud droplet size distribution, whereas cloud liquid water content (LWC) and cloud fraction

are independently parameterized. This approach however carries the implicit assumption that processes affecting the macroscale properties of the cloud do not affect its microphysical properties (and vice-versa). Such is however not the case for entrainment and mixing of dry air which affects droplet activation [208, 11], as well as LWC, cloud fraction and liquid water path [124].

Despite the considerable body of work on large-scale cumulus convection parameterization [e.g., 178, 102, 231, 215], less has been done on linking mixing processes with droplet formation. Although entrainment is usually accounted for when parameterizing LWC in large-scale models [77], it is usually neglected in physically-based parameterizations of CDNC [2, 58, 227]. Although this may be an appropriate assumption near cloud base, it is also well known than entrainment can affect cloud formation modifying the cloud droplet size distribution [e.g., 209, 191, 211-212, 35, 185, 11, 155]. Neglecting entrainment may therefore overestimate CDNC, and produce a too-narrow droplet size distribution when compared to observations [208, 88]. Entrainment and mixing also impact the evolution of the droplet size spectrum [e.g., 140, 35, 22, 232, 177]. Field observations show both CDNC and LWC below those obtained using adiabatic parameterizations, which may result from mixing and entrainment during cloud activation and subsequent evaporation of droplets during the cloud lifetime [22, 37, 155].

Ideally, one would like to describe all of possible entrainment processes during the cloud lifetime (e.g., homogeneous [208] and inhomogeneous mixing, as well as complete droplet evaporation and dilution [e.g., 208, 22, 177]) across all scales. It is however very difficult to calculate (or prescribe) an entrainment profile (Figure 9.1a) that would account for mixing effects during activation and then the subsequent deactivation

(drying) of droplets. Thus, current atmospheric models consider effects of entrainment on liquid water content, but assume that droplet activation proceeds adiabatically i.e., with no mixing effects (Figure 9.1b). This inconsistency can lead to overestimation of CDNC and underestimation of droplet size.
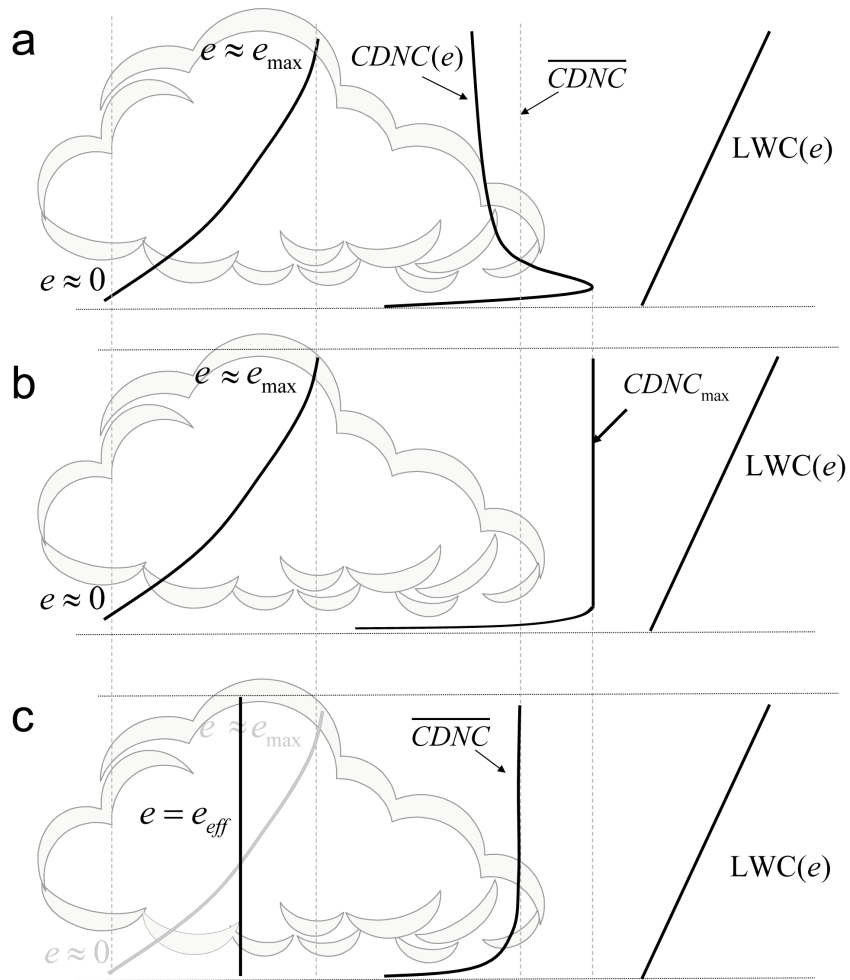
Figure 9.1. CDNC and LWC calculation in GCMs. (a) Representation of the entrainment profile in a real cloud where both LWC and cloud droplet activation are affected by entrainment. (b) Current GCM representation assuming adiabatic activation but LWC affected by entrainment. (c) The activation approach proposed in this study.

In this work, we study the impact of entrainment during cloud droplet activation on the aerosol indirect effect. This is accomplished by implementing the Barahona and Nenes [11] parameterization in the NASA Global Modeling Initiative (GMI) chemistry and transport model [233]. This parameterization accounts for mixing and entrainment by using a per-length fractional entrainment rate, e (m^{-1}) [208] (represented as e_{eff} in Figure 9.1c). The sensitivity of global CDNC, cloud effective radius (R_{eff}) and indirect forcing (IF) to entrainment, using different meteorological fields to drive the GMI model.

9.2. Model Description

The NASA GMI model is a highly modular 3-D chemistry and transport model (CTM) [221] capable of multi-year simulations for assessments of anthropogenic impacts on atmospheric chemistry. GMI computes first-order responses (without feedbacks) of climate to external forcing and is therefore suitable to study the first aerosol indirect effect [248]. The modeling framework used is described by *Sotiropoulou et al.* [233] and is summarized here. The aerosol module is coupled to the GMI-CTM advection core and includes primary emissions, chemical production of sulfate, gravitational sedimentation, dry deposition, wet scavenging, and hygroscopic growth [150]. Anthropogenic and natural aerosol and precursor emissions include SO_2, organic matter, black carbon, oceanic DMS, dust and sea-salt, as described elsewhere [150, 233].

Two types of clouds exist in GMI: convective and stratiform; clouds are allowed to form in any model layer (with the exception of the layer nearest to the surface, as it is very shallow). Large scale cloud fraction, is diagnosed based on large-scale relative humidity [239], RH, using a threshold relative humidity for condensation specified as a

function of pressure [259]. For convective cloud fraction, a parameterization with convective mass flux [259] was adopted. Total cloud fraction, in each layer is obtained from the combination of the large scale cloud fraction and convective cloud fraction assuming random mixing [54], which has been shown to adequately reproduce the observed global distribution of liquid water path.

Following *Hack* [77] the cloud liquid water content (LWC) is vertically distributed using a prescribed cloud liquid water density profile [123] derived from experimental measurements and GCM simulations. In-cloud liquid water path (LWP) at each level is found by the integration of LWC between the two adjacent layers [233]. Cloud forcing and radiative properties are calculated online using the CLIRAD-SW solar radiative transfer model [30], which gives the cloud optical depth and the shortwave radiative flux from the surface to the top of the atmosphere (TOA). Aerosol indirect forcing (IF) is calculated offline, as the difference in the TOA net outgoing shortwave radiative flux between simulations with "present-day" (natural and anthropogenic) and "pre-industrial" (only natural) emissions of aerosols (and their precursors). In computing indirect forcing, surface albedo for direct and diffuse light was obtained by the GEOS4 GCM [20]. Following *Del Genio*, *et al.* [41], liquid clouds were those with a cloud top temperature above 263.15 K over land, and, 269.15 over ocean.

The effect of large-scale dynamics on cloud amount and indirect forcing is accounted for by repeating the assessment using three different meteorological fields to diagnose grid cell *RH*, *T* and *p*. They are taken from simulations made with the NASA Global Modeling and Assimilation Office (DAO), the NASA finite volume GCM (FVGCM), and the Goddard Institute for Space Studies version II' (GISS) GCM. Each of the

archived meteorological data sets spans over one year. Simulations with GMI are done for each meteorological field (DAO, GISS, FVGCM) using both "present day" (i.e., all emissions active) and "preindustrial" (i.e., emissions active except anthropogenic) emissions. The horizontal resolution in all simulations is 4° latitude by 5° longitude. Vertical resolution differs in each meteorological field, being 46, 42, and 23 layers for DAO, FVGCM, and GISS, respectively. Monthly and annually averaged CDNC, R_{eff}, and autoconversion rates (Q_{aut}) are computed from the simulations.

9.2.1. Description of Aerosol-Cloud Interaction Parameterizations

Cloud droplet number is calculated using the parameterization of *Barahona and Nenes* [11, hereafter BN07], which explicitly includes the effects of entrainment and mixing on maximum supersaturation and CDNC. BN07 is an extension of the works of *Nenes and Seinfeld* [189] and *Fountoukis and Nenes* [58], therefore it can treat the effects of externally mixed aerosol, CCN containing surfactants and slowly-growing droplets (expressed by changes in the water vapor mass transfer coefficient). In its adiabatic version the parameterization has been shown to reproduce in situ measurements of CDNC in cumulus and stratocumulus clouds close to cloud base [165, 60]. In this study, the effect of entrained liquid water (associated with aerosol particles) on supersaturation is neglected. This assumption simplifies the solution of the model equations, and introduces less than 1% error in CDNC calculation for most of the globe, being the pristine and moderately polluted environments (aerosol mass $< 10^2$ μg m^{-3}) and ambient conditions far from saturation (*RH* < 0.95 and *T-T'* > 0.3 °C) [11].

The rate of change of supersaturation, *s*, in an ascending cloudy parcel is given by [230, 11],

$$\frac{ds}{dt} = \alpha V\left(1 - \frac{e}{e_c}\right) - \gamma\left[\frac{dW}{dt}\right] \tag{9.1}$$

where $\frac{dW}{dt}$ is the rate of condensation of liquid water onto the drops, and V is the updraft velocity. The critical entrainment rate, e_c, is defined as the entrainment rate that completely prevents droplet activation (i.e., the upper limit in e for which cloud formation is possible) given by [11],

$$e_c = \frac{\alpha}{(1 - RH) - \frac{\Delta H_v M_w}{RT^2}(T - T')} \tag{9.2}$$

where $\alpha = \frac{gM_w \Delta H_v}{c_p RT^2} - \frac{gM_a}{RT}$, RH is the ambient relative humidity and T-T' is the difference between cloud and ambient temperatures. Parcel model simulations show that entrainment would affect CCN activation if $e/e_c > 0.1$ [11]; adiabatic activation occurs when $e = 0$ (i.e., negligible mixing rate). BN07 calculates the number of activated droplets at the maximum supersaturation (s_{max}), determined using the method of "population splitting" as described in *Nenes and Seinfeld* [189], *Fountoukis and Nenes* [58], and *Barahona and Nenes* [11]. BN07 has been evaluated against a detailed numerical parcel model over a wide set of cloud forming conditions that included entrainment; the mean relative error in computed CDNC was $2 \pm 21\%$.

Autoconversion rate of cloud water to rain is computed from the scheme of *Khairoutdinov and Kogan* [116], which is derived from large eddy simulations of drizzling stratocumulus clouds. Autocoversion rate (s^{-1}) is given by

$$Q_{aut} = \left(\frac{q_l}{C_l}\right)^{2.47} (CDNC)^{-1.79} \qquad (9.3)$$

where CDNC is in cm^{-3}. Among current approaches, Eq. (9.3) is a simple correlation that has the strongest dependency on CDNC [87], hence it can express the upper limit of autoconversion sensitivity to CDNC from entrainment.

9.2.1.1 Input Parameters to the CDNC Parameterization

To calculate CDNC *T, p,* aerosol size distribution and composition, *V, e,* and ambient conditions, i.e., *T',* RH, at the scale relevant for cloud activation (~ 50 m), need to be prescribed. Consistently with the cloud scheme, characteristic cloud formation *T* and *p* are taken as the grid-cell average *T* and *p*. Ambient temperature, *T',* is not explicitly calculated and a difference *T-T'* is prescribed from in situ measurements or calculated from the average liquid water content of the grid cell (section 9.3.5). Grid cell average RH is assumed to be representative of the average ambient RH.

Aerosol size distribution: Calculation of CDNC requires knowledge of the size distribution. As currently GMI simulates only aerosol mass, distributions are diagnosed from the online simulation by scaling prescribed distributions obtained from observations [136] to simulated aerosol sulfate, as described in *Sotiropoulou et al.* [233]. In these distributions, aerosol over marine regions is composed of 67 % insoluble material and 33 % ammonium sulfate in the fine mode, and, 95 % sea-salt and 5% insoluble material in the coarse mode. Aerosol over land is composed of 50 % insoluble material and 50 % ammonium sulfate in both the coarse and fine modes. The size distribution mode diameter, geometric standard deviation, and number concentration for marine and

continental aerosol are given in Table 1 of *Sotiropoulou et al.* [233]. The effect of assuming a constant aerosol size distribution is discussed in Section 9.4.

Entrainment rate: Two approaches are used to prescribe *e*. First, adiabaticity (i.e., the ratio of in-cloud LWC to its adiabatic value) is used as proxy for e/e_c, assuring consistency with LWC. Recent in situ observations report ~ 0.6 adiabaticity for small cumulus clouds [155]; this value is taken as upper limit and entrainment effects on CDNC, IF, and Q_{aut} are studied by carrying out simulations with effective *e* equal to $0.0e_c$ (adiabatic), $0.4e_c$, and $0.6e_c$. In the second approach used to diagnose *e*, average values of *e* derived from for LES simulations of shallow convective clouds reported by *Siebesma and Cuijpers* [231] are used; $e = 2 \times 10^{-3}$ m^{-1} for positively buoyant cloudy parcels ("core" case), and, $e = 3 \times 10^{-3}$ m^{-1} for all cloud parcels with positive LWC and *V* ("updraft" case). Similar values have been reported in other published studies [e.g., 159, 211, 72, 185], so $e = 2 \times 10^{-3}$-3×10^{-3} m^{-1} is considered representative of global clouds. The main difference between the two ways of prescribing *e* is that using an average e/e_c implies a spatial variation in *e* (as e_c depends on local RH and *T*, equation (2)), whereas setting *e*, implies a spatial variation in e/e_c; thus, the two approaches represent limits of variability in both *e* and e/e_c.

Updraft velocity: In addition to aerosol size distribution and *e*, CDNC calculation requires knowledge of *V* at the scale of cloud activation. Since this is not directly available in global models, *V* is constrained using values from field campaign studies; an average *V* is prescribed for "continental" and "marine" clouds equal to 1 m s^{-1} and 0.35 m s^{-1}, respectively [136, 233]. Although a simple approach, using a single *V* gives optimal

closure between observations and theory for cloud droplet calculations in cumulus and stratocumulus clouds, provided that it expresses the average vertical velocity distribution in the boundary layer [136, 165, 193, 60].

9.3. Results and Discussion

Entrainment tends to reduce s_{max}, hence the number of activated CCN (CDNC). The extent of the CDNC reduction (compared to assuming adiabatic activation) depends primarily on e/e_c and the characteristics of the aerosol population [11]. Studies are carried out varying e/e_c (Section 9.2.1) in the CDNC parameterization but keeping LWC as given by GMI (Section 9.2). This allows the study of the effect of assuming diabatic/adiabatic activation (Figure 9.1b, c) on IF while independently parameterizing LWC.

Entrainment effects during activation are expressed in terms of an absolute change,

$$\Delta X_{abs} = X - X_{adiabatic} \tag{9.4}$$

where X refers to the annual average of the variable being analyzed (e.g., CDNC, IF) under entraining conditions, and $X_{adiabatic}$ refers to its value assuming adiabatic activation (i.e., $e = 0$). Entrainment effects on X are also expressed in relative terms as

$$\Delta X_{rel} = 100 \frac{\Delta X_{abs}}{X_{adiabatic}} \% \tag{9.5}$$

9.3.1. Critical Entrainment Rate

To comprehend the effect of entrainment on CDNC it is useful to understand how e_c varies with location and meteorological field. Figure 9.2 presents the zonally averaged vertical distribution of e_c and RH for the meteorological fields used in this study. Based on reported values, the value of $T - T'$ was prescribed, equal to 1 K [191] (the sensitivity

of CDNC to the value of $T - T'$ is analyzed in section 9.3.5). High RH is associated with a large e_c, since stronger mixing is required to prevent cloud activation. This is evident in Figure 9.2 for the high midlatitude RH zones, especially in the boundary layer ($p > 800$ hPa). In the tropics (between 30S and 30N), high RH does not correlate as strongly with high e_c, because e_c scales inversely with surface T (as the term including $T - T'$ in Eq. (9.2)) is proportional to T^{-2}), which is highest at the tropics.
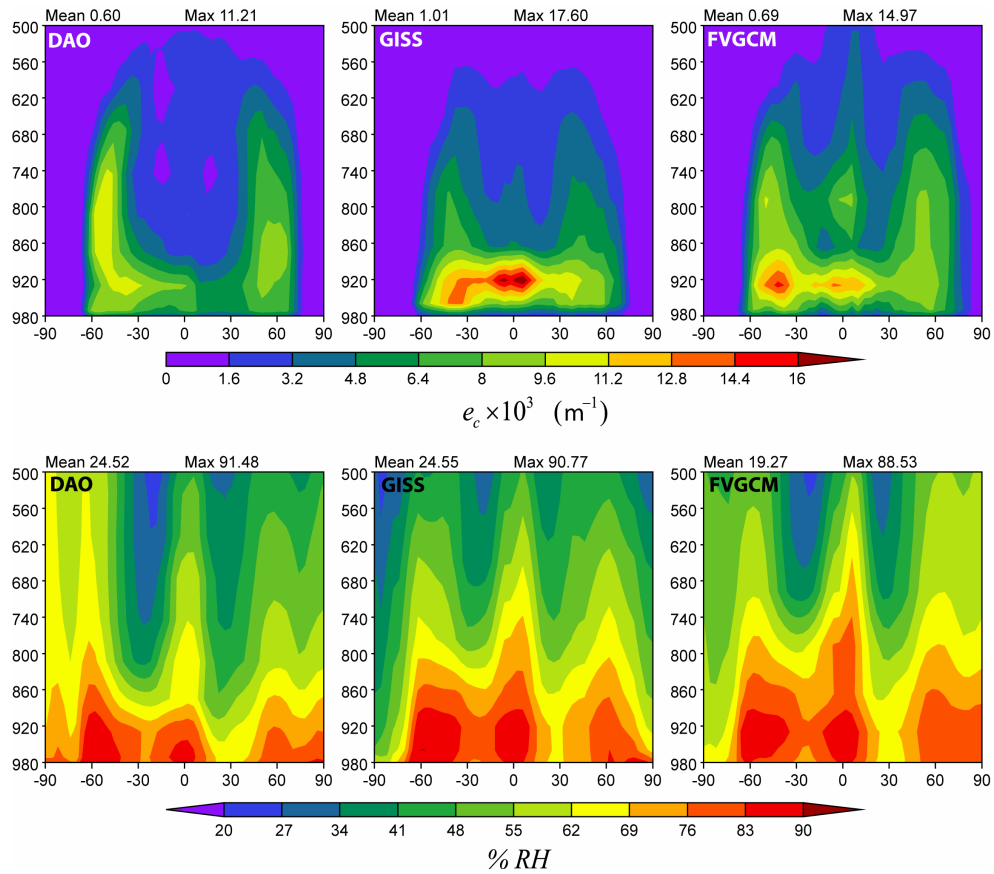
Figure 9.2. Zonal averaged vertical profiles of e_c (top panels) and *RH* (bottom panels) for DAO (left panels), GISS (central panels) and FVGCM (right panels) meteorology.

Global averaged e_c values (including points with $e_c \rightarrow 0$, i.e. upper levels in Figure 9.2) for the simulations in Figure 9.2 are 0.60×10^{-3}, 1.0×10^{-3}, and 0.69×10^{-3} m^{-1}, for DAO,

GISS, and FVGCM fields, respectively. These values are comparable to e obtained from LES simulations of shallow convective clouds [e.g., 231, 141, 139, 35, 72, 185] and from in-situ observations of cloud LWC profiles [e.g., 159, 211, 185].

9.3.2. Entrainment Effects on Droplet Number Concentration

Figure 9.3 presents the annual average CDNC for adiabatic conditions (i.e., using the adiabatic assumption) and $\Delta CDNC_{rel}$ (lower panels) for $T - T' = 1$ K and DAO (left), GISS (center), and FVGCM (right) meteorological fields. $\Delta CDNC_{rel}$ ranges from -6.9 to -8.6 % for $e = 0.4e_c$, and, -12.2 to -15.7 % for $e = 0.6e_c$. The largest $\Delta CNDC_{rel}$ ranges from -23 to -25 % for $e = 0.4e_c$, and -39 to -42 % for $e = 0.6e_c$. For the three meteorological fields used, $\Delta CNDC_{rel}$ is the largest in the tropics, downwind of large emission sources, and in South America and North Africa. The absolute CDNC change, $\Delta CDNC_{abs}$, is largest in regions of high CCN concentrations (i.e., high adiabatic CDNC) associated with regions of aerosol sources, and reaches values below -200 cm^{-3} for simulations with $e = 0.6e_c$ (Figure 9.4, top left panel); this behavior is rationalized below.

Parcel model simulations show that for constant e/e_c, the effect of entrainment strongly depends on the aerosol size distribution and composition (i.e., CCN spectrum) [11]. This is evident in Figure 9.4, which shows $\Delta CDNC_{abs}$ (left, upper panel) and $\Delta CDNC_{rel}$ (right, upper panel) against adiabatic CDNC for $e = 0.6e_c$ and all meteorological fields. $\Delta CDNC_{abs}$ is correlated ($R^2 = 0.67$) to the adiabatic CDNC; that is, areas with high CCN concentrations tend to display large changes in CDNC from entrainment effects. In a relative sense however, clouds with moderate CDNC (100 - 300

cm^{-3}) are most sensitive to entrainment ($\Delta CDNC_{rel} \sim$ -45%), whereas in regions with high

CDNC, $\Delta CDNC_{rel} \sim$ -20 %. At low levels of CDNC, $\Delta CDNC_{rel}$ tends to decrease, but

has a strong dependency on CDNC. The variability in RH and T cause the substantial

scatter seen in $\Delta CDNC_{rel}$ vs. CDNC, and, $\Delta CDNC_{abs}$ vs. CDNC.
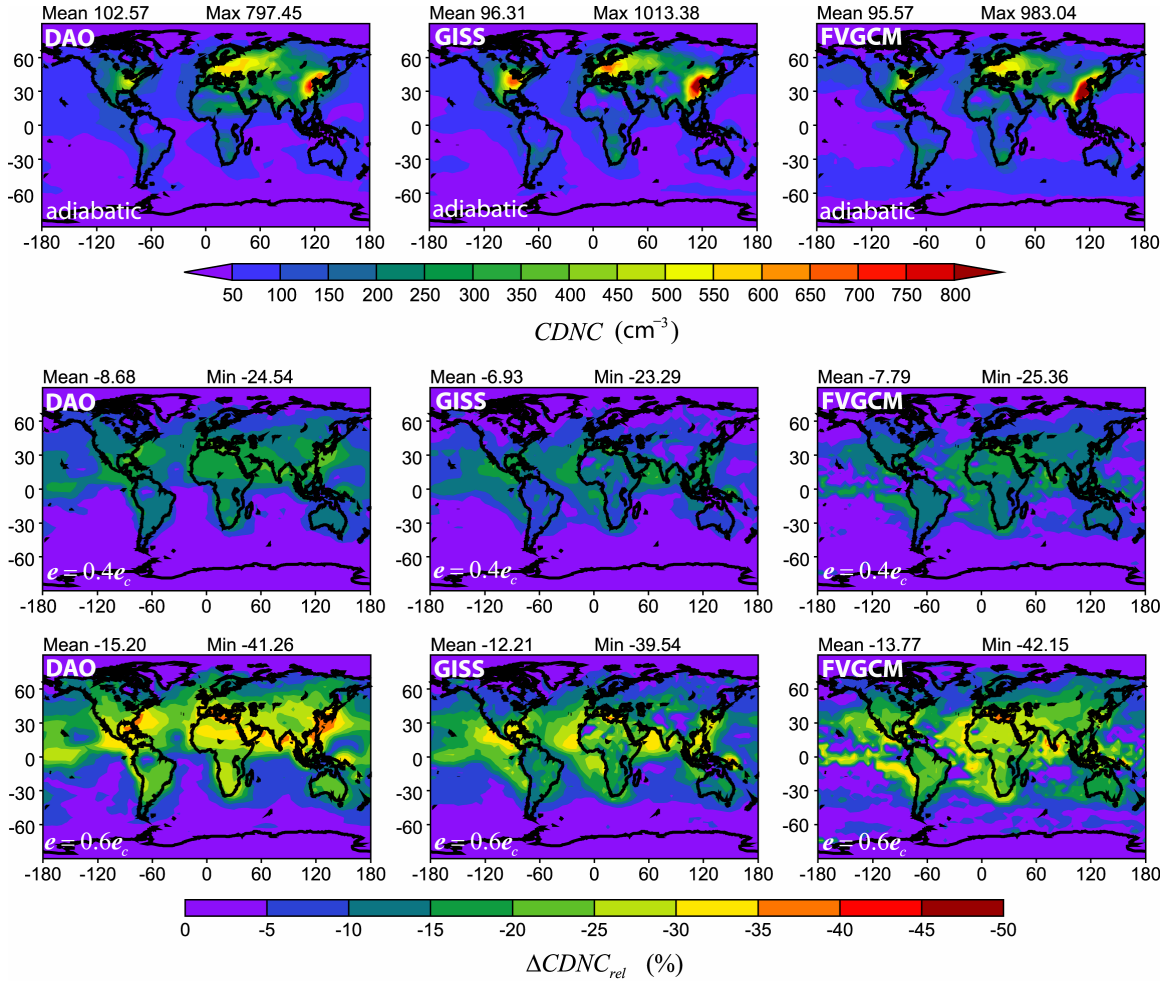
Figure 9.3. Annual adiabatic $CDNC$ (first level) and $\Delta CDNC_{rel}$ for the cases $e = 0.4e_c$ (middle panels) and $e = 0.6e_c$ (bottom panels), and $T - T' = 1K$. Simulations were performed using DAO (left panels), GISS (center panels) and FVGCM (right panels) meteorology. Quantities corresponding to second model layer.
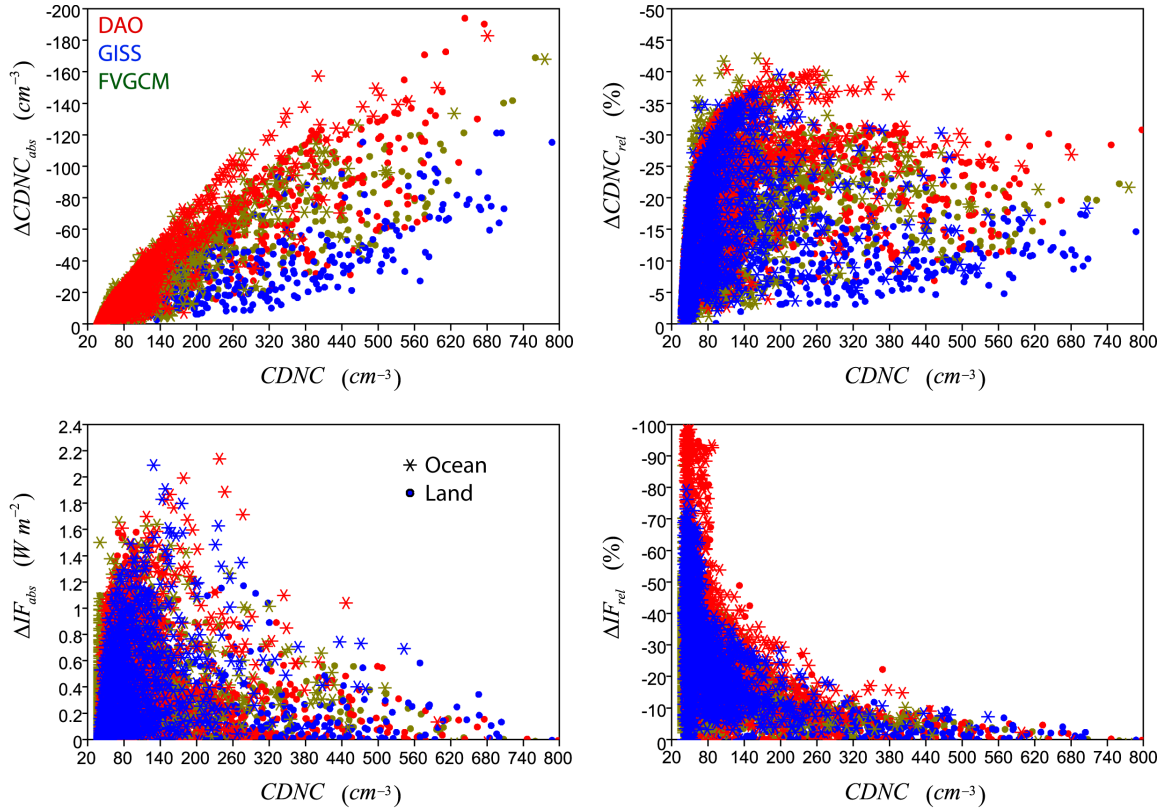
Figure 9.4. Annual $\Delta CDNC_{rel}$, $\Delta CDNC_{abs}$, ΔIF_{abs}, and ΔIF_{rel} as a function of adiabatic CDNC for $e = 0.6e_c$ and $T - T' = 1K$.

The dependency of $\Delta CDNC_{rel}$ on CDNC can be rationalized by considering the sensitivity of CDNC to s_{max} (i.e., the maximum supersaturation achieved during the parcel ascent, calculated for $\dfrac{ds}{dt} = 0$, Equation (9.1)). CCN particles activate into cloud droplets when, as result of cooling from expansion, s exceeds their critical supersaturation [208]. Thus, when s_{max} is reduced by entrainment, the response in CDNC depends on the slope of the CCN spectrum (i.e., the function relating the number of activated CCN and s) at s_{max}. Given that CCN spectra tend to have a sigmoidal shape

243

[e.g., 247, 163], the region where the activation fraction, CCN/CN, is close to 0.5 tends to be steepest (i.e., $dCCN/ds$ is high), while when $CCN/CN \rightarrow 1$, $dCCN/ds \rightarrow 0$. For low activation fractions, $dCCN/ds$ is non-zero but not very large. The dependence of $\Delta CDNC_{rel}$ on activation fraction is presented in Figure 9.5. If high s_{max} is reached, most of the aerosol particles activate and CDNC is not very sensitive to moderate variations in s_{max}. Since high s_{max} is characteristic of clean environments, $\Delta CDNC_{rel}$ and $\Delta CDNC_{abs}$ are low. For higher aerosol loads, CDNC is very sensitive to variations in s_{max}, as the CCN spectrum is very steep (CCN/CN between 0.2 and 0.5). However, for very large CCN concentration, s_{max} is low and the CCN spectrum is somewhat insensitive to changes in s_{max} (CCN/CN below 0.1).
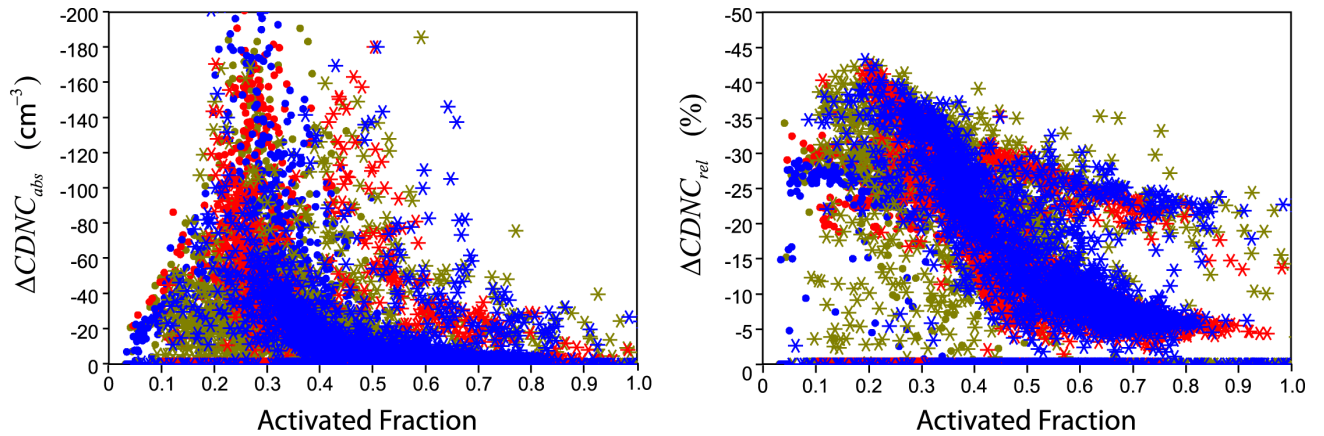
Figure 9.5. Annual $\Delta CDNC_{rel}$, $\Delta CDNC_{abs}$ as a function of aerosol activated fraction for $e = 0.6e_c$ and $T - T' = 1K$; colors and symbols similar to Figure 9.4.

Among the meteorological fields used, $\Delta CDNC_{rel}$ is the largest for DAO (-8.6 and -15.2 % for $e = 0.4e_c$ and $e = 0.6e_c$, respectively, Figure 9.3) and the lowest for GISS (-6.9 and -12.2%), reflecting differences in precursor aerosol concentrations between wind fields

[148]. Simulations using DAO result in moderate CDNC concentrations (100-300 cm^{-3}), hence significant $\Delta CDNC_{rel}$ over most of the northern hemisphere. A similar spatial variation is found using GISS (Figure 9.3), although $\Delta CDNC_{rel}$ is relatively lower. Compared to simulations with DAO and GISS, the usage of FVGCM fields show higher values of $\Delta CDNC_{rel}$ over the southern Atlantic ocean; global annual average $\Delta CDNC_{rel}$ however, is slightly lower than in the simulations using DAO. Figures 9.4 and 9.5 show significant scatter of $\Delta CDNC_{rel}$ and $\Delta CDNC_{abs}$ for all meteorological fields, reflecting the large variability of aerosol concentration in marine (stars) and continental (dots) environments, and the influence of local RH and *T*.

9.3.3. Entrainment Effects on Effective Radius and Autoconversion Rate

Entrainment in ambient clouds tends to reduce CDNC and LWC, leading to a reduction in cloud droplet size. In this study however, we examine the effects of entrainment on CDNC alone keeping LWC constant; hence entrainment, compared to assuming adiabatic activation (Figure 9.1b), increases average droplet size of the cloud droplets (Figure 9.1c). Table 9.1 shows mean and maximum global increase (compared to using the adiabatic assumption) in R_{eff} for the meteorological fields and range of *e* considered in this study. Large areas over the tropics (associated with high LWC and moderate CDNC, Figure 9.3) are characterized by ΔR_{eff} of about 1 μm. Differences in ΔR_{eff} between meteorological fields are quite significant, as the global $\Delta R_{eff,abs}$ from DAO simulations (0.21 and 0.40 μm for $e = 0.4e_c$ and $e = 0.6e_c$, respectively) is almost twice as large as found in FVGCM simulations (0.13 and 0.25 μm); this reflects the larger LWC predicted by DAO.

Table 9.1. Global mean (maximum) $\Delta R_{eff,abs}$ (μm) for the runs using constant e/e_c

e/e_c	T-T' (K)	DAO	GISS	FVGCM
0.4	1.0	0.21 (0.59)	0.16 (0.57)	0.13 (0.55)
0.6	1.0	0.40 (1.19)	0.31 (1.15)	0.25 (1.12)
0.4	Eq.(9.6)	0.25 (0.59)	0.22 (0.58)	0.21 (0.58)
0.6	Eq.(9.6)	0.48 (1.19)	0.43 (1.15)	0.41 (1.16)

A lower CDNC implies that autoconversion will increase if q_l and C_l are constant Eq. (9.3)). This is shown in Figure 9.6, which presents the ratio of Q_{aut} to its "adiabatic" value $Q_{aut,ad}$ (i.e., for $e = 0$), for the range of e and meteorological fields considered in this study. Neglecting entrainment effects on CDNC would underestimate global Q_{aut} between 9 and 12 % for $e = 0.4e_c$ and between 20 and 26 % for $e = 0.6e_c$; locally, Q_{aut} is affected by a factor of two. Thus, accounting for entrainment effects on activation would increase the model's precipitation rates with implications for cloud coverage and lifetime, and the second indirect effect [e.g., 4]. However, if the increased entrainment is accompanied with an increased rate of droplet evaporation, the net increase in Q_{aut} may be negligible [e.g., 99, 257]. Although the global mean $Q_{aut}/Q_{aut,ad}$ is similar for all meteorological fields used, the regional $Q_{aut}/Q_{aut,ad}$ is the largest in Central America and Northern Africa for the DAO simulation whereas for GISS and FVGCM it is the largest in the tropical Atlantic and Pacific oceans. This is because $\Delta CDNC_{rel}$ tends to be larger in marine environments for simulations with the FVGCM and GISS fields, while smaller for the DAO simulations (Figure 9.3).
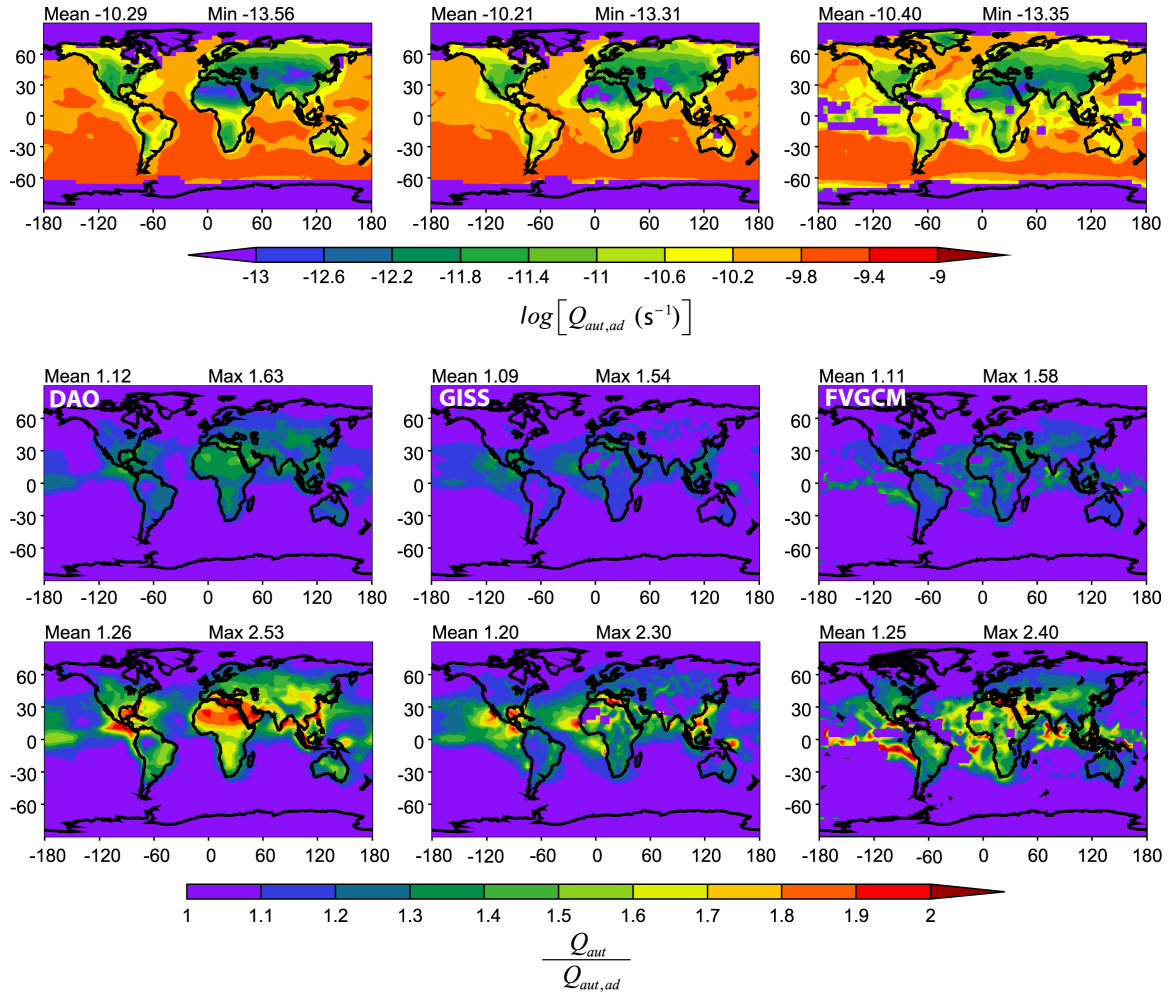
Figure 9.6. Similar to Figure 9.3, but for adiabatic Q_{aut} (upper panels) and $Q_{aut}/Q_{aut,ad}$ (middle and bottom panels).

9.3.4. Entrainment Effects on Indirect Forcing

The low slope of the CCN spectrum at high s_{max} implies that CDNC is less sensitive to entrainment during preindustrial (because low aerosol loads mean a higher activation ratio than for present day) than for present day conditions. $\Delta CDNC_{rel}$ in the preindustrial simulation is lower than for present day simulations, reaching global means around -4 %

and -8 % for $e = 0.4e_c$ and $e = 0.6e_c$, respectively. Thus, entrainment is expected to reduce the magnitude of IF, compared to that computed from adiabatic activation. Figure 9.7 presents the annual average adiabatic IF and ΔIF_{abs} for all meteorological fields of this study, and for $e = 0.4e_c$ and $e = 0.6e_c$. Global mean ΔIF_{abs} ranges from 0.11 to 0.14 W m^{-2} for $e = 0.4e_c$ and from 0.22 to 0.28 W m^{-2} for $e = 0.6e_c$. These values correspond to a global mean ΔIF_{rel} of -7 to -14% for $e = 0.4e_c$, and, of -17 to -25% for $e = 0.6e_c$. Locally, entrainment effects may cancel the indirect effect ($\Delta IF_{rel} \rightarrow 100\%$) in areas of the tropics with very low adiabatic IF. However, in terms of the absolute reduction in IF, ΔIF_{abs} is the strongest (~2.4 W m^{-2}) in regions with moderate adiabatic IF (~-5 W m^{-2}).

Figure 9.4 (lower panels) shows the relation of ΔIF_{abs} and ΔIF_{rel} with adiabatic CDNC. ΔIF_{rel} is the largest at very low CDNC, consistent with the high susceptibility of cloud albedo to CDNC in clean clouds [249], and decreases below -10% for CDNC greater than 300 cm^{-3}. However, the largest ΔIF_{abs}, reaching about 2.4 W m^{-2} (Figure 9.4, lower left panel), is found at moderate CCN concentrations where $\Delta CDNC_{rel}$ is largest (~-40%). Because of this, marine environments with moderate CCN concentration display a larger ΔIF_{abs} (maximum around 2.4 W m^{-2}) compared to over land where the maximum ΔIF_{abs} is ~ 1.5 W m^{-2} ($\Delta CDNC_{rel} \sim$ -35%). ΔIF_{abs} and ΔIF_{rel} are small at large CDNC because the albedo of very polluted clouds is insensitive to variations in CCN concentration [249].
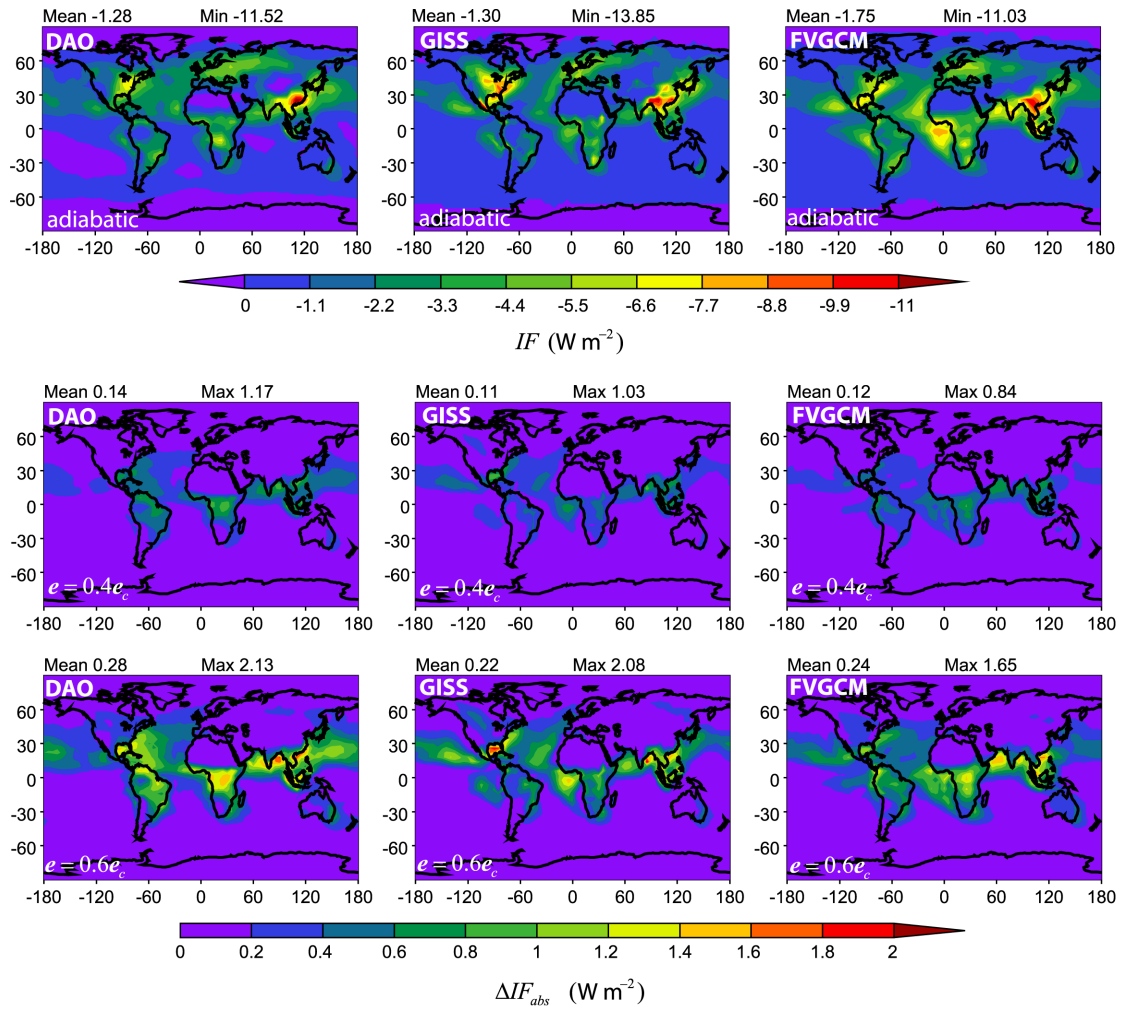
Figure 9.7. Similar as Figure 9.3, but for adiabatic *IF* (upper panels) and ΔIF_{abs} (middle and bottom panels).

The largest global ΔIF_{abs} (Figure 9.7, lower panels) is found for the simulations using the

DAO field, consistent with the highest $\Delta R_{eff,abs}$ and $\Delta CNDC_{rel}$ seen of all three fields.

Global ΔIF_{abs} for GISS is about 0.04 W m^{-2} below DAO values for both, $e = 0.4e_c$ and

$e = 0.6e_c$. Although the largest ΔIF_{abs} is located in the tropics, using DAO fields tends to

concentrate ΔIF_{abs} near the continents, whereas for simulations with GISS and FVGCM

fields, ΔIF_{abs} is largest in the tropical oceans.

9.3.5. Simulations Using Ambient Temperature Difference Diagnosed from LWC

To study sensitivity of our conclusions to local differences between T and T' profiles, the

value of T-T' is approximated using the latent heat released during cloud formation and

assuming that it uniformly raises T. Using the grid cell LWC and cloud fraction C_l,

$$T - T' \approx \left(\frac{\Delta H_v}{c_p} \right) \left(\frac{LWC}{C_l} \right) \tag{9.6}$$

calculated in this way, global average T-T' is about 0.3 K for the three meteorological

fields, with T-T' in marine environments being slightly higher ($\sim$ 0.4 K) due to the larger

LWC in these regions (not shown). Global mean e_c, by application of Eq. (9.2), ranges

from 0.4×10^{-3} to 0.8×10^{-3} m^{-1}, and is slightly below the value of e_c (0.6×10^{-3} to 1.0×10^{-3}

m^{-1}) obtained using a fixed T-T'= 1 K (Figure 9.2). Similar to Figure 9.2, e_c in tropical

marine environments is below the global average due to the higher T associated with

these regions (section 9.3.1).

Using T-T' diagnosed from LWC, the global mean $\Delta CDNC_{rel}$ ranges between -10 % and

-12 % for $e = 0.4e_c$, and, from -17 % to -21 % for $e = 0.6e_c$ (Figure 9.8). $\Delta CDNC_{abs}$

ranges between -13 and -15 cm^{-3} for $e = 0.4e_c$, and, from -23 to -25 cm^{-3} for $e = 0.6e_c$;

the minimum $\Delta CDNC_{abs}$ is close to -350 cm^{-3}. Compared to assuming a fixed T-T'= 1 K

(Figure 9.3), $\Delta CDNC_{rel}$ is larger by about 2 to 3%. Global mean ΔIF_{abs} ranges from 0.17

to 0.19 W m^{-2} for $e = 0.4e_c$, and, from 0.32 to 0.39 W m^{-2} for $e = 0.6e_c$ (Figure 9.9).

These values are about 0.1 W m^{-2} larger than for T-T'= 1 K (Figure 9.7). The global $\Delta CDNC_{rel}$ is the largest for simulations made using the FVGCM field; however, global ΔIF_{abs} (Figure 9.9, left panel) is still the largest for simulations made with DAO, as $\Delta R_{eff,abs}$ changes the most amongst all meteorological fields used (Table 9.1).
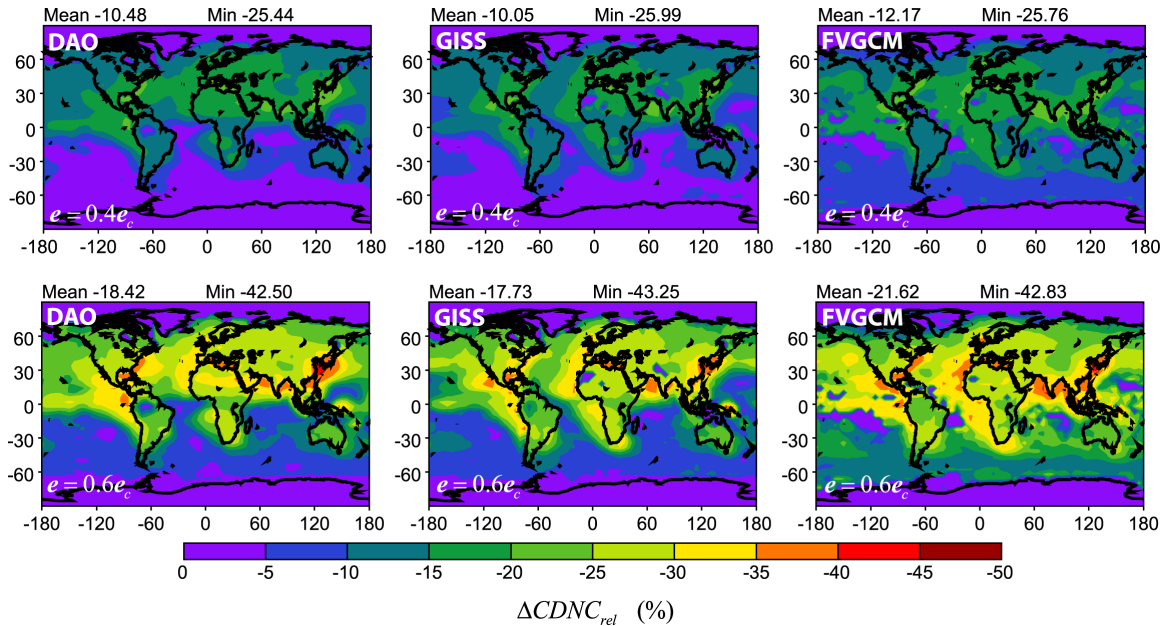
Figure 9.8. Annual $\Delta CDNC_{rel}$ for $e = 0.4 e_c$ (upper panels) and $e = 0.6 e_c$ (lower panels). $T - T'$ is calculated using Eq. (9.6). Simulations were done using DAO (left panels), GISS (center panels) and FVGCM (right panels) meteorology.

The correlation between adiabatic CDNC and $\Delta CDNC_{rel}$ (Figure 9.10, left panel) shows significantly less scatter than for prescribing T-T'= 1 K (Figure 9.4); this is because Eq. (9.6) gives T-T' that is consistent with the grid LWC and RH. The two "branches" that appear are a result of using two prescribed aerosol distributions (marine, continental, section 9.2.2). Figure 9.10 shows that marine environments are more sensitive to entrainment (maximum $\Delta CDNC_{rel}$ ~-45%) than continental regions (maximum

251

$\Delta CDNC_{rel} \sim -30\%$). However, unlike in simulations with constant $T\text{-}T' = 1$ K, $\Delta CDNC_{rel}$

does not decrease at high CDNC and remains almost constant as CDNC increases. As in

the case with $T\text{-}T' = 1$ K (Figure 9.4), IF is more sensitive to entrainment for moderate

CCN concentrations (Figure 9.10, left panel), where roughly 50 % of the aerosol activates

and s_{max} lies in the steepest region of the CCN spectrum.
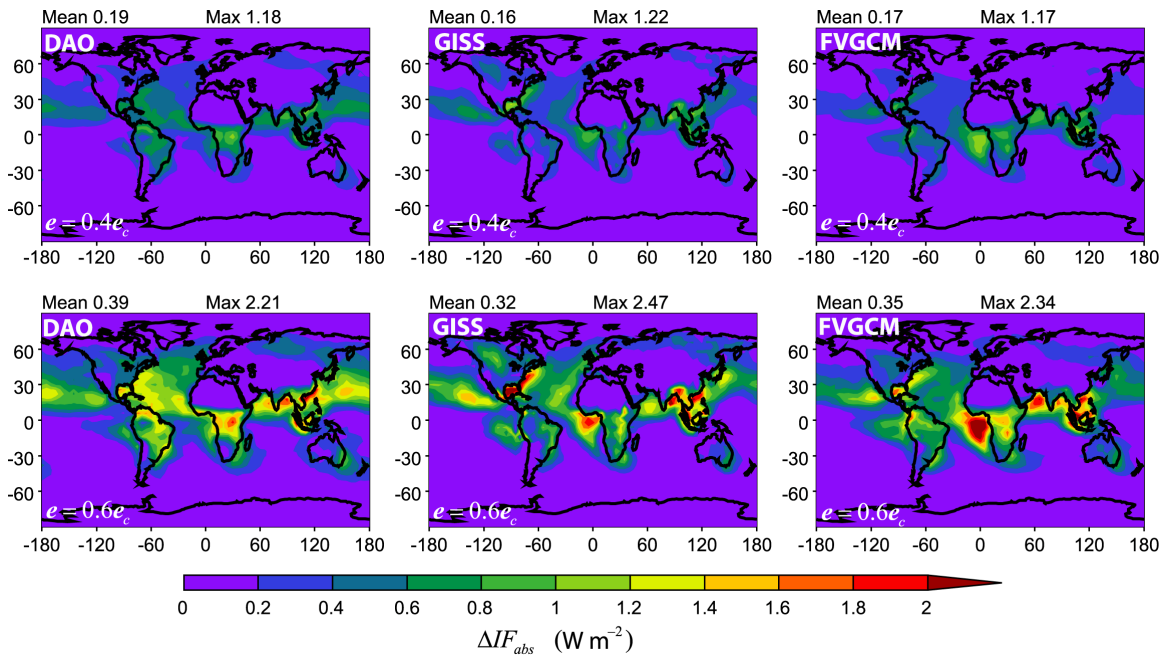
Figure 9.9. Similar as Figure 9.8, but for adiabatic *IF* (upper panels) and ΔIF_{abs} (middle and bottom panels).
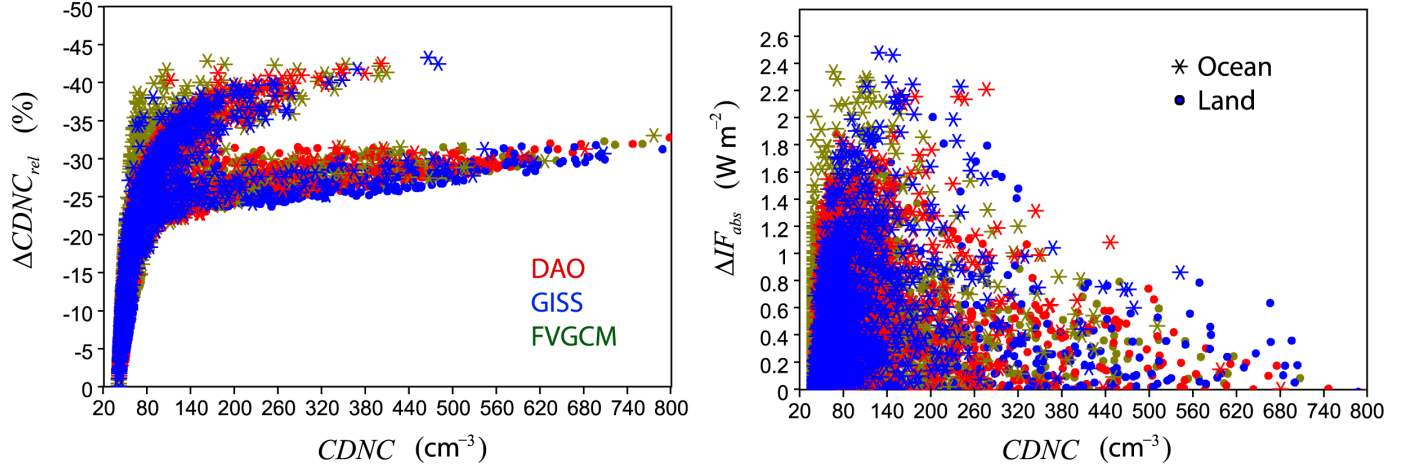
Figure 9.10. Annual $\Delta CDNC_{rel}$ and ΔIF_{abs} as a function of adiabatic CDNC for $e = 0.6 e_c$ and $T - T'$ calculated using Eq. (9.6).

9.3.6. Simulations using Prescribed e

The ratio e/e_c in all simulations has been kept constant; e however is known to be a strong function of the cloud dynamics (i.e., velocity fields, buoyancy and turbulence level) [e.g., 236, 211, 231, 100, 167, 35, 185]. Hence, it is important to explore the sensitivity of our conclusions to variations in e which are independent of e_c.

Prescribing a fixed e implies variability in e/e_c, as e_c is determined by the local thermodynamic conditions. Figure 9.11 (upper level) presents the global distribution of e/e_c for $e = 2 \times 10^{-3}$ m^{-1} (left panels) and $e = 3 \times 10^{-3}$ m^{-1} (right panels), using the GISS meteorological field; global average e/e_c is 0.34 and 0.48, respectively. In the tropics, e/e_c is much above the global average, approaching 0.9, which is explained by the low value of e_c in this region (see section 9.3.1). This suggests that CDNC in the tropics may be more susceptible to neglecting entrainment effects than implied in the simulations with

constant e/e_c, and is reflected in the simulated $\Delta CDNC_{rel}$, $\Delta R_{eff,abs}$, $Q_{aut}/Q_{aut,ad}$, and

ΔIF_{abs} (Figure 9.11). $\Delta CDNC_{rel}$ (second level) ranges between -13% and -20%, which is slightly above those obtained using prescribed e/e_c (Figure 9.8, middle panels). However, $\Delta CDNC_{rel}$ is much larger around the tropics, being as much as -70%.

The lower CDNC when considering entrainment also produces an increased $\Delta R_{eff,abs}$ which is on average 0.3 and 0.6 μm for the core ($e = 2 \times 10^{-3}$ m^{-1}) and updraft ($e = 3 \times 10^{-3}$ m^{-1}) cases, respectively; it is also about 0.1 μm larger than in the simulations assuming constant e/e_c (Table 9.1). The local effects on effective radius can also be large, with $\Delta R_{eff,abs}$ up to 3.0 μm in the tropics (Figure 9.11). Global mean autoconversion rates are increased by a factor of 1.2 in the core case and 1.7 in the updraft case, with respect to assuming adiabatic activation (Figure 9.11). In the tropics, the increase in Q_{aut} can be very high for $e = 3 \times 10^{-3}$ m^{-1}, which is more significant over land (i.e., Central America and Southern Africa). The change in $\Delta CDNC_{rel}$ and $\Delta R_{eff,abs}$, compared to assuming a fixed e/e_c, imply that the pattern in IF may also be substantially affected. Indeed, ΔIF_{abs} ranges between 0.23 and 0.40 W m^{-2} (Figure 9.11) and is globally about 0.1 W m^{-2} greater than assuming a prescribed e/e_c (Figure 9.9, middle panels). This increase results mainly from an increased ΔIF_{abs} in the tropics, which can be as high as 3.5 W m^{-2}.
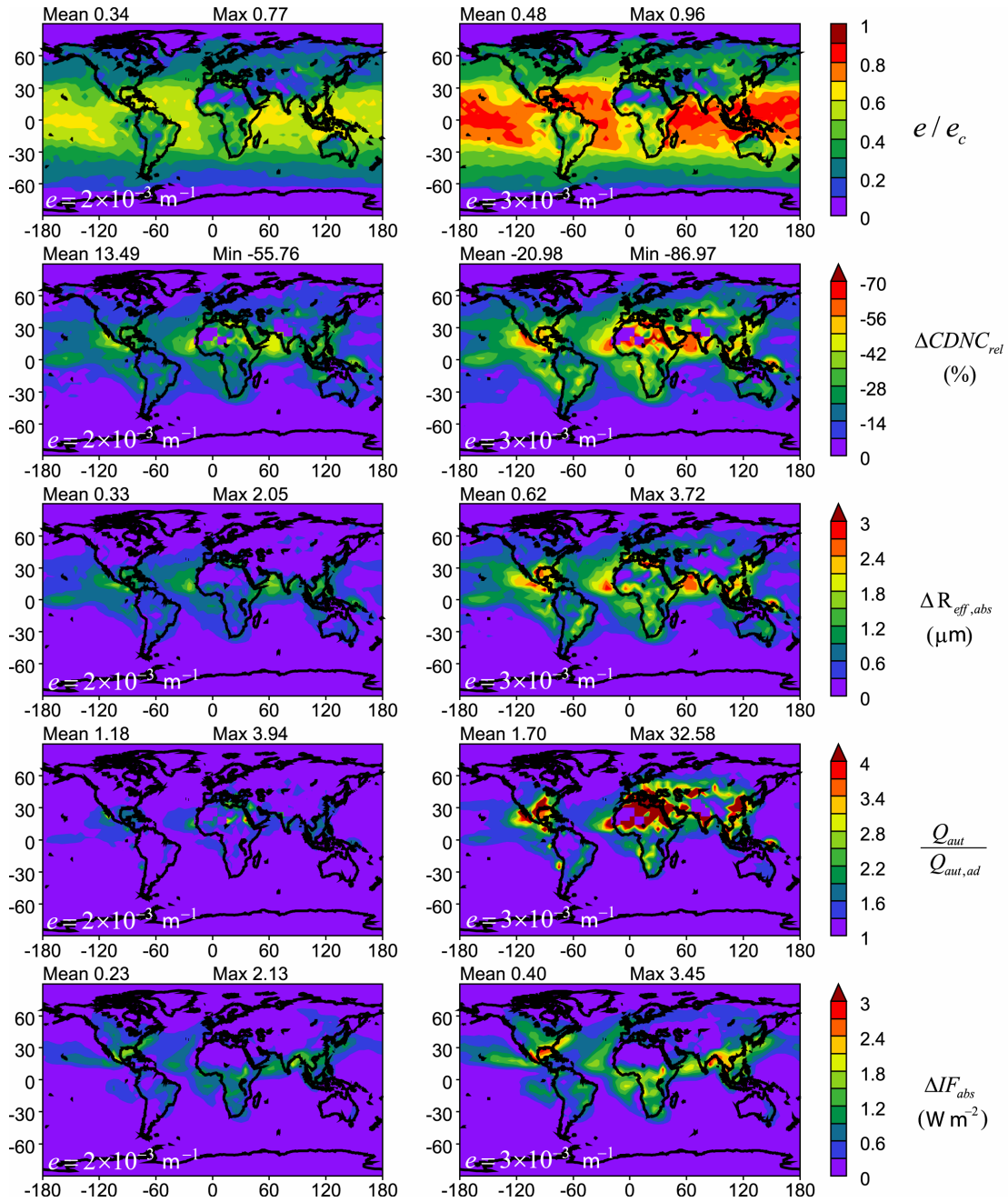
Figure 9.11. Annual global distribution of e/e_c, $\Delta CDNC_{rel}$, $\Delta R_{eff,abs}$, $Q_{aut}\big/Q_{aut,ad}$ and ΔIF_{abs}, for $e = 2\times 10^{-3}$ m^{-1} (left panels) and $e = 3\times 10^{-3}$ m^{-1} (right panels), using GISS meteorology and $T - T'$ calculated from Eq. (9.6).

9.3.7. CDNC Sensitivity to V and e

Finally, we consider the combined effect of entrainment and velocity fluctuations on CDNC. We postulate that the effect on variations in V may be "damped" by an equivalent change in e; this is because an increase in V correlates CDNC, while e is anticorrelated with CDNC. This can be illustrated using a simplified model, as follows. If $0.8 > e/e_c > 0.1$, CDNC relates linearly with e as [11],

$$CDNC \approx CDNC_{ad}\left(1 - \frac{e}{e_c}\right) \tag{9.7}$$

where $CDNC_{ad}$ is the CDNC activated assuming adiabaticity. The dependency of CDNC on V can be approximated as

$$CDNC \approx kV^n \tag{9.8}$$

where k and n depend on cloud formation conditions (T, p, aerosol characteristics). In general n ranges between 0.3 and 1 [136, 31]; for the purpose of this study we select $n \approx 0.5$ [248]. Equations (9.7) and (9.8) can be combined to find the value of entrainment, e_2, required to maintain CDNC constant, when updraft velocity changes from V_1 to V_2,

$$\frac{e_2}{e_c} = \frac{e_1}{e_c} + \left(1 - \frac{e_1}{e_c}\right)\left[\left(\frac{V_2}{V_1}\right)^n - 1\right] \tag{9.9}$$

where e_1 is the entrainment level at V_1.

To illustrate the dampening effect of entrainment on CDNC variability from V fluctuations, we assume that $\dfrac{e}{e_c}$ is (to first order) proportional to V [178],

$$\frac{e_2}{e_c} \approx \frac{e_1}{e_c}\left(\frac{V_2}{V_1}\right) \qquad\qquad (9.10)$$

The relation between e and V, however, may depend on the local level of turbulence and the dynamics of the cloudy parcel [100]. Equations (9.9) and (9.10) indicate that the dampening effect depends on e_1/e_c, which is illustrated in Figure 9.12;
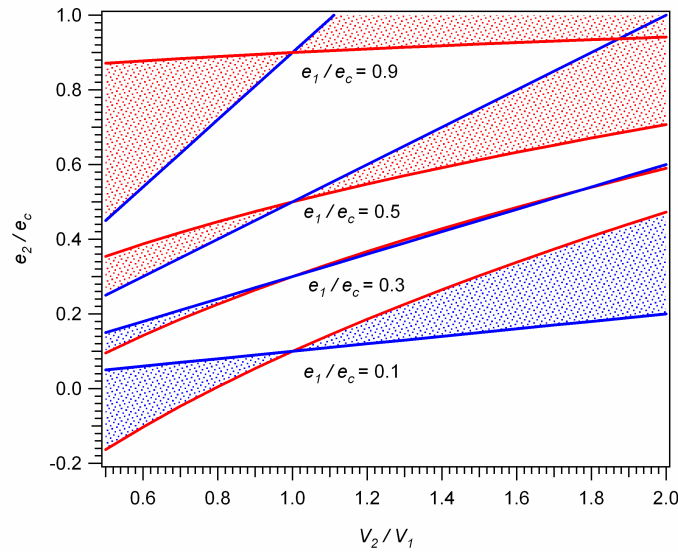
Figure 9.12. Dampening effects of e on V fluctuations. Red shadow indicates combinations of e_1, e_2, and V_1/V_2 where the dampening effect takes place. Blue shadow indicates areas where entrainment does not influence CDNC. Red and blue lines represent Eqs. (9.9) and (9.10), respectively, for each initial entrainment level, $\dfrac{e_1}{e_c}$.

At $e_1/e_c = 0.1$ (close to adiabatic activation) CDNC is not very sensitive to variations in e, and responds strongly to changes in V (blue area). However, as e_1/e_c increases, CDNC is increasingly sensitive to e, and, the dampening effect becomes important (i.e., an increase in e cancels the effect from an increase in V and vice versa), which occurs for $e_1/e_c > 0.3$ (red shaded areas). Given that typical values of e/e_c are above 0.4 (section

2.2), it is likely that entrainment will partially cancel the effect of V fluctuations on CDNC. The magnitude of the effect, however, will depend on the local e/e_c and the relationship between e and V.

9.4. Discussion and Conclusions

The sensitivity of CDNC, IF, R_{eff}, and Q_{aut} to neglecting entrainment in cloud activation parameterizations was studied under several scenarios, and using three different meteorological fields. By carrying out simulations using constant e/e_c and $T-T'$, the effect of aerosol size distribution and load was studied. It was shown that areas with moderate CCN concentration (i.e., activated fraction between 0.2 and 0.5) are most prone to entrainment effects (and therefore may produce a larger bias in R_{eff} when adiabatic CDNC is assumed) as the CCN spectrum is at its steepest, and CDNC most sensitive to variations in s_{max}. When the spatial variability in $T-T'$ and e/e_c was considered, entrainment effects on CDNC, R_{eff}, Q_{aut} and IF were enhanced, with respect to the runs assuming a constant e/e_c, particularly in the tropics where both $T-T'$ and e_c were the lowest.

In general, considering entrainment effects on droplet formation reduced CDNC in all simulations with respect to adiabatic activation; the largest reduction (up to -75%.) was found in the tropics with moderate CCN concentrations. The reduction in CDNC persistently resulted in larger R_{eff} by as much as 3.5 μm over the tropical oceans, and, can partially offset the underestimation in R_{eff} often found in GCM studies [233]. In turn, the CDNC bias from neglecting entrainment effects on droplet number may increase the global mean Q_{aut} by a factor of 1.1 to 1.7, and as high as a factor of 4 in the tropics; IF

may be overestimated between 0.2 and 0.4 W m^{-2}. In all cases, the bias in indirect forcing from neglecting entrainment during droplet activation was more significant for the DAO meteorological field than for GISS and FVGCM as $\Delta CDNC_{rel}$ and $\Delta R_{eff,abs}$ were higher for these simulations.

Using adiabaticity as a proxy for e/e_c assures that our approach is consistent with current observations of the entrainment effect on LWC. However, since e/e_c varies throughout the globe, we considered simulations for which e was constrained using LES simulations and field observations. This, together with diagnosing $T-T'$ from cloud LWC, may be a more accurate representation of T-T' and e/e_c variability. Our results show that IF and CDNC are quite sensitive to the prescribed value of e. Increasing e from 2×10^{-3} to 3×10^{-3} m^{-1} would decrease global mean $\Delta CDNC_{rel}$ between -13 and -20 % and increase the global mean ΔIF_{abs} from 0.23 to 0.40 W m^{-2}. Thus, neglecting entrainment would add about up to 40% uncertainty to estimations of the aerosol indirect effect. As e can vary between 0.5×10^{-3} and 4×10^{-3} m^{-1}, small e variations could largely affect IF assessments (e.g., $e = 4 \times 10^{-3}$ m^{-1} results in about 50% reduction in IF) hence e effects on CDNC (particularly in the tropics where these effects are more significant) may need to be considered in GCM studies.

Finally, we have shown that for the entrainment levels relevant for global clouds, diabatic CDNC vary significantly less with updraft velocity than for adiabatic conditions. This means that GCM simulations are less sensitive to errors and fluctuations in cloud-scale updraft velocity, as changes in CDNC due to positive (negative) bias in updraft

velocity can be partially compensated by a negative (positive) bias from entrainment effects.

An important assumption used in this study is that mixing between cloudy and cloud-free air is instantaneous and homogeneous. In our approach, e and e/e_c represent "effective" mixing rates that would account for the net effect of mixing processes throughout the cloud column, i.e., the reduction in CDNC with respect to adiabatic activation. The main effect of entrainment considered is therefore the redistribution of liquid water into fewer droplets, increasing their average sizes with respect to adiabatic conditions. The errors associated with this approach to describe the effects of inhomogeneous mixing and partial droplet evaporation requires an analysis using ambient cloud data and will be the subject of a future study. Nevertheless, we expect our approach to capture, to first order, the salient effects from entrainment.

Another important assumption is that aerosol distributions are prescribed and scaled to aerosol mass. Although this approach is known to introduce uncertainties in the predicted CCN spectrum (e.g., *Sotiropoulou, et al.* [233]), the conclusions of the present study are not affected, as we are studying the relative impact of entrainment on CDNC, R_{eff}, and IF. Including dynamical and hydrological feedbacks from changes in the radiative balance and autoconversion can dampen (or magnify) the magnitude of CDNC responses to entrainment. All these issues are important and require the application of fully coupled climate model with explicit aerosol microphysics. The current study however clearly shows that neglecting entrainment effects on cloud droplet formation can lead to important biases in predicted cloud microphysical properties.

CHAPTER 10

FUTURE DIRECTIONS

The interaction of many physicochemical processes (deliquescence, dissolution, freezing, activation, growth, sedimentation), occurring at very different scales, during cloud formation introduces challenges to the accurate representation of cloud formation in large-scale atmospheric models. The analytical methods developed in this work represent a step toward achieving such a representation. It is shown that accurate parameterizations can be developed by identifying rate-controlling steps in cloud formation. Thus, a framework is provided that links small-scale processes, dependent on the physicochemical properties of microscopic particles, to observable quantities of clouds like ice and liquid water content, particle size, and number. Chapters 5, 6, and 9, demonstrate that this approach can be very useful in the assessment of the effect of aerosol emissions on global climate and in elucidating the mechanisms that control the evolution of clouds in the atmosphere.

The ice cloud formation framework developed in this work allows the physically-based, computationally efficient, and rigorous description of the formation of ice crystals in atmospheric models. Unlike previous approaches, the new framework analytically reveals the dependency of maximum supersaturation and ice crystal number concentration on conditions of cloud formation, vertical velocity, and aerosol concentration and freezing properties. This framework also provides a benchmark for comparison of different heterogeneous freezing spectra derived either theoretically or

empirically, and for the interpretation of cloud campaign and satellite data. Application of the new framework in an atmospheric model showed that the global properties of cirrus clouds are highly sensitive to heterogeneous freezing, and for the first time allowed the comparison different descriptions heterogeneous freezing within the same dynamic framework in a global modeling context.

Dynamic equilibrium states characterized by the interplay of sedimentation, transport, and nucleation in cirrus clouds were discovered. With this, a new picture of cloud evolution emerged where large scale motion "modulates" a highly dynamic, chaotic cloud field, in which small vertical velocity disturbances can be amplified and propagated to the whole volume of the cloud, ultimately displaying order and pattern formation. The consequences may be quite profound. Clouds in dynamic equilibrium are much less sensitive to aerosols emissions, but at the same time exhibit characteristics strikingly different to the "classical picture" of cirrus formation. For instance, cirrus clouds can remain supersaturated (or subsaturated) for very long periods of time. They can exhibit constant ice crystal production, broad size distributions, and extended pockets of very high supersaturation. These characteristics of cirrus at low temperature can now be understood as the natural response of a highly non-linear system to external perturbation (i.e., large scale dynamic forcing). A question rises whether these states are particular to cirrus clouds or exist in convective systems, mixed-phase, and stratocumulus clouds. Should the latter be the case, a new branch of study will emerge in cloud physics, devoted to finding the favorable conditions for the occurrence of dynamic equilibrium in clouds.

The effect of entrainment and giant CCN on cloud droplet formation was also studied by developing corrections applicable to current cloud formation parameterizations. The development of "corrections" extents the applicability of sophisticated liquid cloud formation parameterization currently available, avoiding their re-derivation and re-implementation in atmospheric models. Accounting for entrainment and giant CCN effects in this fashion helps to understand biases in current aerosol indirect effect studies. The flexibility of the entrainment model developed in this work makes it applicable to other types of clouds (e.g., cirrus and cumulonimbus), and can be extended to account for entrainment in the parameterization of large scale convection in climate models. The approach developed for including giant CCN effects on cloud droplet formation also follows this paradigm.

The methods used in the development of the parameterizations of cold and warm cloud formation presented in this thesis can be extended to the formulation of parameterizations for the formation of mixed-phase clouds. The dynamics of mixed-phase clouds is however very complex and parcels likely interact during cloud formation. Furthermore, mixed-phased clouds can remain in the atmosphere for very long time before dissipating, therefore the effect of preexisting ice crystals and liquid droplets should be accounted for. The stochastic approach presented in Chapter 6 (which takes into account the local depletion of water vapor by preexisting particles) is suited for such a purpose. Collision and coalescence between droplets and ice crystals may however be quite efficient (due to their different sizes) and must be taken into account in the parameterizations. For this, the size distribution resulting from the mixing parcels with different histories within the cloud should be calculated.

The frameworks developed in this study are based on the general type of particle population balance equations known as "condensation/evaporation equations". They are a special case of the general dynamic equations [65-66] in which the size of the particles is mainly dictated by diffusion. Many industrial processes share this feature [66], including the manufacturing of particulate materials by chemical vapor deposition [65], crystallization [222, 210], and combustion [157]. The analytical solutions developed in this work can serve as a first estimate in optimization and process design, and can be incorporated in the real time control of chemical processes, which requires fast and computationally efficient estimates of production variables.

The application of the framework developed here requires input variables at the relevant scale of cloud formation (i.e., tenths of meters), which is currently not resolved in large scale atmospheric models. Cloud droplet and ice crystal number and size are very sensitive to the vertical wind that forces cloud formation and to the characteristics (size and composition) of the precursor aerosol. Efforts should be oriented towards the accurate calculation of the sub-grid scale distribution of these variables. Comparison of cloud field campaign data against satellite retrievals can be useful for this purpose. The input parameters measured in situ can be used along with the framework developed in this thesis to estimate large-scale, retrievable, characteristics of the cloud, and infer the appropriate scaling and averaging arguments. All models developed in this thesis are based on the Lagrangian parcel model approach. Although most clouds do not form by the movement of a single parcel they can be modeled using a distribution of cloud formation conditions. The question however remains as to what the right form of such distribution is. Many developments have been made in this direction; however cloud field

campaign data as well as satellite retrievals are required to evaluate and further constrain the results of parcel models.

The parameters determining the formation and growth of cloud droplets and ice crystals are still uncertain. In particular, the role of organics on the growth of cloud droplets still needs to be accounted for. Regarding ice production, efforts are needed on the study of the conditions that trigger heterogeneous freezing and on the nature of ice nuclei. Laboratory studies and cloud field campaign are required for this purpose. The heterogeneous framework developed in chapter five can be used to interpret field campaign data in terms of the ice nucleation spectrum. If concurrent measurements of aerosol composition and size, and vertical velocity, are available, it can also help to elucidate the water vapor uptake coefficient characteristic of ice crystal growth. For the later, a "capacitance factor" in the equations of growth can be included to account for the shape of ice crystals altering growth rates, which may impact the growth of large ice crystals ($D_c > 100$ μm).

Cloud formation is a highly complex process in which many subprocesses interact. Because of this cloud properties exhibit highly nonlinear responses to external forcing. At the same time, they are elements of the even more complex climate system. The susceptibility of clouds to aerosol emissions from human activities implies an associated climatic response, which so far seems to be a general increase in the planetary reflectivity to increasing levels of aerosol. This may however be only the small-scale and first order response. The self-organization behavior characteristic of many components of the climate system (as exemplified in Chapter 6 for cirrus clouds), and of climate itself, may result in amplification of perturbations, and bifurcation to new states. The high sensitivity

of climate to cloud properties indicates that cloud formation may play a key role in this process. Understanding clouds is therefore crucial to understand when and how those new climate states will onset, and whether our current life style will be still compatible with them. In conclusion, theory and observations must be tightly integrated to understand the effect of human activities on clouds and climate; the theoretical and modeling frameworks developed in this thesis can help achieve this.

REFERENCES

[1]   ABBATT, J. P. D., BENZ, S., CZICZO, D. J., KANJI, Z. and MÖHLER, O. (2006). Solid ammonium sulfate as ice nuclei: a pathway for cirrus cloud formation. *Science* 313, 1770-3.

[2]   ABDUL-RAZZAK, H. and GHAN, S. (2000). A parameterization of aerosol activation, 2. Multiple aerosol types. *Journal of Geophysical Research*, 105(D5), 6837-44, doi:10.1029/999JD901161

[3]   ACKERMAN, A. S., TOON, O. B., STEVENS, D. E., HEYMSFIELD, V., RAMANATHAN, V. and WELTON, J. (2000). Reduction of tropical cloudiness by soot. *Science* 288, 1042-7.

[4]   ALBRECHT, B. A. (1989). Aerosols, cloud microphysics, and fractional cloudiness. *Science*, 245, 1227-30.

[5]   ARCHULETA, C. M., DEMOTT, P. J. and KREIDENWEIS, S. M. (2005). Ice nucleation by surrogates for atmospheric mineral dust and mineral dust/sulfate particles at cirrus temperatures. *Atmospheric Chemistry and Physics*, 5, 2617-34.

[6]   ARTHUR, W. B. (1999). Complexity and the economy. *Science* 284, 107-9.

[7]   ASA-AWUKU, A. and NENES, A. (2007). Effect of solute dissolution kinetics on cloud droplet formation: Extended Köhler theory. *Journal of Geophysical Research*, 112(D22201), doi:10.1029/2005JD006934.

[8]   ASA-AWUKU, A., SULLIVAN, A. P., HENNIGAN, C. J., WEBER, R. J. and NENES, A. (2008). Investigation of molar volume and surfactant characteristics of water-soluble organic compounds in biomass burning aerosol. *Atmospheric Chemistry and Physics*, 8, 799-812.

[9]   BACMEISTER, J., ECKERMANN, S. D., TSIAS, A., CARSLAW, K. S. and PETER, T. (1999). Mesoscale temperature fluctuations induced by a spectrum of gravity waves: A comparison of parameterizations and their impact on stratospheric microphysics. *Journal of the Atmospheric Sciences*, 56, 1913-24.

[10]   BAKER, M. B. and PETER, T. (2008). Small-scale cloud processes and climate. *Nature* 451(17), 299-300.

[11]   BARAHONA, D. and NENES, A. (2007). Parameterization of cloud droplet formation in large scale models: including effects of entrainment. *Journal of Geophysical Research*, 112, D16026; doi: 10.1029/207JD008473.

[12]   BARAHONA, D. and NENES, A. (2008). Parameterization of cirrus formation in large scale models: Homogeneous nucleation. *Journal of Geophysical Research*, 113, D11211, doi:10.1029/2007JD009355.

[13]   BARAHONA, D. and NENES, A. (2009). Parameterizing the competition between homogeneous and heterogeneous freezing in cirrus cloud formation. Monodisperse ice nuclei. *Atmospheric Chemistry and Physics*, 9, 369-81.

[14]   BARAHONA, D. and NENES, A. (2009). Parameterizing the competition between homogeneous and heterogeneous freezing in cirrus cloud formation. Polydisperse ice nuclei. *Atmospheric Chemistry and Physics*, 9, 5933-48.

[15]   BARAHONA, D. and NENES, A. (In review). The two faces of cirrus. *Nature*

267

[16]   BARAHONA, D., RODRIGUEZ, J. M. and NENES, A. (In review). Sensitivity of the global distribution of cirrus Ice crystal concentration to heterogeneous freezing. *Journal of Geophysical Research*.

[17]   BARAHONA, D., SOTIROPOULOU, R. E. P. and NENES, A. (In preparation). Entrainment Effects on Cloud Droplet Formation: an exploratory GCM study.

[18]   BARAHONA, D., WEST, R. E. L., STIER, P., ROMAKKANIEMI, S., KOKKOLA, H. and NENES, A. (2010). Comprehensively accounting for the effect of giant CCN in cloud droplet activation parameterizations. *Atmospheric Chemistry and Physics*, 10, 2467-73.

[19]   BEAVER, M. R., ELROD, M. J., GARLAND, R. M. and TOLBERT, M. A. (2006). Ice nucleation in sulfuric acid/organic aerosols: Implications for cirrus cloud formation. *Atmospheric Chemistry and Physics* 6, 3231-42.

[20]   BLOOM, S., DA SILVA, A., DEE, D., BOSILOVICH, M., CHERN, J.-D., PAWSON, S., SCHUBERT, S., SIENKIEWICZ, M., STAJNER, I., TAN, W.-W. and WU, M.-L. (2005). Documentation and Validation of the Goddard Earth Observing System (GEOS) Data Assimilation System - Version 4. *Technical Report Series on Global Modeling and Data Assimilation*, 26, 104606.

[21]   BOUCHER, O. and LOHMANN, U. (1995). The sulfate-CCN-cloud albedo effect: A sensitivity study with 2 general circulation models. *Tellus Series B*, 47, 281-300.

[22]   BRENGUIER, J. L. and CHAUMAT, L. (2001). Droplet spectra broadening in cumulus clouds. Part I: broadening in adiabatic cores. *Journal of the Atmospheric Sciences*, 58, 628-41.

[23]   CANTRELL, W. and HEYMSFIELD, A. J. (2005). Production of ice in tropospheric clouds. *Bulletin of the American Meteorological Society*, 86(6), 795-807.

[24]   CHARLSON, R. J., SCHWARTZ, S. E., HALES, J. M., CESS, R. D., COAKLEY, J. A., HANSEN, J. and HOFMAN, D. J. (1992). Climate forcing by anthropogenic aerosols. *Science* 255, 423-30.

[25]   CHARLSON, R. J., SEINFELD, J. H., NENES, A., KULMALA, M., LAAKSONEN, A. and FACCHINI, M. C. (2001). Reshaping the theory of cloud formation. *Science* 292, 2025-6.

[26]   CHEN, J.-P., HAZRA, A. and LEVIN, Z. (2008). Parameterizing ice nucleation rates using contact angle and activation energy derived from laboratory data. *Atmospheric Chemistry and Physics*, 8, 7431-49.

[27]   CHEN, Y., DEMOTT, P. J., KREIDENWEIS, S. M., ROGERS, D. C. and SHERMAN, D. E. (2000). Ice formation by sulfate and sulfuric acid aerosol particles under upper-tropospheric conditions. *Journal of the Atmospheric Sciences*, 57, 3752-66.

[28]   CHEN, Y., KREIDENWEIS, S. M., MCINNES, L. M., ROGERS, D. C. and DEMOTT, P. J. (1998). Single particle analyses of ice nucleating aerosols in the upper troposphere and lower stratosphere. *Geophysical Research Letters*, 25(9), 1391-4.

[29]   CHEN, Y. and PENNER, J. E. (2005). Uncertainty analysis for estimates of the first indirect aerosol effect. *Atmospheric Chemistry and Physics*, 5, 2935-48.

[30]   CHOU, M.-D., SUAREZ, M. J., HO, C.-H., YAN, M. M.-H. and LEE, K.-T. (1998). Parameterizations for cloud overlapping and shortwave single-scattering properties for use in general circulation and cloud ensemble models. *Journal of Climate*, 11(2), 202-14.

[31] CHUANG, P. Y. (2006). Sensitivity of cloud condensation nuclei activation processes to kinetic parameters. *Journal of Geophysical Research*, 111(D09201), doi:10.1029/2005JD006529.

[32] CHUANG, P. Y., CHARLSON, R. J. and SEINFELD, J. H. (1997). Kinetic limitations on droplet formation in clouds. *Nature*, 390(11), 594-6.

[33] CHYLEK, P., DUBEY, M. K., LOHMANN, U., RAMANATHAN, V., KAUFMAN, Y. J., LESINS, G., HUDSON, J., ALTMANN, G. and OLSEN, S. (2006). Aerosol indirect effect over the Indian Ocean. *Geophysical Research Letters*, 33, L06806.

[34] COHARD, J.-M., PINTY, J., -P. and SUHRE, K. (2000). On the parameterization of activation spectra from cloud condensation nuclei microphysical properties *Journal of Geophysical Research*, 105(D9), 11753-66, doi:10.1029/1999JD901195.

[35] COHEN, C. (2000). A quantitative investigation of entrainment and detrainment in numerically simulated cumulonimbus clouds. *Journal of the Atmospheric Sciences*, 57, 1657-74.

[36] COMSTOCK, J. M., LIN, R., STARR, D. and YANG, P. (2008). Understanding ice supersaturation, particle growth, and number concentration in cirrus clouds *Journal of Geophysical Research*, 113, D23211, doi:10.1029/2008JD010332.

[37] CONANT, W. C., VANREKEN, T. M., RISSMAN, T. A., VARUTBANGKUL, V., JONSSON, H. H., NENES, A., JIMENEZ, J. L., DELIA, A. E., BAHREINI, R., ROBERTS, G. C., FLAGAN, R. C. and SEINFELD, J. H. (2004). Aerosol-cloud drop concentration closure in warm clouds. *Journal of Geophysical Research*, 109, D13204, doi:10.1029/2003JD004324.

[38] COZIC, J., VERHEGGEN, B., MERTES, S., CONNOLLY, P., BOWER, K., PETZOLD, A., BALTENSPERGER, U. and WEINGARTNER, E. (2006). Scaveging of black carbon in mixed phase clouds at the high alpine site Jungfraujoch. *Atmospheric Chemistry and Physics Discussions*, 6, 11877-912.

[39] CURRY, J. A., SCHRAMM, J. L., ROSSOW, W. B. and RANDALL, D. (1996). Overview of Arctic Cloud and Radiation Characteristics. *Journal of Climate*, 9(8), 1731-64.

[40] CZICZO, D. J. and ABBATT, J. P. D. (2001). Ice nucleation in NH_4HSO_4, NH_4NO_3, and H_2SO_4 aqueous particles: Implications for cirrus formation. *Geophysical Research Letters*, 28(6), 963-6.

[41] DEL GENIO, A. D., YAO, M., KOVARI, W. and LO, K. (1996). A prognostic cloud water parameterization for global climate models. *Journal of Climate*, 9, 270.

[42] DEMOTT, P. J., CHEN, Y., KREIDENWEIS, S. M., ROGERS, D. C. and SHERMAN, D. E. (1999). Ice formation by black carbon particles. *Geophysical Research Letters*, 26(16), 2429-32.

[43] DEMOTT, P. J., CZICZO, D. J., PRENNI, A. J., MURPHY, D. M., KREIDENWEIS, S. M., THOMPSON, D. S., BORYS, R. and ROGERS, D. C. (2003). Measurements of the concentration and composition of nuclei for cirrus formation. *Proceedings of the National Academy of Sciences of the United States of America*, 100(25), 14655-60.

[44] DEMOTT, P. J., MEYERS, M. P. and COTTON, R. W. (1994). Parameterization and impact of ice initiation processes relevant to numerical model simulations of cirrus clouds. *Journal of the Atmospheric Sciences*, 51(1), 77-90.

[45]   DeMott, P. J., Rogers, D. C. and Kreidenweis, S. M. (1997). The susceptibility of ice formation in upper tropospheric clouds to insoluble aerosol components. *Journal of Geophysical Research*, 102(D16), 19575-84.

[46]   DeMott, P. J., Rogers, D. C., Kreidenweis, S. M., Chen, Y., Twohy, C. H., Baumgardner, D. G., Heymsfield, A. J. and Chan, K. R. (1998). The role of heterogeneous freezing nucleation in upper tropospheric clouds: Inferences from SUCCESS. *Geophysical Research Letters*, 25(9), 1387-90.

[47]   DeMott, P. J., Sassen, K., Poellot, M. R., Baumgardner, D. G., Rogers, D. C., Brooks, S. D., Prenni, A. J. and Kreidenweis, S. M. (2003). African dust aerosols as atmospheric ice nuclei. *Geophysical Research Letters*, 30(14), 1732, doi:10.029/2003GL017410.

[48]   Dowling, D. R. and Radke, L. F. (1990). A summary of the physical properties of cirrus clouds. *Journal of Applied Meteorology*, 29, 970.

[49]   Durant, A. J. and Shaw, R. A. (2005). Evaporation freezing by contact nucleation inside-out. 32, L20814; doi:10.1029/2005GL024175.

[50]   Dymarska, M., Murray, B. J., Sun, L., Eastwood, M. L., Knopf, D. A. and Bertram, A. K. (2006). Deposition ice nucleation on soot at temperatures relevant for the lower troposphere. *Journal of Geophysical Research*, 111, D04204; doi:10.1029/2005JD006627.

[51]   Eastwood, M. L., Cremel, S., Gehrke, C., Girard, E. and Bertram, A. K. (2008). Ice nucleation on mineral dust particles: Onset conditions, nucleation rates and contact angles. *Journal of Geophysical Research*, 113, D22203, doi:10.1029/2008JD10639.

[52]   Eidhammer, T., DeMott, P. J. and Kreidenweis, S. M. (2009). A comparison of heterogeneous ice nucleation parameterizations using a parcel model framework. *Journal of Geophysical Research*, 114(D06202), doi:10.1029/2008JD011095.

[53]   Feingold, G. and Heymsfield, A. J. (1992). Parameterization of condensational growth of droplets for use in general circulation models. *Journal of the Atmospheric Sciences*, 49(23), 2325-42.

[54]   Feng, Y., Penner, J. E., Sillman, S. and Liu, X. (2004). Effects of cloud overlap in photochemical models. *Journal of Geophysical Research*, 109, D04310, doi:10.1029/2003JD004040.

[55]   Field, P. R., Möhler, O., Connolly, P., Krämer, M., Cotton, R., Heymsfield, A. J., Saathoff, H. and Schnaiter, M. (2006). Some ice nucleation characteristics of Asian and Saharan desert dust. *Atmospheric Chemistry and Physics*, 6, 2991-3006.

[56]   Fletcher, H. N. (1959). On ice-crystal production by aerosol particles. *Journal of the Atmospheric Sciences*, 16(2), 173-80.

[57]   Fletcher, H. N. (1969). Active sites and ice crystal nucleation. *Journal of the Atmospheric Sciences*, 26, 1266-71.

[58]   Fountoukis, C. and Nenes, A. (2005). Continued development of a cloud droplet formation parameterization for global climate models. *Journal of Geophysical Research*, 110, D11212, doi:10.1029/2004JD005591.

[59]   Fountoukis, C. and Nenes, A. (2007). ISORROPIA II: a computationally efficient thermodynamic equilibrium model for K^+–Ca^{2+}–Mg^{2+}–$NH4^+$–Na^+–

SO4^{2-}–NO3$^-$–Cl$^-$–H2Oaerosols. *Atmospheric Chemistry and Physics*, 7(17), 4639-59.

[60]   FOUNTOUKIS, C., NENES, A., MESKHIDZE, N., BAHREINI, R., CONANT, W. C., JONSSON, H. H., MURPHY, S., SOROOSHIAN, A., VARUTBANGKUL, V., BRECHTEL, F., FLAGAN, R. C. and SEINFELD, J. H. (2007). Aerosol-cloud drop concentration closure for clouds sampled during the International Consortium for Atmospheric Reseach on Transport and Transformation 2004 campaign. *Journal of Geophysical Research*, 112, D10S30, doi:10.129/2006JD007272.

[61]   FRIDLIND, A. M., ACKERMAN, A. S., JENSEN, E. J., HEYMSFIELD, A. J., POELLOT, M. R., STEVENS, D. E., WANG, D., MILOSHEVICH, L. M., BAUMGARDNER, D. G., LAWSON, P., WILLSON, J., FLAGAN, R. C., SEINFELD, J. H., JONSSON, H. H., VANREKEN, T. M., VARUTBANGKUL, V. and RISSMAN, T. A. (2004). Evidence for the predominance of mid-tropospheric aerosols as subtropical anvil cloud nuclei. *Science*, 304, 718-22.

[62]   FROYD, K. D., MURPHY, D. M., SANFORD, T. J., THOMSON, D. S., WILSON, J. C., PFISTER, L. and LAIT, L. (2009). Aerosol composition of the tropical upper troposphere. *Atmospheric Chemistry and Physics*, 9, 4363–85.

[63]   GAO, R. S., POPP, P. J., FAHEY, D. W., MARCY, T. P., HERMAN, R. L., WEINSTOCK, E. M., BAUMGARDNER, D. G., GARRETT, T. J., ROSENLOF, K. H., THOMPSON, T. L., BUI, P. T., RIDLEY, B. A., WOFSY, S. C., TOON, O. B., TOLBERT, M. A., KÄRCHER, B., PETER, T., HUDSON, P. K., WEINHEIMER, A. J. and HEYMSFIELD, A. J. (2004). Evidence that nitric acid increases relative humidity in low-temperature cirrus clouds. *Science* 303, 516-20.

[64]   GAYET, J. F., OVARLEZ, J., SHCHERBAKOV, V., STRÖM, J., SCHUMANN, U., MINIKIN, A., AURIOL, F., PETZOLD, A. and MONIER, M. (2004). Cirrus cloud microphysical and optical properties at southern and northern midlatitudes during the INCA experiment. *Journal of Geophysical Research*, 109, D20206, doi:10.1029/2004JD004803.

[65]   GELBARD, F. and SEINFELD, J. H. (1979). Exact solution of the general dynamic equation for aerosol growth and condensation *Journal of Colloid and Interface Science*, 68(1), 173-83.

[66]   GELBARD, F. and SEINFELD, J. H. (1980). Simulation of multicomponent aerosol dynamics. *Journal of Colloid and Interface Science*, 78(2), 485-501.

[67]   GERBER, H., FRICK, G., MALINOWSKI, S. P., BRENGUIER, J.-L. and BURNET, F. (2005). Holes and entrainment in stratocumulus. *Journal of the Atmospheric Sciences*, 62, 443-59.

[68]   GERSHENZON, M., DAVIDOVITS, P., WILLIAMS, L. R., SHIN, Q., JAYNE, J. T., KOLB, C. H. and WORSNOP, D. R. (2004). Uptake of H$_2$^{17}O(g) and D$_2$O(q) by aqueous sulfuric acid droplets. *Journal of Physical Chemistry A*, 108, 1567-73.

[69]   GIERENS, K. (2003). On the transition between heterogeneous and homogeneous freezing. *Atmospheric Chemistry and Physics*, 3, 437-46.

[70]   GIERENS, K., MONIER, M. and GAYET, J. F. (2003). The deposition coefficient and its role for cirrus clouds. *Journal of Geophysical Research*, 108(D2), 4069.

[71]   GRABOWSKI, W. and PAWLOWSKA, H. (1993). Entrainment and mixing in clouds: the Paluch diagram revisited. *Journal of Applied Meteorology*, 32, 1767-73.

[72]   GREGORY, D. (2001). Estimation of entrainment rate in simple models of convective clouds. *Quarterly Journal of the Royal Meteorological Society*, 127, 53-72.

[73]   GULTEPE, I. and ISAAC, G. A. (1996). The relationship between cloud droplet and aerosol number concentrations for climate models *International Journal of Climatology*, 16(8), 941-6.

[74]   HAAG, W. and KÄRCHER, B. (2004). The impact of aerosols and gravity waves on cirrus at midlatitudes. *Journal of Geophysical Research*, 109, D12202, doi:10.1029/2004JD004579.

[75]   HAAG, W., KÄRCHER, B., SCHAEFERS, S., STETZER, O., MÖHLER, O., SCHURATH, U., KRÄMER, M. and SCHILLER, C. (2003). Numerical simulations of homogeneous freezing processes in the aerosol chamber AIDA. *Atmospheric Chemistry and Physics*, 3, 195-210.

[76]   HAAG, W., KÄRCHER, B., STROM, J., MINIKIN, A., LOHMANN, U., OVARLEZ, J. and STOHL, A. (2003). Freezing thresholds and cirrus formation mechanisms inferred from in situ measurements of relative humidity. *Atmospheric Chemistry and Physics*, 3, 1791-806.

[77]   HACK, J. J. (1998). Sensitivity of the simulated climate to a diagnostic formulation for cloud liquid water. *Journal of Climate*, 11, 1497–515.

[78]   HARTMANN, D. L., HOLTON, J. R. and FU, Q. (2001). The heat balance of the tropical tropopause, cirrus, and stratospheric dehydration. *Geophysical Research Letters*, 28(10), 1969-72.

[79]   HAYNES, D. R., TRO, N. J. and GEORGE, S. M. (1992). Condensation and evaporation of H_2O on ice surfaces. *Journal of Physical Chemistry*, 96, 8502-9.

[80]   HENDRICKS, J., KÄRCHER, B., LOHMANN, U. and PONATER, M. (2005). Do aircraft black carbon emissions affect cirrus clouds on the global scale? *Geophysical Research Letters*, 32, L12814, doi:10.1029/2005GL022740.

[81]   HEYMSFIELD, A. J. and IAQUINTA, J. (2000). Cirrus crystals terminal velocities. *Journal of the Atmospheric Sciences*, 57, 916-38.

[82]   HEYMSFIELD, A. J. and MILOSHEVICH, L. M. (1995). Relative humidity and temperature influences on cirrus formation and evolution: observations from wave clouds and FIRE II. *Journal of the Atmospheric Sciences*, 52(23), 4302.

[83]   HEYMSFIELD, A. J., MILOSHEVICH, L. M., TWOHY, C. H., SACHSE, G. and OLTMANS, S. (1998). Upper-tropospheric relative humidity observations and implications for cirrus ice nucleation. *Geophysical Research Letters*, 25(9), 1343-6.

[84]   HEYMSFIELD, A. J. and PLATT, C. M. (1984). A parameterization of the particle size spectrum of ice clouds in terms of the ambient temperature and ice water content. *Journal of the Atmospheric Sciences*, 41(5), 846-55.

[85]   HEYMSFIELD, A. J. and SABIN, R. M. (1989). Cirrus crystal nucleation by homogenous freezing of solution droplets. *Journal of the Atmospheric Sciences*, 46(14), 2252-64.

[86]   HOYLE, C. R., LUO, B. P. and PETER, T. (2005). The origin of high ice crystal number densities in cirrus clouds. *Journal of the Atmospheric Sciences*, 62, 2658-579.

272

[87] HSIEH, W. C., BUZORIUS, G., FLAGAN, R. C., SEINFELD, J. H. and NENES, A. (in review). On the representation of droplet coalescence and autoconversion: Evaluation using ambient cloud droplet size distributions. *Journal of Geophysical Research*, doi:10.1029/2008JD010502.

[88] HSIEH, W. C., JONSSON, H. H., BUZORIUS, G., FLAGAN, R. C., SEINFELD, J. H. and NENES, A. (in preparation). Parameterization of cloud drop size distribution in regional and large scale models.

[89] HUNG, H., MALINOWSKI, A. and MARTIN, S. T. (2002). Ice nucleation kinetics of aerosols containing aqueous and solid ammonium sulfate. *Journal of Physical Chemistry A*, 106, 293-306.

[90] HUNG, H., MALINOWSKI, A. and MARTIN, S. T. (2003). Kinetics of heterogeneous ice nucleation on the surfaces of mineral dust cores inserted into aqueous ammonium sulfate particles. *Journal of Physical Chemistry A*, 107, 1296-306.

[91] IPCC (2007). *Climate change 2007: the physical basis. Contribution of working group I to the fourth assessment report of the Intergovernmental Panel on Climate Change.* . Cambridge, United Kingdom and New York, NY, USA.: Cambridge University Press.

[92] JENSEN, E. J. and PFISTER, L. (2004). Transport and freeze-drying in the tropical tropopause layer. *Journal of Geophysical Research*, 109, D02207; doi:10.1029/2003JD004022

[93] JENSEN, E. J., PFISTER, L., BUI, T.-P., LAWSON, P. and BAUMGARDNER, D. G. (2009). Ice nucleation and cloud microphysical properties in tropical tropopause layer cirrus. *Atmopsheric Chemistry and Physics Discussions*, 9, 20631-75.

[94] JENSEN, E. J., PFISTER, L., BUI, T.-P., LAWSON, P. and BAUMGARDNER, D. G. (2010). Ice nucleation and cloud microphysical properties in tropical tropopause layer cirrus. *Atmospheric Chemistry and Physics*, 10, 1369-84.

[95] JENSEN, E. J., PFISTER, L., BUI, T. V., LAWSON, P., BAKER, B., MO, Q., BAUMGARDNER, D. G., WEINSTOCK, E. M., SMITH, J. B., MOYER, E. J., HANISCO, T. F., SAYRES, D. S., CLAIR, J. M. S., ALEXANDER, M. J., TOON, O. B. and SMITH, A. (2008). Formation of large (~100 μm) ice crystals near the tropical tropopause. *Atmospheric Chemistry and Physics*, 8, 1621-33.

[96] JENSEN, E. J., SMITH, J. B., PFISTER, L., PITTMAN, J. V., WEINSTOCK, E. M., SAYRES, D. S., HERMAN, R. L., TROY, R. F., ROSENLOF, K., THOMPSON, T. L., FRIDLIND, A. M., HUDSON, P. K., CZICZO, D. J., HEYMSFIELD, A. J., SCHMITT, C. and WILSON, J. (2005). Ice supersaturations exceeding 100% at the cold tropical tropopause: implications for cirrus formation and dehydration *Atmospheric Chemistry and Physics*, 5, 851-62.

[97] JENSEN, E. J. and TOON, O. B. (1994). Ice nucleation in the upper troposphere: sensitivity to aerosol number density, temperature, and cooling rate. *Geophysical Research Letters*, 21(18), 2019-22.

[98] JENSEN, E. J., TOON, O. B., WESTPHAL, D. L., KINNE, S. and HEYMSFIELD, A. J. (1994). Microphysical modeling of cirrus 1. Comparison with 1986 FIRE IFO measurements. *Journal of Geophysical Research*, 99(D5), 10421-42.

[99] JIANG, H., XUE, H., TELLER, A., FEINGOLD, G. and LEVIN, Z. (2006). Aerosol effects on the lifetime of shallow cumulus. *Geophysical Research Letters*, 33(L14806), doi:10.1029/2006GL026024,.

[100] JONAS, P. R. (1996). Turbulence and cloud microphysics. *Atmospheric Research*, 40, 286-306.

[101] JOOS, H., SPICHTINGER, P., GAYET, J. F. and MINIKIN, A. (2008). Orographic cirrus in the global climate model ECHAM5. *Journal of Geophysical Research*, 113(D18205, doi:10.1029/2007JD009605).

[102] KAIN, J. S. and FRITSCH, J. M. (1990). A one-dimensional entraining/detraining plume model and its application in convective parameterization. *Journal of the Atmospheric Sciences*, 47(23), 2784–802.

[103] KANJI, Z. A., FLOREA, O. and ABBATT, J. P. D. (2008). Ice formation via deposition nucleation on mineral dust and organics: dependence of onset relative humidity on total particulate surface area. *Environmental Research Letters*, 3, doi:10.1088/748-9326/3/2/025004.

[104] KÄRCHER, B. and BURKHARDT, U. (2008). A cirrus scheme for global circulation models. *Quarterly Journal of the Royal Meteorological Society*, 134, 1439-61; doi:10.002/Qj.301.

[105] KÄRCHER, B. and HAAG, W. (2004). Factors controlling upper tropospheric relative humidity. *Annales Geophysicae*, 22, 705-15.

[106] KÄRCHER, B., HENDRICKS, J. and LOHMANN, U. (2006). Physically based parameterization of cirrus cloud formation for use in global atmospheric models. *Journal of Geophysical Research*, 111, D01205, doi:10.1029/2005JD006219.

[107] KÄRCHER, B. and KOOP, T. (2005). The role of organic aerosols in homogeneous ice formation. *Atmospheric Chemistry and Physics*, 5, 703-14.

[108] KÄRCHER, B. and LOHMANN, U. (2002). A parameterization of cirrus cloud formation: homogeneous freezing including effects or aerosol size. *Journal of Geophysical Research*, 107(D23), 4698, doi:10.1029/2001JD001429.

[109] KÄRCHER, B. and LOHMANN, U. (2002). A parameterization of cirrus cloud formation: homogeneous freezing of supercooled aerosols. *Journal of Geophysical Research*, 107(D23), 4010, doi:10.1029/2001JD000470.

[110] KÄRCHER, B. and LOHMANN, U. (2003). A parameterization of cirrus cloud formation: Heterogeneous freezing. *Journal of Geophysical Research*, 108(D14), 4402, doi:10.1029/2002JD003220.

[111] KÄRCHER, B., MOHLER, O., DEMOTT, P. J., PECHTL, S. and YU, F. (2007). Insights into the role of soot aerosols in cirrus cloud formation. *Atmospheric Chemistry and Physics*, 7, 4203-27.

[112] KÄRCHER, B. and STRÖM, J. (2003). The roles of dynamical variabilty and aerosols in cirrus cloud formation. *Atmospheric Chemistry and Physics*, 3, 823-38.

[113] KASHCHIEV, D. (2000). *Nucleation: Basic theory with applications*. Oxford: Butterworth-Heinemann.

[114] KAY, J. E., BAKER, M. B. and HEGG, D. (2006). Microphysical and dynamical controls on cirrus cloud optical depth distributions. *Journal of Geophysical Research*, 111, D24205, doi:10.1029/2005JD006916.

[115] KECS, W. (1982). *The convolution product and some applications*. Bucharest, Romania: D. Reidel co.

[116] KHAIROUTDINOV, M. and KOGAN, Y. (2000). A new cloud physics parameterization in a Large-Eddy simulation model of marine stratocumulus. *Monthly Weather Review*, 128(1), 229-43.

[117] KHVOROSTYANOV, V. I. and CURRY, J. A. (2004). The theory of ice nucleation by heterogeneous freezing of deliquescent mixed CCN. Part I: critical radius, energy and nucleation rate. *Journal of the Atmospheric Sciences*, 61, 2676-91.

[118] KHVOROSTYANOV, V. I. and CURRY, J. A. (2005). The theory of ice nucleation by heterogeneous freezing of deliquescent mixed CCN. Part II: parcel model simulations. *Journal of the Atmospheric Sciences*, 62, 261-85.

[119] KHVOROSTYANOV, V. I. and CURRY, J. A. (2007). Refinements to the Köhler's theory of aerosol equilibrium radii, size spectra, and droplet activation: Effects of humidity and insoluble fraction. *Journal of Geophysical Research*, 112, D05206, doi:10.1029/2006JD007672.

[120] KHVOROSTYANOV, V. I. and CURRY, J. A. (2009). Critical humidities of homogeneous and heterogeneous ice nucleation: Inferences from extended classical nucleation theory. *Journal of Geophysical Research*, 114, D04207, doi:10.1029/2008JD011197.

[121] KHVOROSTYANOV, V. I., MORRISON, H., CURRY, J. A., BAUMGARDNER, D. G. and LAWSON, P. (2006). High supersaturation and modes of ice nucleation in thin tropopause cirrus: simulation of the 13 July 2002 cirrus regional study of tropical anvils and cirrus layers case. *Journal of Geophysical Research*, 111, D02201, doi:10.1029/2004JD005235.

[122] KHVOROSTYANOV, V. I. and SASSEN, K. (1998). Toward the theory of homogeneous nucleation and its parameterization for cloud models. *Geophysical Research Letters*, 25(16), 3155-8.

[123] KIEHL, J. T. (1994). Sensitivity of a GCM climate simulation to differences in continental versus maritime cloud drop size. *Journal of Geophysical Research*, 99, 23 107–23 15.

[124] KIM, B., MILLER, M. A., SCHWARTZ, S. E., LIU, Y. and MIN, Q. (2008). The role of adiabaticity in the aerosol first indirect effect. *Journal of Geophysical Research*, 113, D05210; doi:10.1029/2007JD008961.

[125] KIM, Y.-J., ECKERMANN, S. D. and CHUN, H.-Y. (2003). An overview of the past, present, and future of gravity-wave drag parameterization for numerical climate and weather prediction models. *Atmosphere-Ocean*, 41(1), 65-98.

[126] KNIGHT, C. G., KNIGHT, S. H. E., MASSEY, N., AINA, T., CHRISTENSEN, C., FRAME, D. J., KETTLEBOROUGH, J. A., MARTIN, A., PASCOE, S., SANDERSON, S., STAINFORTH, D. A. and ALLEN, M. R. (2007). Association of parameter, software, and hardware variation with large scale behavior across 57000 climate models. *Proceedings of the National Academy of Sciences of the United States of America*, 104(30), 12259-64.

[127] KOENIG, R. L. (1972). Parameterization of ice growth for numerical calculations of cloud dynamics. *Monthly Weather Review*, 100(6), 417-23.

[128] KOHLER, H. (1936). The nucleus in and the growth of hygroscopic droplets. *Transactions of the Faraday Society*, 32, 1152-61.

[129] KOOP, T., LUO, B., TSLAS, A. and PETER, T. (2000). Water activity as the determinant for homogeneous ice nucleation in aqueous solutions. *Nature* 406, 611-4.

[130] KOROLEV, A. V. and ISAAC, G. A. (2000). Drop growth due to high supersaturation caused by isobaric mixing. *Journal of the Atmospheric Sciences*, 57, 1675-85.

[131] KOROLEV, A. V. and MAZIN, I. P. (2003). Supersaturation of water vapor in clouds. *Journal of the Atmospheric Sciences*, 60, 2957-74.

[132] KRÄMER, M., SCHILLER, C., AFCHINE, A., BAUER, R., GENSCH, I., MANGOLD, A., SCHLICHT, S., SPELTEN, N., SITNIKOV, N., BORRMANN, S., REUS-D, M. and SPICHTINGER, P. (2009). Ice supersaturation and cirrus cloud crystal numbers. *Atmospheric Chemistry and Physics*, 9, 3505-22.

[133] KRUEGER, S. K. (2000). *Cloud System Modeling. In: General Circulation Model Development* (Vol. 70). Orlando, FL, USA: Academic Press.

[134] KUMAR, P., SOKOLIK, I. N. and NENES, A. (2008). Parameterization of cloud droplet formation for global and regional models: including adsorption activation from insoluble CCN. *Atmospheric Chemistry and Physics Discussions*, 8, 16851-90.

[135] KUMAR, P., SOKOLIK, I. N. and NENES, A. (2009). Parameterization of cloud droplet formation for global and regional models: including adsorption activation from insoluble CCN. *Atmos. Chem. Phys.*, 9(7), 2517-32.

[136] LANCE, S., NENES, A. and RISSMAN, T. A. (2004). Chemical and dynamical effects on cloud droplet number: Implications for estimates of the aerosol indirect effect. *Journal of Geophysical Research*, 109(D22), D22208.

[137] LAU, K. M. and WU, H. T. (2003). Warm rain processes over tropical oceans and climate implications. *Geophysical Research Letters*, 30(24), 2290, doi:10.1029/2003GL018567.

[138] LAWSON, P., PILSON, B., BAKER, B., MO, Q., JENSEN, E. J., PFISTER, L. and BUI, P. T. (2008). Aircraft measurements of microphysical properties of subvisible cirrus in the tropical tropopause layer. *Atmospheric Chemistry and Physics*, 8, 1609–20.

[139] LIN, C. (1999). Some bulk properties of cumulus ensembles simulated by a cloud-resolving model. Part II: Entrainment profiles. *Journal of the Atmospheric Sciences*, 56, 3736-48.

[140] LIN, C. and ARAKAWA, A. (1997). The macroscopic entrainment processes of simulated cumulus ensemble. Part I: entrainment sources. *Journal of the Atmospheric Sciences*, 54, 1027-43.

[141] LIN, C. and ARAKAWA, A. (1997). The macroscopic entrainment processes of simulated cumulus ensemble. Part II: Testing the entraining-plume model. *Journal of the Atmospheric Sciences*, 54, 1044-53.

[142] LIN, H., NOONE, K. J., STRÖM, J. and HEYMSFIELD, A. J. (1998). Dynamical influences on cirrus cloud formation process. *Journal of the Atmospheric Sciences*, 55, 1940-3.

[143] LIN, R., STARR, D., DEMOTT, P. J., COTTON, R., SASSEN, K., JENSEN, E. J., KÄRCHER, B. and LIU, X. (2002). Cirrus parcel model comparison project. Phase 1: The critical components to simulate cirrus initiation explicitly. *Journal of the Atmospheric Sciences*, 59(15), 2305-28.

[144] LINZ, P. (1985). *Analytical and numerical methods for Volterra equations*. Philadelphia, PA, USA: SIAM.

[145] LIOU, K. (1986). Influence of cirrus clouds on weather and climate processes: a global perspective. *Monthly Weather Review*, 114(6), 1167-99.

[146] LIOU, K. (2002). *An Introduction to Atmospheric Radiation* (Vol. 84). San Diego, CA, USA: Academic Press.

[147] LIU, X. and PENNER, J. E. (2005). Ice nucleation parameterization for global models. *Meteorologische Zeitschrift*, 14(4), 499-514.

[148] LIU, X., PENNER, J. E., DAS, B., BERGMANN, D., RODRIGUEZ, J. M., STRAHAN, S., WANG, M. and FENG, Y. (2007). Uncertainties in global aerosol simulations: Assessment using three meteorological data sets *Journal of Geophysical Research*, 112, D11212; doi:10.1029/2006JD008216.

[149] LIU, X., PENNER, J. E., GHAN, S. J. and WANG, M. (2007). Inclusion of ice microphysics in the NCAR Community Atmospheric Model version 3 (CAM3). *Journal of Climate*, 20, 4526-47.

[150] LIU, X., PENNER, J. E. and HERZOG, M. (2005). Global modeling of aerosol dynamics: Model description, evaluation, and interactions between sulfate and nonsulfate aerosols. *Journal of Geophysical Research*, 110(D18206), doi:10.1029/2004JD005674.

[151] LOHMANN, U. and FEICHTER, J. (2005). Global indirect aerosol effects: a review *Atmospheric Chemistry and Physics* 5, 715-37.

[152] LOHMANN, U. and KÄRCHER, B. (2002). First interactive simulations of cirrus clouds formed by homogeneous freezing in the ECHAM general circulation model *Journal of Geophysical Research*, 107(D10), 4105, doi:10.1029/2001JD000767.

[153] LOHMANN, U., KÄRCHER, B. and HENDRICKS, J. (2004). Sensitivity studies of cirrus clouds formed by heterogeneous freezing in the ECHAM GCM. *Journal of Geophysical Research*, 109(D16204), doi:10.1029/2003JD004443.

[154] LOHMANN, U., SPICHTINGER, P., JESS, S., PETER, T. and SMIT, H. (2008). Cirrus cloud formation and ice supersaturated regions in a global climate model. *Environmental Research Letters*, 3, 045022; doi:10.1088/1748-9326/3/4/.

[155] LU, M., FEINGOLD, G., JONSSON, H. H., CHUANG, P. Y., GATES, H., FLAGAN, R. C. and SEINFELD, J. H. (2008). Aerosol-cloud relationships in continental shallow cumulus. *Journal of Geophysical Research*, 113(D15201), doi:10.1029/2007JD009354.

[156] MAGEE, N., MOYLE, A. M. and LAMB, D. (2006). Experimental determination of the deposition coefficient of small cirrus-like ice crystals near -50°C. *Geophysical Research Letters*, 33, L17813, doi:10.1029/2006GL026665.

[157] MAHONEY, A. W. and RAMKRISHNA, D. (2002). Efficient solution of population balance equations with discontinuities by finite elements. *Chemical Engineering Science* 57, 1107-19.

[158] MARCOLLI, C., GEDAMKE, S., PETER, T. and ZOBRIST, B. (2007). Efficiency of immersion mode ice nucleation on surrogates of mineral dust. *Atmospheric Chemistry and Physics*, 7, 5081-91.

[159]   McCarthy, J. (1974). Field verification of the relationship between entrainment rate and cumulus cloud diameter. *Journal of the Atmospheric Sciences*, 31, 1028-39.

[160]   McFiggans, G., Artaxo, P., Baltensperger, U., Coe, H., Facchini, M. C., Feingold, G., Fuzzi, S. G., M., Laaksonen, A., Lohmann, U., Mentel, T. F., Murphy, D. M., O'Dowd, C. D., Snider, J. R. and Weingartner, E. (2005). The effect of physical and chemical aerosol properties on warm cloud droplet activation. *Atmospheric Chemistry and Physics*, 5, 8507-646.

[161]   McNeill, F., Loerting, T., Geiger, F. M., Trout, B. L. and Molina, M. J. (2006). Hydrogen chloride-induced surface disordering on ice. *Proceedings of the National Academy of Sciences of the United States of America*, 103(25), 9422-7; doi: 10.1073/pnas.0603494103.

[162]   Medina, J. and Nenes, A. (2004). Effects of film-forming compounds on the growth of giant cloud condensation nuclei: Implications for cloud microphysics and the aerosol indirect effect. *Journal of Geophysical Research*, 109, D20207, doi:10.1029/2004JD004666.

[163]   Medina, J., Nenes, A., Sotiropoulou, R. E. P., Cottrell, L. D., Ziemba, L. D., Beckman, P. J. and Griffin, R. J. (2007). Cloud condensation nuclei closure during the International Consortium for Atmospheric Research on Transport and Transformation 2004 campaign: Effects of size resolved composition. *Journal of Geophysical Research*, 112(D10S31), doi:10.1029/2006JD007588.

[164]   Menon, S., Del Genio, A. D., Koch, D. and Tselioudis, G. (2002). GCM simulations of the aerosol indirect effect: sensitivity to cloud parameterization and aerosol burden. *Journal of the Atmospheric Sciences*, 59, 692-713.

[165]   Meskhidze, N., Nenes, A., Conant, W. C. and Seinfeld, J. H. (2005). Evaluation of a new cloud droplet activation parameterization with in situ data from CRYSTAL-FACE and CSTRIPE. *Journal of Geophysical Research*, 110, D16202, doi:10.1029/2004JD005703.

[166]   Meyers, M. P., DeMott, P. J. and Cotton, R. (1992). New primary ice-nucleation parameterization in an explicit cloud model. *Journal of Applied Meteorology*, 31, 708-21.

[167]   Michaud, L. M. (1998). Entrainment and detrainment required to explain updraft properties and work dissipation. *Tellus*, 50A(3), 283-301.

[168]   Ming, Y., Ramaswamy, V., Donner, L. J. and Phillips, V. T. J. (2006). A new parameterization of cloud droplet activation applicable to general circulation models. *Journal of the Atmospheric Sciences*, 63, 1348-56.

[169]   Minnis, P. (2004). Contrails, cirrus trend, and climate. *Journal of Climate*, 17(8), 1671-85.

[170]   Mitchell, J. F. B., Johns, T. C., Gregory, J. M. and Tett, S. F. B. (1995). Climate response to increasing levels of greenhouse gases and sulphate aerosols. *Nature* 376, 501-4.

[171]   Möhler, O., Büttner, S., Linke, C., Schnaiter, M., Saathoff, H., Stetzer, O., Wagner, R., Krämer, M., Mangold, A., Ebert, V. and Schurath, U. (2005). Effect of sulfuric acid coating on heterogeneous ice nucleation by soot aerosol particles. *Journal of Geophysical Research*, 110, D11210, doi:10.1029/2004JD005169.

[172] MÖHLER, O., DEMOTT, P. J., VALI, G. and LEVIN, Z. (2007). Microbiology and atmospheric processes: the role of biological particles in cloud physics *Biogeosciences*, 4, 1059-71.

[173] MÖHLER, O., FIELD, P. R., CONNOLLY, P., BENZ, S., SAATHOFF, H., SCHNAITER, M., WAGNER, R., COTTON, R., KRÄMER, M., MANGOLD, A. and HEYMSFIELD, A. J. (2006). Efficiency of the deposition mode ice nucleation on mineral dust particles. *Atmospheric Chemistry and Physics*, 3007-21.

[174] MÖHLER, O., STETZER, O., LINKE, C., SCHNAITER, M., TIEDE, R., SAATHOFF, H., KRÄMER, M., MANGOLD, A., BUDZ, P., ZINK, P., SCHREINER, J., MAUERSBERGER, K., HAAG, W., KÄRCHER, B. and SCHURATH, U. (2003). Experimental investigation of homogeneous freezing of sulfuric acid particles in the aerosol chamber AIDA. *Atmospheric Chemistry and Physics*, 3(1), 211-23.

[175] MONIER, M., WOBROCK, W., GAYET, J. F. and FLOSSMAN, A. (2006). Development of a detailed microphysics cirrus model tracking aerosol particles histories for interpretation of the recent INCA campaign. *Journal of the Atmospheric Sciences*, 63, 504-25.

[176] MOORE, R. H. and NENES, A. (2009). Scanning Flow CCN Analysis - A Method for Fast Measurements of CCN Spectra. *Aerosol Science and Technology*, 43, 1192-207

[177] MORRISON, H. and GRABOWSKI, W. (2008). Modeling supersaturation and subgrid-scale mixing with two-moment bulk warm microphysics. *Journal of the Atmospheric Sciences*, 65(3), 792-812.

[178] MORTON, B. R., TAYLOR, S. G. and TURNER, J. S. (1956). Turbulent gravitational convection from maintained and instantaneous sources. *Proceedings of the Royal Society of London Series A*, 234(1196), 1-23.

[179] MURPHY, D. M. and KOOP, T. (2005). Review of the vapour pressures of ice and supercooled water for atmospheric applications. *Quarterly Journal of the Royal Meteorological Society*, 131, 1539-65.

[180] MURPHY, D. M., SOLOMON, S., PORTMANN, R. W., ROSENLOF, K., FORSTER, P. and WONG, T. (2009). An observationally based energy balance for the Earth since 1950. *Journal of Geophysical Research*, 114, D17107; doi:10.1029/2009JD012105.

[181] MURRAY, B. J. (2008). Inhibition of ice crystallisation in highly viscous organic acid droplets. *Atmospheric Chemistry and Physics*, 8, 5423-33.

[182] MURRAY, B. J., KNOPF, D. A. and BERTRAM, A. K. (2005). The formation of cubic ice under conditions relevant to Earth's atmosphere. *Nature* 434, 202-5.

[183] MURRAY, B. J., WILSON, T. W., DOBBIE, S., CUI, Z., AL-JUMUR, S. M. R. K., MÖHLER, O., SCHNAITER, M., WAGNER, R., BENZ, S., NIEMAND, M., SAATHOFF, H., EBERT, V., WAGNER, S. and KÄRCHER, B. (2010). Heterogeneous nucleation of ice particles on glassy aerosol under cirrus conditions. *Nature Geoscience*, 3, 233-7.

[184] MYHRE, C. E., NIELSEN, C. J. and SAASTAD, O. E. (1998). Density and surface tension of aqueous H_2SO_4 at low temperatures *Journal of Chemical and Engineering Data*, 43, 617-22.

[185] NEGGERS, R. A. J., DUYNKERKE, P. G. and RODTS, M. A. (2003). Shallow cumulus convection: A validation of large-eddy simulation against aircraft and Landsat

observations. *Quarterly Journal of the Royal Meteorological Society*, 129, 2671-96.

[186] NENES, A., CHARLSON, R. J., FACCHINI, M. C., KULMALA, M., LAAKSONEN, A. and SEINFELD, J. H. (2002). Can chemical effects on cloud droplet number rival the first indirect effect? *Geophysical Research Letters*, 29(17), doi:10.1029/2002GL015295.

[187] NENES, A., CHUANG, P. Y., FLAGAN, R. C. and SEINFELD, J. H. (2001). Theoretical analysis of cloud condensation nucleus (CCN) instruments. *Journal of Geophysical Research*, 106 (D4), 3449-74

[188] NENES, A., GHAN, S., ABDUL-RAZZAK, H., CHUANG, P. Y. and SEINFELD, J. H. (2001). Kinetic limitations on cloud droplet formation and impact on cloud albedo. *Tellus*, 53B(2), 133-49.

[189] NENES, A. and SEINFELD, J. H. (2003). Parameterization of cloud droplet formation in global climate models. *Journal of Geophysical Research*, 108(D14), 4415, doi:10.1029/2002JD002911.

[190] O'DOWD, C. D., SMITH, M. H., CONSTERDINE, I. E. and LOWE, J. A. (1997). Marine aerosol, sea-salt, and the marine sulphur cycle: A short review. *Atmospheric Environment*, 31(1), 73-80.

[191] PALUCH, I. R. (1979). The entrainment mechanism in colorado cumuli. *Journal of the Atmospheric Sciences*, 36, 2467-78.

[192] PALUCH, I. R. and BAUMGARDNER, D. G. (1989). Entrainment and fine-scale mixing in convective cloud. *Journal of the Atmospheric Sciences*, 46(2), 261-78.

[193] PENG, Y., LOHMANN, U. and LEAITCH, W. R. (2005). Importance of vertical velocity variations in the cloud droplet nucleation process of marine stratocumulus. *Journal of Geophysical Research*, 110, D21213, doi:10.1029/2004JD004922.

[194] PENNER, J. E., CHEN, J.-P., WANG, M. and LIU, X. (2009). Possible influence of anthropogenic aerosol on cirrus clouds and anthropogenic forcing *Atmospheric Chemistry and Physics* 9, 879-96.

[195] PENNER, J. E., LISTER, D. H., GRIGGS, D. J., DOKKEN, D. J. and MCFARLAND, M. (1999). *Aviation and the global atmosphere - A special report of IPCC working groups I and III. Intergovernmental Panel on Climate Change*. Cambridge University Press.

[196] PETER, T. (1997). Microphysics and heterogeneous chemistry of polar stratospheric clouds *Annual Review of Physical Chemistry*, 48, 785-822.

[197] PETER, T., MARCOLLI, C., SPICHTINGER, P., CORTI, T., BAKER, B. and KOOP, T. (2006). When dry air is too humid. *Science*, 314, 1399-401.

[198] PHILLIPS, V. T. J., DEMOTT, P. J. and ANDRONACHE, C. (2008). An empirical parameterization of heterogeneous ice nucleation for multiple chemical species of aerosol. *Journal of the Atmospheric Sciences*, 65, 2757-83, doi:10.1175/2007JAS546.1.

[199] PHILLIPS, V. T. J., DONNER, L. J. and GARNER, S. T. (2007). Nucleation processes in deep convection simulated by a cloud-system-resolving model with double-moment bulk microphysics. *Journal of the Atmospheric Sciences*, 64, 738-61; doi:10.1175/JAS3869.1.

[200] PHINNEY, L. A., LOHMANN, U. and LEAITCH, W. R. (2003). Limitations of using an equilibrium approximation in an aerosol activation parameterization. *Journal of Geophysical Research*, 108(D12), 4371, doi:10.1029/2002JD002391.

[201] PONTIKIS, C. A. and HICKS, E. M. (1993). The influence of clear air entrainment on the droplet effective radius of warm maritime convective clouds. *Journal of the Atmospheric Sciences*, 50(17), 2889-900.

[202] PONTIKIS, C. A., RIGAUD, A. and HICKS, E. M. (1987). Entrainment and mixing as related to the microphysical properties of shallow warm cumulus clouds. *Journal of the Atmospheric Sciences*, 44(15), 2150-65.

[203] POPOVICHEVA, O., KIREEVA, E., PERSIANTSEVA, N., KHOKHLOVA, T., SHONIJA, N., TISHKOVA, V. and DEMIRDJIAN, B. (2008). Effect of soot on immersion freezing of water and possible atmospheric implications. *Atmospheric Research*, 90, 326-37.

[204] PRATT, K. A., DeMOTT, P. J., FRENCH, J. R., WANG, Z., WESTPHAL, D. L., HEYMSFIELD, A. J., TWOHY, C. H., PRENNI, A. J. and PRATHER, K. A. (2009). *In situ* detection of biological particles in cloud ice-crystals *Nature Geoscience*, 2, 398-401.

[205] PRENNI, A. J., DeMOTT, P. J., TWOHY, C. H., POELLOT, M. R., KREIDENWEIS, S. M., ROGERS, D. C., BROOKS, S. D., RICHARDSON, M. S. and HEYMSFIELD, A. J. (2007). Examinations of ice formation processes in Florida cumuli using ice nuclei measurements of anvil ice crystal particle residues. *Journal of Geophysical Research*, 112, D10121, doi:10.1029/2006JD007549.

[206] PRENNI, A. J., PETTERS, M. D., KREIDENWEIS, S. M., HEALD, C. L., MARTIN, S. T., ARTAXO, P., GARLAND, R. M., WOLLNY, A. G. and PÖSCHL, U. (2009). Relative roles of biogenic emissions and Saharan dust as ice nuclei in the Amazon basin. *Nature Geoscience*, 2, 402-5.

[207] PROSPERO, J. M. and LAMB, D. (2003). African Droughts and Dust Transport to the Caribbean: Climate Change Implications. *Science*, 302, 1024-7.

[208] PRUPPACHER, H. R. and KLETT, J. D. (1997). *Microphysics of clouds and precipitation* (2nd ed.). Boston, MA Kluwer Academic Publishers.

[209] PRUPPACHER, H. R. and LEE, I. (1976). A comparative study of the growth of cloud drops by condensation using an air parcel model with and without entrainment *Pure and Applied Geophysics*, 115(3), 523-45.

[210] QAMAR, S., ELSNER, M. P., ANGELOV, I. A., WARNECKE, G. and SEIDEL-MORGENSTERN, A. (2006). A comparative study of high resolution schemes for solving population balances in crystallization. *Computers and Chemical Engineering*, 30, 1119-31.

[211] RAGA, G. B., JENSEN, J. B. and BAKER, M. B. (1990). Characteristics of cumulus band clouds off the coast of Hawaii. *Journal of the Atmospheric Sciences*, 47(3), 338-5.

[212] RAGA, G. B. and JONAS, P. R. (1993). On the link between cloud-top radiative properties and sub-cloud aerosol concentrations. *Quarterly Journal of the Royal Meteorological Society*, 119, 1419-25.

[213] RAMANATHAN, V. and COLLINS, W. (1991). Thermodynamic regulation of ocean warming by cirrus clouds deduced from observations of 1987 El Nino. *Nature*, 351, 27-32.

[214] RAMANATHAN, V., CRUTZEN, P. J., KIEHL, J. T. and ROSENFELD, D. (2001). Aerosols, climate, and the hydrological cycle. *Science*, 294(7), 2119-24.

[215] RANDALL, D., KHAIROUTDINOV, M., ARAKAWA, A. and GRABOWSKI, W. (2003). Breaking the parameterization deadlock. *Bulletin of the American Meteorological Society*, 84, 1547-64.

[216] REN, C. and MACKENZIE, A. R. (2005). Cirrus parameterization and the role of ice nuclei. *Quarterly Journal of the Royal Meteorological Society*, 131, 1585-605.

[217] RIND, D. (1999). Complexity and climate. *Science* 284, 105-7.

[218] RIND, D. and LERNER, J. (1996). Use of on-line tracers as a diagnostic tool in a general circulation model development. *Journal of Geophysical Research*, 101(12), 12667-83.

[219] ROGERS, D. P., TELFORD, J. W. and CHAI, S. K. (1985). Entrainment and the temporal development of the microphysics of convective clouds. *Journal of the Atmospheric Sciences*, 42(17), 1846-58.

[220] ROSSOW, W. B. and SCHIFFER, R. A. (1999). Advances in understanding clouds from ISCCP. *Bulletin of the American Meteorological Society*, 80, 2266-88.

[221] ROTMAN, D. A., TANNAHILL, J. R., KINNISON, D. E., CONNELL, P. S., BERGMANN, D., PROCTOR, D., RODRIGUEZ, J. M., LIN, S. J., ROOD, R. B., PRATHER, M. J., RASCH, P. J., CONSIDINE, D. B., RAMAROSON, R. and KAWA, S. R. (2001). Global Modeling Initiative assessment model: Model description, integration, and testing of the transport shell. *Journal of Geophysical Research*, 106(D2), 1669-91.

[222] RUBISOV, D. H. and PAPANGELAKIS, V. G. (1997). Solution techniques for population balance equations as applied to heterogeneous aqueous processes in stirred tank reactors. *Computers and Chemical Engineering* 21(9), 1031-42.

[223] SASSEN, K. and BENSON, S. (2000). Ice nucleation in cirrus clouds: a model study of the homogeneous and heterogeneous modes. *Geophysical Research Letters*, 27(4), 521-4.

[224] SASSEN, K., DEMOTT, P. J., PROSPERO, J. M. and POELLOT, M. R. (2003). Saharan dust storms and indirect aerosol effects on clouds: CRYSTAL-FACE results. *Geophysical Research Letters*, 30(12), 1633, doi:10.029/2003GL017371.

[225] SASSEN, K. and DODD, G. C. (1998). Homogeneous nucleation rate for highly supercooled cirrus cloud droplets. *Journal of the Atmospheric Sciences*, 45(8), 1357-69.

[226] SATO, K. (1990). Vertical wind disturbances in the troposphere and lower stratosphere observed by the MU radar. *Journal of the Atmospheric Sciences*, 47(23), 2803-17.

[227] SEGAL, Y. and KHAIN, A. (2006). Dependence of droplet concentration of aerosol conditions in different cloud types: Application to droplet concentration parameterization of aerosol conditions. *Journal of Geophysical Research*, 111(D15204), doi:10.1029/2005JD006561.

[228] SEIFERT, M., STROM, J., KREJCI, R., MINIKIN, A., PETZOLD, A., GAYET, J.-F., SCHLAGER, H., ZIEREIS, H., SCHUMANN, U. and OVARLEZ, J. (2004). Aerosol-cirrus interactions: a number based phenomenon at all? *Atmospheric Chemistry and Physics*, 4, 293-305.

[229] SEINFELD, J. H. (1998). Clouds, contrails and climate. *Nature* 391, 837-8.

[230] SEINFELD, J. H. and PANDIS, S. N. (1998). *Atmospheric Chemistry and Physics*. New York, NY, USA: John Wiley and Sons.

[231] SIEBESMA, A. P. and CUIJPERS, J. W. M. (1995). Evaluation of parametric assumptions for shallow cumulus convection. *Journal of the Atmospheric Sciences*, 52(6), 650-66.

[232] SNIDER, J. R., GUIBERT, S., BRENGUIER, J. L. and PUTAUD, J.-P. (2003). Aerosol activation in marine stratocumulus clouds: 2. Kohler and parcel theory closure studies. *Journal of Geophysical Research*, 108(D15), 8629, doi:10.1029/2002JD002692.

[233] SOTIROPOULOU, R. E. P., MESKHIDZE, N., KOUATCHOU, J., DAS, B., OREOPOULOS, L., RODRIGUEZ, J. M. and NENES, A. (In review). Aerosol-cloud interactions in the NASA GMI: model development and indirect forcing assessments for sulfate aerosol. *Atmospheric Chemistry and Physics Discussions*, 7, 14295-330.

[234] SPICHTINGER, P. and GIERENS, K. (2009). Modelling of cirrus clouds – Part 2: Competition of different nucleation mechanisms. *Atmospheric Chemistry and Physics*, 9, 2319–34.

[235] SPICHTINGER, P. and GIERENS, K. M. (2009). Modeling of cirrus clouds - part 1b: Structuring cirrus clouds by dynamics. *Atmospheric Chemistry and Physics*, 9, 707-19.

[236] STOMMEL, H. (1947). Entrainment of air into a cumulus cloud. *Journal of Meteorology*, 4, 91-4.

[237] STUBER, N., FORSTER, P., RADEL, G. and SHINE, K. (2006). The importance of the diurnal and annual cycle of air traffic for contrail radiative forcing. *Nature* 441, 864-7.

[238] SU, C., KRUEGER, S. K., MCMURTRY, P. A. and AUSTIN, P. H. (1998). Linear eddy modeling of droplet spectral evolution during entrainment and mixing in cumulus clouds. *Atmospheric Research*, 47-78, 41-58.

[239] SUNDQVIST, H., BERGE, E. and KRISTJANSSON, J. E. (1989). Condensation and cloud parameterization studies with a mesoscale numerical weather prediction model *Monthly Weather Review*, 117, 1641-57.

[240] TABAZADEH, A. and JENSEN, E. J. (1997). A model description for cirrus nucleation from homogeneous freezing of sulfate aerosols *Journal of Geophysical Research*, 102(D20), 23845-50.

[241] TABAZADEH, A., JENSEN, E. J. and TOON, O. B. (1997). A model description for cirrus cloud nucleation from homogeneous freezing of sulfate aerosols. *Journal of Geophysical Research*, 102(D20), 23485-850.

[242] TABAZADEH, A., MARTIN, S. T. and LIN, J. (2000). The effect of particle size and nitric acid uptake on the homogeneous freezing of aqueous sulfuric acid particles. *Geophysical Research Letters*, 27(8), 1111-4.

[243] TABAZADEH, A., TOON, O. B. and JENSEN, E. J. (1997). Formation and implications of ice particle nucleation in the stratosphere. *Geophysical Research Letters*, 24(16), 2007-10.

[244] THOMAS, C. D., CAMERON, A., GREEN, R. E., BAKKENES, M., BEAUMONT, L. J., COLLINGHAM, Y., ERASMUS, B. F. N., FERRERA, S. M., GRAINGER, A., HANNAH, L., HUGHES, L., HUNTLEY, G. F., MILES, L., ORTEGA-HUERTA, M. A., PETERSON,

A. T., PHILLIPS, O. L. and WILLIAMS, S. E. (2004). Extinction risk from climate change. *Nature* 427, 145-8.

[245] TRENBERTH, K. E., FASULLO, J. T. and KIEHL, J. T. (2009). Earth's global energy budget. *Bulletin of the American Meteorological Society*, 90, 311-22.

[246] TWOMEY, S. (1959). The nuclei of natural cloud formation. II. The supersaturation in natural clouds and the variation of cloud droplet number concentration. *Pure and Applied Geophysics*, 43(1), 243-9, doi:10.1007/BF01993560.

[247] TWOMEY, S. (1977). *Atmospheric aerosols*. New York, NY, USA: Elsevier Scientific Publishing Co.

[248] TWOMEY, S. (1977). The influence of pollution on the shortwave cloud albedo of clouds. *Journal of the Atmospheric Sciences*, 34(7), 1149.

[249] TWOMEY, S. (1991). Aerosols, clouds and radiation. *Atmospheric Environment*, 25A(11), 2435-42.

[250] UNO, I., EGUCHI, E., YUMIMOTO, K., TAKEMURA, T., SHIMIZU, A., UEMATSU, M., LIU, Z., HARA, Y. and SUGIMOTO, N. (2009). Asian dust transported one full circuit around the globe. *Nature Geoscience*, 2, 557-60; doi:10.1038/NGEO583.

[251] VALI, G. (1994). Freezing rate due to heterogeneous nucleation. *Journal of the Atmospheric Sciences*, 51(13), 1843-56.

[252] VALI, G. (2008). Repeatability and randomness in heterogeneous freezing nucleation. *Atmos. Chem. Phys.*, 8(16), 5017-31.

[253] WALISER, D. E., LI, J. F., WOODS, C. P., AUSTIN, R. T., BACMEISTER, J., CHERN, J., DEL GENIO, A. D., JIANG, J. H., KUANG, Z., MENG, H., MINNIS, P., PLATNICK, S., ROSSOW, W. B., STEPHENS, G. L., SUN-MACK, S., TAO, W., TOMPKINS, A. M., VANE, D. G., WALKER, C. and WU, D. (2009). Cloud ice: A climate model challenge with signs and expectations of progress. *Journal of Geophysical Research*, 114(D00A21), doi:10.1029/2008JD10015.

[254] WANG, M. and PENNER, J. E. (2009). Cirrus clouds in a global climate model with a statistical cirrus cloud scheme. *Atmospheric Chemistry and Physics Discussions*, 9, 16607-82.

[255] WELTI, A., LÜÖND, F., STETZER, O. and LOHMANN, U. (2009). Influence of particle size on the ice nucleating ability of mineral dusts. *Atmospheric Chemistry and Physics*, 9, 6929-55; doi:10.5194/acpd-9-6929-2009.

[256] WHITBY, K. T. (1978). The physical characteristics of sulfur aerosols *Atmospheric Environment*, 12(1-3), 135-9.

[257] WOOD, R. (2007). Cancellation of aerosol indirect effects in marine stratocumulus through cloud thinning. *Journal of the Atmospheric Sciences*, 64, 2657-69.

[258] WOOD, S. E., BAKER, M. B. and CALHOUN, D. (2001). New model for the vapor growth of hexagonal ice crystals in the atmosphere. *Journal of Geophysical Research*, 106(D5), 4845-70.

[259] XU, K. and KRUEGER, S. K. (1991). Evaluation of cloudiness parameterizations using a cumulus ensemble model. *Monthly Weather Review*, 119, 342-67.

[260] ZOBRIST, B., KOOP, T., LUO, B., MARCOLLI, C. and PETER, T. (2007). Heterogeneous ice nucleation rate coefficient of water droplets coated by a nonadecanol monolayer. *Journal of Physical Chemistry C*, 111(5), 2149-55.

[261] ZOBRIST, B., MARCOLLI, C., KOOP, T., LUO, B., MURPHY, D. M., LOHMANN, U., ZARDINI, A., KRIEGER, U. K., CORTI, T., CZICZO, D. J., FUEGLISTALER, S.,

HUDSON, P. K. and PETER, T. (2006). Oxalic acid as a heterogeneous ice nucleus in the upper troposphere and its indirect aerosol effect. *Atmospheric Chemistry and Physics*, 6, 3115-29.

[262] ZOBRIST, B., MARCOLLI, C., PETER, T. and KOOP, T. (2008). Heterogeneous ice nucleation in aqueous solutions: the role of water activity. *Journal of Physical Chemistry A*, 112, 3965-75.

[263] ZUBERI, B., BERTRAM, A. K., CASSA, C. A., MOLINA, L. T. and MOLINA, M. J. (2002). Heterogeneous nucleation of ice in $(NH_4)_2SO_4$-H_2O particles with mineral dust immersions. *Geophysical Research Letters*, 29(10), 1504, doi:10.029/2001GL014289.